

The  
University  
Of  
Sheffield.

**Titanium Alloy Lattices with Regular  
and Graded Porosity for Dental  
Implant Applications**

**Zena J. Wally**

**A Thesis Submitted in Partial Fulfillment of the**

**Requirements for the Degree of**

**Doctor of Philosophy**

**Department of Materials Science and Engineering**

**University of Sheffield**

**United Kingdom**

**October 2018**

**Abstract**

Interconnected porous titanium components prepared by additive manufacturing technologies have a great potential in dental and orthopaedic implants, due to their biocompatibility, lower stiffness and larger surface area compared to dense structures. Therefore they should permit better bone-implant integration. Graded porosity may provide large pores for bone ingrowth on the periphery of an implant and a denser core to sustain mechanical loading. However, the optimal porosity and structure for the mechanical and biological performance of load-bearing implants remains undefined. Given the small size of dental implants it is very challenging to achieve gradations in porosity. Therefore, this thesis aimed to develop a range of lattices from the titanium alloy Ti-6Al-4V of regular and graded porosity via selective laser melting. The effects of pore variance on mechanical and biological properties were investigated. These lattices were designed to be rod-shaped with dimensions representing the size of current dental implants. Surface chemistry and mechanical properties of these components were investigated. The potential to support bone in-growth was evaluated by direct seeding of bone cells on the lattices and cell viability, and extracellular matrix deposition was evaluated. To evaluate cell migration, an *in vitro* 3D culture model was invented; the porous Ti-6Al-4V lattices were implanted into a ring of porous polymer sponge that had been pre-seeded with bone-forming cells. Our results confirmed that Ti-6Al-4V lattices were duplicated from the CAD models and characterised by interconnected porosity. Mechanical tests revealed good strength properties comparable to bone tissue, but a dense core was required to maintain strength in the high porosity structures. All samples were a suitable for growing osteoblast cells and supporting bone formation with good mineral deposition. It was demonstrated that a tissue engineering approach could be used to examine optimum cell migration and extracellular bone matrix deposition on the implanted titanium *in vitro* and bone formation within the pores of the implanted titanium after explantation was confirmed.

**Acknowledgements**

I am very grateful to the great and almighty God, Allah for giving me the strength to undertake this project and to keep me till the end of my PhD. I would like to express my gratitude to my primary supervisor, Dr. Gwendolen Reilly for her constant help, guidance and encouragement during the period of my research. Without her support, this achievement would not have been possible. I cannot express enough thanks to my secondary supervisors Dr Russell Goodall and Dr Frederik Claeysens for their contribution towards this project. I would also like to thank Abdul Haque and the Medical Advanced Manufacturing Research Centre, UK for designing and manufacturing variant of titanium lattices based on a sample configuration that I sketched in the early stage of this study. A special mention should go to my colleagues, Hossein for modifying and translating the initial sketching to the ‘spider web’ design used in this thesis, Rob, Dirar, Liam and Julie for their advice and suggestions that were very helpful for my experiments. My appreciation goes to Dr Nicola Green for the confocal imaging. I would especially like to thank the University of Kufa, Iraqi cultural attache and the Iraqi Ministry of Higher Education and Scientific Research, who gave me the opportunity to study in the United Kingdom at their full expense. I also wish to thank my extended family members, especially my sisters, brothers, mother in-law, sisters-in-law, brothers-in-law, who have prayed for me throughout this journey. My deepest appreciation goes to my wonderful husband, Ibrahem for his never ending support and motivation, particularly during the tough times. A very special thank you to my lovely children Maryam, Mustafa and Mohammed for their understanding and patience during the long hours I spent in the lab and writing my papers and this thesis. Finally, I would like to thank my late father Jihad W. Malik who taught me to love learning. My mother Saadiyah Awad passed away when I was studying my PhD, thank you Mum for showing me that the key to life is praying. Now I want to dedicate my thesis to her memory.

**Dedication**

*I dedicate this work to my:*

- *Late Mother Saadiyah Awad ...*
- *Late Father Jehad Wally ...*
- *Wonderful Husband Ibrahim ...*
- *Lovely Children Maryam, Mustafa & Mohammed ...*

*I could not have done this without you all!*

## **Publications**

### **Review Papers**

1. **Wally, Z.J.**, van Grunsven, W., Claeysens, F., Goodall, R., Reilly, G.C., 2015. Porous Titanium for Dental Implant Applications. *Metals (Basel)*. 5, 1902–1920.  
A full copy of this publication is available in the appendix, 9.1.

### **Research Papers**

1. **Wally, Z.J.**, Haque, A.M., Feteira, A., Claeysens, F., Goodall, R., Reilly, G.C., 2019. Selective Laser Melting processed Ti-6Al-4V lattices with graded porosities for dental applications. *J. Mech. Behav. Biomed. Mater.* 90, 20–29.  
A full copy of this publication is available in the appendix, 9.2.
2. Elbadawi, M., **Wally, Z.J.**, Reaney, I.M., 2018. Porous hydroxyapatite-bioactive glass hybrid scaffolds fabricated via ceramic honeycomb extrusion. *J. Am. Ceram. Soc.* 101, 3541–3556.
3. Bhaskar, B., Owen, R., Bahmaee, H., **Wally, Z.**, Sreenivasa Rao, P., Reilly, G.C., 2018. Composite porous scaffold of PEG/PLA support improved bone matrix deposition *in vitro* compared to PLA-only scaffolds. *J. Biomed. Mater. Res. Part A* 106, 1334–1340.

### **Publications in Preparation**

1. Shbeh, M, **Wally, Z.**, Elbadawi M, Mosalagae M, Al-Alak, H., Reilly, G., Goodall, R. Incorporation of HA into Porous Titanium to Form Ti-HA Biocomposite Foams. Submitted to *Journal of the Mechanical Behavior of Biomedical Materials*.

### ***Publications and conferences***

2. **Wally, Z.J.**, Haque, A.M., Nicola H.Green., Claeysens, F., Goodall, R., Reilly, G.C., “*In vitro* 3D Culture Model for 3D printed porous titanium alloy dental implant testing.
3. **Wally, Z.J.**, Haque, A.M., Feteira, A., Claeysens, F., Goodall, R., Reilly, G.C. Biological assessment of Ti-6Al-4V microparticles used for Selective Laser Melting process.

### **Conferences**

#### **Oral Presentations**

1. Porous Titanium for Dental Implant Applications. The 16th MEIbioeng conference, Keble College, Oxford, UK. 5-6 September 2016.
2. Selective Laser Melted Ti6Al4V with graded porosity for Dental Implants”, 96th General Session and Exhibition of the International Association for Dental Research (IADR). the ExCeL London Convention Center, London, UK. 25-28th July 2018.

#### **Poster Presentations**

1. A comparison of Core and Non-Core Based Lattices with Regular and Graded Porosity for Improved Dental Implant Design. United Kingdom Society for Biomaterials 15th Annual Conference (UKSB), University of Westminster, UK. 30th June-1st July 2016.
2. Titanium (Ti-6Al-4V) lattices via Selective Laser Melting (SLM) for Dental and Orthopaedic Applications”, ORS 2017 Annual Meeting, San Diego Convention Center in San Diego, California, USA. 19-22 March 2017.

***Publications and conferences***

3. Porous Ti-6Al-4V Lattices for Dental Implants Fabricated by Selective Laser Melting. The 23rd ESB Congress. the Higher Technical School of Engineering of the University of Seville, Spain. 2nd - 5th of July 2017.
4. *In vitro* Biological Properties of Additive Manufactured Porous Ti-6Al-4V Surfaces for Dental Implants. 28th Annual Meeting of the European Society for Biomaterials (ESB), Athens, Greece. 4 - 8 September 2017.
5. *In vitro* 3D Culture Model for Bone Cell Ingrowth. Biomaterials & Tissue Engineering Group 19th Annual White Rose Work in Progress Meeting, University of Leeds, UK. 18th December 2017.

**Table of Contents**

Abstract ..... I  
Acknowledgements ..... II  
Dedication ..... III  
Publications ..... IV  
Conferences ..... V  
Table of Contents ..... VII  
List of Figures ..... XIII  
List of Tables ..... XXI  
Abbreviations ..... XXIII  
Nomenclature ..... XXV  
Chapter 1 : Introduction ..... 1  
Chapter 2 : Review of the literature ..... 7  
    2.1 Dental implant – types, materials and osseointegration ..... 7  
        2.1.1 Implant designs ..... 7  
        2.1.2 Dental implant materials ..... 10  
            2.1.2.1 Titanium and its alloys as dental implant materials ..... 12  
        2.1.3 Bone implant integration ..... 15  
            2.1.3.1 Bone physiology, composition, formation, remodelling and properties 15  
                2.1.3.1.1 Bone anatomy ..... 15  
                2.1.3.1.2 Bone composition ..... 17  
                2.1.3.1.3 Cell biology and formation of bone ..... 19  
                2.1.3.1.4 Bone remodelling ..... 21  
                2.1.3.1.5 Mechanical properties of bone ..... 22  
            2.1.3.2 Osseointegration of dental implants ..... 25  
    2.2 Load transfer in dental implants ..... 26  
    2.3 Surface Modifications to improve ososseointegration ..... 28  
    2.4 Factors affecting dental implant failures ..... 31  
    2.5 *In vitro* and *in vivo* testing ..... 32  
    2.6 *In vitro* bone model ..... 32  
    2.7 Characteristic features of porous metal ..... 34  
    2.8 Fabrication methods and mechanical evaluation of porous dental implants ..... 38  
    2.9 Selective laser melting ..... 47



2.10 Biological interaction and porous surface geometry .....	48
2.11 Chapter summary .....	52
2.12 Thesis Aim and Objectives .....	53
Chapter 3 : Materials and Methods .....	56
3.1 Introduction .....	56
3.2 Ti-6Al-4V Powder Particles .....	56
3.3 Fabrication of Selective Laser Melting (SLM) Ti-6Al-4V lattices .....	58
3.4 Sample preparation.....	58
3.4.1 Ti-6Al-4V lattices .....	58
3.4.2 Polyurethane (PU) scaffolds .....	59
3.3 Structural characterisation .....	61
3.3.1 Scanning Electron Microscopy (SEM) and Energy Dispersive X-Ray Spectroscopy (EDX).....	61
3.3.1.2 Ti-6Al-4V lattices without cells.....	61
3.3.1.2 Ti-6Al-4V lattices with cells.....	61
3.3.2 Micro-computed tomography (MicroCT).....	62
3.3.3 Archimedes method .....	62
3.4 Chemical Characterization .....	62
3.4.1 Inductively Coupled Plasma Optical Emission Spectroscopy (ICP-OES) Analysis .....	62
3.4.2 LECO (Laboratory Equipment Corporation) Analysis.....	63
3.5 Mechanical Characterization of SLM Ti-6Al-4V lattices in compression and three-point bending test.....	63
3.6 Powder removal measurement .....	63
3.7 Biological Characterization.....	63
3.7.1 Materials .....	64
3.7.2 Cultured cell lines .....	64
3.7.2.1 MLO-A5 Murine Cells .....	64
3.7.2.2 Human mesenchymal stem cells from bone marrow (hBMSCs).....	65
3.7.2.3 MG-63 Human Osteosarcoma Cells .....	65
3.7.3 Culture media compositions .....	65
3.7.4 General cell culture conditions .....	66
3.7.5 Cell seeding .....	67
3.7.5.1 Monolayer cell culture .....	67

3.7.5.2 Three-Dimensional Cell Culture.....	68
3.7.6 Metabolic activity assay .....	68
3.7.7 Calcium Staining Assay.....	69
3.7.8 Collagen Staining Assay.....	70
3.7.9 Xylenol Orange.....	71
3.7.10 Cell fixation .....	72
3.7.11 Statistical Analysis .....	72
Chapter 4 : Characterisation and Mechanical Properties of SLM processed Ti-6Al-4V lattices. ....	73
4.1 Introduction .....	73
4.2 Aim.....	76
4.3 Materials and Methods .....	77
4.3.1 Design and fabrication of porous Ti-6Al-4V lattices .....	77
4.3.1.1 Unit cell and CAD design .....	77
4.3.1.2 Selective Laser Melting for the production of porous Ti-6Al-4V .....	80
4.3.2 Structural Characterization .....	83
4.3.2.1 Scanning electron microscopy and energy dispersive X-ray spectroscopy .....	83
4.3.2.2 Inductively Coupled Plasma Optical Emission Spectroscopy (ICP-OES) Analysis.....	83
4.3.2.3 LECO (Laboratory Equipment Corporation) Analysis.....	83
4.3.2.4 Micro-Computed Tomography (MicroCT).....	84
4.3.2.5 Archimedes method .....	85
4.3.3 Mechanical Testing.....	85
4.3.3.1 Compression testing.....	85
4.3.3.2 Three-point bending testing .....	87
4.4 Results .....	89
4.4.1 Structural characterisation .....	89
4.4.1.1 SEM and EDX .....	89
4.4.1.2 ICP-OES and LECO analysis .....	93
4.4.1.3 Micro-Computed Tomography .....	94
4.4.1.4 Archimedes method .....	97
4.4.2 Mechanical testing .....	99
4.4.2.1 Compression test.....	99

4.4.2.2 Three-point bending test .....	105
4.5 Discussion .....	111
4.6 Chapter summary .....	118
Chapter 5 : Biological Assessment of Porous Ti-6Al-4V Lattices .....	119
5.1 Introduction .....	119
5.2 Aim.....	121
5.3 Methods.....	121
5.3.1 Ultrasonic cleaning of components and measurement of unfused particles released .....	121
5.3.2 Cytotoxicity analysis of Ti-6Al-4V particles on bone cells growth .....	122
5.3.3 Cell culture on SLM Ti-6Al-4V lattices .....	124
5.4 Results .....	126
5.4.1 Removal of Unfused Ti-6Al-4V Powder Particles from SLM Processed Components .....	126
5.4.1.1 The number of loose particles significantly reduced with time 2h post cleaning. ....	126
5.4.1.2 Particles ranged 15-25 micron were the highest at all cleaning periods .....	127
5.4.1.3 The average mass of total particles release form 30 mm Ti-6Al-4V lattices was about 30 mg. ....	128
5.4.2 Cytotoxicity.....	130
5.4.2.1 No toxic effect of Ti-6Al-4V particles up to 10 mg/ml on MLO-A5 .....	130
5.4.2.2 No toxic effect of Ti-6Al-4V particles up to 10 mg/ml on hBMSCs cells.....	133
5.4.2.3 No toxic effect of Ti-6Al-4V particles up to 10 mg/ml on hBMSCs cells with OGM .....	136
5.4.3 Cell culture on Ti-6Al-4V scaffolds .....	139
5.4.3.1 SLM Ti-6Al-4V scaffolds supported cell viability of MLO-A5 cells over 28 days of cell culture .....	139
5.4.3.2 Calcium and collagen staining .....	141
5.4.3.3 Scanning electron microscopy .....	143
5.5 Discussion .....	147
5.6 Chapter summary .....	153

Chapter 6 : *In vitro* 3D Culture Model for Testing 3D Printed Porous Dental Implant ..... 154

6.1 Introduction ..... 154

6.2 Aim..... 157

6.3 Methods ..... 157

6.3.1 Cell migration using Eclipse fluorescent microscope ..... 157

6.3.2 Cell culture..... 159

6.3.3 Culture conditions..... 160

6.3.4 Experimental groups ..... 162

6.4 Results ..... 164

6.4.1 The migration potential of MLO-A5 cells is higher than that of MG63 cells ..... 164

6.4.2 Experiment 1: PU scaffolds can support MLO-A5 cells attachment and proliferation over long-term (56 days) ..... 166

6.4.2.1 Cell Viability..... 166

6.4.2.2 Calcium and collagen production ..... 167

6.4.3 Experiment 2: Increasing cell density (30,000 and 60,000) of MLO-A5 does not affect calcified minerals and extracellular deposition on implanted Ti-6Al-4V lattices ..... 168

6.4.3.1 Cell Viability..... 168

6.4.3.2 Calcium and collagen production ..... 169

6.4.4 Experiment 3: A narrow connection between PU and Ti scaffolds enables cell migration and bone matrix deposition ..... 170

6.4.4.1 Cell Viability..... 171

6.4.4.2 Calcium and collagen production ..... 172

6.4.5 Experiment 4: The migration of osteoblasts and deposition of extracellular matrix into the implanted Ti-6Al-4V lattices (GP/400-300 and SW) increased with longer implantation time..... 173

6.4.5.1 Cell Viability..... 173

6.4.5.2 Calcium and collagen production ..... 174

6.4.5.3 Scanning electron microscopy ..... 176

6.4.5.4 Xylenol orange staining ..... 177

## *List of Contents*

6.4.6 Experiment 5: Bone marrow human mesenchymal stem cells (hBMSCs) are able to migrate into the implanted constructs after 42 days of implantation and produce a mineralised extracellular matrix.....	179
6.4.6.1 Cell Viability.....	179
6.4.6.2 Calcium and collagen production .....	180
6.4.6.3 Scanning electron microscopy .....	181
6.4.6.4 Xylenol orange staining .....	182
6.5 Discussion .....	184
6.6 Chapter summary .....	188
Chapter 7 : Conclusions and future perspectives .....	190
7.1: Conclusions .....	190
7.2: Future perspectives.....	195
Chapter 8 : References .....	197
Chapter 9 : Appendix .....	222
9.1 Porous Titanium for Dental Implant Applications .....	222
9.2 Selective Laser Melting processed Ti6Al4V lattices with graded porosities for dental applications .....	241
9.3 Fabrication of 3- Dimensional Porous Poly (ethylene glycol) Diacrylate Template by Microstereolithography. ....	251
9.3.1 Introduction.....	251
9.3.2 Materials and methods .....	252
9.3.2.1 Structure design .....	253
9.3.2.2 Preparing Prepolymer and light absorber .....	254
9.3.2.3 Structure fabrication.....	255
9.3.3 Results .....	256
9.3.4 Discussion.....	261
9.3.5 Conclusions .....	262
9.3.6 References.....	263
9.4 Renishaw system data sheet .....	264
9.5 Material validation sheet of the Renishaw system .....	266

**List of Figures**

Figure 1.1 A diagram shows the main parts of natural tooth (left) and dental implant (right). Adapted from <https://www.orthodontisteenligne.com/en/dental-implants/>..... 2

Figure 2.1 Design and radiographic images of the commercially available dental implants inserted in the jawbone, (A) threaded cylindrical-shaped or (B) conical (root)-shaped and (C) pressfit. A and B Adapted from Baltic Osseointegration Academy/Public Information (<http://www.boaoffice.lt/EN/9/>) and (Alghamdi, 2018), (C) Adapted from [https://www.medeco.de/zahnheilkunde\\_dentalatlas/implantologie/implantatformen](https://www.medeco.de/zahnheilkunde_dentalatlas/implantologie/implantatformen). .... 9

Figure 2.2 The design of the commercially available “Trabecular Metal™” enhanced titanium dental implants (left) and the cross sectional of the middle-third of the implant that has outer layer of porous tantalum and dense titanium (right). Adapted from (Liu et al.2015). .... 10

Figure 2.3 The structure of cortical and trabecular bone of the human (A) maxilla (B) mandible. Adapted from (<https://pocketdentistry.com/11-bone-density/>)..... 16

Figure 2.4 General structure of bone. Adapted from (Jiroušek, 2012), Under Creative Commons Attribution License. .... 17

Figure 2.5 Hierarchical structure of bone. Adapted from (Kane and Ma, 2013)..... 19

Figure 2.6 Bone remodeling cycle. Adapted from (Ralston, 2009)..... 22

Figure 2.7 Bone Classification according to density. Adapted from (Alghamdi, 2018). .... 24

Figure 2.8 Young’s modulus versus apparent density of bone types 1, 2, 3 and 4. Adapted from (Seth and Kalra, 2013). .... 24

Figure 2.9 Pictures show different patterns of bone formation (A) distance osteogenesis, where the osteogenic cells line the surrounded bone and there is a gap between the cells and the surface of the implant and (B) contact osteogenesis, where bone is formed directly on the implant surface. Adapted from (Davies, 2003)..... 26

Figure 2.10 Diagram describing biological objective of surface coatings on dental implants. Bioactive materials able to be delivered to the surrounded bone, osteogenic factors help to increase osteoblast differentiation and mineralization. Adapted from (Alghamdi, 2018)..... 30

Figure 2.11 SEM images of different diameter sizes of TiO<sub>2</sub> nanotubes, (A) 30; (B) 50; (C) 70 and (D) 100 nm using 200 nm scale bar. Adapted from (Yi et al., 2015). .... 31

## List of Figures

Figure 2.12 (A) SEM image of graded diamond lattice structure; (B) Micro CT scan of 3D image shows different strut thicknesses. Adapted from (van Grunsven, 2014).....	36
Figure 2.13 SEM images of dental root implants fabricated by the SLM and SLS processes with two different zones, (A) the sintered zone close to the surface and (B) the remelted core. Adapted from (Tolochko et al., 2002).....	44
Figure 2.14 CAD model of dental root implant with porous covering (A), built SLM titanium cylinder (15 x 15 mm <sup>2</sup> ) (B) with pore/channel (100 - 200 µm) on surface. Adapted from (Laoui et al., 2006).....	44
Figure 2.15 Selective laser melting process schematic. Adapted from <a href="https://www.fusionimplants.com/r-d/">https://www.fusionimplants.com/r-d/</a> .....	48
Figure 3.1 SEM image of Ti-6Al-4V powder particles at x120 magnification, Adapted from Material validation sheet of Renishaw's titanium alloy (Ti-6Al-4V) (appendix 9.5). .....	57
Figure 3.2 Particle size distribution of Ti-6Al-4V powder used for Renishaw system. Reprinted from Material validation sheet of Renishaw's titanium alloy (Ti-6Al-4V) (appendix 9.5). .....	57
Figure 3.3 Sectioning Ti-6Al-4V lattices (A) Secotom-50 cutting machine (B) 11-4217-010 diamond cut-off wheel (C) Ecomet-250 grinder - polishing machine (D) Ti-6Al-4V lattices before cutting (E) Ti-6Al-4V lattices after cutting. ....	59
Figure 3.4 Epilog Mini laser cutter machine (B) PU scaffold with initial size dimensions (B) Final size dimensions used for the <i>in vitro</i> 3D culture model. ....	60
Figure 3.5 Standard curve for the calcium staining assay. This can be used to convert plate reader absorbance to a known concentration of stain. ....	70
Figure 3.6 Standard curve for the collagen staining assay. This can be used to convert plate reader absorbance to a known concentration of stain. ....	71
Figure 4.1 Initial construct profile used to design the variants of SLM Ti-6Al-4V lattices. ....	78
Figure 4.2 A diamond unit cell built on 3 planes used to design the variants of SLM Ti-6Al-4V lattices. ....	78
Figure 4.3 The CAD models of the variant lattices built on the diamond unit cell: P400/1C, P650/1C and GP/650-400, prototype shown in 3-matics software, provided by Abdul M Haque who manufactured them at the Advanced Manufacturing Research Centre. ....	79

Figure 4.4 The CAD model of the ‘Spider Web’ prototype shown in 3-matics software. .... 79

Figure 4.5 Renishaw AM250 used to build the variants of SLM Ti-6Al-V lattices.... 82

Figure 4.6 Post-build Ti-6Al-4V samples of (A) ‘Spider Web’ (diameter = 4.33 mm and height = 6.76 mm) built horizontally and (B) variant of diamond unit cell lattices built vertically (diameter = 5 mm and height = 20 mm) on the building substrate, yellow arrows indicate building direction..... 82

Figure 4.7 Ti-6Al-4V sample under the compression plates of the Zwick Roell machine. .... 87

Figure 4.8 Stress-strain curve with the trend lines that were used to determine the Young’s modulus and yield strength at 0.2% offset. .... 87

Figure 4.9 Three-point bending test to measure flexural strength of Ti-6Al-4V samples using the Zwick Roell machine..... 89

Figure 4.10 SEM images of diamond unit cell lattices A- P400, B- P400/1C, C- P650, D- P650/1C, E- GP/650-400 and F-‘Spider Web’, yellow arrows show closed porosity, (scale bar: 500  $\mu$ m). .... 90

Figure 4.11 Representative SEM images with EDX analysis of Ti-6Al-4V lattices of A- P400, B- P650, C- GP/400-300 and D- ‘Spider Web’, scale bar: 500  $\mu$ m. .... 92

Figure 4.12 MicroCT reconstruction images, top (side view) and bottom (cross - section) of P400, P400/1C, P400/2C, P650, P650/1C, GP/650-400, GP/400-300 and ‘Spider Web’ lattices, (scale bar=1mm). .... 95

Figure 4.13 Comparison between open and total (%) of P400, P400/1C, P400/2C, P650, P650/1C, GP/650-400, GP/400-300 and ‘Spider Web’ lattices measured by MicroCT. .... 97

Figure 4.14 Comparison between overall porosity (%) of P400, P400/1C, P400/2C, P650, P650/1C, GP/650-400, GP/400-300 and ‘Spider Web’ lattices measured by MicroCT and Archimedes..... 98

Figure 4.15 Silhouette images obtained from the video extensometer at different time points (minutes) in Zwick Roell testing machine showing the failure mode of the various SLM Ti-6Al-4V lattices; P400, P400/1C, P650, P650/1C, GP/650-400 and ‘Spider Web’ before and after compression. .... 100

Figure 4.16 Figure 4.16 Stress-strain curves obtained by compression test of the eight Ti-6Al-4V lattices; P400, P400/1C, P400/2C, P650, P650/1C, GP/650-400, GP/400-300 and Spider Web, (n=6). Samples were tested in compression at 1 mm/min speed,



20 kN load cell and 10 kN maximum force in Zwick Roell machine. Each line is the stress/stress curve for an individual sample. .... 101

Figure 4.17 A comparison of the mechanical properties in compression test (A) Mean  $\pm$  SD Young’s modulus, (B) Mean  $\pm$  SD yield strength of the regular and graded Ti5Al4V lattices plotted against % mean porosity by volume as assessed by MicroCT. .... 105

Figure 4.18 Ti-6Al-4V sample during three-point bending test to measure flexural strength using the Zwick Roell machine. .... 106

Figure 4.19 Linear force–displacement curves and images of the Ti-6Al-4V lattices; P400, P400/1C, P400/2C, GP/400-300 and Spider Web, tested in three-point bending (n=3). Each line is the force curve for an individual sample. .... 107

Figure 4.20 A comparison of the mechanical properties in three-point bending test (A) Mean  $\pm$  SD flexural modulus, (B) Mean  $\pm$  SD flexural strength of the regular and graded Ti5Al4V lattices plotted against % mean porosity by volume as assessed by CT scan. .... 110

Figure 5.1 Representative image under a light microscope showing particle distribution (black dots) on squares of the haemocytometer, scale bar=250  $\mu$ m. .... 122

Figure 5.2 Photograph of well plates used for *in vitro* 2D cytotoxicity test of Ti-6Al-4V microparticles used for two types of bone cells (MLO-A5 and hBMSCs). .... 124

Figure 5.3 Cell viability standard curve of 2D cell culture on different cell numbers. Points represent mean  $\pm$  SD, n=6. .... 125

Figure 5.4 (A) Number of Ti-6Al-4V particles released from SLM Ti-6Al-4V lattices after different cleaning periods (15, 30 mins and, 1, 2, 4, 8, 16, 32, 64 and 128 hours) in an ultrasonic bath. (B) SEM image reveals partially fused particles in the SLM Ti-6Al-4V lattices after the longest cleaning time. .... 127

Figure 5.5 Percentage of Ti-6Al-4V particles at each diameter range ( $\mu$ m) released from SLM Ti-6Al-4V lattices after different cleaning periods (15, 30 mins and 1, 2, 4, 8, 16, 32, 64 and 128 hours) in an ultrasonic bath. .... 128

Figure 5.6 (A): Mass (mg) of Ti-6Al-4V particles released from SLM Ti-6Al-4V lattices after different cleaning periods (1/4, 1/2, 1, 2, 4, 8, 16, 32, 64 and 128 hours) in an ultrasonic bath. (B): Percent of Ti-6Al-4V particles released from SLM Ti-6Al-4V lattices at each cleaning period. (C) An average of total mass of Ti-6Al-4V particles collected from all cleaning periods (n=3). .... 129

Figure 5.7 Cytotoxicity of Ti-6Al-4V micro particles with different concentrations (0, 2.5, 5, 7.5, 10, 25, 50 and 100 mg/ml) on the metabolic activities of MLO-A5 cells seeded on 2D well plate over 7 days in respect of (A) fluorescence value of RR to time, (B) relative viability to time and (C) relative viability to the mass of particles. These data are expressed as the means  $\pm$  SD of three independent experiments performed in triplicate (n=9). ..... 131

Figure 5.8 Representative images under light microscope showing MLO-A5 cell growth on a 2D well plate with different concentrations (0, 2.5, 5, 7.5, 10, 25, 50 and 100 mg/ml) of Ti-6Al-4V powder particles after day 1, 3 and 7, scale bar= 100  $\mu$ m. .... 132

Figure 5.9 Cytotoxicity of Ti-6Al-4V micro particles with different concentrations (0, 2.5, 5, 7.5, 10, 25, 50 and 100 mg/ml) on the metabolic activities of hBMSCs cells seeded on 2D well plate over 14 days in respect of A= fluorescence value of RR, B= relative viability to time and C= relative viability to mass of particles. These data are expressed as the means  $\pm$  SD of three independent experiments performed in triplicate for (n=9). ..... 134

Figure 5.10 Representative images under light microscope showing hBMSCs cells growth on 2D well plate with different concentrations (0, 2.5, 5, 7.5, 10, 25, 50 and 100 mg/ml) of Ti-6Al-4V powder particles after day 1, 3, 7 and 14, scale bar = 100  $\mu$ m. .... 135

Figure 5.11 Cytotoxicity of Ti-6Al-4V micro particles on hBMSCs cells precultured with OGM at different concentrations (0, 2.5, 5, 7.5, 10, 25, 50 and 100 mg/ml). Metabolic activity of cells seeded on 2D well plate over 14 days measured by RR assay. (A) fluorescence value, (B) relative viability to time and (C) relative viability to mass of particles. These data are expressed as the means  $\pm$  SD of three independent experiments performed in triplicate for (n=9). ..... 137

Figure 5.12 Representative images under light microscope showing hBMSCs cell growth on 2D well plate with OGM and different concentrations (0, 2.5, 5, 7.5, 10, 25, 50 and 100 mg/ml) of Ti-6Al-4V powder particles after day 1, 3, 7 and 14, scale bar = 100  $\mu$ m. .... 138

Figure 5.13 Mean  $\pm$  SD of preliminary results of resazurin fluorescence as a measure of (A) cell attachment at day 1 and (B) metabolic activity of MLO-A5 cells on P400, P400/1C, P650, P650/1C, GP/650-400 and ‘Spider Web’ scaffolds over 28 days of cell culture, (n=6). ..... 139

## List of Figures

Figure 5.14 Yellow arrows on light microscopic image show MLO-A5 cells attachment on ‘Spider Web’ scaffold after 28 days (A). Mean $\pm$ SD of resazurin fluorescence as a measure of (B) cell attachment and (C) metabolic activity of MLO-A5 cells on P400, P400/1C, P400/2C, GP/400-300 and ‘Spider Web’ scaffolds over 28 days of cell culture, (n=9).....	140
Figure 5.15 Day 28 Calcium and collagen staining before destaining on P400, P400/1C, P400/2C, GP/400-300 and ‘Spider Web’ scaffolds seeded with MLO-A5cells.....	141
Figure 5.16 Mean $\pm$ SD for (A) ARS staining of MLO-A5on P400, P400/1C, P650, P650/1C, GP/650-400 and ‘Spider Web’ scaffolds (B) SR staining on day 28 of cell culture, (n=6).....	142
Figure 5.17 Mean $\pm$ SD for (A) ARS staining of MLO-A5on P400, P400/1C, P400/2C, GP/400-300 and ‘Spider Web’ scaffolds (B) SR staining on day 28 of cell culture, (n=9). .....	142
Figure 5.18 Representative SEM images of scaffolds only (left) and MLO-A5cells on P400 after 28 days of cell culture using different scale bars (1000, 500, 100 and 20 $\mu$ m) The scaffold surface is covered with cellular material. ....	144
Figure 5.19 EDX spectrum analysis of carbon coated Ti-6Al-4V components (A) blank P400 and the extracellular matrix deposition produced by MLO-A5cells on cell seeded (B) P400, (C) P400/1C, (D) P400/2C, (E) GP/400-300 and (F) spider web after 28 of cell culture. The result of EDX shows the presence of the calcium and phosphorous beside Ti-6Al-4V elements, scale bar 200 $\mu$ m.....	146
Figure 6.1 Image shows dental implant placing into the mandible of Wistar male rat, Adapted from (Semenoff-Segundo et al., 2015). ....	155
Figure 6.2 Cell migration measurement of MLO-A5 and MG63 cells in two dimensions culture under Eclipse fluorescent microscope chamber, the microscope was controlled by 5% CO <sub>2</sub> at 37°C. Cells were monitored by taking pictures at 20 minutes regular intervals over 24 hours. ....	158
Figure 6.3 3D <i>in vitro</i> bone model for implant testing, PU scaffolds implanted with 3D printed titanium lattices (scale bar = 5 mm) (A) and maintained over long-term (28 and 42 days) in a cultured media (scale bar = 10 mm) (B), images taken at day 0 insertion. .....	160
Figure 6.4 Culture conditions used for the <i>in vitro</i> 3D bone model including time of insertion titanium implants into PU scaffolds and duration of implantation period, A-	

titanium inserted at day 0, 4 and 28 and implanted for 28 days. B-titanium inserted at day 0 and 7 and implanted either for 28 or 42 days. .... 161

Figure 6.5 An overview of cell migration analysis of MLO-A5 and MG63 cells. The migration potential of 10 cells of (A) MLO-A5 and (C) MG63 from each well was determined every 20 minutes over 24 hours (1440 minutes). The yellow arrows on two images show individual (B) MLO-A5 and (C) MG63 cell movement during 20 minutes. (E) The bar chart represents mean  $\pm$  SD for significant differences in average total distance movement in pixel per 24 hours..... 165

Figure 6.6 Metabolic activity of MLO-A5 cells on PU scaffold and titanium with different insertion times (day 0, 4 and 28) at (A) day 1 after cell seeding which represent cell attachment on PU scaffolds and well plates (B) several time points (1, 4, 7, 14, 21, 28, 32, 35, 42, 49 and 56) (n=9)..... 166

Figure 6.7 Mean  $\pm$  SD for (A) ARS staining and (B) SRS staining of MLO-A5 cells on PU scaffold on day 28 of cell culture, (n=9)..... 167

Figure 6.8 Mean  $\pm$  SD for the metabolic activity of MLO-A5 cells with different cell densities (30,000 and 60,000) on PU scaffold and titanium inserted either at day 0 and 7, at (A) day 1 after cell seeding which represents cell attachment on PU scaffolds and well plates (B) at several time points (1, 7, 14, 21, 28, and 35), n=9. \*\*\*\* indicates  $p < 0.0001$ . .... 169

Figure 6.9 Mean  $\pm$  SD for the quantitative analysis of (A- B) Alizarin Red Destaining and (C) Sirius Red Destaining of MLO-A5 cells on PU Scaffold and extracted titanium after 28 days, (n=9). \*\*\*\* indicates  $p < 0.0001$ ..... 170

Figure 6.10 Mean  $\pm$  SD for the metabolic activity of MLO-A5 cells on (A) PU scaffolds with a different inner diameter (4.5 and 3.5 mm) and titanium inserted at day 0 and 7 at different time points over 28 days of implantation. (B) PU and titanium after extraction with 28 days implantation. (C) Microscopic photographs show MLO-A5 cells migration from PU scaffolds into implanted titanium after 28 days implantation, n=9. \* indicates  $p < 0.05$ . .... 172

Figure 6.11 Mean  $\pm$  SD for calcium (A) and collagen (B) staining of MLO-A5 cells on the PU scaffolds with 3.5 and 4.5 mm inner diameter and titanium with day 0 and 7 insertions after 28 days. (C) Photograph of mineral deposition on extracted titanium and PU scaffolds with 3.5 mm inner diameter after 28 days implantation, (n=9)..... 173

Figure 6.12 Mean  $\pm$  SD for the cell viability of MLO-A5 cells on PU scaffold, and titanium lattices (GP/400-300 and SW) inserted at day 0 and 7 at (A) Indicates cell

*List of Figures*

attachment on PU scaffolds and wells at day 1 after cell seeding and (B) at several time points (1, 7, 14, 21, 28, 35, 42, 49, and 56) (C) After 28 and 42 days of explanting titanium from PU scaffolds, (n=9). ..... 174

Figure 6.13 Mean  $\pm$  SD for calcium (A) and collagen (B) staining of MLO-A5 cells after 28 days implantation on the PU scaffolds 3.5 mm inner diameter and titanium (GP/400-300 and SW) inserted at day 0 and 7 and implanted for 28 and 42 days, ( n=9). ..... 175

Figure 6.14 Organic material, and extracellular matrix cover cell seeded Ti-6Al-4V surfaces and are distributed across the porosity after 42 days of insertion into PU scaffolds. A dense cell layer was found covering the entire surfaces of PU scaffolds. .... 176

Figure 6.15 Confocal microscopy images of xylenol orange stained mineralised deposits of MLO-A5 cells cultured on auto-fluorescent PU scaffolds and implanted titanium lattices (GP/400-300 and spider web) implanted for 28 and 42 days using two insertion conditions (day 0 and day7), scale bar=100  $\mu$ m. .... 178

Figure 6.16 Mean  $\pm$  SD for the cell viability of hBMSCs cells on PU scaffold, and titanium lattices (GP/400-300) inserted at day 0 and 7, (A) Indicates cell attachment on PU scaffolds and well at day 1 after cell seeding (B) At several time points (1, 7, 14, 21, 28, 35, 42, 49, and 56) (C) After explanting implanted titanium from PU scaffolds with 42 days implantation, (n=6). ..... 180

Figure 6.17 Mean  $\pm$  SD for the of calcium (A) and collagen (B) staining of hBMSCs cells on PU scaffolds with 3.5 mm inner diameter and titanium (GP/400-300) inserted at day 0 and 7 and implanted for 42 days. Photograph of (C) mineral deposition and (C) collagen production on extracted titanium and PU scaffolds, (n=6). .... 181

Figure 6.18 SEM images showing hBMSCs cells layers distributed on (top) implanted titanium lattices and (bottom) PU scaffolds over 24 days implantation period, scale bar= 200  $\mu$ m). ..... 182

Figure 6.19 Confocal microscopy images of xylenol orange stained mineralised deposits of hBMSCs cells cultured on auto-fluorescence PU scaffolds and implanted titanium lattices (GP/400-300) with 42 days implantation using two insertion conditions (day 0 and day7), scale bar=100  $\mu$ m. .... 183

**List of Tables**

Table 2.1 Classification of dental implant materials, adapted from (Sykaras et al., 2000).  
..... 11

Table 2.2 Summary of the different test methods used to determine the elastic modulus  
of cancellous bone, Adapted from (Rho et al., 1998). ..... 23

Table 2.3 Comparison table of the main fabrication methods used for creating rough  
and porous implants with potential dental and/or orthopedic applications..... 40

Table 3.1 Chemical composition of the plasma atomised Ti-6Al-4V Extra Low  
Interstitial (ELI) grade 23. Provided by material validation sheet of Renishaw’s titanium  
alloy (Ti-6Al-4V). ..... 56

Table 3.2 Cultured media compositions used in this thesis, Basal media (BM),  
supplemented media (SM), osteogenic induction media (OIM)..... 66

Table 4.1 A summary of the different Ti-6Al-4V lattice designs and the nomenclature  
used to refer to them in this study. Samples are grouped according to the nominal pore  
size, strut thickness, and presence or absence of a dense core..... 80

Table 4.2 Mean  $\pm$  S.D of average pore size, and average strut thickness of variable Ti-  
6Al-4V lattices were analysed by Image J (n=300). ..... 91

Table 4.3 Mean  $\pm$  S.D of surface chemistry (EDX) analysis, elemental composition  
(weight %) of variable Ti-6Al-4V lattices. .... 91

Table 4.4 Surface chemistry analysis (ICP) for the major and (LECO) for the interstitial  
elements level of the SLM produced Ti-6Al-4V lattices and, elemental composition  
(weight %) of the variable..... 93

Table 4.5 Mean  $\pm$  S.D of the average percentages of open, closed and total porosity and  
object surface to volume ratio of variable titanium lattices calculated by 3D analysis of  
the MicroCT cross-sectional images using CTAn software. These data were collected  
for three samples for each group. .... 96

Table 4.6 Mean  $\pm$  S.D of the average total porosity of variable titanium lattices  
calculated by 3 D analysis of the MicroCT and Archimedes method (no 3)..... 98

Table 4.7 Mechanical properties (Young's modulus and yield strength) of all Ti-6Al-4V  
lattices under compression (Mean  $\pm$  SD). ..... 102

Table 4.8 Significant differences between A- Young’s modulus and B- Yield strength  
of variant Ti-6Al-4V lattices under compression, \*=p<0.05, \*\*=p<0.01, \*\*\*=p<0.001  
and \*\*\*\*=p<0.0001. .... 103

*List of Tables*

Table 4.9 Mean  $\pm$  SD of the mechanical properties (flexural modulus and flexural strength) of Ti-6Al-4V lattices P400, P400/1C, P400/2C, GP/400-300 and Spider Web under three-point bending test. .... 108

Table 4.10 Significant differences of A- Flexural modulus and B- Flexural strength of variant Ti-6Al-4V lattices under three-point bending test, \*=p<0.05, \*\*= p<0.01, \*\*\*=p<0.001 and \*\*\*\*=p<0.0001..... 108

Table 6.1 A summary of the experimental trials of different culture conditions used to optimise the *in vitro* 3D bone model. Trials are grouped according to the inner diameter of PU scaffolds, cell type, cell density, the design of Ti-6Al-4V lattices, and insertion time of titanium into PU scaffolds and duration of implantation. .... 164

**Abbreviations**

2D	Two Dimensional
3D	Three Dimensional
$\alpha$	Alpha
$\beta$	Beta
$\beta$ GP	Beta-Glycerolphosphate
$\mu$ SL	Microstereolithography
AA-2P	Ascorbic Acid-2-Phosphate
AMRC	Advanced Manufacturing Research Centre
ANOVA	Analysis of Variance
ARS	Alizarin Red S
BM	Basal Media
CAD	Computer aided design
CLSM	Confocal Laser Scanning Microscopy
CTan	CT Analyse Software
Dex	Dexamethasone
diH <sub>2</sub> O	Deionised water
DMSO	Dimethyl Sulfoxide
DR80	Direct red 80
ECM	Extracellular Matrix
EDTA	Ethylene Diamine Tetraacetic Acid
EDX	Energy-dispersive X-ray spectroscopy
EM	Expansion media
FBS	Foetal Bovine Serum
HA	Hydroxyapatite



## *Abbreviations*

hBMSCs	Human Mesenchymal Stem Cells Derived from Bone Marrow
HCL	Hydrochloric Acid
HEPES	4-(2-hydroxyethyl)-1-piperazineethanesulfonic acid
HMDS	Hexamethyldisilazane
ICP-OES	Inductively Coupled Plasma Optical Emission Spectroscopy
LECO	Laboratory Equipment Corporation
MEM	Minimum essential medium
MG63	Human Osteosarcoma Cells
MG-63	Human Osteosarcoma Cells
MicroCT	Micro Computed Tomography
MLO-A5	Murine Long Bone Osteocyte - A5
NaOH	Sodium Hydroxide
OIM	Osteoinductive media
PBS	Phosphate-Buffer Saline
pH	Potential of Hydrogen
PU	Polyurethane Polymer or Scaffold
ROI	Region of Interest
RPM	Round per Minute
RR	Resazurin Reduction
SD	Standard Deviation
SEM	Scanning Electron Microscope
SM	Supplemented Medium Consists of AA, $\beta$ -GP in the Basic Culture
SM+Dex	Supplemented Medium with 100nM of Dex
SR	Sirius Red
XO	Xylenol Orange

**Nomenclature**

<b>Model type</b>	<b>Pore size (<math>\mu\text{m}</math>)</b>	<b>Strut thickness (<math>\mu\text{m}</math>)</b>	<b>Dense core (mm)</b>
<b>P400</b>	400	400	None
<b>P400/1C</b>	400	400	1
<b>P400/2C</b>	400	400	2
<b>P650</b>	650	300	None
<b>P650/1C</b>	650	300	1
<b>Graded (GP/650-400)</b>	400 (inner layer)	400 (inner layer)	1
	650 (outer layer)	300 (outer layer)	
<b>Graded (GP/400-300)</b>	300 (inner layer)	300 (inner layer)	1
	400 (outer layer)	400 (outer layer)	
<b>'Spider Web'</b>	250	250	1.73

## **Chapter 1 : Introduction**

Dental implants aim at improving aesthetics, speech, mastication efficiency and physical health by replacing the root parts of natural teeth that have been lost due to fracture, periodontitis (Mehrali et al., 2013) or ageing (Cheng et al., 2014) to give support to a dental prosthesis (crowns or bridges) (Elias, 2011) (Figure 1.1). The next stage of treatment is dental prosthesis placement which commonly needs three to six months after implant insertion to permit sufficient healing and integration into the jaw bone (Mangano et al., 2015). An estimated two million people per year worldwide are treated with dental implants (Cheng et al., 2014). The global costs of dental implant treatment have increased progressively from US\$3.4 billion in 2011 to US\$6.4 billion in 2018 (Alghamdi, 2018). The increasing demand for dental implants can be attributed to their ability to completely restore dentition, the significant increase in the mean age of the world population, the higher number of elderly people in the population and higher public awareness (Junker et al., 2009). Additionally, there are complications associated with conventional removable dentures, fixed crowns and bridges; for example, a reduction in the bearing area that supports the removable prosthesis due to the gradual bone resorption of the residual ridge following tooth extraction. Thus, using endosseous titanium implants is more convenient with better functionality than conventional dentures (Boerrigter et al., 1995). Despite being very successful in healthy patients, around 10% of dental implants fail to integrate with the bone as a result of poor bone quality and quantity (Gaviria et al., 2014). Implant loosening is also reported in patients with poor bone healing, including smokers, people with diabetes (Mendonça et al., 2008), elderly people and those with osteoporosis (Junker et al., 2009). There is therefore still the need to establish implant surfaces that will improve the ability to support implant-bone integration.

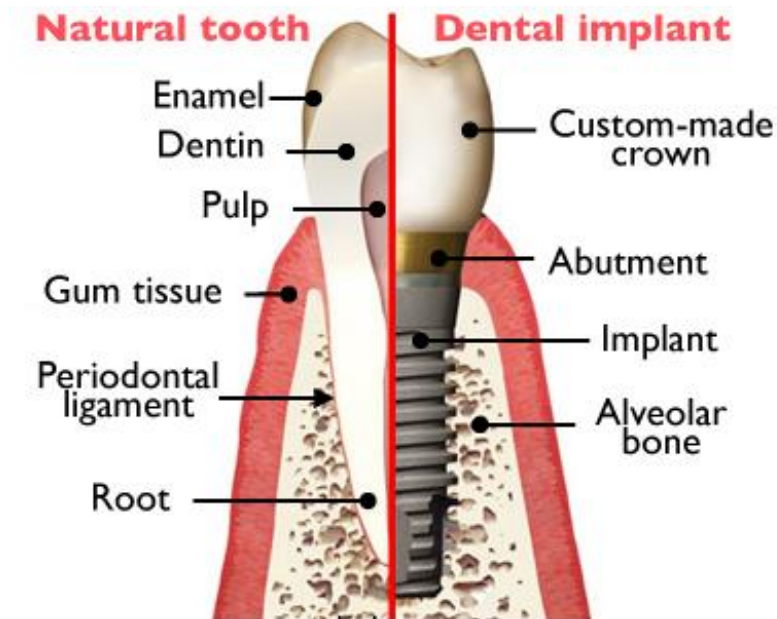


Figure 1.1 A diagram shows the main parts of natural tooth (left) and dental implant (right). Adapted from <https://www.orthodontisteenligne.com/en/dental-implants/>

Fundamentally, implants need to be constructed from biomaterials compatible with the human body environment. Titanium and its alloys have been reported as the gold standard in orthopaedic and dental implant applications due to their outstanding mechanical properties and biocompatibility (Nouri et al., 2010). However, the Young's modulus of these materials is higher than that of mineralised tissue (Nouri et al., 2010). Furthermore, the traditional structure of titanium for medical and dental implants is non-porous. Researchers have suggested that the dense structure of implants may lead to 'stress shielding', where there is a mismatch between Young's modulus of the implant, for example Ti-6Al-4V (110 GPa) (Özcan and Hämmerle, 2012) and natural cortical (17–20 GPa) and cancellous bone (around 4 GPa) (Nouri et al., 2010). Since bone is a living tissue which is continuously modified by the bone cells in response to external signals, reduced mechanical loading leads to resorption of bone, implant loosening and ultimately failure, which has particularly been a problem for orthopaedic implants in the past (Krishna et al., 2007). Alternatively, overloading also creates high stresses in

local regions of bone which can also initiate resorption (Isidor, 2006). Accordingly, many attempts have been undertaken to develop biomaterials with mechanical properties well-suited to the bone tissue. Most of these studies have aimed at optimising the important features of interactions between the implant surface and bone tissue. Advances in orthopaedic and dental implant design, as well as scaffolds for bone tissue engineering, have all contributed to the fabrication of novel porous titanium structures, and these fields draw on each other's technologies.

Implant morphology has a crucial role in bone-implant contact and can enhance the osseointegration process (Pelaez-Vargas et al., 2011). To improve dental implant stability, different surface modifications have been proposed to adapt the properties of titanium dental implants (Le Guéhennec et al., 2007). Modifying the implant surface can improve the implant to bone interaction. However, there is not always a clear explanation for the mechanism of improvement. For example, a morphological or a chemical mechanism, such as roughening the implant surface can also create modifications in the chemistry of the dental implant surface. Plasma spraying with different powder particles such as titanium oxide, calcium phosphate and hydroxyapatite has been used to coat dental implants (Gaviria et al., 2014). Sandblasting with stiff particles such as alumina,  $\text{TiO}_2$  and ceramic has also been suggested to roughen the dental implant surface (Le Guéhennec et al., 2007). Çelen & Özden supported another more controllable system of laser micro-machining of commercially pure titanium dental implant (Çelen and Özden, 2012). Materials with nanometer-scale porosity such as  $\text{TiO}_2$  nanotubes (30, 50, 70 and 100 nm) on the titanium dental implant have also been used recently as implant surface-treatments (Yi et al., 2015).

Despite being very successful, there are some shortcomings associated with these procedures; the bulk structure is still high-density titanium, the coating materials can

dissolve over a long period of time. Moreover, coating particles that break away from the surface could have an adverse biological effect on the adjacent tissue such as peri-implantitis (Gaviria et al., 2014). Therefore, several alternative approaches have been proposed to overcome these drawbacks of coating materials by creating porous biomaterials as a substitute for the classical dense structure. Porous structures have the advantage that their effective stiffness can be manipulated to match bone tissue (Wu et al., 2014) and the porosity provides a larger surface area, which in turn encourages the attachment and proliferation of bone cells, enables bone ingrowth into the material and improves osseointegration (Teixeira et al., 2012). A high surface area eliminates early micromotion of implants (de Vasconcellos et al., 2010), micromotion promotes fibrous tissue rather than osseointegration and causes initial instability (Fernández et al., 2017), as demonstrated by commercially available dental implants from Zimmer with a porous tantalum trabecular covering. To my knowledge, the Zimmer implant is the only porous dental implant on the market and animal, and short-term clinical studies indicate excellent bone integration and implant stability (Bencharit et al., 2014). However, tantalum is an expensive material which may not be affordable to many seeking dental implant treatments, and, therefore, methods of providing a porous structure in titanium or a titanium alloy is of substantial interest to the dental implant community (Mohandas et al., 2014).

Since pore parameters such as size, shape and the overall amount of porosity have been shown to play a vital role in bone cell ingrowth ( de Vasconcellos et al., 2008), this necessitates using a processing method able to produce optimal porosity in a metallic biomaterial, as achieving both the required biological and mechanical properties is essential for implant applications. To date, numerous studies have been undertaken to manipulate the mechanical and topographical properties of titanium implants. In many

studies, micro- and nanoporous titanium has been proposed as a promising alternative to bulk structures for biomedical and dental implant applications.

In recent years, additive manufacturing, including Electron Beam Melting (EBM) and Selective Laser Melting (SLM) have been increasingly considered as economically viable techniques to fabricate challenging structures (Koike et al., 2011). With SLM, dental and orthopaedic implant prototypes have been developed with complex pore geometries by melting Ti powder microparticles using a focused laser beam according to a computer-generated three-dimensional design (Tolochko et al., 2002, Mullen et al., 2009 and Moin et al., 2013). However porosity within the bulk metal structure reduces mechanical properties, and as a result, unless this can be controlled, such materials are unlikely to be used for bone replacement devices in load-bearing areas (Ryan et al., 2006). In an attempt to withstand physiological loads, a structure with a dense core and porous shell has been suggested, which might be more acceptable for oral implantology (Laoui et al., 2006). Another suggestion includes graded porous architecture with a dense core, where the core will provide mechanical stability and the graded porosity allows ingrowth (van Grunsven et al., 2014). Such a structure could also reduce the stress concentrations occurring on loading between adjacent layers with very different Young's moduli (Joshi et al., 2013), as can happen when porous materials are bonded to dense materials.

With the breadth and versatility of processing methods, the optimal pore structure for bone cell ingrowth remains to be elucidated. This thesis focuses on comparing a range of Ti-6Al-V micro-lattice structures of approximately cylindrical/ rod-like form, which could form the basis of a porous dental implant using a Selective Laser Melting (SLM) process. Variable pore sizes and strut thicknesses were used to create regular and graded porous structures with and without a dense core using a novel 'Spider Web' design and

lattices based on a diamond unit cell. These lattices were evaluated for physical characterisation, surface chemistry and mechanical testing under compression and three-point bending tests. In terms of biological characterisation, cytotoxicity of Ti-6Al-V powder particles on bone forming cells was assessed. Biological performance of post processing Ti-6Al-V lattices on bone cells was also assessed using direct cell seeding and a novel *in vitro* 3D culture bone model. The aims and objectives of this thesis can be found after the literature review.



## **Chapter 2 : Review of the literature**

Sections 2.1.2.1, 2.7, 2.8 and 2.10 of this chapter have been published as a review article in the Journal of Metals as: Zena J Wally, William van Grunsven, Frederik Claeysens, Russell Goodall and Gwendolen C Reilly, “Porous Titanium for Dental Implant Applications”. Journal of Metals (2015) Vol 5, pp. 1902-1920. This is an open-access article distributed under the Creative Commons Attribution License. A full copy of this publication is available in the appendix, 9.1.

### **2.1 Dental implant – types, materials and osseointegration**

#### **2.1.1 Implant designs**

Dental implants are inserted surgically into the jaw bone in order to restore the natural root of the lost teeth and support the dental prosthesis (Gaviria et al., 2014). The global growing interest in dental implants is mainly attributed to their firm bone integration and permanent dental root replacement. Dental implants are also known as endosseous, intraosseous and endosteal implants. Dental implants were introduced in the 1960s by Professor Per Ingvar Brånemark and his colleagues in Sweden. Since then a wide range implant designs have been developed in the dental implant market, they all aimed at improving the long-term success of bone-implant integration and proper functionality with the prosthetic replacement (Velmurugan et al., 2017). The variety of implant designs is mostly related to the shape, the presence or absence of threads, additional macro-irregularities and type of prosthetic interface. These implants are generally categorized according to their shape, surface roughness, surface treatment and the connection type with the prosthetic part. Implant design and surface environments have been shown to play a vital role in stress distributions and the success rate of implant treatments. The length and diameter of commercially available dental implants vary according to the clinical treatment requirements. For example, the dimensions of

## ***Chapter 2: Review of the literature***

cylindrical thread dental implants range from 3.25 to 6.0 mm in diameter and 5 to 18 mm in length (Nelson, 2011). From a biomechanical point of view, wider implants can improve implant stability and load distribution (Velmurugan et al., 2017). Commercially available titanium dental implants are generally available in cylindrical and conical shape. They are also classified into three main forms screw threads; solid body press-fit and porous-coated design. A threaded cylindrical or root like shape (conical) design has been the classical shape of dental implants (Alghamdi, 2018) as shown in (Figure 2.1). The presence of threads increases the surface area of osseointegration, at the bone-implant interface, thus helping to significantly improve primary stability (Sykaras et al., 2000), which is very important for the fixation and long-term success of the implant afterwards healing process afterwards (Steigenga et al., 2003). The distribution of biomechanical stress on the implant was also found to be influenced by the geometry of the threads, such as thickness, depth, pitch, face angle, and helix angle. Another dental implant design with double threaded or triple-threaded was also developed and found to improve implant contact with bone, this design was recommended for highly porous (cancellous) bone (Sykaras et al., 2000).

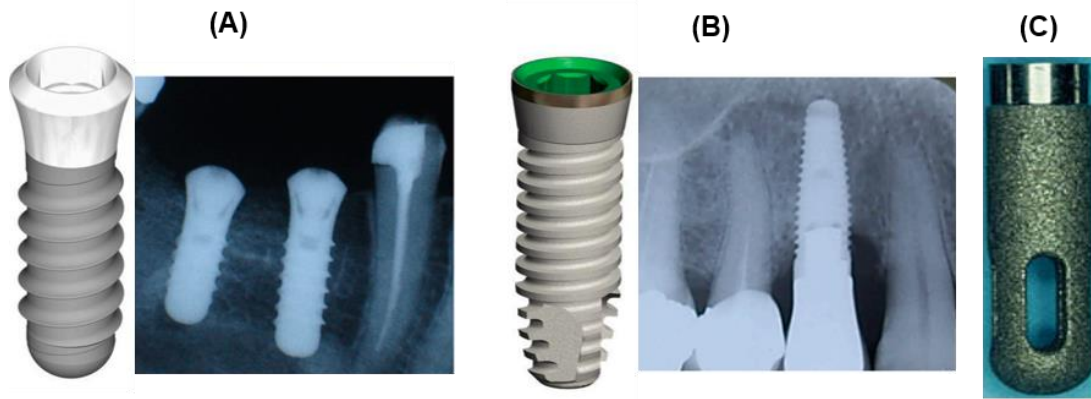


Figure 2.1 Design and radiographic images of the commercially available dental implants inserted in the jawbone, (A) threaded cylindrical-shaped or (B) conical (root)-shaped and (C) pressfit. A and B Adapted from Baltic Osseointegration Academy/Public Information (<http://www.boaoffice.lt/EN/9/>) and (Alghamdi, 2018), (C) Adapted from [https://www.medeco.de/zahnheilkunde\\_dentalatlas/implantologie/implantatformen](https://www.medeco.de/zahnheilkunde_dentalatlas/implantologie/implantatformen).

Recently, porous coated dental implants have shown a wide range of success in areas of low bone quality with shorter healing time than that of screw shape dental implant. The “Trabecular Metal™ Dental Implant” was developed by Zimmer Dental Inc. This design is made of a dense titanium core surrounded by a porous tantalum layer which resembles trabecular bone. The porous cover aims to support bone ingrowth and the dense titanium improves mechanical properties compared to a completely porous structure (Liu et al., 2015) as shown in figure 2.2. The porosity enables anchorage for bone growth, thus significantly enhancing the bonding strength between the bone and implant. Though the level of implant anchorage is not only influenced by the implant morphology but also controlled by the quantity and quality of the host bone (Steigenga et al., 2003).

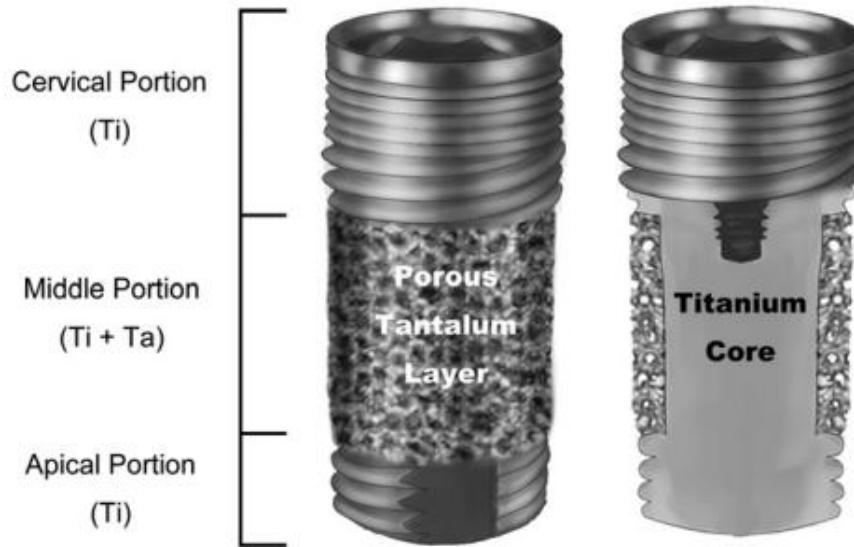


Figure 2.2 The design of the commercially available “Trabecular Metal™” enhanced titanium dental implants (left) and the cross sectional of the middle-third of the implant that has outer layer of porous tantalum and dense titanium (right). Adapted from (Liu et al.2015).

### 2.1.2 Dental implant materials

Dental implants need to be constructed from biomaterials that do not trigger a negative biological response such as allergic reactions or toxicity when implanted into natural bone with long-term clinical application. Since their introduction by Brånemark in the 1960s, many materials were used for dental implant applications either as a coating layer or to create the bulk of the implant. These materials are primarily classified according to their chemistry as metals, ceramics or polymers; or by their bio-dynamic activity as biotolerant, bioinert or bioactive, as reviewed in the literature (Table 2.1) (Sykaras et al., 2000). Despite the variety of biomaterials used in dental implant applications, there is no optimum material completely accepted by the biological environment. Implants of biotolerant materials show excellent biocompatibility, but can be found surrounded by a fibrous capsule which leads to implant instability. Bioinert materials are not rejected by the body and can induce bone deposition on the implant

surfaces. Bioactive materials refer to those materials that allow ionic exchange at implant and bone interface resulting in chemical bonding and a surface that stimulates the cells to undertake new bone formation. Osteoconductive term are used for both bioinert and bioactive materials which can be used to produce implantable components facilitating bone growth (Sykaras et al., 2000).

Table 2.1 Classification of dental implant materials, adapted from (Sykaras et al., 2000).

<b>Biodynamic activity</b>		<b>Biotolerant</b>	<b>Bioinert</b>	<b>Bioactive</b>
<b>Chemical composition</b>	<b>Metals</b>	Gold Cobalt-chromium alloys Stainless steel Zirconium Niobium Tantalum	Commercially pure titanium Titanium alloy (Ti-6Al-4V)	
	<b>Ceramics</b>		Aluminium oxide Zirconium oxide	Hydroxyapatite Tricalcium phosphate Tetracalcium phosphate Calcium pyrophosphate Fluorapatite Brushite Carbon: vitreous, pyrolytic Carbon-silicon Bioglass
	<b>Polymers</b>	Polyethylene Polyamide Polymethylmethacrylate Polytetrafluoroethylene Polyurethane		

The flexibility of polymeric dental implants imitate the micromovement of the periodontal ligament, but the lack of bone integration, inferior strength properties and adverse immunologic responses have restricted the use of polymers as coating materials and shock-absorbing parts connected to dental prostheses (Velmurugan et al., 2017). Ceramic materials have been used for entire implant fabrication and as a coating layer

onto a metallic core. Commonly used bioactive ceramics are hydroxyapatite, tricalcium phosphate, and bioglasses. Despite the attractive ability of bioactive materials to create a chemical bond with the surrounding natural bone, there are concerns associated with the dissolution or breakdown of the coating layer (Steigenga et al., 2003). Additionally, the brittleness and inferior flexural strength of ceramic materials causes them to crack when used in load bearing areas (Duraccio et al., 2015). Metal dental implants were introduced into the dental implant industry use several metals and alloys such as gold, stainless steel, cobalt-chromium, titanium and its alloys. In early experiments by Brånemark in 1964, stainless steel and titanium chambers were implanted in rabbit and dog legs, the titanium implants were found to firmly integrate with the bone tissue. Since then titanium based dental implants have been introduced for human use with high range of osseointegration (Elias, 2011). Most commercially available dental implants are made of titanium alone or the titanium alloy (Ti-6Al-4V) due to the high corrosion resistance of these materials.

### **2.1.2.1 Titanium and its alloys as dental implant materials**

In this thesis the focus will be on titanium alloy (Ti-6Al-4V) as the preferred biomaterial for dental implant applications. Ever since the 1960s, commercially pure titanium and its alloys have shown to be versatile biomaterials that can be used to produce a variety of medical devices including those used in dentistry (Özcan and Hämmerle, 2012). This is mostly related to their unique properties such as excellent mechanical behaviour, superior corrosion resistance (Dabrowski et al., 2010), as well as the high ratio of strength to weight (Li et al., 2005). Titanium is biocompatible because it is nearly biologically inert and well tolerated by the environment of the human body. According to the British Standards for surgical implants the oxygen percentage should not exceed 0.5% (Van Noort, 1987). Furthermore, the properties of titanium are influenced by its

structure which has two allotropic structures: a close packed hexagonal ( $\alpha$  phase) and body-centered cubic crystal ( $\beta$  phase). These phases enable titanium to undergo a reversible transformation; at room temperature it tends to categorize as  $\alpha$  phase and transfer to  $\beta$  phase as the temperature exceeds 883°C (Nouri et al., 2010).

The strength properties of commercially pure titanium are weaker than that required for medical implants (Nouri et al., 2010). Thus, to improve these properties titanium alloys have been proposed via incorporation with various types and quantities of elements such as Aluminium, Molybdenum, Vanadium, Niobium, Tantalum, Manganese, Iron, Chromium, Cobalt, Nickel and Copper. Each of these elements has a different impact on the transition temperature of titanium alloys. Those that increase the transition temperature, such as aluminium, are identified as  $\alpha$  stabilizing element, whereas those that decrease it, such as vanadium, are referred to as  $\beta$  stabilizing elements. Accordingly, alloys are classified into three main types ( $\alpha$ ,  $\beta$ , and  $\alpha+\beta$  alloys) depending on their transition temperature (Nouri et al., 2010).

Through the years, several types of titanium alloys have been developed as implant biomaterials such as Ti-6Al-4V, Ti-Nb-Ta-Zr (Niinomi et al, 2004), Ti-Ni-Ta (Gong et al., 2006), Ti-15Mo-5Zr-3Al (Niinomi et al., 2004), Ni-Ti (Shishkovsky, 2005) and Ti-Sn-Nb (Nouri et al., 2010). Among the aforementioned alloys Ti-6Al-4V (Nouri et al., 2010) and NiTi (Bahraminasab and Sahari, 2013) have been reported as the most widely used biomedical materials for bone replacement devices, also in comparison to other medical grade alloys such as stainless steel and Co-29Cr-6Mo. This is due to better mechanical performance of these titanium alloys (Li et al., 2005) (Bahraminasab and Sahari, 2013), and their significant corrosion resistance, especially for the interconnected porous titanium structures due to the free flow fluid inside the pores (Seah and Thampuran, 1998). This allows them to be used as load-bearing implants for

tissue engineering scaffolds (Andani et al., 2014) (Arifvianto et al., 2014). Nevertheless, Andani et al. stated that despite the flexible modulus of elasticity of NiTi, it was not straightforward to design interconnected porous structured scaffolds with this alloy because of its high melting point (Andani et al., 2014). Even with the popularity of Ti-6Al-4V and NiTi the potentially adverse biological reaction to their elements by the living tissue still remains a matter of concern. This has directed researchers to keep developing alloys aimed at improving biocompatibility such as Ti-6Al-7Nb, Ti-13Nb-13Zr. These are more likely to mimic the biological and mechanical properties of Ti-6Al-4V (Rack and Qazi, 2006).

The elastic modulus of pure titanium and its alloy (Ti-6Al-4V) is half that of Co-Cr, thus stress shielding is lower (Ryan et al., 2006). In order to produce titanium alloy with reduced Young's modulus and adequate strength for orthopaedic implants, various attempts have been reported in the literature. For instance, in 1998, Kuroda et al. introduced Ti-Nb-Ta-Zr, Ti-Nb-Ta-Mo and Ti-Nb-Ta-Sn (Kuroda et al., 1998) . Matsumoto et al. (2005) introduced B-type titanium alloys (Ti-29Nb-13Ta-4.6Zr) and (Ti-Nb-Sn) which showed a remarkably lower Young's modulus (Matsumoto et al., 2005). Attempts have also been made to produce porous Ti alloy compacts (Ti-15Mo-5Zr-3Al) using a hot-pressing technique, which could reduce Young's modulus to within the range of cortical bone (Nomura et al., 2005). Another possibility is to incorporate hydroxyapatite particles with titanium powder using an infiltration method and sintering (Nomura et al., 2010). The addition of hydroxyapatite has the additional aim of improving bone fixation because bone cells attach well to hydroxyapatite surfaces (Deligianni et al., 2000). The Young's modulus of porous titanium-hydroxyapatite composites can be controlled by changing the percentage of hydroxyapatite particles (Nomura et al., 2010).



### **2.1.3 Bone implant integration**

#### **2.1.3.1 Bone physiology, composition, formation, remodelling and properties**

##### **2.1.3.1.1 Bone anatomy**

The bones of the human skeleton support the movements of the body and protect the individual organs. There are different types of bone, which can be calcified according to their shape as long, round, irregular or flat bones (Moore and Dalley, 1999) or location in the axial (Pelvis, Vertebrae, Skull) or appendicular (Femur, Humerus, Tibia) skeleton. Dental implants are installed into the jaw bone (mandible or maxilla) which is located in the facial skeleton (Figure 2.3). Jaw bone functions to protect and support teeth. The term woven and lamellar bone are also used to describe the anatomical organisation of any bone. Woven bone is immature bone which is commonly found in the fetus, early stages of human skeleton development during childhood and in fracture healing. Woven bone is characterised by the irregular arrangement of cells, mineral and collagen fibres. Woven bone becomes a lamellar bone during the remodelling process, where the lamellar bone is denser and more highly organised and aligned than woven bone (Feldman et al., 2007) (Figure 2.4).

Osseous tissue can also be classified into cortical and cancellous. Cortical (or compact) bone forms around 80% of skeletal bone mass (Ralston, 2009) and forms the outer layer of bones (Wilkinson 2001; Marieb 2004; Shapiro 2008). The structure of cortical bone is strong and dense with 4-27 GPa stiffness and 5-30% porosity (Carter and Spengler, 1978), it is made from a highly ordered network of collagen fibres arranged into concentric sheets of lamellae, surrounding a central canal of blood vessels. Cancellous (also known as spongy or trabecular) bone forms the inner layer of the bone with higher surface area and porosity of approximately 30-90%. Its stiffness is about 0.1-3 GPa (Ralston, 2009). It is an open cell sponge due to its trabecular structure, which has 50-

400  $\mu\text{m}$  interconnecting rods and plates of bone (Clarke, 2008). The trabeculae are filled with bone marrow and blood vessels. The jaw (mandible or maxilla) is mostly cancellous bone with a thin cortical region (Kim et al., 2012) (Figure 2.3).

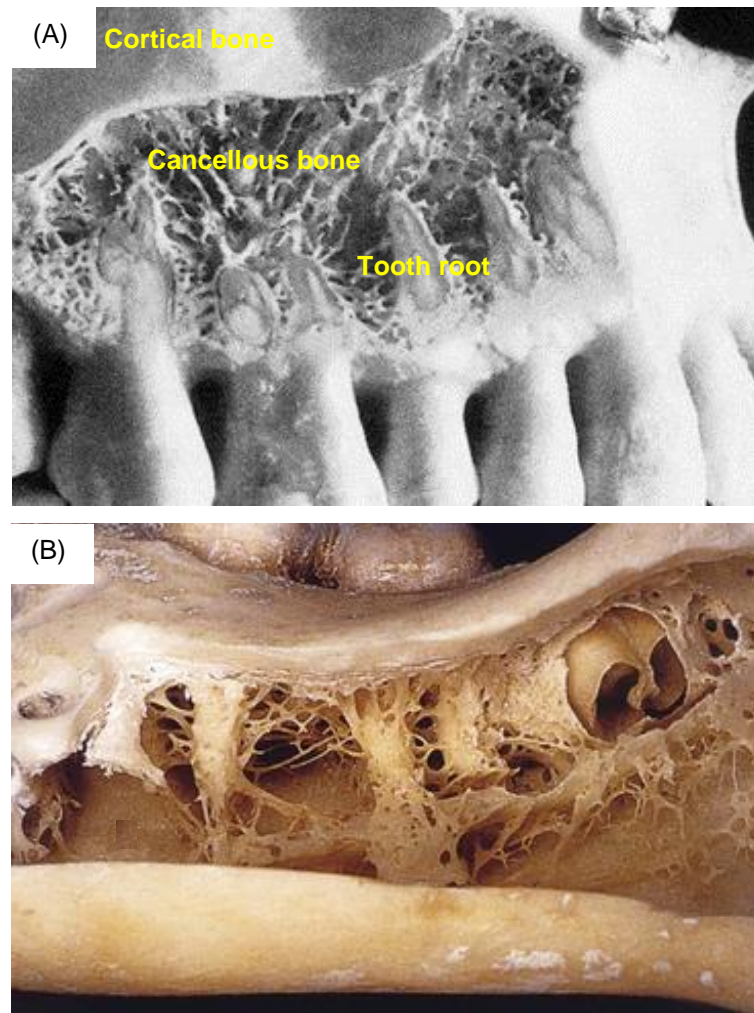


Figure 2.3 The structure of cortical and trabecular bone of the human (A) maxilla (B) mandible. Adapted from (<https://pocketdentistry.com/11-bone-density/>).

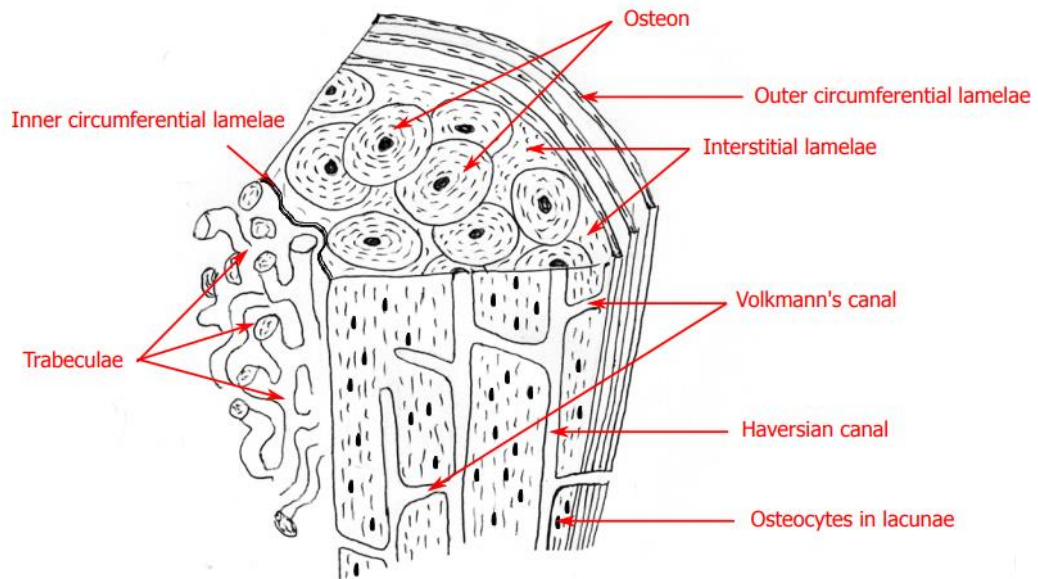


Figure 2.4 General structure of bone. Adapted from (Jiroušek, 2012), Under Creative Commons Attribution License.

#### 2.1.3.1.2 Bone composition

Bone is made by bone cells in the form of a matrix composite consisting of approximately 40% a protein-rich organic matrix, around 60% mineral rich inorganic components, and traces of water and lipids. The function of the organic substance is to reduce bone brittleness and provide bending and tensile strength while the inorganic material provides bone with compressive strength.

The organic substance of bone consists mostly of collagen type I, around 90%, and traces of type III and V; there is also about 10% of non-collagenous proteins such as osteopontin, osteocalcin, proteoglycans, bone sialoprotein and other phosphoproteins and proteolipids (Bonucci, 2000). The presence of arginine-glycine-aspartic (RGD) acid in most of these proteins helps the attachment bone cells to extracellular matrix and cellular activity during bone remodelling. There are also very small amounts of growth factors that help in bone differentiation, activation, growth and overall turnover,

with a potential function to act as a coupling factor for the processes of bone remodelling (Feldman et al., 2007).

The main component of the inorganic material is about 95% of carbonated hydroxyapatite crystals,  $[\text{Ca}_{10}(\text{PO}_4)_6(\text{OH}_2)]$  on collagen fibres shown in (Figure 3.4) (Kane and Ma, 2013), their function is to reinforce the bone matrix and provide structural integrity (Bonfield, 1971; Rehman and Bonfield, 1997). The remaining 5% consists of small amounts of other minerals and impurities (Feldman et al., 2007). Bone mineralisation is a complex process regulated by cells, physiochemical activities and extracellular matrix.

Bone has a hierarchical structure, which consists of a general macrostructure of cortical and cancellous bone, microstructure (from 10 to 500  $\mu\text{m}$ ) made up of osteons and trabeculae, sub microstructure (10  $\mu\text{m}$  - 1  $\mu\text{m}$ ) of lamellae, nanostructure of collagen fibres (1  $\mu\text{m}$  - 500 nm), and the sub-nanostructure (less than 500 nm) is fibrils and calcium phosphate nanocrystals forming the collagen fibres (Figure 2.5). Mineralized collagen is accumulated into small fibrils, which combine to form collagen fibres. In cortical bone, the mineralised fibres wrap around a central hollow core to form a circular osteon, while in cancellous bone these fibres are randomly arranged in struts to form a porous open cell foam (Kane and Ma, 2013). The cortical bone is denser and stronger than cancellous bone because the amount of mineralised tissue in the cortical bone is approximately 80-90%. For spongy bone, this elastic tissue makes 15-25% of the volume and the rest is occupied by a highly vascular network of the red bone marrow and the bone marrow stroma. (Wilkinson 2001, Marip 2004, Shapiro 2008).

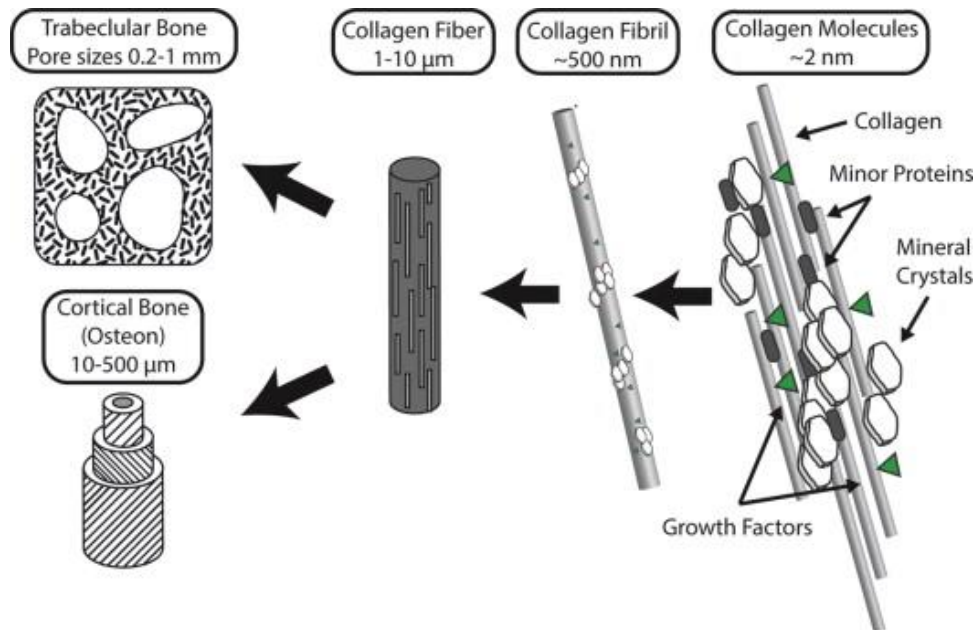


Figure 2.5 Hierarchical structure of bone. Adapted from (Kane and Ma, 2013)

#### 2.1.3.1.3 Cell biology and formation of bone

Bone contains four main cell types, mesenchymal progenitors cells, osteoblasts, osteoclasts, and osteocytes, each playing a different role and function in bone formation. Mesenchymal stem cells (MSCs), also called marrow stroma cells are undifferentiated cells derived from the bone marrow stroma and are capable of differentiating into fat cells, chondrocytes, muscle or osteoblasts cells depending on the environmental conditions (Ralston, 2009). MSCs are attractive cells for bone regeneration research due to their ability to proliferate and differentiate into osteogenic cells.

Osteoblasts are large, cuboidal and single nucleus cells responsible for bone formation, and regulation of extracellular matrix and mineralisation. These cells synthesise the collagen type I required to form new bones. Osteoblasts cells can produce approximately 0.5-1.5 μm of extracellular matrix daily (Sommerfeldt and Rubin, 2001). They are present on the surface of the osteoid and depend on cellular communication

## *Chapter 2: Review of the literature*

and through specific receptors to detect factors such as cytokines, hormones and growth factors to maintain cellular function. (Sommerfeldt and Rubin, 2001). The organic matrix of bone (collagen and non-collagenous organic) is deposited by osteoblasts cells. Some osteoblasts become fully embedded within calcified osteoid and change their role to become osteocytes.

Osteocytes are star-shaped and derived from osteoblasts. They are smaller than osteoblasts and found within the lacunae of mature bone tissue. These cells can live in the lacunae for decades. They have multiple cytoplasmic extensions which reside in the canaliculi that connect the lacunae; gap junctions help osteocyte cells to communicate with adjacent osteocytes and the osteoblasts lining the bone surface. Osteocytes facilitate communication between cells and regulate the exchange of minerals in the bone fluid within the cell-bone spaces. Osteocyte death creates empty spaces in the lacunae of the old bone matrix (Verborg et al., 2000).

Osteoclasts are multinucleated cells that can have 6-12 nuclei. They are derived from hematopoietic stem cells and are found within endosteal or periosteal surfaces. These cells are responsible for bone resorption which is the first step in the bone remodelling process. Osteoclasts initially resorb the mineral content of bone matrix and then the organic component using specific enzymes such as hydrochloric acid and tartrate-resistant acid phosphatase (Jeon et al., 2012).

Bone formation (or ossification) begins during fetal development and occurs in two ways intramembraneous ossifications or endochondral ossification (Holtrop, 1967). Intramembraneous ossification indicates the direct differentiation of progenitors, mesenchymal cells, into bone cells, which produce flat bones, such as the lower jaw and the upper jaw. Endochondral ossification refers to the differentiation of MSCs into

cartilage cells (chondroblasts), which leads to the formation of cartilage that is later replaced by bone tissue (Ralston, 2009). Bone formation occurs in both modelling (resorption or formation) and remodelling (both resorption and formation) phases.

#### **2.1.3.1.4 Bone remodelling**

Bone remodelling is an active process that occurs in compact and spongy bone and continues throughout life. Osteoblasts and osteoclasts are the dominant cells involved in bone maintenance. Remodelling is regulated by a harmonised response of mineral resorption by osteoclast and bone deposition by osteoblasts (Compston and of London, 1996). This process relies on complex interactions between bone cells. Initially new osteoclasts are stimulated to form from hematopoietic stem cells and and osteoblasts from mesenchymal stem cells. Osteoclasts starts to dissolve the present bone matrix. This is followed by the appearance of new osteoblasts to replace the resorbed bone. The newly formed bone remains as a mature bone until a new cycle of remodelling starts again (Frost, 1966) as shown in figure 2.6. It is estimated that 10% of the adult skeleton is remodelled at any time (Ralston, 2009). Bone has the ability to adapt its structure in response to direct and adjacent mechanical stimulation, such as compression, tension, bending or torsion. When bone is subjected to significant mechanical stresses, its response is to synthesise higher density and stronger bone. Conversely, the lack of loading leads to low density and weak bones (Currey, 2002). Remodelling is controlled by mechanical and molecular stimuli and metabolic factors (Lee and Taylor, 1999; Burr and Martin, 1989). Controlled remodelling occurs when bone tissue detects physical stimuli and grows in response to imposed stresses (Kane and Ma, 2013). Unbalanced remodelling results in compromised bone architecture and strength. For example, in the alveolar processes, gradual resorption occurs in places where teeth are missing, due to a lack of mechanical stimuli (Hansson and Halldin, 2012).

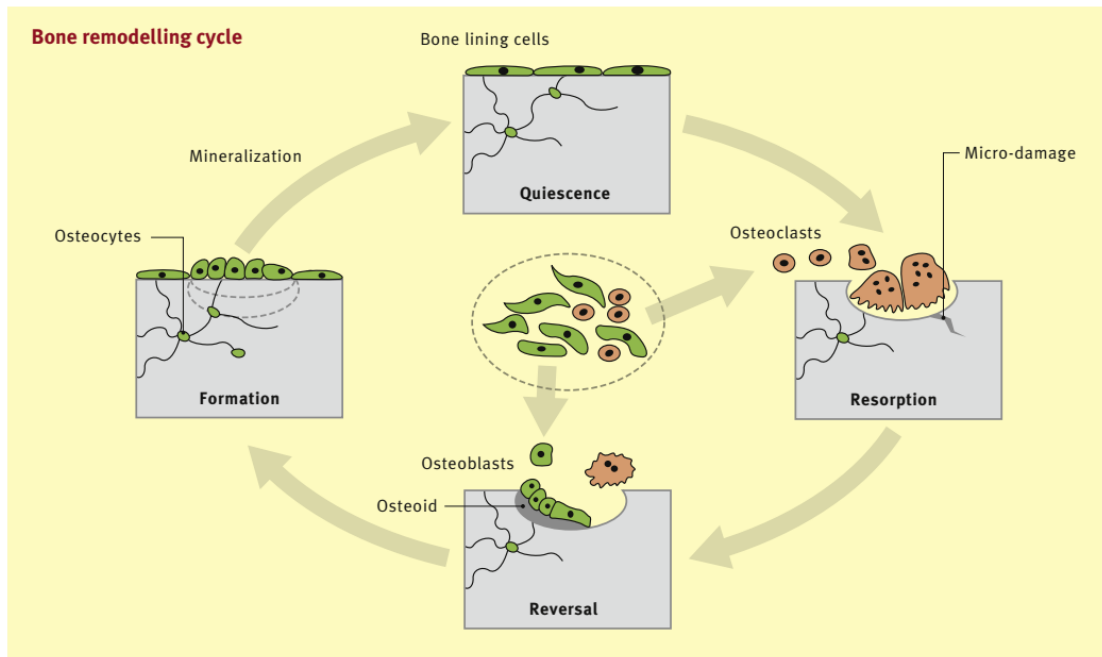


Figure 2.6 Bone remodeling cycle. Adapted from (Ralston, 2009).

#### 2.1.3.1.5 Mechanical properties of bone

For medical implant design, it is important to understand the mechanical properties of the native tissue. Mechanical properties refer to the response of the material under mechanical load which can be in different ways such as compression, tension, bending or torsion (Currey, 2012). Bone strength refers to the amount of energy required to resist fracture. Strain is a measure of deformation in response to the applied force. The relationship between load and displacement is commonly translated to a stress–strain curve. Stiffness is commonly in the elastic region where there is a linear relationship between stress and strain, which is specified as the ‘Young’s modulus’ (Turner, 2006). It is not straightforward to accurately quantify the mechanical properties of bone due to its complex network structure of compact and trabecular bone and the presence of the interstitial fluid. Different methods have been described in the literature to estimate the stiffness of cancellous bone (Table 2.2). The ranges of bone mechanical characteristics measured are highly dependent on the test conditions (Halgrin et al., 2012). The



modulus (stiffness) of mandibular cortical and cancellous bone was reported in the range of 17.6-31.2 GPa, and 1.5-4.5 GPa, respectively (Andani et al., 2014).

Table 2.2 Summary of the different test methods used to determine the elastic modulus of cancellous bone, Adapted from (Rho et al., 1998).

Source	Test method	Estimate of elastic modulus (GPa)
Wolff (1892)	Estimated	17–20 (assumption)
Runkle and Pugh (1975)	Buckling	8.69 ± 3.17 (dry)
Townsend et al. (1975)	Inelastic buckling	11.38 (wet)
Williams and Lewis (1982)	Back-calculating from FE models	1.30
Ashman and Rho (1988)	Ultrasound test method	12.7 ± 2.0 (wet)
Ryan and Williams (1989)	Tensile testing	0.76 ± 0.39
Hodgskinson et al. (1989)	Microhardness	15 (estimation)
Kuhn et al. (1989)	Three-point bending	3.81 (wet)
Mente and Lewis (1989)	Cantilever bending with FE analysis	7.8 ± 5.4 (dry)
Choi et al. (1990)	Four-point bending	5.35 ± 1.36 (wet)
Rho et al. (1993)	Tensile testing	10.4 ± 3.5 (dry)
	Ultrasound test method	14.8 ± 1.4 (wet)
Rho et al. (1997)	Nanoindentation	19.6 ± 3.5 (dry): longitudinal direction
		15.0±3.0 (dry): transverse direction

The Young’s modulus of jaw bone varies according to the bone type, which is classified into four types (Figure 2.7). Type 1, the bulk bone is thick cortical bone, type 2, a thick layer of cortical bone surrounding a core of dense spongy bone, type 3, a thin layer of cortical bone surrounding a core of spongy bone and type 4 consists of very thin layer

of cortical bone with low density trabecular bone (Alghamdi, 2018). Bone type 1 and 2 provide high Young's modulus, whereas type 3 and 4 offer low Young's modulus (Figure 2.8). A high success rate of about 90% has been reported for dental implants placed into types 1 to 3 bones, while approximately 35% of dental implant failure was found when they were inserted in to bone type 4 (Seth and Kalra, 2013).

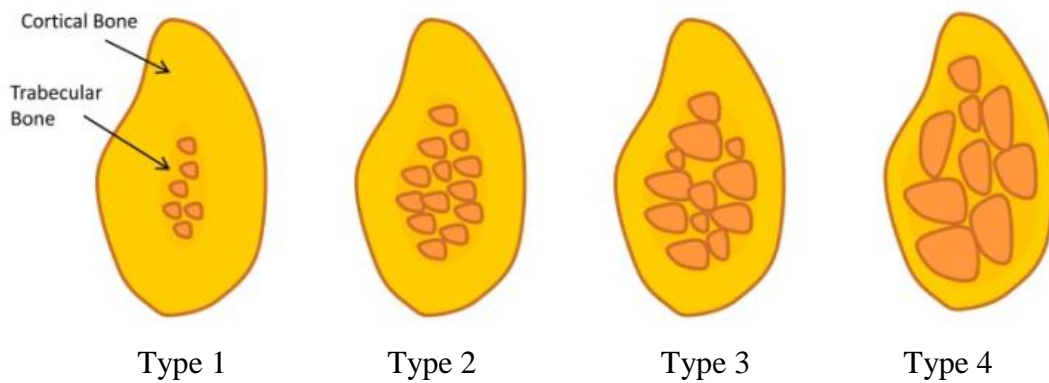


Figure 2.7 Bone Classification according to density. Adapted from (Alghamdi, 2018).

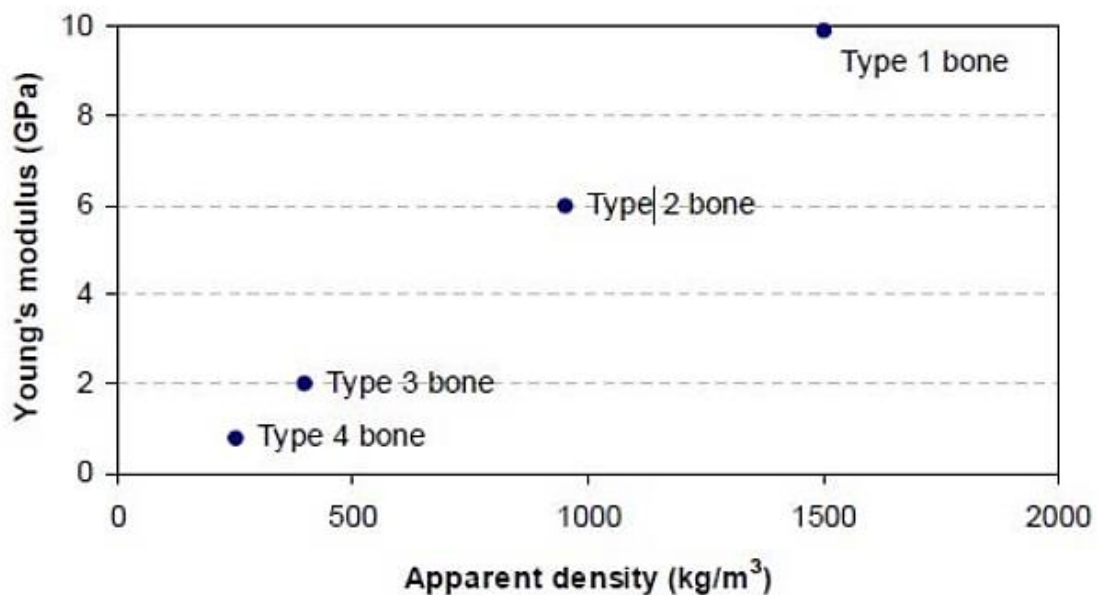


Figure 2.8 Young's modulus versus apparent density of bone types 1, 2, 3 and 4. Adapted from (Seth and Kalra, 2013).

### **2.1.3.2 Osseointegration of dental implants**

The term osseointegration was introduced by Brånemark in the 1960s to refer to bone-implant integration, where bone cells are integrated around the surface of the dental implant which consequently is anchored mechanically by the jaw bone. The mechanical interlocking between dental implants and the surrounding bone help to withstand implant failure against oral loading (Mello et al., 2016). The initiation of the healing process is expected to occur within a few days of dental implant insertion into the bone. The body environment around the recently inserted implant material is rich in different blood cells, proteins and inflammatory mediators. The initial response is the formation of haematoma (blood clot) on the implant surface that occurs within minutes of implantation. Within the following 24 hours, the inflammatory incidence recruits inflammatory cells (lymphocyte), macrophages, growth factors, and progenitor (MSCs) to the implant site (Kohli et al., 2018). Immune cells (macrophages) determine the next step, which is either fibrotic foreign body reaction or bone formation (Al-Maawi et al., 2017). The immune response is significantly influenced by the characteristics of the implant, such as material, particle size, porosity and the ions released from the implant (Boehler et al., 2011). At the early stage of implantation, the implant material is surrounded by a matrix of fibroblasts which support the growth of blood vessels. The invasion of large blood vessels in the implant stimulates bone formation by increasing osteoblast secretion of collagen fibres, this is subsequently mineralised to woven bone (Schindeler et al., 2008). The new woven bone eventually is remodelled into lamellar bone, in healthy bone, this process may require three to six months.

There are two phenomena also described for bone regeneration on implant surfaces, contact osteogenesis and distance osteogenesis. In contact osteogenesis new bone is formed directly on the surface of the implant while in distance osteogenesis bone

formation starts at bone itself towards the implant (Davies, 2003) as shown in figure 2.9. Consequently, the immature bone is replaced by mature bone at the implant surface, providing biomechanical fixation.

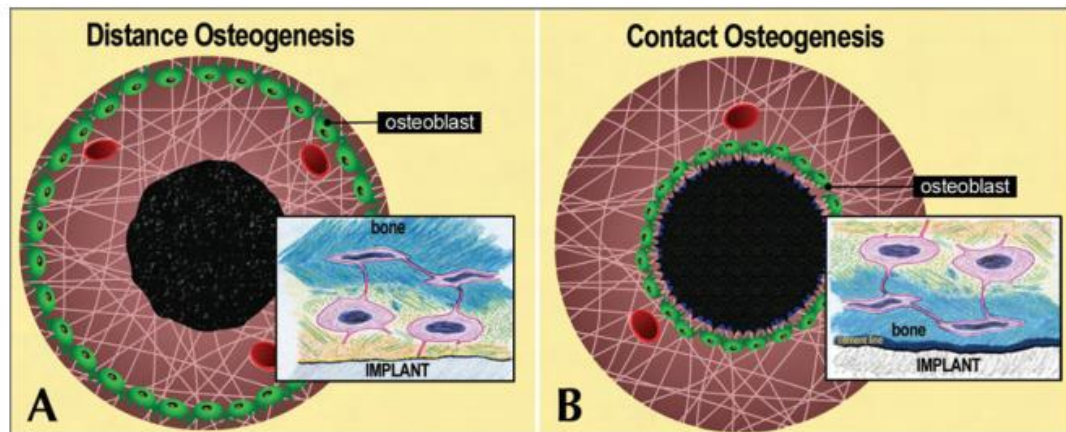


Figure 2.9 Pictures show different patterns of bone formation (A) distance osteogenesis, where the osteogenic cells line the surrounded bone and there is a gap between the cells and the surface of the implant and (B) contact osteogenesis, where bone is formed directly on the implant surface. Adapted from (Davies, 2003).

## **2.2 Load transfer in dental implants**

A dental implant is subjected to oral forces which mainly arise from muscle movements. In natural teeth, the root portion is dentine which is enclosed by cementum; periodontal ligament holds the tooth into the jaw bone. Occlusal forces for each tooth are transmitted from enamel via dentine to the root, then from cementum through the periodontal ligament to the cancellous bone to the end at the ramus of the jaw (Currey, 2012). The Young's modulus of dentine is about 20-25 GPa (Kinney et al, 2003) which is close to cortical bone (17–20 GPa) (Nouri et al., 2010). However, in dental implants, there is direct contact between the jaw bone and the implant. Dental implants should withstand physiological function during mastication. The mastication force for natural teeth ranges between 75 to 135 N, and the maximum biting force is from 230 - 450 N in the molar region (Wen, 2017). These forces significantly affect the maintenance of implant

stability and integration to the surrounding bone. The impact of stress could be positive or negative; these forces may result in a small loss at the marginal bone or complete loss of osseointegration and eventually implant failure (Isidor, 2006). These stresses may exceed the mechanical load-bearing capacity of the integrated implant. Jaw bones (maxilla and mandible) like other bones in the body carry loads and are able to adapt their mechanical properties to the applied force. Applied forces result in bone deformation as a response to bone strain which is different depending on the stiffness of the bone. It has been estimated that a load of 1–2 MPa is able to create the optimal functional strains of cortical lamellar bone which range between 50–1500 microstrain. A mild overloading occurs when a strain in the bone is increased to over 1500 microstrain. Continuous loading to about 60 MPa leads to bone deformation of more than 3000 microstrain which results in a fatigue failure. In contrast, the remodelling process does not occur when functional loading fails to exceed 50–100 microstrain of bone strain. Forces of over 120 MPa create 25,000 microstrain and lead to sudden fracture (Isidor, 2006).

In early stages of implant loading, microdamage is expected to occur in the surrounding bone tissue. The subsequent healing and adaptation process of the bone restores the damaged area and resists the progressive loading on the dental implant. Gradually increased implant loading has been used in clinical dentistry to stimulate bone repair by changing the height of the occlusal table from below-occlusion to full occlusion level. Progressive loading demonstrated a continuous increase in bone density around dental implants.

Implant design and surface morphology may influence load and strain distribution around the implant. For example, cylindrical implants showed lower bone-implant integration than screw implants (Isidor, 2006). The stiffness of natural bone is several

times lower than that of titanium dental implants. Dense implant materials may result in a failed load transmission from the implant to the bone, this known as stress-shielding, which may result in bone resorption, due to micromotion arising between the bone and the implant (Nouri et al., 2010)

### **2.3 Surface Modifications to improve osseointegration**

Several surface treatments have been used to increase the long-term survival rate of dental implants. The main objective is to improve the integration rate at the bone-implant interface. The most common surface modifications to enhance osseointegration are surface roughening or the application of osteoconductive coatings to titanium dental implants. The roughness of the titanium implant surfaces is accomplished at three scale levels: macro, micro-and nano using different methods such as, plasma-spraying, grit-blasting, acid-etching and anodization. Plasma spraying with different powder particles such as titanium oxide, calcium phosphate and hydroxyapatite have been used to coat dental implants (Gaviria et al., 2014). As previously mentioned, sandblasting with stiff particles such as alumina, TiO<sub>2</sub> and ceramic has also been suggested to roughen the dental implant surface (Le Guéhennec et al., 2007). Sandblasting with TiO<sub>2</sub>, Al<sub>2</sub>O<sub>3</sub> or calcium phosphate grits are used widely to create surface roughness at a macro scale while acid etching with hydrofluoric, nitric, sulfuric acid are used commonly for microroughness (Mendonça et al., 2008). However, the risk of ionic leakage and peri-implantitis has been reported with these surfaces (Le Guéhennec et al., 2007). Bone integration on implant surface relies on the biological interaction between bone and implants (Figure 2.10) (Alghamdi, 2018). Various methods have been developed for coating titanium dental implants, such as plasma spraying, spray deposition and sol-gel. Coating implant surfaces with osteoconductive materials such as calcium phosphates has been used extensively due to their chemical similarity to the mineral of natural bone,

which enhances biological fixation between bone and titanium. The released calcium phosphate on the implant surfaces result in apatite layer formation and attachment of endogenous proteins which act as a matrix for osteogenic cell attachment and bone growth (Le Guéhennec et al., 2007). Although the coating layer has a high tendency to facilitate adhesion of the bone surface, delamination of the coating layer from the implant surface is a major concern (Tomisa et al., 2011). The coating layer was also reported to be released when the implants were introduced into dense bone (Le Guéhennec et al., 2007). A coating of bioactive molecules such as extracellular matrix (ECM) proteins collagen, enzymes, growth factors (Junker et al., 2009) and collagen type-I also been used on titanium implants, this was able to enhance osseointegration in osteoporotic and healthy conditions (Alghamdi et al., 2013).

Çelen & Özden in 2012 supported another more controllable technique of laser micro-machining of commercially pure titanium dental implant (Çelen and Özden, 2012). Materials with nanometer-scale porosity such as TiO<sub>2</sub> nanotubes have also been used recently as implant surface-treatments. These materials can be generated on the titanium dental implant by controlling the anodizing process (Figure 2.11) (Yi et al., 2015).

## Promoting Bone-Implant Regeneration

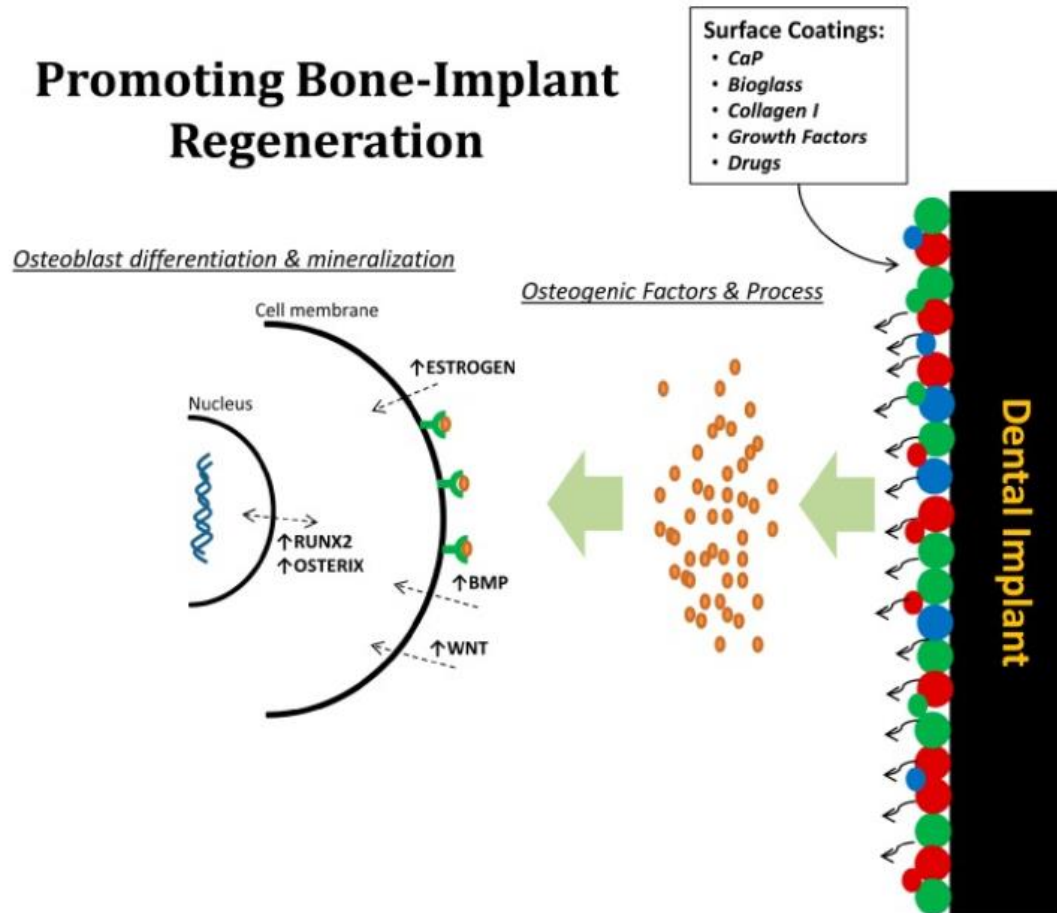


Figure 2.10 Diagram describing biological objective of surface coatings on dental implants. Bioactive materials able to be delivered to the surrounded bone, osteogenic factors help to increase osteoblast differentiation and mineralization. Adapted from (Alghamdi, 2018).



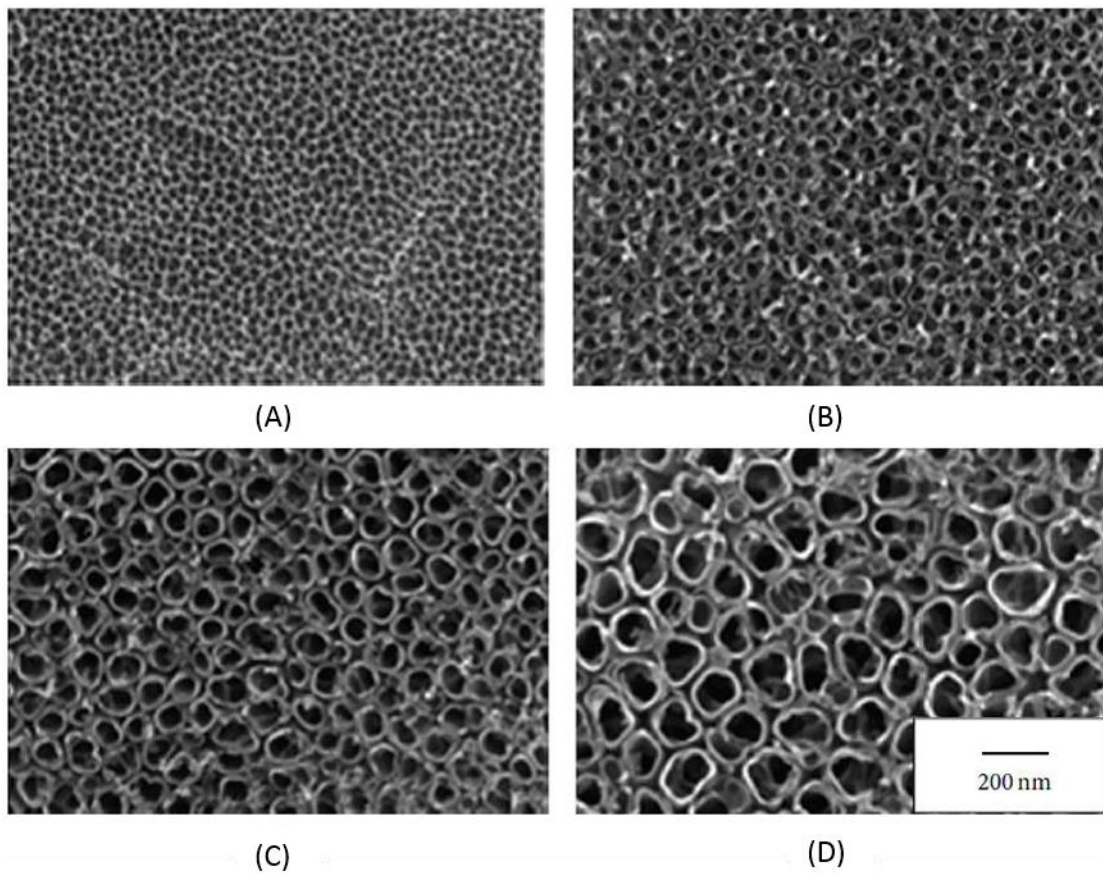


Figure 2.11 SEM images of different diameter sizes of TiO<sub>2</sub> nanotubes, (A) 30; (B) 50; (C) 70 and (D) 100 nm using 200 nm scale bar. Adapted from (Yi et al., 2015).

#### 2.4 Factors affecting dental implant failures

Despite the remarkable success of 90%- 95% dental implants of healthy patients, dental implants are in some cases not recommended. Smokers and patients with poor oral hygiene or systemic diseases such as unstable diabetics (Gaviria et al., 2014), heart problems and allergies are not preferred candidates for treatment with dental implants (Chaudhry et al., 2016). Lack of surgical skills and experience in dental implants is the main cause of implant failure. Dental implant stability is challenging in elderly patients and people with poor bone quality, such as osteoporosis, with a decreased osteogenic capacity of bone. A notable feature of the compromised bone condition is a significant reduction in the quality and quantity of the bone, which is inadequate to support implant osseointegration. In recent decades, many investigations have focused on the

development of surgical techniques, the design of implants and the properties of materials and surfaces to improve bone regeneration in compromised bone healing (Alghamdi, 2018).

### **2.5 *In vitro* and *in vivo* testing**

All new biomaterials and bone implants need to be tested physically, chemically, mechanically and biologically to confirm their efficacy and safety for clinical applications. A range of standard mechanical tests need to be applied such as compression, and three-point tests as described in chapter 4. *In vitro* and *in vivo* experiments are mainly used to test the biocompatibility and expected mechanical stability of the dental and orthopaedic implant.

Two dimensional (2D) *in vitro* tests are the main methods used to evaluate the compatibility of components used for dental and orthopaedic applications. In 2D cell culture, bone cells are mostly seeded directly on to the tested material, and the cellular response is evaluated. However, the absence of a dynamic environment in this method and the inability to assess the mechanical strength between the bone and the implant material limit the use of this method. *In vivo* animal testing is therefore used to test bone integration in to implants that are surgically placed in holes surgically created in the bone of an animal. Nevertheless, the disadvantages of animal models are that they are expensive, the animals have to be sacrificed and the variation between animal and human behaviour and structure may give miss-leading results. Many countries have legislation restricting the use of animals for scientific research purposes, for example in the EU (Parliament and Union, 2010).

### **2.6 *In vitro* bone model**

Recently, substantial progress has been made to develop *in vitro* bone tissue engineering. Such laboratory-grown bone-like constructs are created for regenerative

purposes but they can also be used as an alternative to costly animal models (Shea et al., 2000; Petite et al., 2000; Meinel et al., 2004). However, bone is a complex tissue and limited progress has been achieved in developing an ideal 3-D bone model to understand the development of bone diseases such as osteoporosis or to test osseointegration (Owen and Reilly, 2018).

Such *in vitro*, 3D bone models can be used in cancer research since bone is identified as the preferred location for breast cancer metastasis (Chen et al., 2010 and Holen et al. 2015). It also could be another way to understand mechanisms at bone implant interface and even for testing new implant materials. So far, a few trials have been undertaken to develop an *in vitro* 3D bone model for implant testing purposes. Blocks of natural carbonated hydroxyapatite seeded with adipose-derived stem cells (ADSCs) (Sivolella et al., 2015) and osteoconductive composite of polyurethanes-hydroxyapatite (PU-HA) scaffolds (Tetteh et al., 2016) are some of few studies reported in the literature to test implants.

Such a model requires scaffold materials that are easy to manufacture and capable of supporting the deposition of the bone matrix. Polyurethanes (PUs) were first introduced previously in our group as a scaffold for an *in vitro* bone model which is capable of supporting cell attachment, proliferation and calcified matrix deposition (Tetteh et al., 2016). Polyurethanes have attractive mechanical flexibility and ease of fabrication which has stimulated researchers' interest in PUs as biomaterials for medical devices and bone tissue engineering (Tortelli and Cancedda, 2009). Polyurethanes have a unique segmented structure due to the thermodynamic incompatibility between the hard and soft segments. Due to the versatile chemical properties of PUs, they can be used to make a diversity of materials, including segmented elastomers, elastomeric foams and injectable foams (Tetteh et al., 2016). As a scaffold to hold bone cells over long-term

culture the advantage of PU is its ability to undergo high strains under elastic deformation (springing back into shape), meaning that a PU foam can be highly porous without pore collapse and retain its shape over long term culture. It can be handled and manipulated without damaging it and is manufactured using high throughput and reproducible methods.

## **2.7 Characteristic features of porous metal**

Due to their morphology, physical and mechanical properties, porous metal structures have many possible applications in several different industries (Thiyagasundaram et al., 2010), including medicine (Ahmadi et al., 2014). Several classification systems have been used in the literature for porous metals of different types; these can, for example, be based on the structure, applications, properties or fabrication processes used. For bone applications, porous metal is typically classified into three main forms, which describe the nature of the whole component: 1) completely porous across the whole metal parts, 2) an entirely or partially porous layer coating on a dense core or 3) a structure composed of a fully solid and a porous metal part joined together (Ryan et al., 2006). Considering the porous part, Goodall et al. classified porous metals according to their structure, producing five groups: materials containing isolated porosity, true metal foams, particle packing to form a porous body, precursor based metal foams and lattices (Goodall and Mortensen, 2014). Additionally, for any of these types, porosity can be designed in a graduated manner, for example, by increasing in quantity from the core to the superficial layer (Kutty et al., 2001 and Kutty et al., 2004). Nevertheless, due to the reduction in mechanical properties that the incorporation of porosity brings, an entirely porous metal structure is unlikely to be suitable for an implant with a load bearing requirement. Therefore, a porous cover on a solid substrate is often

preferentially chosen for dental implants to ensure sufficient strength to tolerate the physiological loads (Ryan et al., 2006).

Porous metals exist in both closed (fully isolated pores) and open cell forms (connected with each other and the external environment). Although both types are widely used, the open type is evidently better for medical implant applications, because a degree of ingrowth into the structure is desired (Aly et al., 2005). As well as providing a suitable environment for the bone cells such that they infiltrate into the porosity, an interconnected foam with sufficiently large pores allows the formation of the vascular system required for bone maintenance (Murray and Semple, 1981 and Li et al., 2005).

Within the porous metals and the classification system used by Goodall et al. (Goodall and Mortensen, 2014), lattices are those structures made up of a regular repeating array of simple structural elements. These have certain attractive features, such as the fact that the properties can, in principle, be predicted to greater accuracy than when the pores are randomly located. However, they have formerly been difficult to produce in anything other than elementary forms and small sizes, barring certain structures such as honeycombs. However, this is changing with the growth in, and further development of, additive manufacturing technologies, which deposit or fuse material, building up a 3D structure (as detailed in Section 2.8). Within the lattices, the regular repeating unit cell structure has a dominant role in determining the mechanical properties of the structure overall (Ahmadi et al., 2014). An almost infinite array of designs is possible, and many have been produced, two dimensional honeycombs (Li et al., 2010), simple cubic lattices (Parthasarathy et al., 2010), rhombic dodecahedron (Harrysson et al., 2008) and diamond lattice (a cubic unit cell where the struts are positioned in the same way as the atomic structure of diamond) (Campoli et al., 2013 and Heintl et al., 2008). Graded lattices are also possible; recently, van Grunsven et al. used different strut

thicknesses to produce a diamond lattice structure with graded porosity (Figure 2.12). In this study, it was found that the mechanical properties that could be achieved could be relevant for orthopaedic implants (van Grunsven, 2014). Analytical and numerical solutions for the mechanical properties of a diamond lattice structure of Ti-6Al-4V were reported by Ahmadi et al. The results were compared with experimental observations. According to their findings, there was a good agreement between the analytical solutions and experimental observations, whereas the prediction of the finite element models was less likely to be accurate when compared with the experimental observations (Ahmadi et al., 2014). This is somewhat unexpected as finite element methods should allow more complex behaviour to be captured, but may indicate imperfect input parameters for the base alloy. It has been pointed out that the mechanical properties of the porous Ti-6Al-4V alloy with a diamond unit cell are similar to those of trabecular bone (Heinl et al., 2008). A similar approach, but for random porous structures, has been used by Cheng et al., in which they used human trabecular bone as a template to define a structure allowing an interconnected porous Ti-6Al-4V structure to be created using different levels of porosity (15%–70%). By increasing the porosity, a structure was created which closely mimics that of trabecular bone (Cheng et al., 2014).

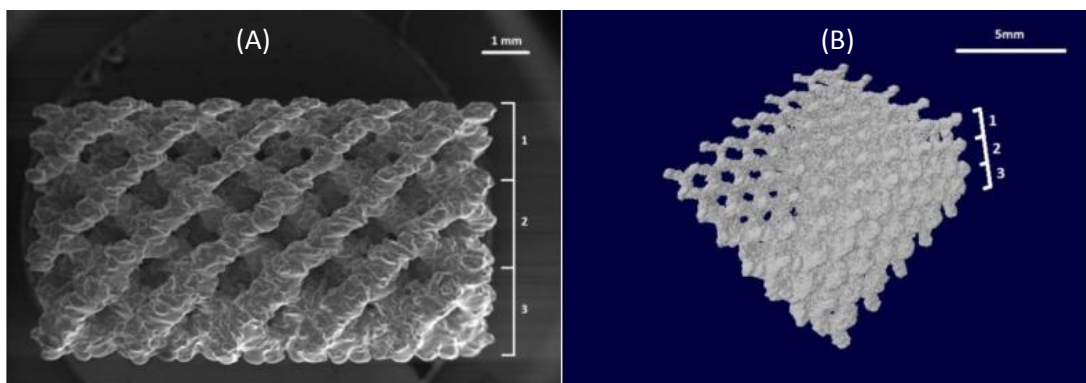


Figure 2.12 (A) SEM image of graded diamond lattice structure; (B) Micro CT scan of 3D image shows different strut thicknesses. Adapted from (van Grunsven, 2014).

Typically, a porosity of 75%–85% and a pore size of more than 100  $\mu\text{m}$  are considered to be preferable for rapid bone ingrowth (Mour et al., 2010). Wen et al. revealed that porous titanium with pore size ranging from 200–500  $\mu\text{m}$  was sufficient for adequate bone formation and fluid transport (Wen et al., 2001). Otsuki et al. have examined sintered porous titanium implants with different levels of porosity (50% and 70%) and pore sizes (250–500  $\mu\text{m}$ ) and (500–1500  $\mu\text{m}$ ). The results indicated 500–1500  $\mu\text{m}$  was the optimal pore size for bone tissue ingrowth for both levels of porosity (Otsuki et al., 2006), whereas Murphy et al. stated that the ideal pore size for bone ingrowth was around 325  $\mu\text{m}$  (Murphy et al., 2010). A graded structure as a coating with macro and nanoporosity (at a level of more than 70%) on titanium substrates was another approach developed by Fu et al. Three different materials (hydroxyapatite, calcium carbonate and titanium) and a combination of a modified plasma spray method and anodic oxidation process were used to produce porous scaffolds with macro-, micro- and nanopores (100–350  $\mu\text{m}$ , 0.2–90  $\mu\text{m}$  and 100 nm, respectively). The result showed that the mechanical properties were close to those of bone (Fu et al., 2011). Chen et al. created titanium scaffolds with a uniform and highly porous structure. The porous specimens were produced by stack sintering of microporous Ti spheres using centrifuge granulation technique. Based on the properties of the original titanium powders, specimens should have micro- and macroporosity of 6.1–11.8  $\mu\text{m}$  and 180.0–341.8  $\mu\text{m}$ , respectively, and the mechanical properties were reported as being suitable for implant applications in load-bearing areas (Chen et al., 2014).

As can be seen, there is no clear identification of the optimum pore size for bone ingrowth. In general, the mechanical and biological performance of the porous metal structure is governed by the combined effects of characteristic features of the porosity such as pore shape, size, distribution and their interconnectivity, as well as the base

metal from which the porous structure is made (Hoffmann et al., 2014). Thus, with the current level of understanding the pore geometry needs to be optimised for each specific case to achieve a suitable environment for the surrounding bone tissue. Furthermore, it should be noted that not only the properties of the coating, but also those of the underlying base material will affect the mechanical properties of the final product.

## **2.8 Fabrication methods and mechanical evaluation of porous dental implants**

Titanium is well known as a relatively high cost engineering material due to the difficulties in the extraction, forming and machining processes (Sidambe, 2014). Traditionally, a titanium alloy dental root implant is manufactured via a casting or powder metallurgy route (Tolochko et al., 2002). With the casting method, in particular, machining and other finishing steps are required with a large amount of waste material (Nouri et al., 2010). Furthermore, the high melting temperature of the titanium base alloy and the high reactivity of titanium with atmospheric gasses at elevated temperatures make it challenging to adapt many existing techniques which were developed for lower melting point metals, such as aluminium (Ryan et al., 2006).

Powder metallurgy is less expensive and has reduced amounts of waste compared to the other production methods available (Nouri et al., 2010). Relatively simple techniques for the production of porous materials include sintering hollow spheres or the use of thermal decomposition of, for example,  $\text{TiH}_2$ . Fairly homogenous foam structures have been made from high melting temperature metals such as titanium and its alloys (Mour et al., 2010) and this method is also suitable for the production of titanium foams with pore sizes meeting the standard requirements considered to be suitable for bone ingrowth (Teixeira et al., 2012). Improving the compaction process of alloy powder also has an influence on the accuracy and degree of porosity of the final part (Lapteva et al., 2004).



## ***Chapter 2: Review of the literature***

For porous materials as a whole, there are certain potential disadvantages for use as implants. For example, the fatigue strength is unlikely to satisfy the requirements of implant devices. Nevertheless, this can be improved. For example, it has been shown that, for cases where a foaming agent is combined with metal powder, the fatigue life can be increased by having a more uniform foam structure through reduced stress concentrations. This is achieved by adjustments to the mixing strategy for the powder of foaming agent, metal and binder as reviewed by Ryan et al. (Ryan et al., 2006). Other methods have shown their suitability for the production of medical grade titanium alloy for medical applications, including sintering of powders, compressing and sintering of titanium beads or fibers to create interconnected porous structures (Kutty et al., 2004).

Table 2.3 Comparison table of the main fabrication methods used for creating rough and porous implants with potential dental and/or orthopedic applications.

Fabrication methods	References
Plasma spraying with different powder particles such as: -titanium oxide -calcium phosphate -hydroxyapatite	(Gaviria et al., 2014)
Sand blasted with stiff particles such as: -alumina -TiO <sub>2</sub> -ceramic	(Le Guéhennec et al., 2007)
Laser micro-machining technique	(Çelen and Özden, 2012)
Anodization TiO <sub>2</sub> nanotube	(Yi et al., 2015)
Electron-discharge compaction	(Lifland et al., 1993)
One-step microwave processing method	(Kutty et al., 2004)
Powder metallurgy -sintering hollow spheres -thermal decomposition -sintering of powders, compressing and sintering of titanium beads or fibers.	(Mour et al., 2010, Kutty et al., 2004)
Removable space holder and titanium metal powder particles: - saccharose crystals - NaF - NaCl - polymer granules - Magnesium - ammonium hydrogen carbonate	(Jakubowicz et al., 2013, Bansiddhi and Dunand, 2007, Bansiddhi and Dunand, 2008, van Grunsvan et al., 2012, Jee et al., 2000, Kim et al., 2013, Jurczyk et al., 2013)
Additive manufacturing technology: - selective laser sintering - selective laser melting - electron beam melting	(Tolochko et al., 2002, van Grunsvan et al., 2012, Hrabe et al., 2011)

For more regular titanium pore geometries, a controlled mix of removable space holder and titanium metal powder particles has been suggested and explored by a considerable number of studies. The range of materials used as a space holder includes saccharose crystals (Jakubowicz et al., 2013), NaF (Bansiddhi and Dunand, 2007), NaCl (Bansiddhi and Dunand, 2008 and van Grunsven et al., 2012) and polymer granules (Jee et al., 2000). Magnesium has also been used as a space holder to produce porous dental and orthopedic implants (Kim et al., 2013). Jurczyk et al. recommended ammonium hydrogen carbonate to produce a porous nanocomposite scaffold using titanium containing 10 wt. % SiO<sub>2</sub> appropriate for dental applications (Jurczyk et al., 2013). Caution is recommended though as a strong reaction has been reported between titanium and some space holders with both high and low melting temperatures, leading to the formation of impurities within the foam (Li et al., 2014).

With all the aforementioned approaches, titanium implants can be made with entirely porous or solid structures though it is not straightforward to produce a porous shell on a solid core. A variety of methods have been developed over the last few decades to create dental root implants which mimic the morphology and mechanical properties of natural dental roots (Tolochko et al., 2002). One method involving an electron-discharge compaction has also been reported to produce porous surface on the commercially dental implant, porosity on a compact core was created using input energy 1–2.5 kJ/g to atomized the Ti–6Al–4V powder (Lifland et al., 1993). A one-step microwave processing method has also been suggested to sinter titanium powders in order to produce dental implants, with gradient porosity, microwave power energy of 1–1.5 kW and a 30 min soaking period used. The pore size was about 30–100 μm and thickness was ranging from 100–200 μm, as determined by the level of microwave power (Kutty et al., 2004).

Among these methods, additive manufacturing technology has been considerably developed (Mangano et al., 2012) including selective laser sintering (SLS) (Traini et al., 2008), selective laser melting (SLM), described in detail in section 2.9, and electron beam melting (EBM) (Hrabe et al., 2011). The additive manufacturing approach is based on building up a three-dimensional structure from a computer aided design (CAD) model (Ryan et al., 2006). Each fabrication method will have many variables; for example, for SLS, parameters would include laser power, scanning speed, laser beam diameter and layer thickness (Mangano et al., 2014). Additive processes are in general less time consuming overall (Mangano et al., 2014) and allow the creation of porous structures with different unit cells (Ahmadi et al., 2014) and high resolution (i.e., small cell sizes) (Cheng et al., 2014).

Additive manufacturing technology has more specifically been applied to produce non-porous parts with complex geometry for use in implants, such as dental, craniofacial, maxillofacial and orthopedic implants (Murr et al., 2010). In 2002, Tolochko et al. demonstrated the possibility of producing dental root implants from Ti powders with two different zones, comprising a compact core and irregular porous shell by incorporating (SLS) for the porous surface and (SLM) for the solid core. The thickness of both layers was determined by the laser power. Microscopical examination showed that the average pore size was 100–200  $\mu\text{m}$  and the porosity 40%–45% (Tolochko et al., 2002) (Figure 2.13). Dental implant models with a dense core and porous layer consisting of a series of channels which are 1 mm in depth and 1 mm in diameter have been considered. Laser-forming techniques (laser sintering and laser melting) with continuous wave and pulsed lasers were used (Figure 2.14). The channel diameters of the products were lower than those of the CAD model. The fatigue and tensile strength of the titanium samples produced were influenced by the different processing

## *Chapter 2: Review of the literature*

parameters utilized in this study. These variables include the scanning speed of the laser, the laser peak power and the hatching pitch, all of which combine to alter the amount of energy input into the material, and thus influence the solidification and cooling. The effect is to alter the microstructure of the material, which occurs in complex ways as the flow of thermal energy is also affected by part shape and location in the part. The processing parameters were found to be optimal at a scan speed of 6 mm/s, a laser peak power of 1 kW, and a hatching pitch of 0.4 mm (Laoui et al., 2006). Traini et al. have also produced titanium dental implants incorporating graduated porosity from the inner core of the structure to the outer surface using titanium alloy (Ti-6Al-4V) powders with a laser sintering procedure. The average porosity was 28.7% and the modulus value of the dense core was similar to that of a machined titanium implant whereas the porous part was comparable to that of bone tissue (Traini et al., 2008). The study of Mangano et al. did not go quite as far as producing a fully porous structure, rather stating that direct laser fabrication is an economical technique that has potential to produce dental implants with irregular and narrow intercommunicating crevices and shallow depressions using titanium alloy powder. The surfaces were analyzed under stereo scanning electron microscopy. However, there was a residue of metal particles on the implant surface. Thus, they suggested acid etching as treatment to eliminate the adherent particles (Mangano et al., 2009).

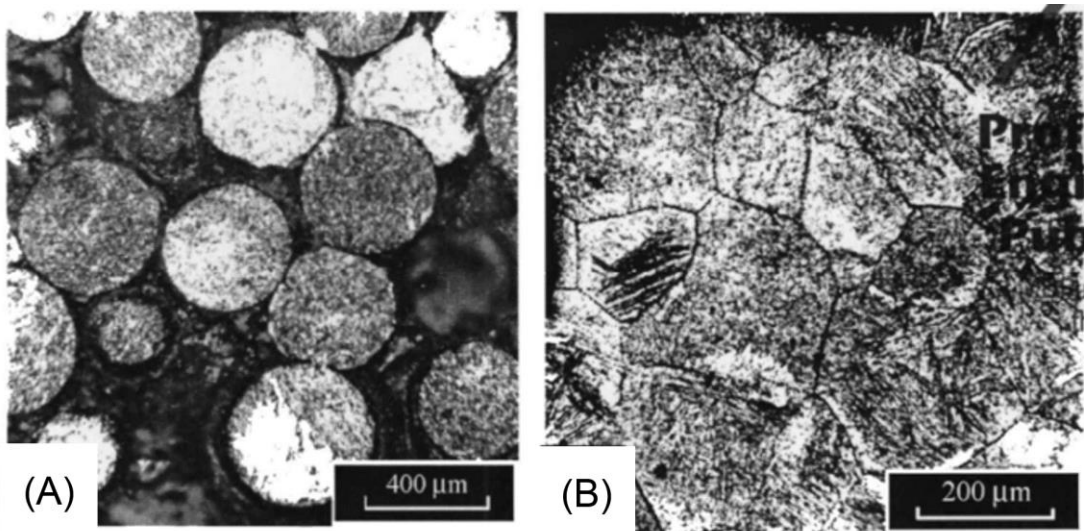


Figure 2.13 SEM images of dental root implants fabricated by the SLM and SLS processes with two different zones, (A) the sintered zone close to the surface and (B) the remelted core. Adapted from (Tolochko et al., 2002).

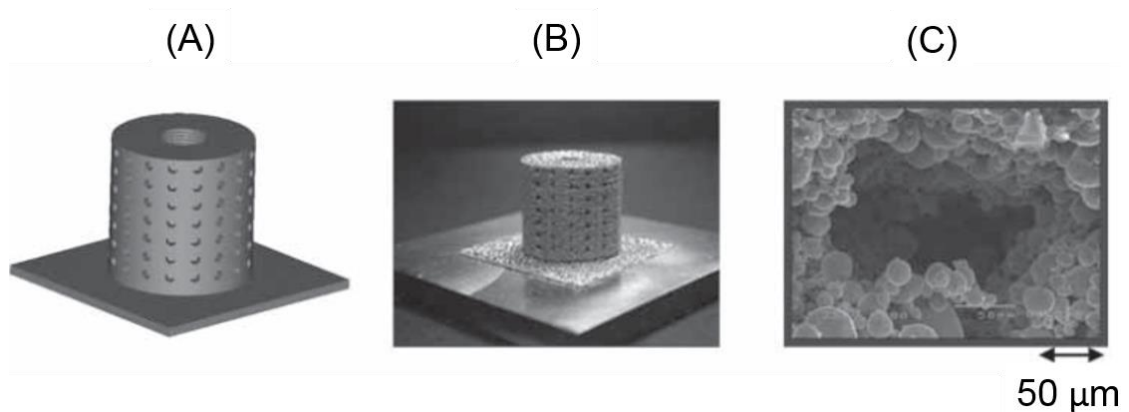


Figure 2.14 CAD model of dental root implant with porous covering (A), built SLM titanium cylinder ( $15 \times 15 \text{ mm}^2$ ) (B) with pore/channel ( $100 - 200 \text{ μm}$ ) on surface. Adapted from (Laoui et al., 2006).

Schiefer et al. examined the long-term stability and mechanical properties of two types of porous dental implants under static and dynamic conditions. Implants were surrounded by porous layers that were made using ammonium hydrogen-carbonate ( $\text{NH}_4\text{HCO}_3$ ) as space holder particles. Fatigue analysis suggested that these implants would struggle to perform well against forces in a range similar to that produced by

human jaw. Moreover, pore alignment can affect the mechanical properties of porous titanium (Schiefer et al., 2009). Murr et al. in 2010 used electron beam melting (EBM) to produce Ti-6Al-4V open cellular foams with different cell wall structures (solid and hollow). The elastic moduli were found to decrease with increasing porosity as widely known for porous metals of all types. However, the micro indentation hardness of the solid cell wall structure was lower than that of the hollow cell wall (Murr et al., 2010). Li et al. established that the electron beam melting process has the potential to process Ti-6Al-4V implants with versatile pore geometry. The compressive properties of porous implants are variable with pore architecture and can be similar to those of natural bone (Li et al., 2010). To improve the surface wear resistance of the titanium structures, Laoui et al. applied laser gas nitriding using a CW Nd:YAG laser, and the coating layer was able to withstand more cycles without fracturing (Laoui et al., 2006).

Microstereolithography ( $\mu$ SL), where a laser is used to polymerise a structure from a solution bath, based on a CAD model, is another type of rapid prototyping technology used to produce polymeric dental root implants with a dense core and porous surface using photocurable resin using a laser power (Bártolo, 2005).  $\mu$ SL was also used to produce base polymer templates which were converted by coating into metallic microlattices for medical devices (Zheng et al., 2014). Some researchers used  $\mu$ SL in combination with nanoscale coating and post-processing techniques to produce ultralight microlattices with relatively stiff properties and low density. Electroless nickel plating was used to produce metallic hollow-tube nickel-phosphorus (Ni-P) with metal films thickness ranging (100 nm-2  $\mu$ m). However, the thickness of coating layer was determined by the plating time. Atomic layer deposition was used to produce hollow-tube aluminum oxide (amorphous Al<sub>2</sub>O<sub>3</sub>, alumina) with alumina thicknesses from (40 to 210 nm) (Zheng et al., 2014). Despite the ability of  $\mu$ SL to create complex

microstructures, the main concern is the scarcity of biocompatible polymers and the photoinitiators used could be toxic. In addition, the lower mechanical properties of photopolymerized resin limit its use in hard tissue engineering (Chia and Wu, 2015).

One of the essential requirements of dental implants is to have a rough surface with macroscopic grooves and threads or a porous surface to provide primarily mechanical stabilization between implants and bone tissues (Tolochko et al., 2002). Furthermore, sufficient mechanical support should be provided between the root of the dental implant and its superstructure crown. This can be achieved by creating a solid core and porous shell as a substitute to an entirely porous structure (Tolochko et al., 2002). As stated in section 2.3 when providing a porous coating one concern is that stress concentrations could arise at the junction area of the shell and core of the implant where the mechanical properties change rapidly (Ryan et al., 2006). This weakens the bond between the covering layer of the implant and the core. To reduce residual stresses, a post-sintering heat treatment has been suggested by Clook and co-workers, which showed an improvement in the fatigue strength of titanium alloy by about 15% (Cook et al., 1988). Nevertheless, the idea of creating functionally graded structures can be helpful to avoid the stress concentration between the interface layers where the elastic modulus changes suddenly (Joshi et al., 2013). The concept of the creation of functionally graded structures in porous materials by changing the structure of the lattice has also been investigated (van Grunsven et al., 2014).

Bandyopadhyay and colleagues suggested laser engineered net shaping (LENS™) to construct porous structures from Ti–6Al–4V alloy across the range 23%–32% porosity with low modulus (7–60 GPa) which can be tailored to match human cortical bone (Bandyopadhyay et al., 2010). Nomura et al. in 2010 recommended the infiltration technique in a vacuum with sintering to create porous titanium/hydroxyapatite



composites. The Young's modulus was estimated using the percentage of porosity and it was tailored to be in the range of bone tissue (given by 24%–34% porosity). Porosity can be controlled by modifying the temperature and pressure applied in a hot-pressing stage. Witek et al. measured the bone implant contact and removal torque of dental implants with a porous layer produced by laser sintering and compared them with sandblasted-acid etched implant (i.e., those with a rough, but not porous, surface). They concluded that porous dental implants produced by the sintering process showed better biomechanical properties and biocompatibility (Witek et al., 2012). The widely used fabrication methods for the production of porous materials in this section are listed in Table 2.3.

## **2.9 Selective laser melting**

In this thesis the focus will be on selective laser melting as the preferred fabrication technique. SLM is an additive manufacturing technique able to create 3D components using a technique where the material is added progressively, layer by layer. SLM of titanium alloys was introduced in the 2000s (Simonelli, 2014) (Figure 2.15). A Renishaw AM250 machine is a common SLM system with a 200 W fixed fibre and controlled pulsed laser. This system typically works with a vacuum chamber which is occupied by an inert gas such as Ar or N to reduce the risk of titanium oxidation or contamination. These gases are transparent at laser wavelengths (Gibson et al., 2010). SLM initially forms a thin layer of around 50  $\mu\text{m}$  covering the building platform and maintains it at a lower temperature (less than 200°C). A high powered laser is then used for the following layer to melt the selected spots in the powder bed. As the laser scanning is completed, the building platform is lowered to the thickness of the next layer with the application of a new powder layer. The process of scanning melting is repeated until the part is built. (Simonelli, 2014). The platform is loaded with a substrate

typically the same material as deposited powder to ensure that the printed structure is firmly attached and with same rate of thermal expansion is maintained during melting of layers (Mezzetta, 2016). The laser can focus on small point size, leading to a structure with a high level of accuracy (Simonelli, 2014). A diagram for the principle of the SLM process is shown in Figure 2.15. SLM used to produce Ti alloys dental roots, teeth models and hard tissue prosthesis (Tolochko et al., 2002, Laoui et al., 2006, Gebhardt et al., 2010, Wehmöller et al., 2005).

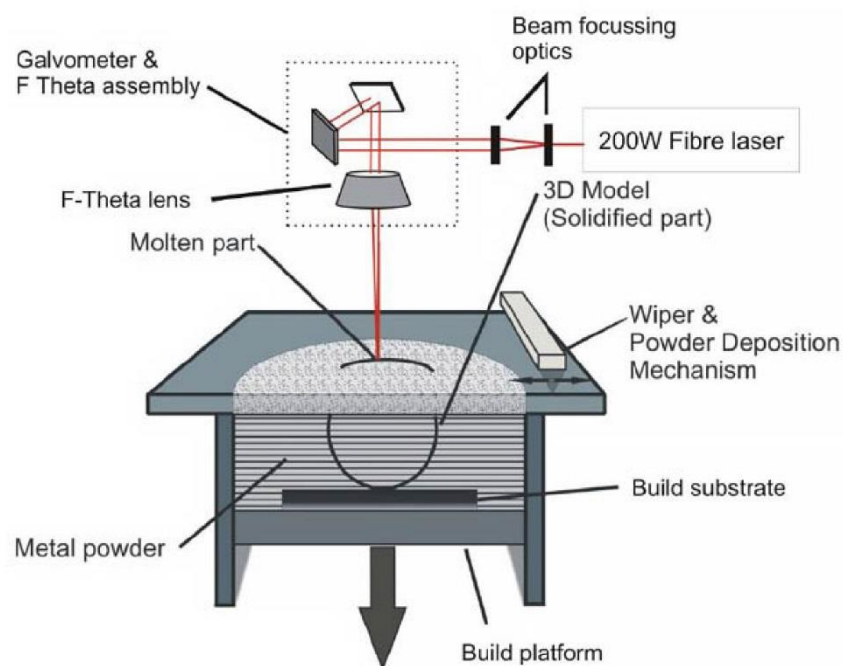


Figure 2.15 Selective laser melting process schematic. Adapted from <https://www.fusionimplants.com/r-d/>.

## **2.10 Biological interaction and porous surface geometry**

Most dental implant materials aim to support cell attachment by conferring a suitable area for cell adhesion (Bidan et al., 2013). It has been demonstrated that bone cell interactions are mainly modulated by the chemistry and mechanical properties of the substrate, the structure of the implanted material and the fabrication method. Cell behavior has been stated to be more influenced by the topography of the surface, it

encounters than by the chemistry of implant material or processing method (Kumar et al., 2011), although these effects are difficult to separate as they are all interrelated (Bidan et al., 2013). *In vivo* and *in vitro* observations of the micro- and macro-roughness of the surfaces of dental and orthopedic implants have been shown to play an important role in improving the response of bone-forming cells (osteoblasts) (Cheng et al., 2014). Rough surfaces provide better osteoblast attachment (Mour et al., 2010), improved cell proliferation and extracellular matrix formation which in turn enhance the osseointegration process and durability of dental implants (De Wild et al., 2013).

A porous implant surface has a high surface area which should enable more cells to attach compared to a planar surface. *In vitro* observations have demonstrated a good range of bone ingrowth in porous titanium implant using different manufacturing techniques (Teixeira et al., 2012). Teixeira et al. examined the osteoblastic response on porous titanium with different pore sizes (312, 130, 62  $\mu\text{m}$ ) using a powder metallurgy technique. The result showed the highest gene expression of bone markers was with 62  $\mu\text{m}$  porosity (Teixeira et al., 2012). Mangano et al. seeded human dental pulp stem cells on direct laser metal sintered titanium scaffolds and acid etched surfaces. They observed that gene expression and protein secretion were faster on laser sintered scaffolds (Mangano et al., 2010). Another comparative study has been proposed between porous and non-porous titanium alloy Ti-6Al-4V samples. The pore diameters were 500, 700 and 1000  $\mu\text{m}$ . The result showed that the osteoblast cell viability was maintained over 14 days and the cells entirely covered the porous structure (Hollander et al., 2006). Cheng et al. proposed using a template from human trabecular bone to fabricate porous Ti-6Al-4V materials using additive manufacturing technology, laser sintering in particular. Different porosities (low, medium and high) ranging from 15%–70% with interconnected structure were fabricated to produce structures that mimicked the

trabecular bone of the human body. After specific surface treatment with calcium phosphate particles and acid etching, the trabecular bone structure exhibited micro and nanoscale porosity which was able to enhance osteoblast cell differentiation. Thus, a trabecular structure has the potential to produce devices well-suited for dental and orthopedic implants (Cheng et al., 2014). Another attempt to improve the mechanical and biological properties of porous titanium structures also incorporated a modified sponge replication method and anodization process. Titanium scaffolds with elongated pores were produced by coating a stretched polymeric sponge template with TiH<sub>2</sub>. The anodization of the titanium can produce a nanoporous surface that can increase osteoblast cell (MC3T3-E1) proliferation and attachment on implant surfaces (Schiefer et al., 2009).

Pore geometry (shape) is also likely to have a strong effect on cell attachment and matrix formation (Rumpler et al., 2008) but researchers rarely investigate different pore geometries within a single material and manufacturing process. Recently, such a study was undertaken by Markhoff et al. who evaluated the viability and proliferation of human osteoblast cells in porous Ti-6Al-4V using different scaffold designs and cultivation methods. Additive manufacturing technology was used to produce different pore geometries (cubic, diagonal, pyramidal), and static and dynamic culture methods were used. Interestingly, there were no significant differences between the static and dynamic cultivation methods, but cell activity and migration were best in the pyramidal design with a 400–620 μm pore size and 75% porosity (Markhoff et al., 2015).

Although *in vitro* studies are often an essential step in the discovery of novel implant materials and structures, there are many inherent limitations to the use of cell culture to predict the long-term survival of an implant. These include the absence of a 3D environment that adequately mimics the chemical and mechanical properties of bone,

the lack of mechanical forces acting at the bone-implant interface after implantation, the absence of the complex matrix of proteins and different types of bone cells that are present at the bone-implant interface *in vivo* and the difficulty of maintaining the culture for long time periods. While researchers are attempting to improve *in vitro* studies using 3D environments and bioreactors, the current information regarding long-term implant stability comes from *in vivo* studies.

*In vivo* studies by Mangano and co-workers used a laser sintering process to design titanium dental implants with interconnected pores and irregular crevices. The clinical observation showed 95% success after one year post operation (Mangano et al., 2012). In histological evaluations, Shibli et al. measured human bone tissue response to three types of dental implants: direct laser fabrication, sand-blasted acid-etched and machined commercially pure titanium under unloaded conditions. The result indicated that after eight weeks of implant insertion, the bone-implant contact produced by the direct laser and the sandblasted acid-etched processes was not significantly different but was higher than that of machined implant, and there were no significant differences between them. The authors attributed their finding to the surface roughness that was produced by the laser and sandblasting techniques, which enhanced the osseointegration process (Shibli et al., 2009). Another study using male Sprague-Dawley rats indicated that biological fixation was influenced by the percentage of porosity in titanium implants (25%, 11%, 3%). After 16 weeks' examination, the concentration of calcium ions increased proportionally with the increasing porosity percentage (Bandyopadhyay et al., 2010). Laoui et al. inserted a Ti implant into a dog's lower jaw and revealed clear bone growth into the porous structure within the porous surface layer, and no signs of inflammation at the interface were observed (Laoui et al., 2006). Tolochko et al. inserted a prototype porous dental implant into the lower jaw of a cadaver and demonstrated that the implant

was firmly integrated into the alveolar ridge of the lower jaw with a maximum gap width of 200–300  $\mu\text{m}$  between the implant and the bone (Tolochko et al., 2002). Another attempt was made to reduce the healing period required for the dental implant and bone by coating a titanium dental implant with  $\text{TiO}_2$  nanotubes, which was tested in a rat femur. Variable diameter sizes were used (30 nm, 50 nm, 70 nm, and 100 nm nanotubes), the highest removal torque and osseointegration rates were observed in the 30 nm implants after two weeks whereas the 70 nm implants exhibited the highest value after six weeks for both tests (Yi et al., 2015).

### **2.11 Chapter summary**

Lack of dental implant stability and durability have been a major concern, especially in compromised bone quality. This occurs due to the high density of implant materials that are not able to provide sufficient loading to the underlying bone resulting in poor osseointegration. Introducing porosity into titanium structures has been proposed to improve implant stability, however the optimum pore size, geometry and graduation for the most effective biomechanical and biological properties has not yet been identified. Several methods have been described to produce porous titanium components. Additive manufacturing technologies have attracted researchers' attention due to their ability to create complex structures that are impossible with traditional methods. Such 3D printed porous components should be designed with mechanical properties comparable to bone tissue and pore geometry desirable for bone ingrowth for better functionality in load bearing areas. Work in this area is promising and provides a basis for dramatic improvements in the design of a dental implant for patients with compromised bone healing. The aim and objectives of this project described in the following section (2.12) are to determine the feasibility of advanced manufacturing technologies for the production of a range of novel porous titanium rods representing the size of current

dental implants and to use a structural, mechanical and biological characterisation to assess their suitability for bone ingrowth.

## **2.12 Thesis Aim and Objectives**

The main aim of this thesis was to develop a range of lattices from the titanium alloy Ti-6Al-4V of regular and graded porosity and novel ‘spider web’ design via selective laser melting. The effects of pore variance on mechanical and biological properties were investigated. These lattices were designed to be rod-shaped with dimensions representing the size of current dental implants. Surface chemistry and mechanical properties of these components were investigated. The potential to support bone ingrowth was evaluated by direct seeding of bone cells on the lattices and cell viability, and extracellular matrix deposition was evaluated. A novel *in vitro* 3D culture model was also developed; the porous Ti-6Al-4V structures were implanted into a ring of porous polymer sponge that had been pre-seeded with osteoblast cells. To achieve this goal, the work was divided into the following tasks:

1. Due to the feasibility of Selective Laser Melting system to produce complex porous structures as described in 2.9 section, it will be used to produce a novel ‘Spider Web’ design and a range of titanium alloy micro-lattice structures based on a diamond unit cell. Different pore sizes (250, 300, 400 and 650  $\mu\text{m}$ ) and strut thicknesses (250, 300 and 400  $\mu\text{m}$ ) and graded porous structures with and without a dense core will be designed and printed in chapter four.

- a. As pore geometry and interconnectivity play a vital role in scaffolds for bone regeneration (described in section 2.10) the physical properties of these lattices will be evaluated in chapter four using SEM,  $\mu\text{CT}$  and Archimedes method.

## *Chapter 2: Review of the literature*

b. Surface chemistry of 3D printed Ti-6Al-4V components is a matter of concern due to the potential of titanium contamination by the interstitial elements during laser manufacturing as described in section 2.9. In chapter four, LECO and ICP system will be used to quantify the amount of the main and interstitial elements (oxygen, nitrogen and carbon) of the built SLM lattices and compare it with the raw Ti-6Al-4V particles provided by the Medical Advanced Manufacturing Research Centre.

c. Strength properties of porous biomaterials is required to be manipulated to closely match those of human bone (described in section 2.8). Mechanical properties of the lattices in compression and three-point bending will be evaluated in chapter four.

2. Bone ingrowth is influenced by pore geometry of implant materials and it is possible that Ti-6Al-4V has a cytotoxic effect on bone cells (as described in section 2.10) Therefore, the biological effects of the SLM Ti-6Al-4V powder particles and built components on bone forming cells will be assessed in chapter five.

a. Evaluate the amount and diameter of the unfused Ti-6Al-4V particles released from the lattices using an ultrasonic cleaning bath over a series of cleaning periods (15 mins, 30 mins, 1, 2, 4, 8, 16, 32, 64 and 128 hours).

b. Determine whether there is a cytotoxic effect of the of micro Ti-6Al-4V particles used for the SLM system on two types of bone cells, MLO-A5 and hBMSCs growth.

c. Examine and compare the ability SLM Ti-6Al-4V lattices with different designs to support bone cell growth and extracellular matrix deposition using MLO-A5 cells.



3. Providing an *in vitro* bone model could reduce costly animal testing and may also be used for newly developed implant testing (as described in section 2.6). In chapter six a novel *in vitro* 3D bone model will be developed and assessed for testing 3D printed porous implants to replicate the osseointegration process.

- a. Find out whether an industrial PU foam would be suitable for a long-term *in vitro* 3D culture model.
- b. Compare different insertion conditions, and identify the best time point, for inserting titanium lattices to support cell migration and extracellular matrix deposition into the implanted constructs.
- c. Compare the influence of different implantation periods on the extracellular matrix deposition into the implanted titanium.
- d. Use the *in vitro* model to compare bone matrix deposition on two different designs of 3D printed Ti-6Al-4V lattices; GP/300-400 and spider web.
- e. Demonstrate the ability of the method to determine human bone ingrowth using human primary bone marrow derived mesenchymal stem cells.

## **Chapter 3 : Materials and Methods**

### **3.1 Introduction**

The following chapter describes materials and experimental work commonly employed in achieving the outcomes given in the following chapters of this thesis. The specific procedures related to only one section can be found in the relevant chapter. All Ti-6Al-4V scaffolds used in this work were manufactured by SLM process in the Medical Advanced Manufacturing Research Centre (AMRC), UK. All experimental procedures were carried out with facilities accessible in the Materials Science and Engineering Laboratory of the University of Sheffield, UK, unless otherwise stated.

### **3.2 Ti-6Al-4V Powder Particles**

The Plasma atomised Ti-6Al-4V particles provided by the Medical Advanced Manufacturing Research Centre (AMRC) were used with Renishaw AM250 machine to fabricate all Ti-6Al-4V scaffolds used in this thesis. The chemical composition of used particles is shown in Table 3.1 as reported in the datasheet and material validation sheet of the Renishaw system (appendix 9.4 and 9.5)

Table 3.1 Chemical composition of the plasma atomised Ti-6Al-4V Extra Low Interstitial (ELI) grade 23. Provided by material validation sheet of Renishaw's titanium alloy (Ti-6Al-4V).

<b>Chemical composition/percent by mass</b>							
<b>Ti</b>	<b>Al</b>	<b>V</b>	<b>N</b>	<b>C</b>	<b>O</b>	<b>H</b>	<b>Fe</b>
Balance	5.5 -6.5	3.5 - 4.5	<0.03	<0.08	<0.13	<0.012	<0.25

Ti-6Al-4V powder particles (Figure 3.1) used with the Renishaw system were spherical, and the diameter size had distribution between 15 – 55  $\mu\text{m}$  as shown in figure 3.2. The average particle size was between 30 and 34  $\mu\text{m}$ .

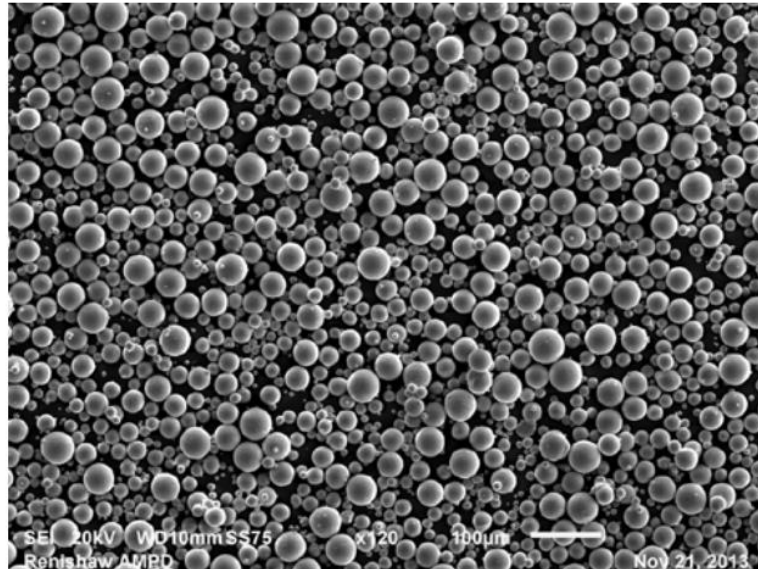


Figure 3.1 SEM image of Ti-6Al-4V powder particles at x120 magnification, Adapted from Material validation sheet of Renishaw’s titanium alloy (Ti-6Al-4V) (appendix 9.5).

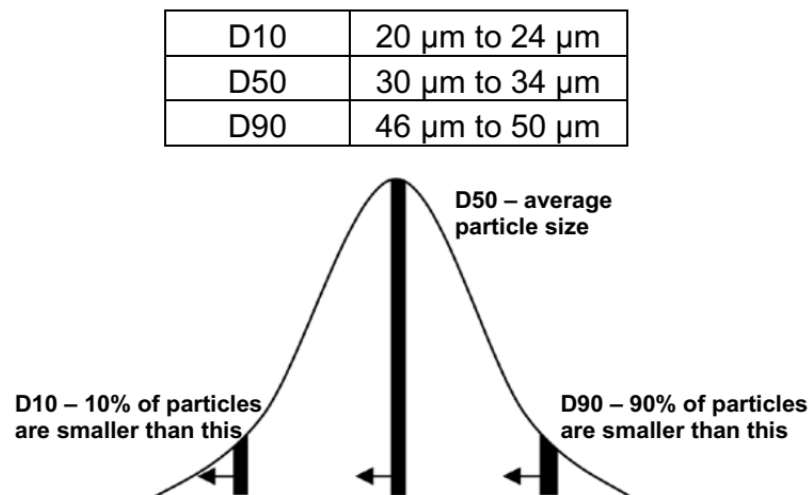


Figure 3.2 Particle size distribution of Ti-6Al-4V powder used for Renishaw system. Reprinted from Material validation sheet of Renishaw’s titanium alloy (Ti-6Al-4V) (appendix 9.5).

### **3.3 Fabrication of Selective Laser Melting (SLM) Ti-6Al-4V lattices**

Due to the feasibility of the SLM system to produce complex porous components (Simonelli, 2014), it was used to create different titanium lattices in this research study. All Ti-6Al-4V lattices of varying design were manufactured on the Renishaw AM250 Laser Melting System in the Medical Advanced Manufacturing Research Centre (AMRC), UK. Details on these CAD models and production system are provided in section 4.3.1.1 and 4.3.1.2, respectively.

### **3.4 Sample preparation**

#### **3.4.1 Ti-6Al-4V lattices**

To prepare SLM titanium alloy (Ti-6Al-4V) lattices for physical, chemical, mechanical (compression and three-point bending) and biological examination, lattices were cut through the axis into about  $7 \pm 0.2$  mm height cylinders using Secotom-50 cutting machine and abrasive wheel (Diamond wafering blad) 11-4217010, BUEHLER. To obtain flat surfaces cut samples were polished on the Ecomet-250 grinder - polishing machine, using SiC papers with 500 and 1000 grits (Figure 3.3). Then they were cleaned for 30 minutes with an ultrasonic bath to remove loose powder particles from the built components.

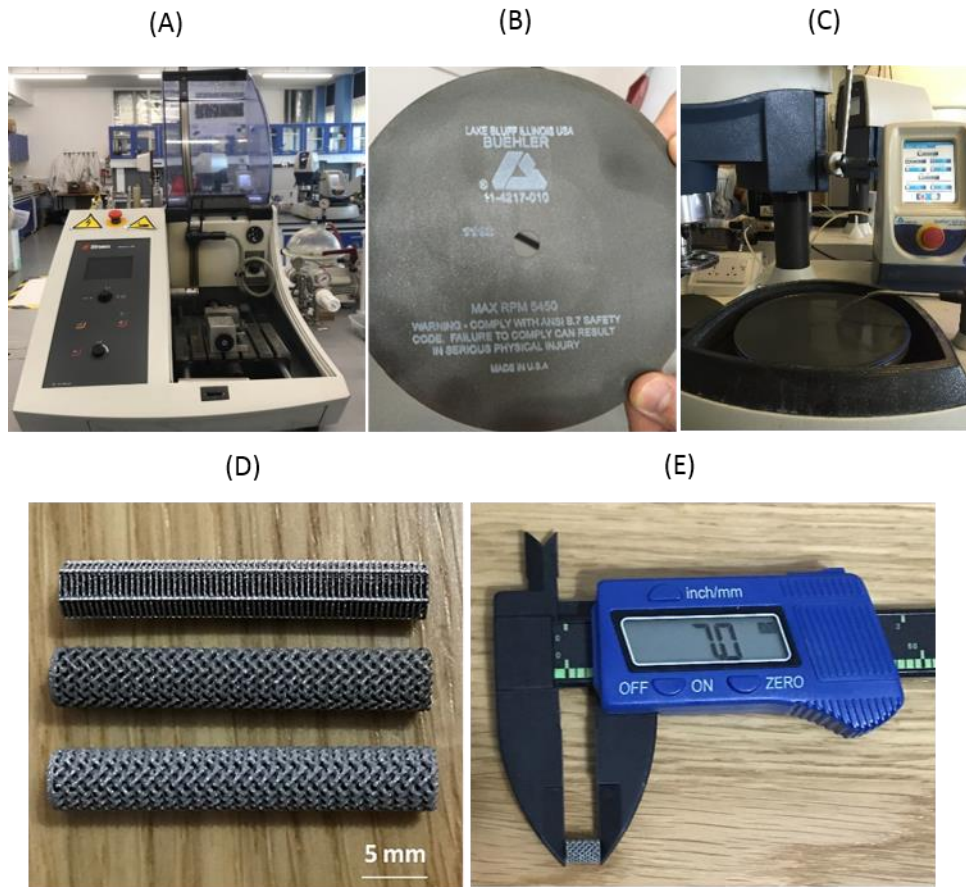


Figure 3.3 Sectioning Ti-6Al-4V lattices (A) Secotom-50 cutting machine (B) 11-4217-010 diamond cut-off wheel (C) Ecomet-250 grinder - polishing machine (D) Ti-6Al-4V lattices before cutting (E) Ti-6Al-4V lattices after cutting.

### 3.4.2 Polyurethane (PU) scaffolds

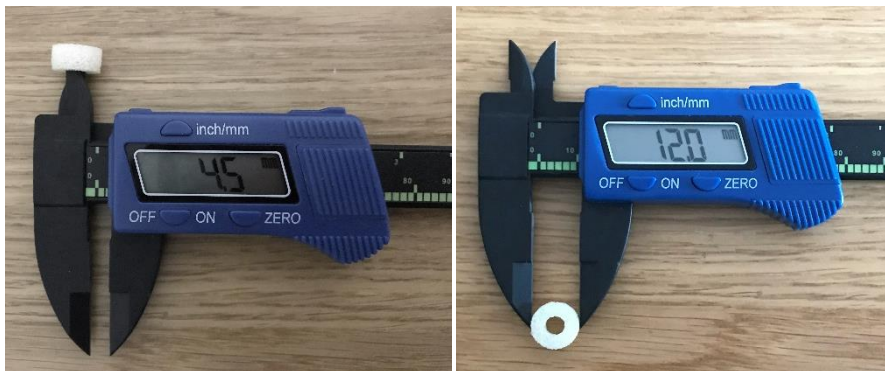
Polyurethane (PU) scaffolds were used for the current *in vitro* 3D bone model because they provide several advantages, such as biocompatibility, mechanical flexibility, cost-effectiveness and ease of fabrication (Tetteh et al., 2016). PU scaffolds were laser cut into specific size using Epilog Mini 40 W laser cutter from Epiloglaser (USA). Scaffolds were cut with vector settings at a speed of 15% and a laser power of 7% with 8 repeat cuts to ensure a precise cut from top to bottom. Initial samples were cut into cylindrical rings with an internal diameter of 4.5 mm and an external diameter of 12

mm. Then the diameter was reduced to 3.5 and 10 mm for the internal and external diameters, respectively (Figure 3.4).

(A)



(B)



(C)



Figure 3.4 Epilog Mini laser cutter machine (B) PU scaffold with initial size dimensions (C) Final size dimensions used for the *in vitro* 3D culture model.

### **3.3 Structural characterisation**

#### **3.3.1 Scanning Electron Microscopy (SEM) and Energy Dispersive X-Ray Spectroscopy (EDX)**

##### **3.3.1.2 Ti-6Al-4V lattices without cells**

The morphology of preliminary Ti-6Al-4V samples were evaluated using a scanning electron microscope (FEI Nova 200) of the Materials Engineering and Research Institute, Sheffield Hallam University, Sheffield, UK. Subsequently the Philips XL 30S FEG scanning electron microscope equipped with a field emission gun at the Sorby centre of the University of Sheffield was used to perform pore geometry and EDX analysis of all lattices. Samples were mounted onto aluminium stubs using carbon adhesive tab discs. All samples were conductive, so gold or carbon coating was not required. Images were obtained at an accelerating voltage of 20 kV. Three samples of each designed porosity were investigated. From images captured, the average pore size and strut thickness were evaluated in Image J software (NIH, USA).

##### **3.3.1.2 Ti-6Al-4V lattices with cells**

To prepare cell-seeded scaffolds for SEM, scaffolds were removed from culture media and the cells fixed as described in section 3.7.10. Scaffolds were washed twice in PBS, then dehydrated using graded ethanol (50/70/80/90/100/100 vol% in diH<sub>2</sub>O) for ten minute exposure at each concentration. Subsequently, scaffolds were immersed in a drying agent, 100% hexamethyldisilazane (HMDS) for three minutes. After removing the HMDS, the scaffolds were left to dry for 2-3 days in a fume cabinet. All scaffolds were then mounted on aluminium stubs and sputter coated with gold (SC500, emscope) for 2 minutes at 0.05 atm with a 15 mA current before SEM visualisation in a Philips XL 30S FEG with an emission gun and 20 kV beam energy. A carbon coating (Edwards "Speedivac" Carbon Coating Units, England) was also performed for cell seeded

scaffolds and compared with blank (no cells) scaffolds to perform element analysis using EDX provided by the SEM machine.

### **3.3.2 Micro-computed tomography (MicroCT)**

A micro-computed tomography (MicroCT) system provides an opportunity to visualise the internal geometry of the physical object (Jones et al., 2007). MicroCT, Bruker system was used to examine the porous Ti-6Al-4V structure in detail, at high-resolution 3D imaging was used to evaluate the interconnectivity and overall porosity. The Skyscan 1172 MicroCT scanner in the Bone Analysis Laboratory, Mellanby Centre for Bone Research was used to scan all titanium lattices, the parameter used are described in section 4.3.2.4.

### **3.3.3 Archimedes method**

The porosity % of the SLM Ti-6Al-V built components was also examined traditionally by the Archimedes method and compared with the pore analysis achieved from micro-CT. This method is described in 4.3.2.5.

## **3.4 Chemical Characterization**

### **3.4.1 Inductively Coupled Plasma Optical Emission Spectroscopy (ICP-OES) Analysis**

Inductively Coupled Plasma Optical Emission Spectroscopy (ICP-OES) is used to precisely quantify the major elements in titanium lattices (Shbeh and Goodall, 2015). Therefore, this method was used to assess surface chemistry of the SLM Ti-6Al-4V lattices produced in this research study. The analysis was performed by the AMG Analytical, UK, using Thermo ICP-OES (ICAP-6500). More details are described in section 4.3.2.2.



### **3.4.2 LECO (Laboratory Equipment Corporation) Analysis**

Carbon, nitrogen and oxygen contamination is a matter of concern in manufacturing 3D printed titanium components. Therefore, it is necessary to evaluate the amount of these interstitial elements in the SLM Ti-6Al-4V builds. LECO (Laboratory Equipment Corporation) system is reported to measure the amount of impurities in porous titanium implants (Schiefer et al., 2009). Titanium lattices produced in this study were evaluated by AMG Analytical, UK using a LECO melt extraction as described in section 4.3.2.3.

### **3.5 Mechanical Characterization of SLM Ti-6Al-4V lattices in compression and three-point bending test**

The mechanical properties of SLM Ti-6Al-4V built with different pore geometry were measured in compression and three-point bending using a universal testing machine (Zwick Roell) as discussed in section 4.3.3.1 and 4.3.3.2 respectively.

### **3.6 Powder removal measurement**

Because these scaffolds were built using titanium powder particles in a single processing step, additional cleaning processes were required to measure the amount and size of unfused Ti-6Al-4V particles removal from the porous components constructed using conventional ultrasonic bath over a series of cleaning times as described in section 5.3.1.

### **3.7 Biological Characterization**

In order to evaluate the suitability of manufactured SLM Ti-6Al-4V lattices as useful components for dental implant applications. Biological characterisation was undertaken on the raw Ti-6Al-4V powder particles and post processing built lattices. Characterization was carried out in *in vitro* experiments using animal and human osteoblast cell lines. Cells were seeded on the Ti-6Al-4V lattices and cultured with the

titanium alloy particles for a period of time. An *in vitro* 3D culture model was developed in this thesis for testing additively manufacture titanium lattices.

### **3.7.1 Materials**

All chemicals used for cell culture work were purchased from Sigma-Aldrich (UK) unless otherwise stated. Tissue culture plastic was obtained from Thermo Fisher Scientific (UK).

### **3.7.2 Cultured cell lines**

Three different cell types were used in this work: MLO-A5 osteoblast-like cell line, primary human mesenchymal stem cells from bone marrow (hBMSCs) and MG-63 osteosarcoma cells. MLO-A5 cells were used initially to practice cell culturing protocols and develop standardisation curves and were then used in the direct cell seeding method for Ti-6Al-4V lattices. Both MLO-A5 and hBMSCs cells from an adult healthy male donor were used to perform the cytotoxicity analysis of SLM titanium alloy (Ti-6Al-4V) powder particles and *in vitro* 3D culture bone model for implant testing. MG-63 osteosarcoma cells were used and compared to MLO-A5 cells in cell migration testing.

#### **3.7.2.1 MLO-A5 Murine Cells**

Professor Lynda Bonewald (University Missouri) kindly donated the MLO-A5 osteoblast-like cell line. MLO-A5 cells represent the post-osteoblast / pre-osteocyte cells which are characterised by rapid deposition of extracellular matrix in sheets rather than in nodules within three days of culture (Kato et al., 2001). These cells were derived from the long bones of transgenic mice which is a genetically modified mouse model used to study osteoblast differentiation and mineralisation (Kato et al., 2001). The passage numbers of cells were between 44–50.

### **3.7.2.2 Human mesenchymal stem cells from bone marrow (hBMSCs)**

Human mesenchymal stem cells (hBMSCs) are harvested from bone marrow and used widely for regenerative medicine. They were purchased from (Lonza®). One human donor of hBMSCs was used to perform part of the cell culture work. The progenitor and differentiation potential of hBMSCs is reduced with increasing passage number (Caplan, 2005). Thus, lower passage numbers (1-2) of cells were used in this study.

### **3.7.2.3 MG-63 Human Osteosarcoma Cells**

MG-63 cells are a cancerous human osteoblastic cell line extracted from malignant bone tumours (osteosarcomas). They have been used widely as an osteoblastic cell model in bone tissue engineering (Benayahu *et al.*, 2002). These cells can produce an extracellular matrix and firmly adhere to culture surfaces. They express a higher level of proliferation when compared to normal osteoblast-like cells (Clover and Gowen, 1994). They produce collagen type III and IV which is different from that in non-cancerous osteoblasts cells (Pautke *et al.*, 2004). The passage numbers of cells were between 10-15.

### **3.7.3 Culture media compositions**

An appropriate basal culture media was used to grow bone cells. The basal media (BM) was consisted of minimum essential Medium- $\alpha$  ( $\alpha$ -MEM, Lonza, UK), 10% foetal bovine serum (FBS, Labtech, UK), 2 mM L-Glutamine and antibiotic containing 100 U/mL penicillin and 100  $\mu$ g/mL streptomycin. Two types of differentiated media of specific supplements were used during the cell culture work, supplemented media (SM) and osteoinductive media (OIM). SM is BM with additives that enhance the formation of an extracellular matrix (5 mM beta-glycerol phosphate ( $\beta$ GP) and 50  $\mu$ g/mL ascorbic acid 2-phosphate (AA-2P), while OIM is referred to SM in addition to the corticosteroid

dexamethasone (Dex) to encourage osteogenic differentiation. The compositions of all cultured media used are summarised in table 3.2.

Table 3.2 Cultured media compositions used in this thesis, Basal media (BM), supplemented media (SM), osteogenic induction media (OIM).

<b>Cultured media</b>	<b>AA-2P</b>	<b>BGP</b>	<b>Dex</b>
<b>BM</b>	0	0	0
<b>SM</b>	5 mM	50 µg/ml	0
<b>OIM</b>	5 mM	50 µg/ml	100 nM

### **3.7.4 General cell culture conditions**

During cell passaging, all cells were grown with BM in T-75 flasks coated with 0.1 w/v% gelatine to enhance cell adhesion. An appropriate basal culture media was used to expand cell number under incubation at 37°C in 5% CO<sup>2</sup>. The culture medium was changed every 2-3 days. Cells were allowed to reach 70-80% confluency before passaging. To passage cells, the culture media was discarded and the flask was washed twice with 10 mL PBS to remove traces of remaining media. Then 2.5 mL of trypsin/EDTA was added with five minutes incubation to enzymatically detach the cells from the old flask. Then the flask was sharply knocked by hand to ensure cell detachment. Trypsin was deactivated by adding 5 mL of a fresh basal culture media. Cell suspension was transferred to a centrifuge tube and centrifuged at 1,000 rpm for five minutes. The supernatant was carefully disposed and the cell pellet was resuspended with 1ml of the basal culture media. Then in a 1.5 mL tube, 20 µL of suspension was combined with 20 µL of Trypan Blue® dye which is only able to stain

dead cells, thus the live cells to be counted look bright. To count cell number, 15  $\mu$ L of stained cell suspension was transferred on each side of the hemacytometer and the cells counted under a light microscope. The average number of cells counted was used to estimate the total number in the cell suspension. Finally, a required cell number was either transferred to a new culture flask or seeded on the scaffolds.

In order to obtain enough cells with identical passage numbers, cryopreservation of cells was saved for future experiments. To freeze down cells, the total cell number was determined then resuspended 1 mL of a freezing solution consisted of dimethyl sulfoxide (DMSO) and FBS, (1:10 DMSO: FBS v/v) per 1 million cells. One mL of cell suspension was moved to each cryovial and frozen in a Mr. Frosty container containing isopropanol at  $-80^{\circ}\text{C}$  overnight and then transferred to the liquid nitrogen at  $-196^{\circ}\text{C}$  for long term storage.

To defrost frozen cells that had been stored in the liquid nitrogen, the cryovial was thawed in the water bath at  $37^{\circ}\text{C}$  and then transferred to 15 mL of warm BM in a 50 mL centrifuge tube and centrifuged at 1,000 rpm for five minutes. The supernatant was then removed from the cell pellet and resuspended with 12.5 mL of warm BM to be moved into a new T75 flask. The flask was gently rocked and incubated under standard culture conditions. Cell proliferation and morphology was checked regularly using a light microscope. The passage numbers of cells in this work were between 44–50, 10-15 and 1-2 for MLO-A5, MG63 and hBMSCs, respectively.

### **3.7.5 Cell seeding**

#### **3.7.5.1 Monolayer cell culture**

In the monolayer (2D) cell culture experiments cells were initially detached from T-75 flasks and the required cell number was mixed and resuspended with the culture media and then seeded directly in the polystyrene tissue culture well plates with gentle rocking

to ensure homogeneous cell distribution. The number of cells and volume of media were determined by cell type, size of cell culture well plate and duration of the experiment. Regular media changes were performed every 2-3 days. Cell density and morphology were monitored under light microscopy. 2D cell culture was used to create a standard curve at different cell densities of MLO-A5 cells. This was subsequently used in cell migration experiments to evaluate the migration potential of MG63 and MLO-A5 cells. Cytotoxicity analysis of Ti-6Al-4V powder particles on MLO-A5 and hBMSCs cells was also performed in monolayer cell culture.

### **3.7.5.2 Three-Dimensional Cell Culture**

Three-Dimensional (3D) cell culture was employed in two ways, direct cell seeding on SLM Ti-6Al-4V lattices and an *in vitro* 3D culture model where cells were seeded on cylindrical rings of PU scaffolds which then used to implant cylinders of SLM Ti-6Al-4V lattices. In direct cell seeding only MLO-A5 cells were used, while both MLO-A5 and hBMSCs cells were used with an *in vitro* 3D culture model. Details of cell seeding in both methods are described in relevant chapters.

### **3.7.6 Metabolic activity assay**

The resazurin reduction (RR) assay is a common method of measuring metabolic activity of cells. The RR assay was carried out to evaluate cell proliferation continuously on the following experiments: directly seeded on SLM Ti-6Al-4V scaffolds using MLO-A5 cells, cytotoxicity of Ti-6Al-4V powder particles and *in vitro* 3D culture model using both MLO-A5 and hBMSCs cells. This assay was also used to create a standard curve of different cell densities of MLO-A5 cells. The fluorescence intensity is associated with the metabolic activity of cells (O'Brien et al., 2000). Resazurin sodium salt is a blue and non-fluorescent stain that is reduced by the metabolic activity of cells to resorufin, a fluorescent pink color. The reduction

procedure of Resazurin sodium salt is probably related to oxygen consumption through metabolism (Fields and Lancaster, 1993). Another suggested mechanism of reduction is likely to be by mitochondrial enzymes, however there is no clear explanation whether this process happens inside the cells, on the surface of the plasma membrane or in the culture media as a chemical reaction (De Fries and Mitsuhashi, 1995). RR solution was prepared by adding 1 mM Resazurin Sodium Salt to deionized water and diluting this to 10 vol % in culture media. For each assay on 2D experiments, media was removed from each well and substituted with a known volume of the RR solution. The well plate was then wrapped in aluminium foil due to its light sensitivity and incubated for four hours at 37 °C. For 3D cell culture, 2 ml RR solution was added to each scaffold after moving to a new well plate to ensure only cells attached to the scaffold were analysed. In a 96-well plate, 200 µL of the reduced solution was transferred in triplicate, and subsequently read with a microplate reader (Tecan infinite 200-pro) at 540 nm excitation wavelength and 590 nm emission wavelength. Fresh culture media was added after twice washing the samples with PBS, with 20 minutes incubation between washes.

### **3.7.7 Calcium Staining Assay**

To evaluate the extracellular mineral deposited by osteoblast cells, an organic Alizarin Red S (ARS) stain was used which has a high affinity for calcium. This assay is simple and efficient for calcium analysis in which the stain can be extracted and assessed in a colorimetric manner, thus the quantified amount of stain represents the mineral content (Gregory et al., 2004). To prepare the stain, ARS powder was dissolved in deionized water (dH<sub>2</sub>O) at 1 w/v% and filtered through a 0.2 µm filter to ensure no undissolved particles remained. The pH was adjusted to 4.1 with drops of NaOH to enhance staining. The fixed scaffolds were washed three times with dH<sub>2</sub>O to remove any remaining formalin solution. Each scaffold was submerged with 2 ml of ARS with orbital shaking

for 30 minutes at 100 rpm. Then the ARS was removed and any excess was washed off every 5 minutes with dH<sub>2</sub>O and gentle orbital shaking until the water remained clear. The scaffolds were destained with 2 ml of 5% v/v perchloric acid in distilled water on an orbital shaker for 15 minutes. Triplicate samples of 150 µl of destaining solution from each well were then added to a transparent 96 well plate and absorption was measured at 405 nm in a plate reader (Tecan infinite 200-pro). ARS concentration was determined by a standard curve (Figure 3.5) which was prepared by serially diluting the same ARS solution in the destain. This can be used to convert the absorption units to the quantity of ARS.

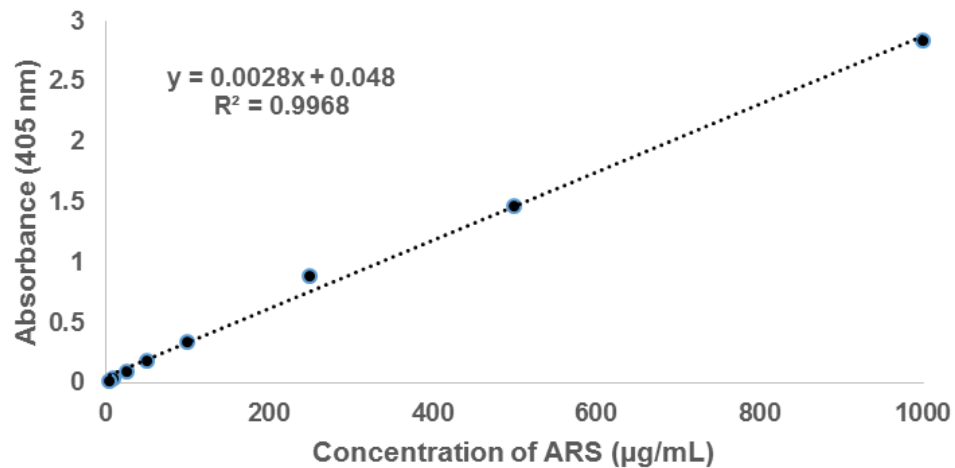


Figure 3.5 Standard curve for the calcium staining assay. This can be used to convert plate reader absorbance to a known concentration of stain.

### **3.7.8 Collagen Staining Assay**

To identify collagen production produced by both MLO-A5 and hBMSCs, a Sirius Red Stain Assay (SRS) was used. This method is a simple and sensitive assay used to quantify collagen (Junqueira *et al.*, 1979). A main advantage of this technique is that the dye stains collagen strongly and permanently. SRS was carried out on cell seeded SLM Ti-6Al-4V lattices at various time-points of the experiments. To form Sirius red solution direct red 80 was dissolved in saturated picric acid (1% w/v). To remove



undissolved particulates the solution was filtered with 0.2 µm filter. After the ARS assay was performed the scaffolds were washed three times with dH<sub>2</sub>O to remove any of the ARS destain, 2 ml of SRS was then added to each sample. The plate was placed on an orbital shaker for 18 hours at 100 rpm. The SRS was removed and any excess was washed off with dH<sub>2</sub>O every five minutes on an orbital shaker at 100 rpm until no further stain was observed. The scaffolds were then de-stained with 2 ml of 0.2 M NaOH: methanol (1:1) on an orbital shaker for 20 minutes at 100rpm. Triplicate samples of 150 µl of solution from each well plate was added to a clear 96 well plate and absorption was measured at 405nm in a plate reader (Tecan infinite 200-pro). SRS concentration was determined by a standard curve (Figure 3.6) which prepared by serially diluting the same SRS solution in the destain. This can be used to convert the absorption units to the quantity of SRS.

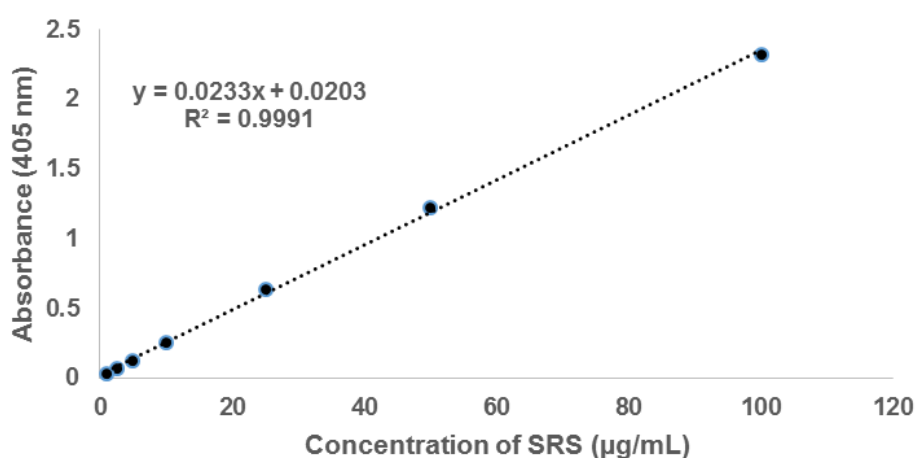


Figure 3.6 Standard curve for the collagen staining assay. This can be used to convert plate reader absorbance to a known concentration of stain.

### **3.7.9 Xylenol Orange**

Xylenol orange staining has been shown to be an effective method to evaluate newly formed mineral nodules in biomaterials. This stain can bind to newly form calcified tissue which contains calcium phosphate. Xylenol orange tetrasodium salt was prepared

in a 20 mM stock solution with distilled water and stored in the refrigerator at 4°C. Before staining, the stock solution of Xylenol orange was diluted in a fresh culture media at a dilution of 1:1000 with a final concentration of 20 µM. 2 ml of a final concentration of each titanium and PU scaffold was added and incubated for at least 12 hours. Blank control scaffolds without cells were also stained. The media containing Xylenol orange was removed and washed twice with PBS. Before imaging with confocal microscopy (Zeiss LSM 510 META), scaffolds were submerged with PBS and images were taken from top and side view of the implanted titanium using an excitation wavelength of 570 nm.

#### **3.7.10 Cell fixation**

Cell seeded scaffolds were fixed for ARS, SRS assays and in preparation for SEM. Media was removed from the scaffolds and washed twice with PBS. Scaffolds were then submerged in a fixing solution, 10% formalin for 30 minutes. The fixative was then removed, and the scaffolds washed twice in PBS and then store in PBS in the fridge until needed.

#### **3.7.11 Statistical Analysis**

The obtained data are displayed as means  $\pm$  standard deviation (SD). Preliminary experiments were performed with (n = 6 / group) for P400, P400/1C, P400/2C, P650, P650/1C, (GP/650-400), (GP/400-300) and ‘Spider Web’ scaffolds to perform compression tests, (n = 3 / group) for three-point bending tests and (n = 9 / group) for biological tests. Data were analysed by a GraphPad Prism 7 software using one (one factor) or two (two factors) –way ANOVA followed by a Tukey's multiple comparisons post-hoc test.  $p < 0.05$  to determine significant difference. All experiments were performed a minimum of two times in triplicate for each condition where possible. Numbers of replicates (n) is stated in the figure legend.

**Chapter 4 : Characterisation and Mechanical Properties of SLM processed Ti–6Al–4V lattices.**

Part of this chapter has been published in the Journal of the Mechanical Behavior of Biomedical Materials as: Zena J Wally, Abdul M Haque, Antonio Feteira, Frederik Claeysens, Russell Goodall and Gwendolen C Reilly, “Selective Laser Melting processed Ti-6Al-4V lattices with graded porosities for dental applications”. J. Mech. Behav. Biomed. Mater. 90, 20–29. A full copy of this publication is available in the appendix, 9.2.

**4.1 Introduction**

Bulk ‘titanium-based’ devices have been the traditional form used for dental implants, but dense titanium has a higher elastic modulus than human bone (Wally et al., 2015). Consequently, this may cause the load distribution between hard tissue and the implant to be non-uniform, and researchers have suggested that this leads to ‘stress shielding’ and bone resorption and may result in loosening and failure of the implant in particular when used for patients with compromised bone healing (Li et al., 2010). There is consequently still the need for implants with enhanced capability to support osseointegration. Roughening implant surfaces has been shown to increase bone-implant integration. Over the last years, different surface-treatments have been proposed in the literature to decrease the smoothness of dental implant features, such as plasma spraying, sandblasting and laser micro-machining (Le Guéhennec et al., 2007). However, there are some limitations raised with such techniques, for example, the overall structure is still high-density titanium, and the coating materials may dissolve over a period of time. Also, coating layers that break away from the surface could have an adverse biological consequence on the nearby tissue such as peri-implantitis ( Le Guéhennec et al., 2007). Additionally, it is not straightforward to produce porous

components with controlled internal porosity as well as the external implant geometry (Andani et al., 2014). To overcome the shortcomings of coating materials, the cellular structure has been recommended as a substitute to the classical dense structure. Porous structures have the advantage that their effective stiffness can be manipulated to match bone tissue (Kalita et al., 2003). This also provides an appropriate biological surface for the bone cell attachment and proliferation into the pores (Mour et al., 2010) and offers initial implant stability as validated by commercially available porous tantalum – titanium dental implants from Zimmer (President and Affairs, 2012).

Previous studies in the literature have attempted to manipulate the structural and mechanical properties of metallic biomaterials so that they more closely match that of the human bone using various titanium foams or lattices either for coating or within the bulk of a structure for dental and orthopaedic implant applications. On the other hand, the porous metal structure as a whole reduces mechanical properties, and as a result, unless this can be controlled, such materials are unlikely to be used for medical implants in load-bearing areas (Ryan et al., 2006). To tolerate physiological loads of mastication which are imposed on the human jaw, titanium dental implants with a combination of a dense core and porous covering were suggested using different processing methods (Ryan et al., 2006). An electron-discharge compaction process was used to make a porous surface on a compact core of commercially available dental implant, using input energy 1–2.5 KJ/g to atomise the Ti–6Al–4V powder (Lifland et al., 1993). Porous tantalum trabecular metal – enhanced titanium dental implants are produced by Zimmer, where tantalum coats a titanium core. The tantalum section is made using a foam-like vitreous carbon scaffold then coated with tantalum by chemical vapor diffusion process. However, a mechanical concern has been raised around structures produced by such

methods, for example, the junction between two different zones may be susceptible to break when implanted in hard bone (Bencharit et al., 2014).

A graded porous architecture on a dense core has also been recommended, where the core will provide mechanical stability, and the graded porosity permits bone ingrowth (van Grunsven, 2014). Such a structure could also reduce the stress concentrations occurring on loading between adjacent layers with very different Young moduli (Ryan et al., 2006), as can happen when porous materials are bonded to dense materials. A microwave processing method has also been suggested to sinter titanium powders to produce dental implants, with gradient porosity ranged from 30–100  $\mu\text{m}$  at 100–200  $\mu\text{m}$  thickness (Kutty et al., 2004).

Several processing methods have evolved to produce biomimetic porous titanium for bone replacement devices via powder metallurgy. In particular, space-holder sintering which was able to adapt the pore geometry and porosity ranging from 200 to 500  $\mu\text{m}$ . Over the last few years, rapid prototyping technologies, including Electron Beam Melting (EBM) and Selective Laser Melting (SLM) developed rapidly due to their ability to produce metal components with customised parts and complex pore geometries that are impossible to achieve with traditional processing (Koike et al., 2011). SLM can build structures layer by layer by fusing Ti powder microparticles together using a focused laser beam. According to the desired shape from a digital model (Tolochko et al., 2002, Mullen et al., 2009, Moin et al., 2013), the successive layers are deposited and fused together. With this process, an inert gas or a vacuum is required during the building process to produce titanium components, as these are easily oxidised in air (Koike et al., 2011). However, small amount of interstitial elements Carbon (C), Oxygen (O) and Nitrogen (N) are still usually found with the main alloying elements present in the most common alloy Titanium, Aluminium, and Vanadium. The

main elements may interact with the air and form their corresponding oxide layers, C and N are introduced according to the air conditions. C, O and N react with many bulk metals with air and form their oxides, carbides, and their corresponding nitrides depending on atmospheric conditions (Vaithilingam et al., 2016)

Earlier studies of SLM on Ti alloys have highlighted the construction of porous structures for medical devices such as dental roots and hard tissue replacements with a significantly less waste product that would have been extremely expensive to make using conventional processing methods (Nouri et al., 2010).

Overall, it is not straightforward to create a dense core with a porous shell with traditional processing methods, and the effects of differences of pore geometry on the mechanical properties of porous titanium structures need to be explored. Here the aim was to investigate the feasibility of the SLM process to produce a range of titanium lattices of approximately cylindrical form, which could form the basis of a porous dental implant. These lattices were tested mechanically to determine their stiffness and strength.

## **4.2 Aim**

The primary aim of this chapter is to design and compare a range of porous titanium structures with uniform and graded forms that would be desirable for a dental implant application, in particular for patients with compromised bone healing, using advanced manufacturing technology.

The aim of this chapter will be met by achieving the following objectives:

- Evaluate the feasibility of the Selective Laser Melting (SLM) process to produce a range of titanium micro-lattice structures using Ti-6Al-V particles. Variable pore sizes (250, 300, 400 and 650  $\mu\text{m}$ ) and strut thicknesses (250, 300 and 400  $\mu\text{m}$ ) will be used to create regular and graded porous structures, with and

without a dense core using a novel ‘Spider Web’ design and lattices based on a diamond unit cell.

- Assess surface chemistry and physical and mechanical properties (compression strength and three-point bending tests) of the built porous components.

### **4.3 Materials and Methods**

#### **4.3.1 Design and fabrication of porous Ti-6Al-4V lattices**

##### **4.3.1.1 Unit cell and CAD design**

Titanium lattices were designed using Materialise 3-Matics version 9.1 additive manufacturing software. Concepts variants were based on an initial invented design (Figure 4.1) of approximately cylindrical with 5 mm diameter, which could form the basis of a porous dental implant. The unit cell of choice used was a diamond lattice (Figure 4.2), as it has been previously used for similar medical applications to mimic the properties of cancellous bone (van Grunsven et al., 2014). Variants included different pore sizes by changing strut thicknesses, and the presence of a dense core of different diameters. In the diamond-based lattices, interconnected porosity was created to be either regular or graded. The grading was created by combining two layers of different strut thickness surrounding a dense core. Pore sizes of 400 and 650  $\mu\text{m}$  were used to create lattices with uniform porosity, while the graded lattices were varied in pore size ranging from 300 and 650  $\mu\text{m}$  and 300 and 400  $\mu\text{m}$  for the inner and outer layer respectively. Strut thicknesses were either 300 to 400  $\mu\text{m}$  which created variant in porosity (Figure 4.3). A novel ‘spider web’ design with 250  $\mu\text{m}$  radial spokes and circumferential connecting struts was also invented to form titanium hexagonal prisms (diameter: 4.33 mm and height: 6.76 mm) as shown in figure 4.4. Nomenclature was given to each designed porosity according to the pore parameters used, as tabulated in table 4.1.

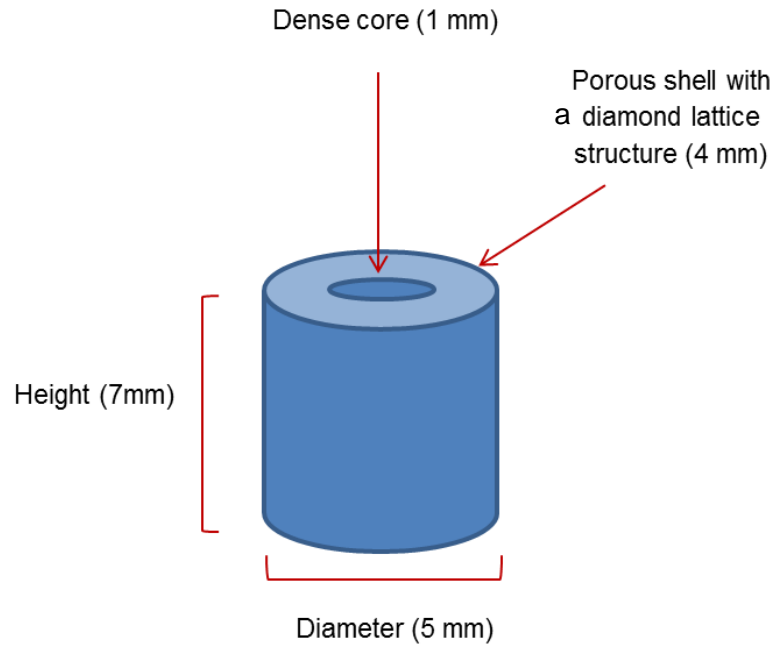


Figure 4.1 Initial construct profile used to design the variants of SLM Ti-6Al-4V lattices.

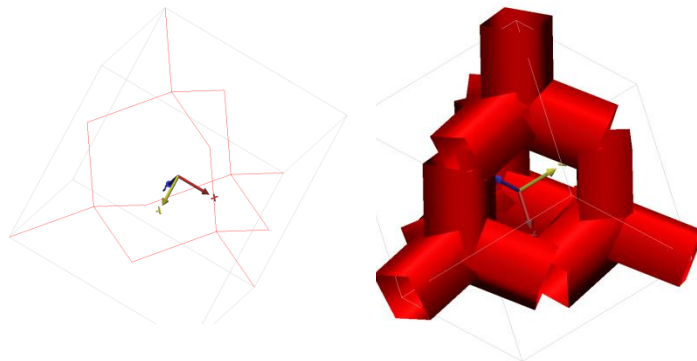


Figure 4.2 A diamond unit cell built on 3 planes used to design the variants of SLM Ti-6Al-4V lattices.



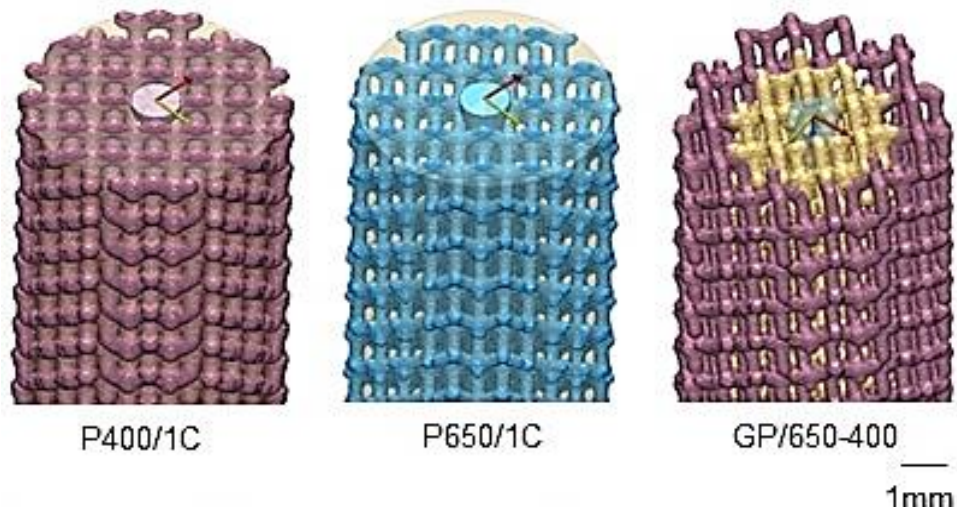


Figure 4.3 The CAD models of the variant lattices built on the diamond unit cell: P400/1C, P650/1C and GP/650-400, prototype shown in 3-matics software, provided by Abdul M Haque who manufactured them at the Advanced Manufacturing Research Centre.

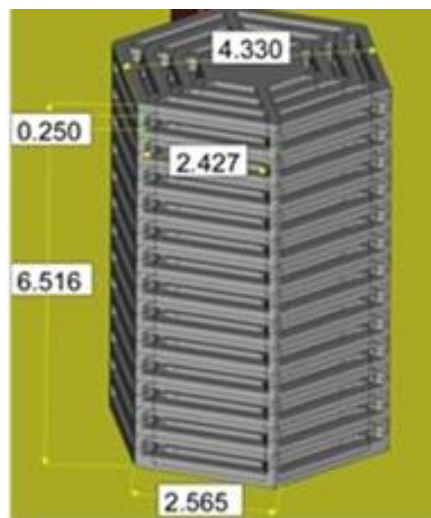


Figure 4.4 The CAD model of the 'Spider Web' prototype shown in 3-matics software.

Table 4.1 A summary of the different Ti-6Al-4V lattice designs and the nomenclature used to refer to them in this study. Samples are grouped according to the nominal pore size, strut thickness, and presence or absence of a dense core.

<b>Model type</b>	<b>Pore size (<math>\mu\text{m}</math>)</b>	<b>Strut thickness (<math>\mu\text{m}</math>)</b>	<b>Dense core (mm)</b>
<b>P400</b>	400	400	None
<b>P400/1C</b>	400	400	1
<b>P400/2C</b>	400	400	2
<b>P650</b>	650	300	None
<b>P650/1C</b>	650	300	1
<b>Graded (GP/650-400)</b>	400 (inner layer)	400 (inner layer)	1
	650 (outer layer)	300 (outer layer)	
<b>Graded (GP/400-300)</b>	300 (inner layer)	300 (inner layer)	1
	400 (outer layer)	400 (outer layer)	
<b>'Spider Web'</b>	250	250	1.73

#### **4.3.1.2 Selective Laser Melting for the production of porous Ti-6Al-4V**

Selective laser melting is a type of additive manufacturing process which is able to create components from CAD slice geometry through successive fusion of fine metallic powders; these layers can range between 20 and 100  $\mu\text{m}$  (Simonelli, 2014). A Renishaw AM250 system (Figure 4.5) was used to manufacture different porous titanium structures using plasma atomised spherical Ti-6Al-4V ELI grade 23 powder microparticles with particle sizes ranging from 15 - 55  $\mu\text{m}$  (Figure 4.6). The melting

process was performed by a fibre laser firing successive points onto the build substrate; each firing point creates a melt pool of approximately 0.2 mm in diameter, these firing points allow for full melting of the metallic powder. Melting takes place through a combination of factors relating to the amount of energy density achieved for a given material using the previously optimised SLM process parameters. The machine was controlled by a 200 W pulsed ytterbium (Yb) fibre laser with a wavelength of 1070 nm. The diameter of the laser beam was 70  $\mu\text{m}$  with 30  $\mu\text{m}$  layer thickness, 5000 mm/s laser scan speed and 0.075 mm hatch distance. The oxygen level was 1000 ppm (0.1%) during the process. The maximum temperature of the build chamber was set at 170 °C. The CAD geometries at the STL level of the structure are sent into the processing system and virtually sliced in 30-micron layers with a defined laser path. Slices are fused layer-by-layer over a number of hours to form regions of porous and dense metal as desired. During the build process, an elevator platform was loaded with a Ti-6Al-4V substrate that was heated to 70°C. It is typically necessary that the substrate is the same material as deposited powder to ensure the same rate of thermal expansion is maintained during melting of layers. Following laser scanning of a single layer, the elevator platform is lowered to the set height of the next layer, and the process of scanning/melting is repeated until the part is built. A dosing mechanism deposits a controlled amount of powder in front of a wiper blade which traverses across the substrate to evenly spread the powder.

To reduce the risk of oxidation and contamination, the building procedure was carried out under inert Argon gas. Each sample was positioned onto the software platform 30° from the wiper blade position, which was performed to ensure minimal forces were induced by contact with parts during powder re-coating. All sample components were loaded onto the build platform (Ti-6Al-4V) substrate that was heated to 70°C and

positioned randomly. Lattice-based samples were built vertically on the build substrate while the ‘Spider Web’ samples were oriented horizontally (Figure 4.6 A-B). To remove the loose powders from the built components, they were cleaned for 30 minutes with an ultrasonic bath.



Figure 4.5 Renishaw AM250 used to build the variants of SLM Ti-6Al-V lattices.

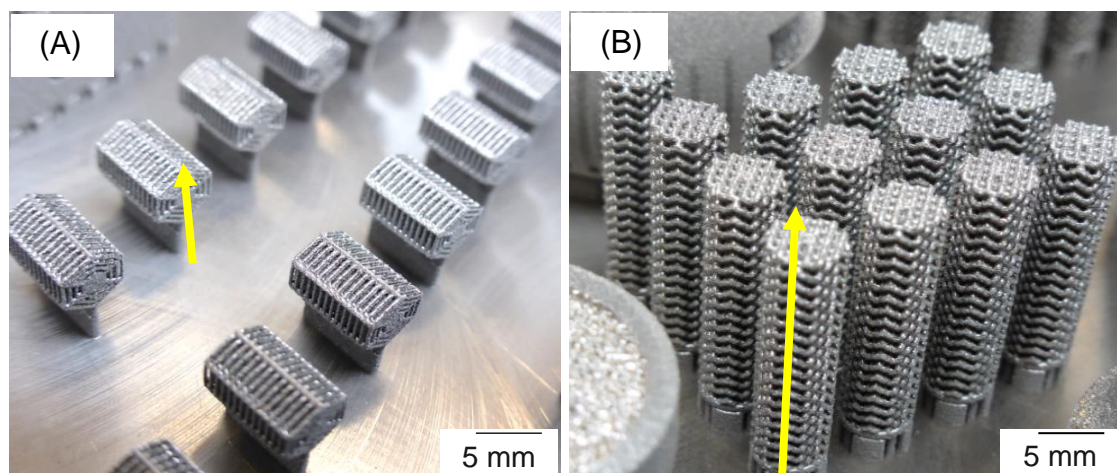


Figure 4.6 Post-build Ti-6Al-4V samples of (A) ‘Spider Web’ (diameter = 4.33 mm and height = 6.76 mm) built horizontally and (B) variant of diamond unit cell lattices built vertically (diameter = 5 mm and height = 20 mm) on the building substrate, yellow arrows indicate building direction..

### **4.3.2 Structural Characterization**

#### **4.3.2.1 Scanning electron microscopy and energy dispersive X-ray spectroscopy**

The internal architecture of the porous titanium components with approximately 7 ( $\pm$  0.2) mm height was evaluated by a Scanning Electron Microscope (SEM), FEI Nova 200, equipped with a field emission gun as described in section (3.3.2). In addition to SEM imaging, energy dispersive X-ray spectroscopy (EDX) was used to perform element analysis qualitatively. The average pore size and strut thickness were evaluated in Image J software from recorded SEM images.

#### **4.3.2.2 Inductively Coupled Plasma Optical Emission Spectroscopy (ICP-OES)**

##### **Analysis**

Inductively Coupled Plasma Optical Emission Spectroscopy (ICP-OES) is a system commonly used to quantify the most common elements in metallic materials accurately (Shbeh and Goodall, 2015). Using Thermo ICP-OES (ICAP-6500) three samples of SLM Ti-6Al-4V were tested by AMG Analytical, UK. Titanium samples were acid dissolved into a solution using HCl/HNO<sub>3</sub>/HF. The instrument was calibrated with certified reference solutions which were prepared from pure materials and/or 1000ppm, 10,000ppm solutions. Additional certified reference materials and/or synthetics were prepared alongside the samples and analysed with the samples to verify the results obtained.

#### **4.3.2.3 LECO (Laboratory Equipment Corporation) Analysis**

One major concern in producing additively manufactured titanium components is carbon, nitrogen and oxygen contamination during the manufacturing process. Low values of these interstitial elements have been shown with the SLM system (Koike et al., 2011). To verify the amount of impurities (carbon, oxygen and nitrogen) in the porous titanium builds, they were assessed using a LECO (Laboratory Equipment

Corporation) melt extraction system by AMG Analytical, UK according to ISO 17025 and ISO 9001. The LECO-CS844 instrument was used for carbon analysis. Samples were burned in the instrument in an oxygen atmosphere with a flux (Tungsten). Carbon present in the samples is converted to Carbon Monoxide/Carbon Dioxide. This was detected by Infra-Red. For LECO nitrogen and oxygen, the LECO-ONH836 device was used. The samples were burned in a graphite crucible in a helium atmosphere with a nickel flux. The nitrogen is determined as N<sub>2</sub> using a thermal conductivity cell, while the oxygen is determined as CO<sub>2</sub>/CO using an Infra-Red cell. Both instruments were calibrated with certified reference materials. Additional certified reference materials were also analysed alongside the sample to validate the results obtained.

#### **4.3.2.4 Micro-Computed Tomography (MicroCT)**

A micro-computed tomography (MicroCT) system offers an opportunity to access and visualise the internal geometry of the physical object (Jones et al., 2007). This system was undertaken to evaluate the percentage of the open, closed and overall porosity, surface area and interconnectivity of SLM Ti-6Al-V scaffolds in three dimensions. Samples (n = 3) for each designed porosity were scanned using a Skyscan 1172 MicroCT scanner (Bruker system).

Prior to scanning and to prevent any artefacts accompanying scaffold movement during the scanning process, each scaffold was inserted inside a plastic straw and held firmly in place by a polystyrene foam disk at each end, then screwed tightly into the stage of the MicroCT machine. Scanning parameters used were scan over an angle of 180° with one image taken every 0.5°, 100 kV voltage, a medium camera binning mode (2000×1024), 1 mm Al filter, 26 minutes acquisition time and 9.92 µm pixel size.

The NRecon R software version: 1.6.9.4 from Skyscan, Belgium, and a GPURecon Server engine version: 1.6.9 were used to perform the reconstruction of the acquired image slices. CTAn software (v.1.15.4.0, Bruker, Belgium) was used to analyse the reconstructed images. A volume of interest (VOI) was selected within the centre of each scaffold, using 500 cross-sectional images which were converted to binary images with an appropriate threshold value, 255-high and 80-low.

#### **4.3.2.5 Archimedes method**

Overall porosity % of the fabricated SLM Ti-6Al-V scaffolds was also determined by the Archimedes method using equation (4.1) below and compared with the pore analysis data that obtained from MicroCT. This method has been used previously in the literature for measuring the density and porosity of porous cylinders (Slotwinski et al., 2014).

$$\text{Porosity} = (1 - \rho_{sc} / \rho^0) * 100\% \quad (4.1)$$

where  $\rho^0$  is the known density of dense Ti-6Al-4V (4.43 g/cm<sup>3</sup>), and  $\rho_{sc}$  is the density of the samples, which is measured by the weight of the sample in air (Ma) and water (Mw) using equation (4.1) above and a Mettler Toledo density balance with 0.1 mg resolution. The density of water  $\rho_w$  was assumed to be 1.0 g/cm<sup>3</sup> at room temperature (15-25 °C) (Slotwinski et al., 2014).

### **4.3.3 Mechanical Testing**

#### **4.3.3.1 Compression testing**

The mechanical properties of cylinders of approximately 7 mm height and 5 mm diameter were tested in compression. All porous Ti-6Al-4V designs were assessed on a universal testing machine (Zwick Roell) according to international standards ISO 17340:2014 (Metallic materials - Ductility testing - High speed compression test for porous and cellular metals). Tested samples were placed on the lower compression plate

of the machine. The long axis of the scaffolds was oriented perpendicular to the loading direction, and the gradient of the core base lattices was radial to the direction of loading (Figure 4.7). The crosshead speed was 1 mm/min. The load cell was 20 kN with 10 kN maximum force. Video recording was performed with the initial samples using TestXpert V.7.1 software provided with the test machine. Using the recorded videos, image changes of the sample during the compression process were obtained. The resulting load-displacement curves were translated to stress-strain curves; stress was calculated according to the equation below:

$$\text{Stress in compression} = \frac{F}{A} \quad (4.2)$$

where  $F$  is the force applied and  $A$  is the cross-sectional area of the object.

The resulting stress-strain curve was used to determine the yield point at which the behaviour of the structure starts to deviate from the linear region using the 0.2% offset strain as shown in figure 4.8. The initial elastic region was used to calculate Young's modulus using the following equation (van Grunsven, 2014).

$$E = \frac{d\sigma}{d\varepsilon} \quad (4.3)$$

where  $E$  is Young's modulus and  $\sigma$  is the stress and  $\varepsilon$  is the strain.

A video extensometer provided with the test machine was used during the compression process. Using the recorded videos, silhouette images of the sample changes during compression were obtained.



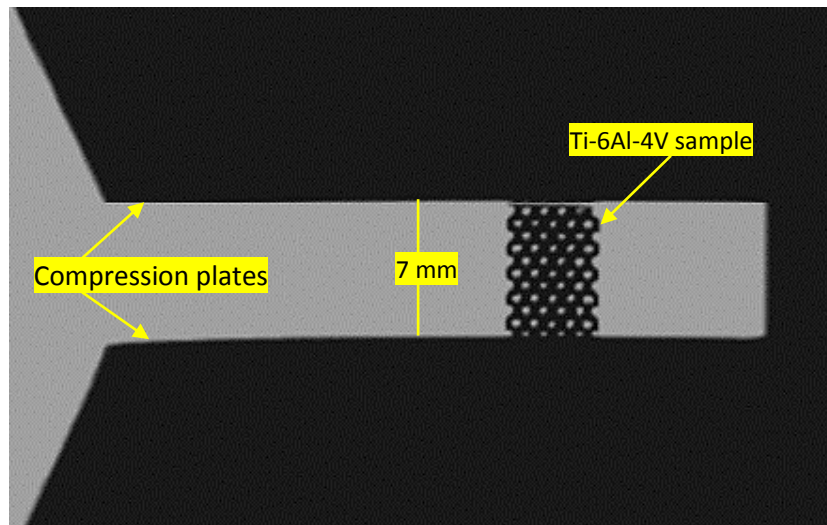


Figure 4.7 Ti-6Al-4V sample under the compression plates of the Zwick Roell machine.

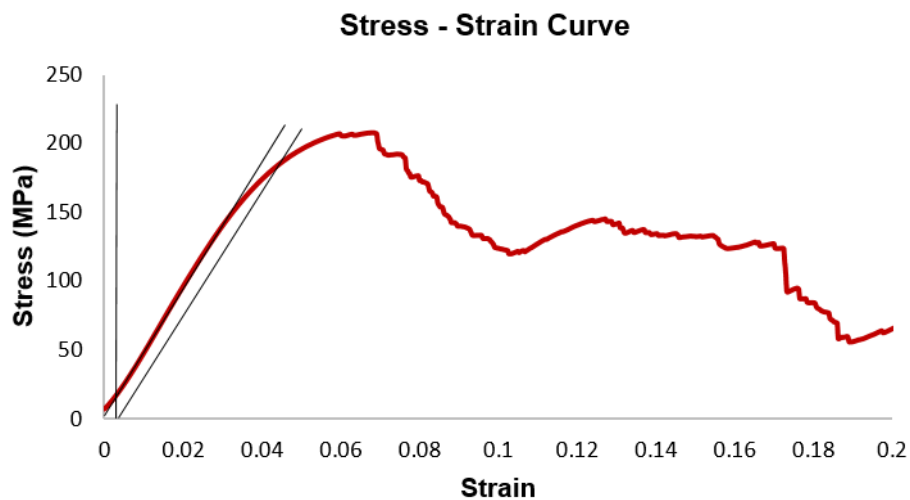


Figure 4.8 Stress-strain curve with the trend lines that were used to determine the Young's modulus and yield strength at 0.2% offset.

#### 4.3.3.2 Three-point bending testing

To measure bending behaviour of these structural designs, three-point bending tests were conducted to test the flexure strength of samples of around 30 mm length and 5 mm diameter constructed titanium lattices, using the Zwick Roell testing machine with 5 kN load cell and 500 N maximum force and 25 mm span length (Figure 4.9).

The tests were performed at a crosshead speed of 2 mm/min. The length to diameter ratio of the tested sample was about 6. Some standards would require a lower ratio (such as the ISO 12986-1 standard for carbonaceous materials, which indicate 3.5, as a minimum value for the length to thickness or diameter of the cylindrical or prismatic specimen). Standards for other materials recommend higher values, such as ISO for flexural properties of plastic materials which specifies  $20 \pm 1$  length to thickness of the tested sample. Because the aim was to test bending properties of structures with specific design and application and not as materials of arbitrary dimensions, there was a restriction in the available sizes of lattices and these standards, designed for other uses, were not followed.

Flexural modulus was calculated using the below equation:

$$E = \frac{L^3}{48I} F \quad (4.4)$$

where  $E$  is the flexure modulus,  $L$  is the span length between the supports.  $I$  is the moment of inertia and  $F$  is the slope of load/displacement at in the initial linear region.

Yield load was evaluated by 0.2% offset strain in a load-displacement curve.

$$\text{Yield strength} = Fy \frac{LD}{4I} \quad (4.5)$$

where  $Fy$  = yield load,  $L$  is the support span,  $D$  is the diameter of the sample, and  $I$  is the moment of inertia.

The moment of inertia of the cylindrical and hexagon prism samples was calculated following the below formulae:

$$I (\text{Cylinder}) = \frac{\pi D^4}{64} \quad (4.6)$$

where  $D$  is the diameter of the sample.

$$I (\text{Hexagon}) = \frac{5\sqrt{3}}{16} a^4 \quad (4.7)$$

where  $a$  is the length of the polygon side of ‘spider’ web sample.

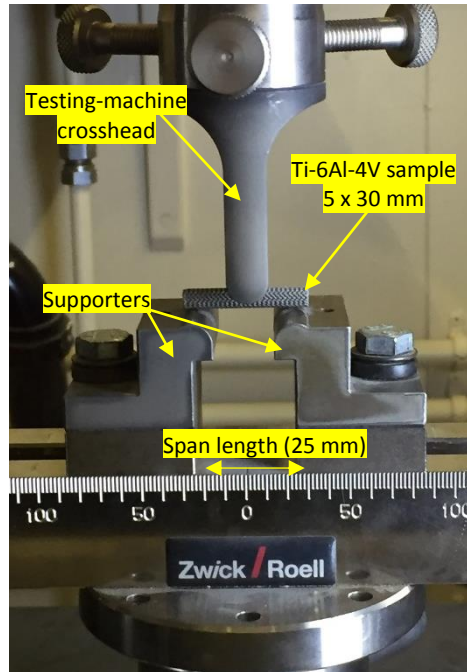


Figure 4.9 Three-point bending test to measure flexural strength of Ti-6Al-4V samples using the Zwick Roell machine.

## 4.4 Results

### 4.4.1 Structural characterisation

#### 4.4.1.1 SEM and EDX

The SEM images (Figure 4.10) revealed that selective laser melted builds of P400, P400/1C, P400/2C, P650, P/C650, GP/650-400, GP/400-300 and ‘spider web’ had interconnected porosity, as intended and expected. A very minor number of closed micropores (yellow arrows) within the structures were also detected within the lattices (Figure 4.10 C and D), as is usual in the additive manufacture of metals. The struts are well-defined and continuous. The average pore size and strut thickness of variable titanium lattices P400, P400/1C, P400/2C, P650, P650/1C, GP/650-400, GP/400-300 and ‘spider web’ were duplicating the CAD models as shown in table 4. 2.

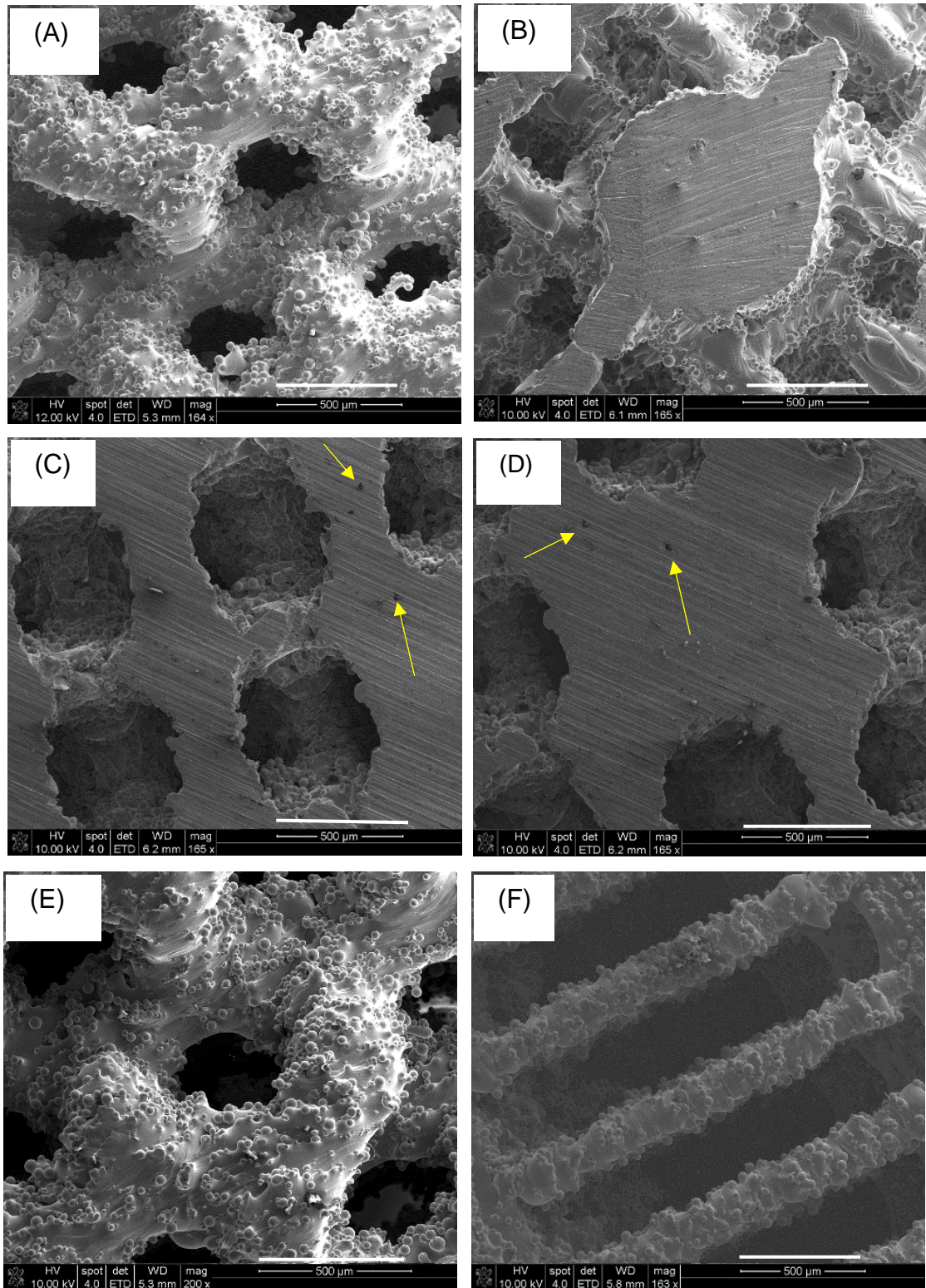


Figure 4.10 SEM images of diamond unit cell lattices A- P400, B- P400/1C, C- P650, D- P650/1C, E- GP/650-400 and F-‘Spider Web’, yellow arrows show closed porosity, (scale bar: 500 μm).

Table 4.2 Mean  $\pm$  S.D of average pore size, and average strut thickness of variable Ti-6Al-4V lattices were analysed by Image J (n=300).

Groups	P400	P400/1C	P400/2C	P650	P650/1C	GP/650-400	GP/400-300	'Spider Web'
Average pore size ( $\mu\text{m}$ )	411 $\pm$ 13	421 $\pm$ 15	423 $\pm$ 24	654 $\pm$ 25	645 $\pm$ 13	655 $\pm$ 25 /420 $\pm$ 16	420 $\pm$ 25 /305 $\pm$ 123	254 $\pm$ 12
Average strut thickness ( $\mu\text{m}$ )	421 $\pm$ 28	412 $\pm$ 22	422 $\pm$ 11	314 $\pm$ 21	333 $\pm$ 22	302 $\pm$ 19 /433 $\pm$ 20	414 $\pm$ 23 /315 $\pm$ 27	230 $\pm$ 18

Surface chemistry (EDX) analysis of porous Ti-6Al-4V components showed no presence of elements different from the raw materials or the carbon coating. Trace elements less than 1% were excluded. Ti, Al and V were the bulk surface composition, with O and a small amount of C as shown in table 4.3 and figure 4.11.

Table 4.3 Mean  $\pm$  S.D of surface chemistry (EDX) analysis, elemental composition (weight %) of variable Ti-6Al-4V lattices.

Groups	Ti	Al	V	O	C
<b>P400</b>	88.45 $\pm$ 1.6	6.3 $\pm$ 0.9	3.25 $\pm$ 0.2	4.85 $\pm$ 2.1	0.75 $\pm$ 0.7
<b>P400/1C</b>	87.05 $\pm$ 1.7	6.75 $\pm$ 2.1	3.60 $\pm$ 0.2	3.95 $\pm$ 0.7	0.45 $\pm$ 0.2
<b>P650</b>	88.30 $\pm$ 1.8	6.20 $\pm$ 1.1	3.65 $\pm$ 0.3	5.3 $\pm$ 2.5	0.30 $\pm$ 0.2
<b>GP/650-400</b>	87.80 $\pm$ 0.7	6.45 $\pm$ 2.6	3.25 $\pm$ 0.2	4.65 $\pm$ 1.2	0.65 $\pm$ 0.7
<b>'Spider web'</b>	86.40 $\pm$ 0.8	5.8 $\pm$ 2.8	3.60 $\pm$ 0.2	4.1 $\pm$ 0.5	0.33 $\pm$ 0.4

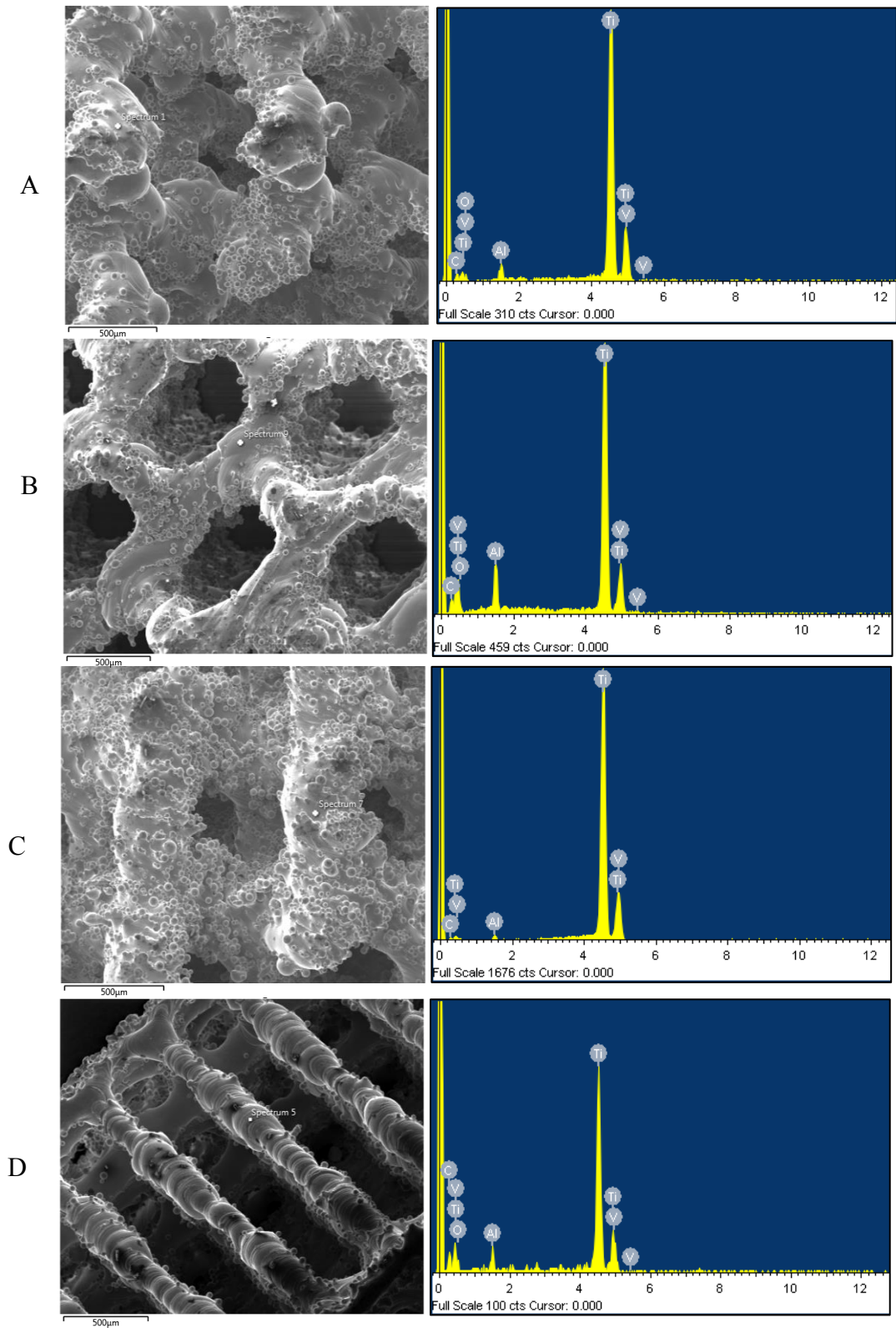


Figure 4.11 Representative SEM images with EDX analysis of Ti-6Al-4V lattices of A- P400, B- P650, C- GP/400-300 and D- ‘Spider Web’, scale bar: 500 µm.

#### 4.4.1.2 ICP-OES and LECO analysis

The results of the ICP and LECO quantitative elemental analysis after production of the SLM porous Ti-6Al-4V structures (P400/1C) are shown in Table 4.4 and are compared with that of laser melting powder titanium alloy Ti-6Al-4V (grade 23) used with the Renishaw system (datasheet) appendix 9.4. As can be seen, the results of ICP analysis confirmed what was found in EDX, where the Ti, Al and V were the main surface chemistries. The results are displayed in table 4.4 and are compared with a Renishaw test Certificate and titanium foam produced by the Metal Injection Moulding method (Shbeh and Goodall, 2015). Our results showed that the level of O, N and C was close to that of raw titanium alloy Ti-6Al-4V powder used for SLM with the Renishaw system, considered representative of the starting material used for such processes. The low interstitial elements content in SLM Ti-6Al-4V structures, when compared with Metal Injection Moulding technique, produced porous titanium indicates the low risk of contamination during SLM building process, which, unlike metal injection moulding method does not need a polymer binder.

Table 4.4 Surface chemistry analysis (ICP) for the major and (LECO) for the interstitial elements level of the SLM produced Ti-6Al-4V lattices and, elemental composition (weight %) of the variable.

Element composition/percent by mass						
Source	Ti	Al	V	O	N	C
SLM Ti-6Al-4V lattices	89.44	6.66	4.05	0.227 ± 0.01	0.044 ± 0.04	0.023 ± 0.00
Renishaw test Certificate	Balance	5.5 - 6.5	3.5 - 4.5	<0.13	<0.03	<0.08
Ti foam produced by MIM	–	–	–	0.66	0.020	0.17

#### **4.4.1.3 Micro-Computed Tomography**

The images from MicroCT cross-sectional (Figure 4.12) revealed that SLM lattices of P400, P400/1C, P400/2C, P650, P/C650, GP/650-400, GP/400-300 and 'spider web' had a mostly interconnected porosity ranging from 50 to 80%. The average open and total porosity are shown in table 4.5. No statistically significant differences were observed between the open and total porosity of all tested lattices (Figure 4.13), indicating that the porosity present is mostly interconnected. As can be seen, the struts are well-defined and constant. The ratio between the object surface area to volume ratio decreased with decreasing porosity. The percentages of open, closed and total porosity and object surface to volume ratio of variable titanium lattices P400, P400/1C, P400/2C, P650, P650/1C, GP/650-400, GP/400-300 and spider web are shown in table 2.



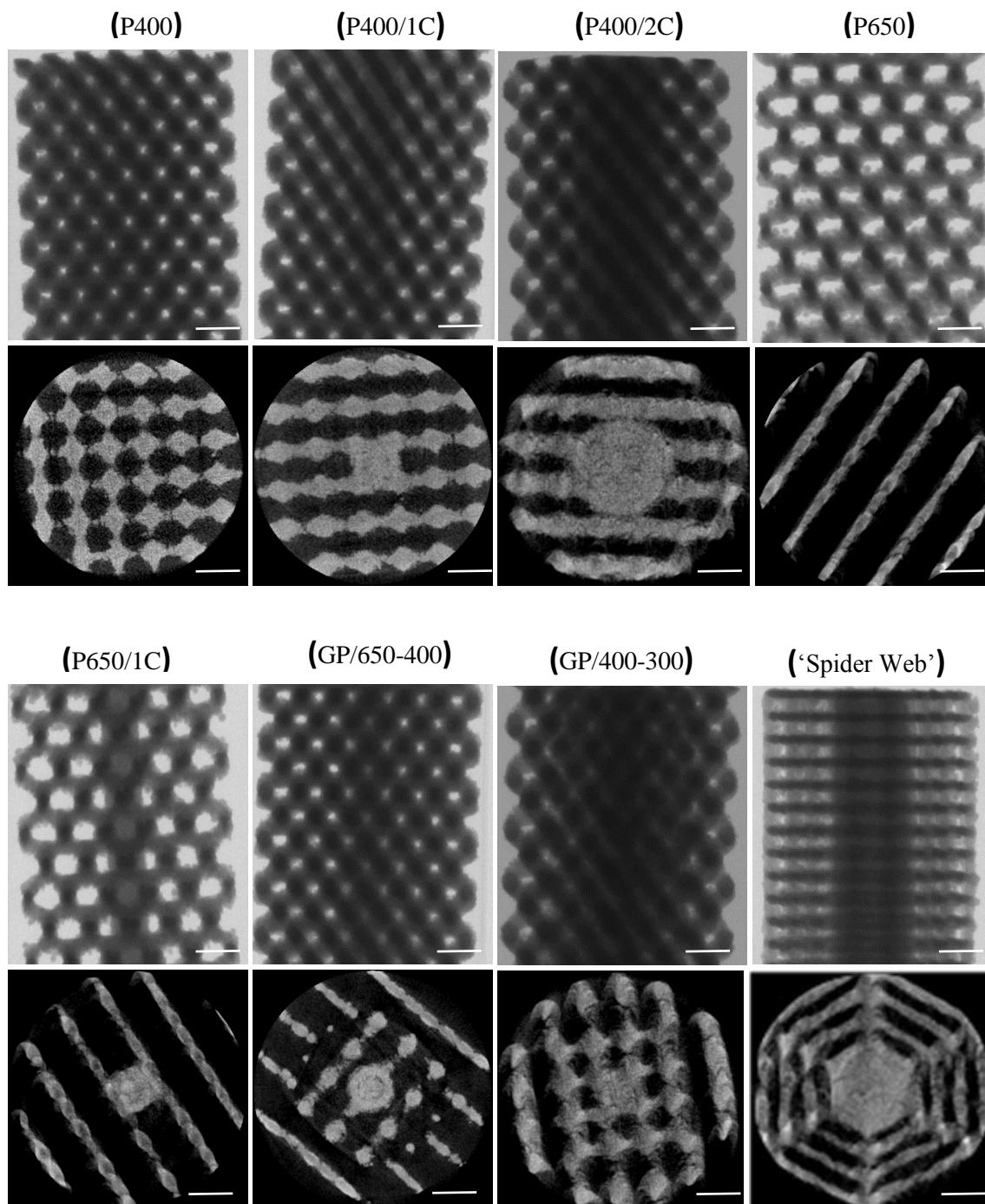


Figure 4.12 MicroCT reconstruction images, top (side view) and bottom (cross - section) of P400, P400/1C, P400/2C, P650, P650/1C, GP/650-400, GP/400-300 and 'Spider Web' lattices, (scale bar=1mm).

Table 4.5 Mean  $\pm$  S.D of the average percentages of open, closed and total porosity and object surface to volume ratio of variable titanium lattices calculated by 3D analysis of the MicroCT cross-sectional images using CTA software. These data were collected for three samples for each group.

<b>Groups</b>	<b>Open porosity %</b>	<b>Closed porosity %</b>	<b>Total porosity %</b>	<b>Object surface / volume ratio</b>
<b>P400</b>	56.8 $\pm$ 1.0	0.29 $\pm$ 0.10	56.9 $\pm$ 1.0	16.6 $\pm$ 0.6
<b>P400/1C</b>	51.2 $\pm$ 0.4	0.04 $\pm$ 0.03	51.5 $\pm$ 0.4	12.3 $\pm$ 0.6
<b>P400/2C</b>	48.4 $\pm$ 0.9	0.30 $\pm$ 0.02	48.6 $\pm$ 1.1	17.0 $\pm$ 1.6
<b>P650</b>	82.8 $\pm$ 0.8	0.08 $\pm$ 0.02	82.9 $\pm$ 0.7	22.1 $\pm$ 0.8
<b>P/C650</b>	80.9 $\pm$ 0.6	0.05 $\pm$ 0.01	80.9 $\pm$ 0.6	20.6 $\pm$ 1.6
<b>GP/650-400</b>	78.5 $\pm$ 0.4	0.12 $\pm$ 0.04	78.5 $\pm$ 0.4	19.2 $\pm$ 1.1
<b>GP/400-300</b>	56.6 $\pm$ 0.8	0.18 $\pm$ 0.04	56.7 $\pm$ 0.8	17.9 $\pm$ 0.3
<b>'Spider Web'</b>	68.5 $\pm$ 1.6	0.320 $\pm$ 0.1	68.6 $\pm$ 1.5	20.2 $\pm$ 1.8

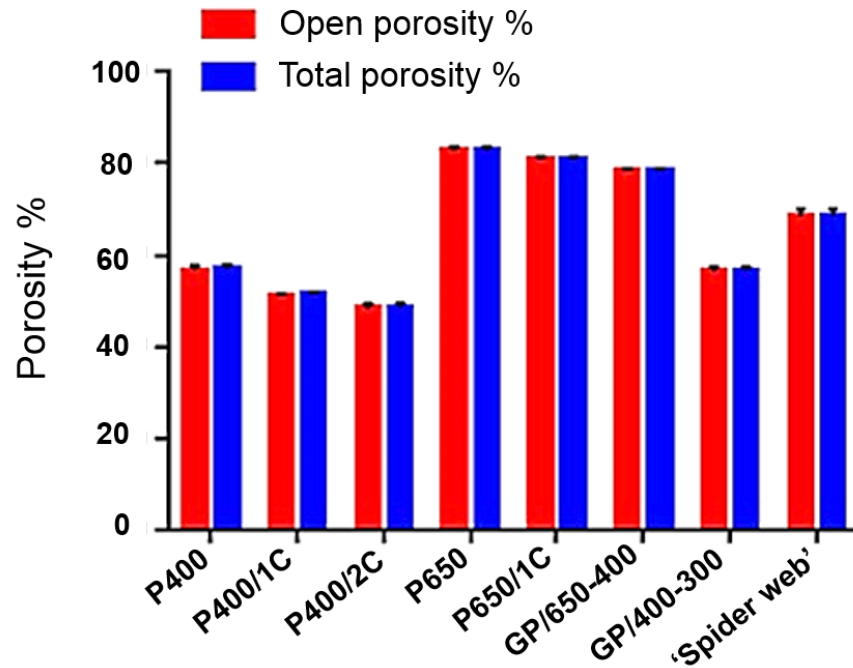


Figure 4.13 Comparison between open and total (%) of P400, P400/1C, P400/2C, P650, P650/1C, GP/650-400, GP/400-300 and 'Spider Web' lattices measured by MicroCT.

#### 4.4.1.4 Archimedes method

The results for the overall porosity of variant titanium lattices, when measured by the Archimedes method were generally in agreement with those calculated by MicroCT, and there was no statistical difference between methods used, as shown in table 4.6 and figure 4.14.

Table 4.6 Mean  $\pm$  S.D of the average total porosity of variable titanium lattices calculated by 3 D analysis of the MicroCT and Archimedes method (no 3).

Total porosity %		
Groups	MicroCT	Archimedes
P400	56.9 $\pm$ 1.0	55.2 $\pm$ 3.0
P400/1C	51.5 $\pm$ 0.4	51.8 $\pm$ 4.5
P400/2C	48.6 $\pm$ 1.1	47.6 $\pm$ 2.4
P650	82.9 $\pm$ 0.7	80.4 $\pm$ 3.6
P650/1C	80.9 $\pm$ 0.6	79.0 $\pm$ 2.9
GP/650-400	78.5 $\pm$ 0.4	76.1 $\pm$ 2.2
GP/400-300	56.7 $\pm$ 0.8	55.7 $\pm$ 1.7
‘Spider Web’	68.6 $\pm$ 1.5	67.4 $\pm$ 1.4

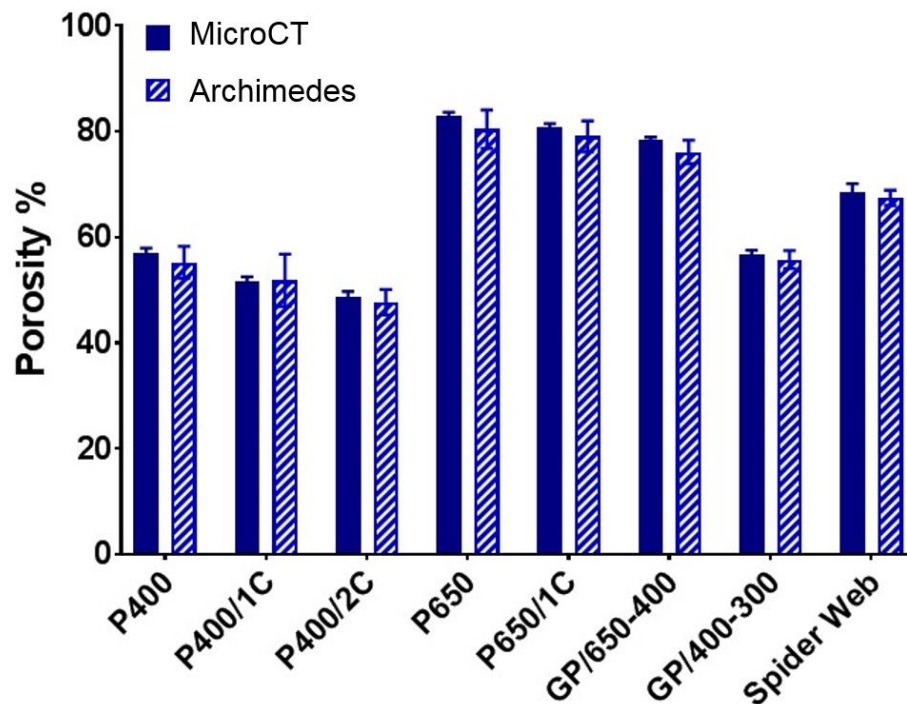


Figure 4.14 Comparison between overall porosity (%) of P400, P400/1C, P400/2C, P650, P650/1C, GP/650-400, GP/400-300 and ‘Spider Web’ lattices measured by MicroCT and Archimedes.

## **4.4.2 Mechanical testing**

### **4.4.2.1 Compression test**

Figure 4.15 shows the failure mode for the titanium lattices of P400, P400/1C, P650, P650/1C, GP/650-400, and ‘Spider Web’ under compression. The deformation of the core-base lattice structures showed initial core buckling and then lattices break before the structure collapses. While structures without a dense core showed a plastic lattice breakdown leading to structure rupture.

Stress-strain curves of all Ti-6Al-4V components under compression (Figure 4.16) exhibited overall linear relationship in the elastic region followed by plastic yield plateau. Six linear elastic regions of each design showed a highly reproducible pattern. The Young’s modulus and yield strength of the uniform and graded structures were comparable between samples of the same design, with a low standard deviation, indicating the scaffold manufacture had high reproducibility concerning bulk mechanical properties (table 4.7). There were higher mechanical properties in samples with a dense core and thicker struts. The highest Young’s moduli and yield strengths were displayed by scaffolds with a ‘spider web’ structure and 2 mm dense core, while the weakest scaffolds were with P650. Interestingly, there were no significant differences between the mechanical properties of the graded structures for either smaller (GP/400-300) or larger (GP/650-400) pore sizes as shown in table 4.8.

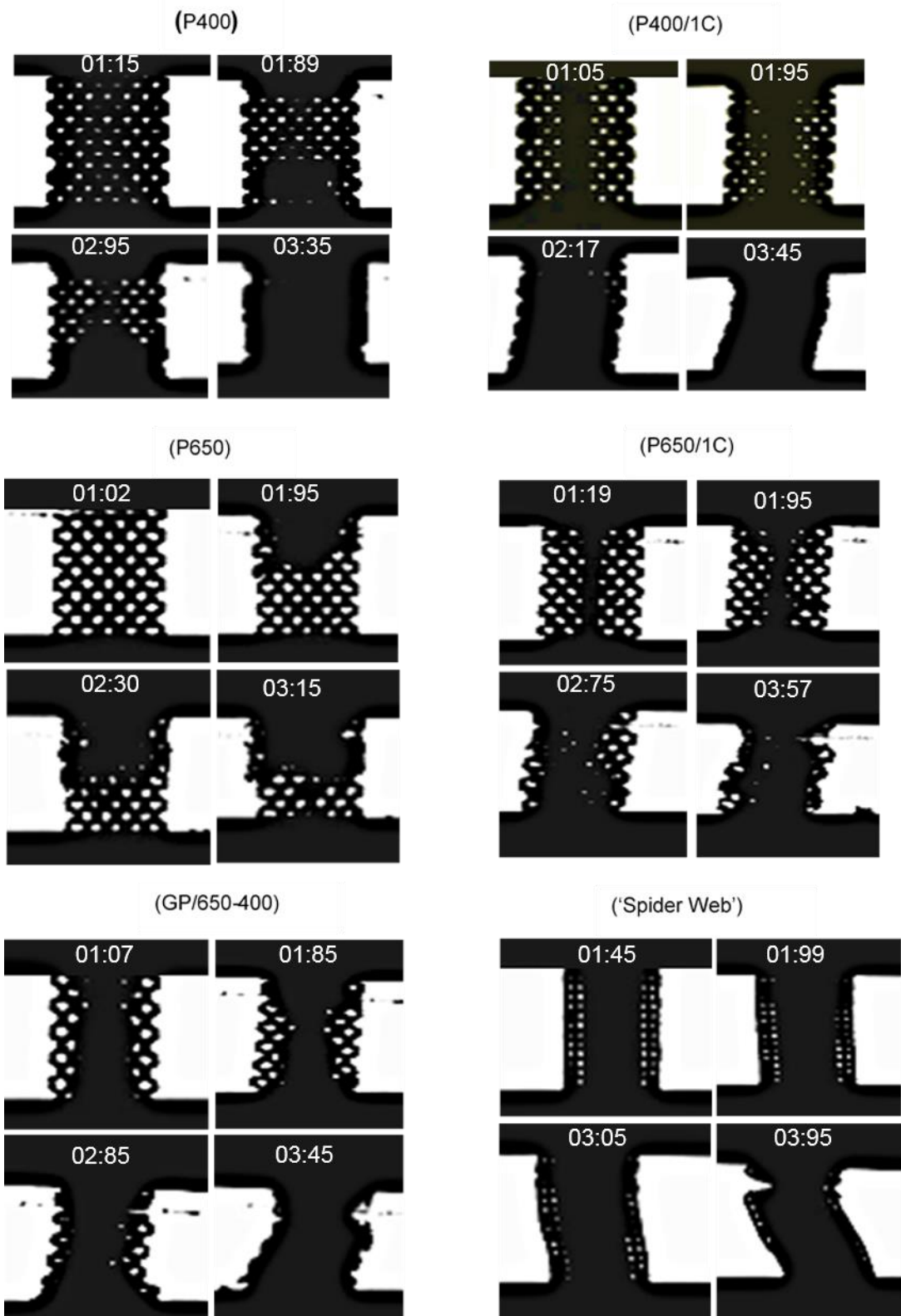


Figure 4.15 Silhouette images obtained from the video extensometer at different time points (minutes) in Zwick Roell testing machine showing the failure mode of the various SLM Ti-6Al-4V lattices; P400, P400/1C, P650, P650/1C, GP/650-400 and 'Spider Web' before and after compression.

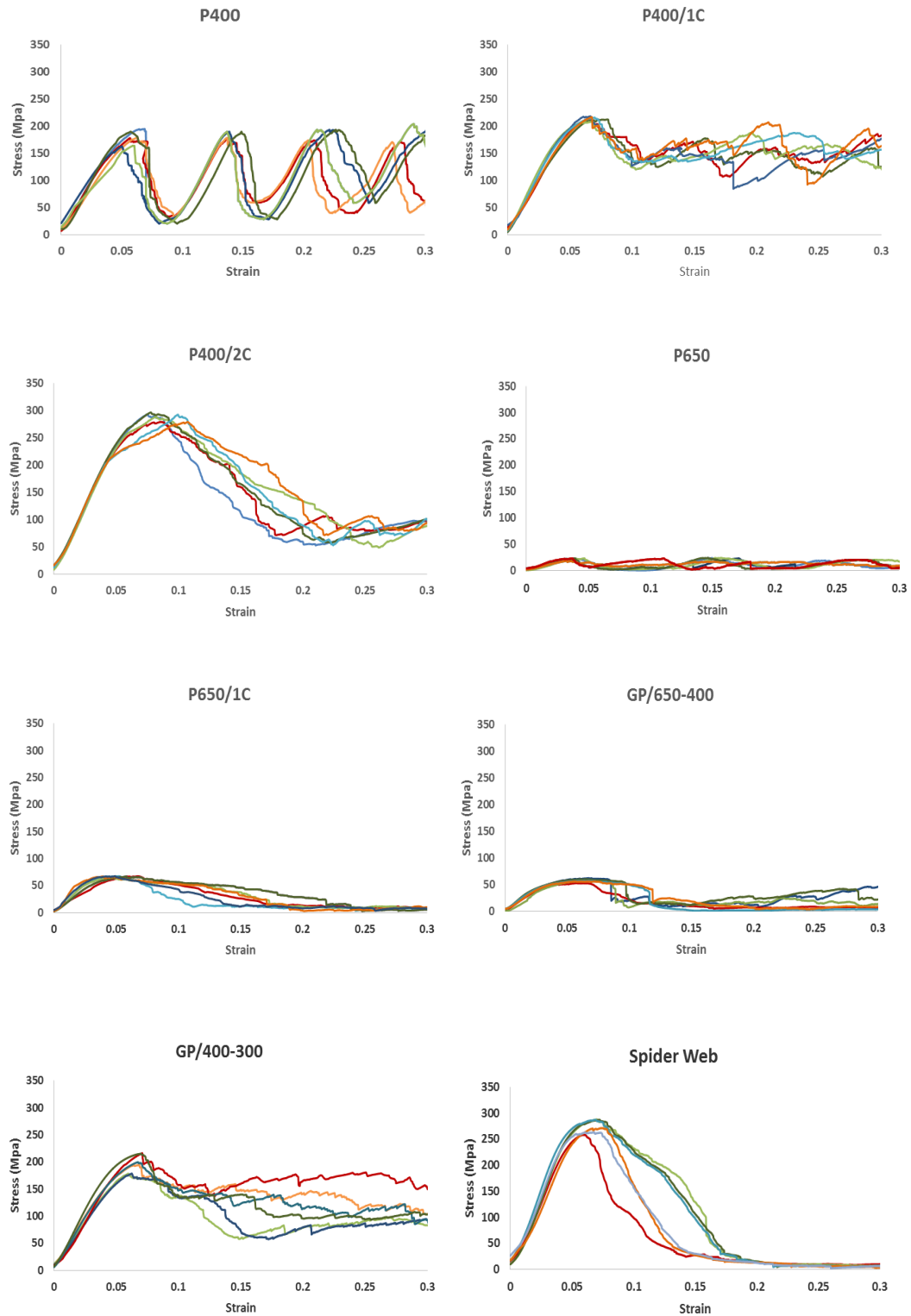


Figure 4.16 Figure 4.16 Stress-strain curves obtained by compression test of the eight Ti-6Al-4V lattices; P400, P400/1C, P400/2C, P650, P650/1C, GP/650-400, GP/400-300 and Spider Web, (n=6). Samples were tested in compression at 1 mm/min speed, 20 kN load cell and 10 kN maximum force in Zwick Roell machine. Each line is the stress/stress curve for an individual sample.

Table 4.7 Mechanical properties (Young's modulus and yield strength) of all Ti-6Al-4V lattices under compression (Mean  $\pm$  SD).

<b>Compression Test</b>		
<b>Groups</b>	<b>Young's Modulus (GPa)</b>	<b>Yield Strength (MPa)</b>
<b>P400</b>	3.3 $\pm$ 0.6	147 $\pm$ 10
<b>P400/1C</b>	4.1 $\pm$ 0.3	178 $\pm$ 10
<b>P400/2C</b>	4.8 $\pm$ 0.6	204 $\pm$ 33
<b>P650</b>	0.7 $\pm$ 0.2	16 $\pm$ 4
<b>P650/1C</b>	2.0 $\pm$ 0.3	55 $\pm$ 4
<b>GP/650-400</b>	1.7 $\pm$ 0.2	48 $\pm$ 1
<b>GP/400-300</b>	3.4 $\pm$ 0.4	147 $\pm$ 31
<b>'Spider Web'</b>	6.0 $\pm$ 0.4	224 $\pm$ 7



Table 4.8 Significant differences between A- Young's modulus and B- Yield strength of variant Ti-6Al-4V lattices under compression, \*=p<0.05, \*\*=p<0.01, \*\*\*=p<0.001 and \*\*\*\*=p<0.0001.

(A)	Young's Modulus								
	Groups	P400	P400/1C	P400/2C	P650	P650/1C	GP/650-400	GP/400-300	Spider Web
<b>P400</b>	-								
<b>P400/1C</b>	S*	-							
<b>P400/2C</b>	S****	S*	-						
<b>P650</b>	S****	S****	S****	-					
<b>P650/1C</b>	S****	S****	S****	S****	-				
<b>GP/650-400</b>	S****	S****	S****	S**	NS	-			
<b>GP/400-300</b>	NS	NS	S****	S****	S****	S****	-		
<b>Spider Web</b>	S****	S****	S***	S****	S****	S****	S****	-	

(B)	Yield Strength							
	Groups	P400	P400/1C	P400/2C	P650	P650/1C	GP/650-400	GP/400-300
P400	-							
P400/1C	S*	-						
P400/2C	S****	NS	-					
P650	S****	S****	S****	-				
P650/1C	S****	S****	S****	S**	-			
GP/650-400	S****	S****	S****	NS	NS	-		
GP/400-300	NS	NS	S****	S****	S****	S****	-	
Spider Web	S****	S*	NS	S****	S****	S****	S****	-

With increasing porosity, Young's modulus and yield strength were lower, as would be expected (Figure 4.17). Most samples lie on the same general curve on a plot of mechanical properties against density, but the spider web design (green circle) is notably higher for a given density. This probably reflects the lower degree of isotropy in this structure, being particularly mechanically efficient along the axial direction tested.

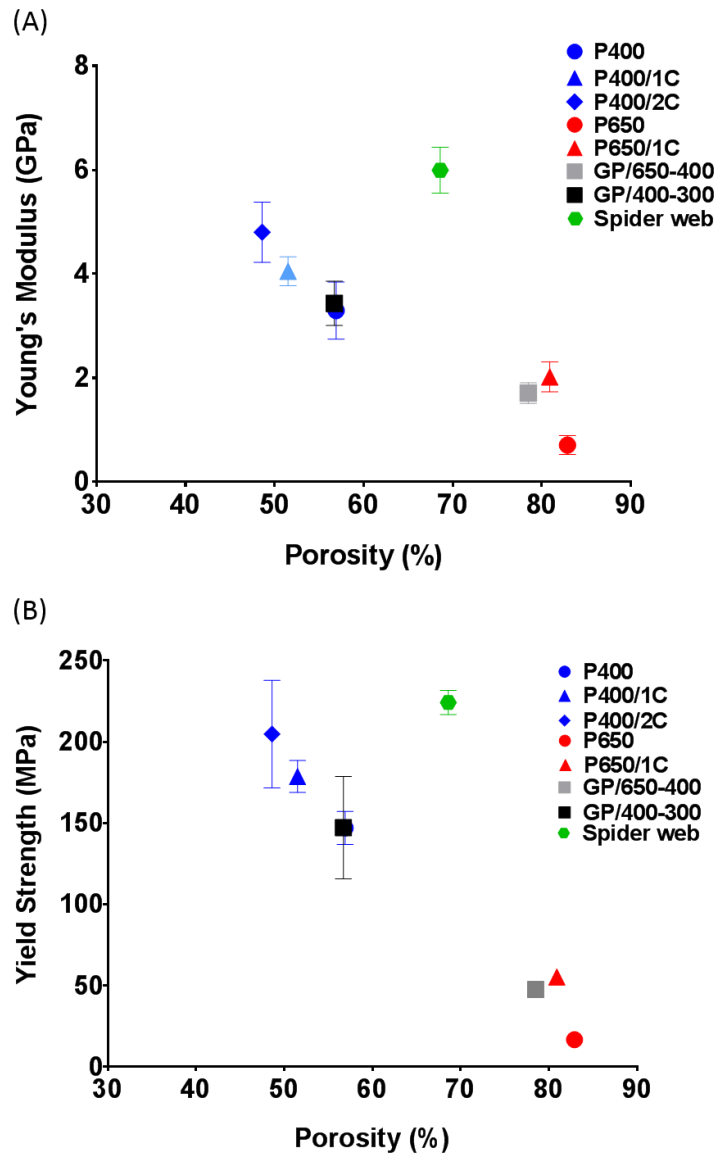


Figure 4.17 A comparison of the mechanical properties in compression test (A) Mean  $\pm$  SD Young's modulus, (B) Mean  $\pm$  SD yield strength of the regular and graded Ti5Al4V lattices plotted against % mean porosity by volume as assessed by MicroCT.

#### 4.4.2.2 Three-point bending test

Figure 4.18 shows the Ti-6Al-4V samples during three-point bending test using the Zwick Roell machine to measure flexural strength. Visual inspection of fractured Ti-6Al-4V lattices showed a typical initial break of struts on the inferior region of the sample opposing to loading area then core buckling resulting in the rupture of the sample. Load-displacement curves of the Ti-6Al-4V components of P400, P400/1C,

P400/2C, GP/400-300 and 'Spider Web' in three-point bending (Figure 4.19) gave a generally linear relationship in the elastic region followed by plastic yielding then a sudden drop in load. The linear elastic regions of each model showed highly repeatable behaviour.

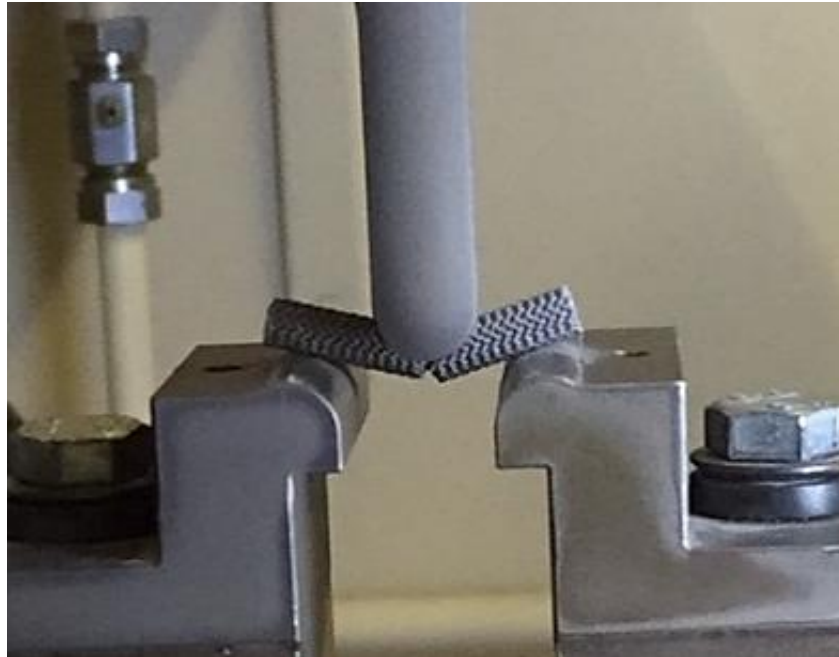


Figure 4.18 Ti-6Al-4V sample during three-point bending test to measure flexural strength using the Zwick Roell machine.

The results of the flexural modulus and flexural strength of the regular and graded porous structures are shown in Table 4.9. The highest value for both flexural modulus and flexural strength was shown in scaffolds with a 2 mm dense core, while the weakest scaffold in bending was the "spider web" design. There are no statistically significant differences in bending stiffness between graded (GP/400-300) and uniform (P400/1C) porous structures as shown in Table 4.10. Interestingly, the 'spider web' was the weakest design, however it showed more plastic deformation. The structure exhibited the lowest load to failure, but it was able to bend a long way before actually reaching the point of breaking (Figure 4.19), indicating high failure strain.

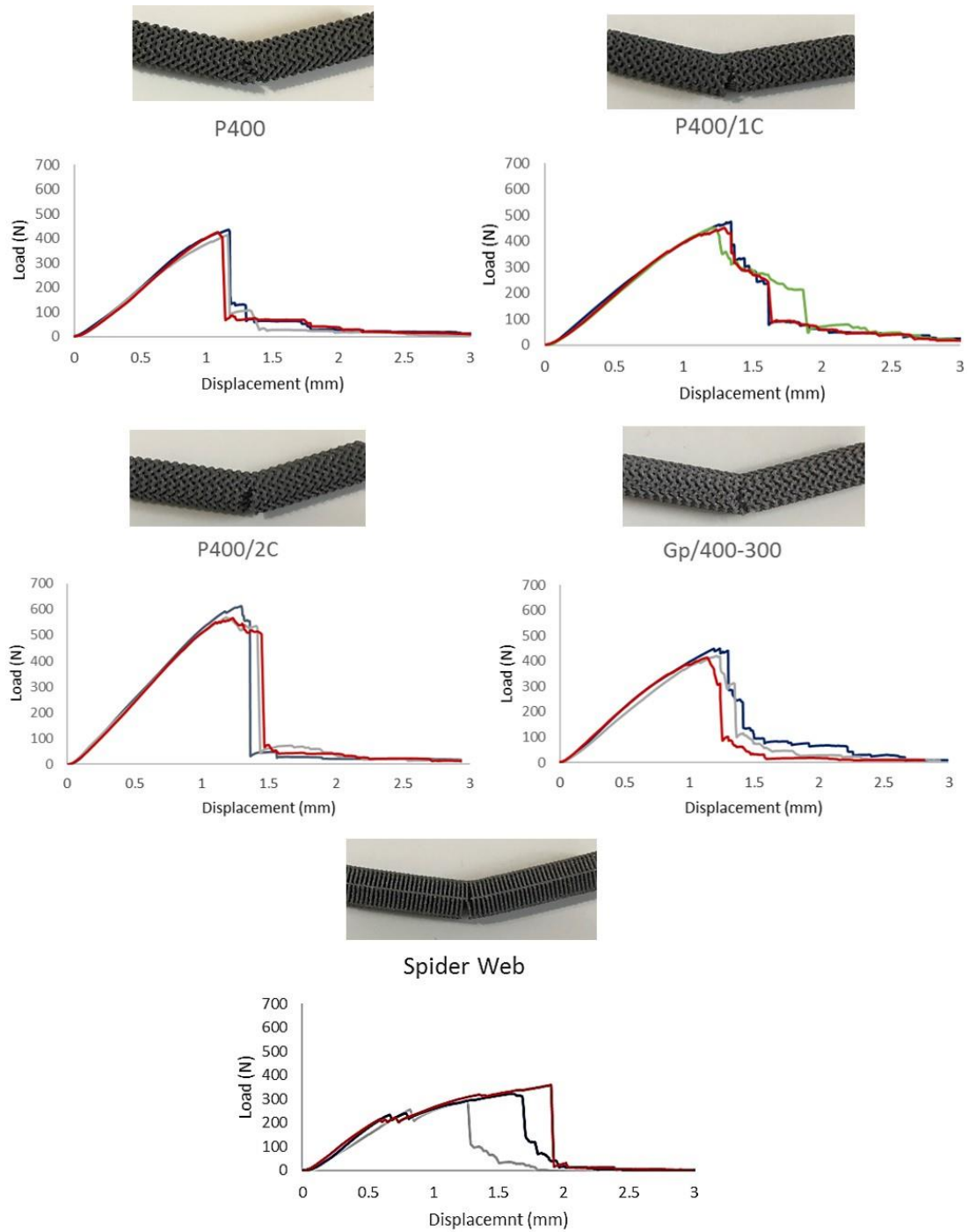


Figure 4.19 Linear force–displacement curves and images of the Ti-6Al-4V lattices; P400, P400/1C, P400/2C, GP/400-300 and Spider Web, tested in three-point bending (n=3). Each line is the force curve for an individual sample.

Table 4.9 Mean  $\pm$  SD of the mechanical properties (flexural modulus and flexural strength) of Ti-6Al-4V lattices P400, P400/1C, P400/2C, GP/400-300 and Spider Web under three-point bending test.

Three-point bending test		
Groups	Flexural Modulus (GPa)	Flexural Strength (MPa)
P400	4.7 $\pm$ 0.1	377 $\pm$ 11
P400/1C	4.9 $\pm$ 0.0	420 $\pm$ 21
P400/2C	6.1 $\pm$ 0.1	537 $\pm$ 19
GP/400-300	4.9 $\pm$ 0.2	382 $\pm$ 12
'Spider Web'	2.6 $\pm$ 0.3	304 $\pm$ 29

Table 4.10 Significant differences of A- Flexural modulus and B- Flexural strength of variant Ti-6Al-4V lattices under three-point bending test, \*=p<0.05, \*\*= p<0.01, \*\*\*=p<0.001 and \*\*\*\*=p<0.0001.

A	Flexural Modulus				
	Groups	P400	P400/1C	P400/2C	GP/400-300
P400	-				
P400/1C	NS	-			
P400/2C	S****	S****	-		
GP/400-300	NS	NS	S****	-	
Spider Web	S****	S****	S****	S****	-

B	Flexural Strength					
	Groups	P400	P400/1C	P400/2C	GP/400-300	Spider Web
P400	-					
P400/1C	NS	-				
P400/2C	S****	S***	-			
GP/400-300	NS	NS	S****	-		
Spider Web	S**	S***	S****	S**	-	

As predicted and similar to what was found in the compression test, flexural modulus and yield strength of Ti-6Al-4V lattices were higher with lower porosity, (Figure 4.20). Generally, all lattices are placed on the same general trend of mechanical properties versus density. In contrast to the mechanical properties of the spider web design in compression it was significantly lower for a given density. This may be related to the anisotropic behaviour of this structure, being particularly mechanically efficient along the axial direction and less able to respond to the shear transfer of load required in bending.

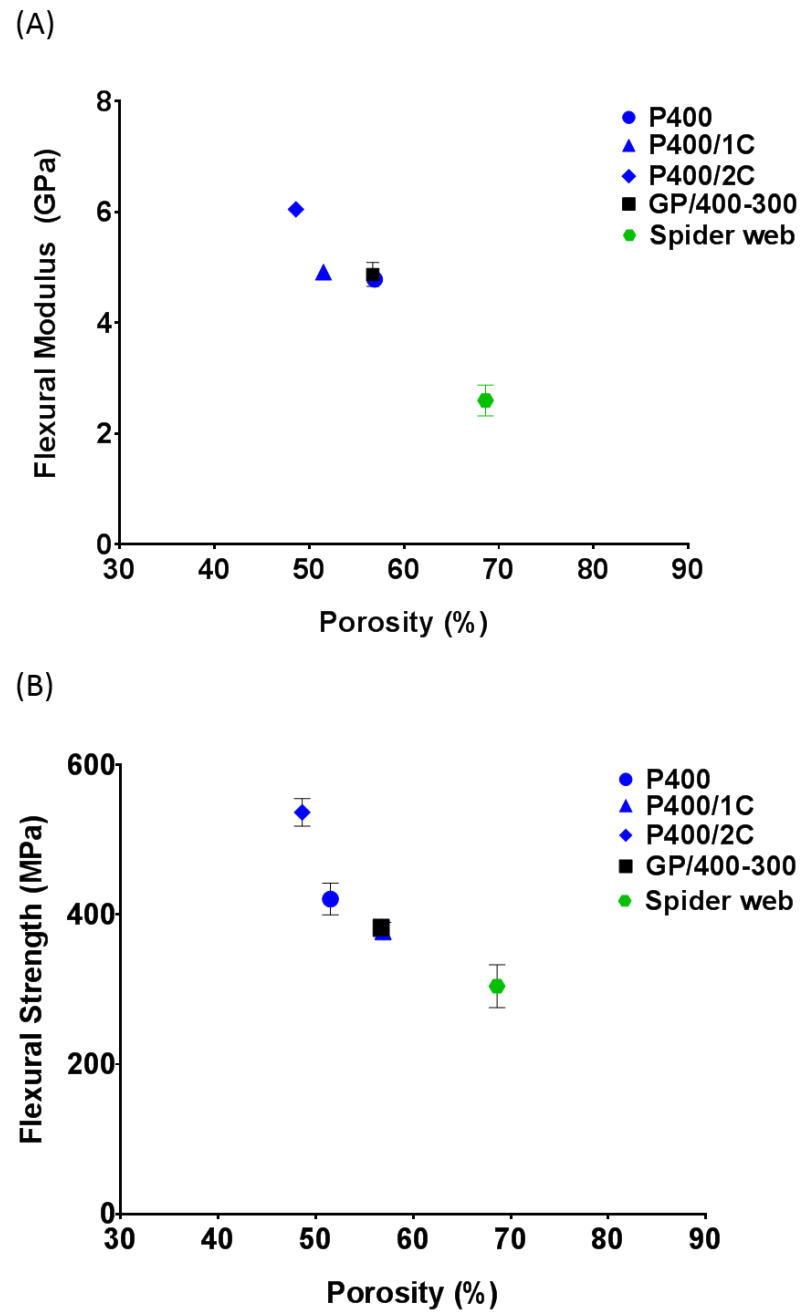


Figure 4.20 A comparison of the mechanical properties in three-point bending test (A) Mean  $\pm$  SD flexural modulus, (B) Mean  $\pm$  SD flexural strength of the regular and graded Ti5Al4V lattices plotted against % mean porosity by volume as assessed by CT scan.



## **4.5 Discussion**

The work implemented in this chapter primarily aimed to determine the feasibility of the SLM process for the production of complex geometric shapes of porous Ti-6Al-4V to be used in dental implants to improve implant fixation and bone ingrowth. In order to achieve this aim, a variety of porous Ti-6Al-4V scaffolds based on the approximately cylindrical shape of the size that represents dental implants were investigated. The porosity was designed in a regular and graded array using different pore shape, size and proportion with and without a dense core referred to as P400, P400/1C, P400/2C, P650, P650/1C, GP/650-400, GP/400-300 and 'Spider Web' (Table 4.1). Here we assessed surface chemistry, structural and mechanical properties (compression and three-point bending test) of the resulting structures. The most promising structures were subsequently tested biologically for bone cell ingrowth using different cell culture methods are described in chapter 5.

The Selective Laser Melting method was selected for the production of titanium components because of the many potential advantages, as described in 2.9, such as rapid and easy production of complex geometry with less waste production. Ti-6Al-4V was chosen as a raw material due to its excellent biocompatibility for orthopaedic implant applications.

The selected unit cell used was a diamond lattice (Figure 4.2) due to its simple structure with relatively low stiffness compared to its density. This has been suggested previously for medical applications due to it exhibiting similar properties to cancellous bone (van Grunsven et al., 2014). Additionally, a new 'spider web' design was invented and compared, this was an effective method for the production of a structure with graded porosity, but to the best of knowledge, such a radial pore structure has not previously been evaluated for its suitability for the design of medical implants.

Several groups have reported research on the production of medical devices using titanium alloy Ti-6Al-4V and SLM. Despite the fact that titanium and its alloys have been introduced as bioinert and biocompatible materials for dental and orthopaedic implants (Nouri et al., 2010), it is essential to assess surface chemistry and the biofunctional properties of structures from these materials made by advanced manufacturing technology. Bulk chemistry analysis by an EDX spectrum and the ICP system of titanium lattices used in this study determined a typical spectrum of Ti-6Al-4V and confirmed no change in the main elements Ti, Al and V of the as-built Ti-6Al-4V lattices (Figure 4.11) (Table 4.3) and (Table 4.4). The level of interstitial elements (O, N and C) of the built SLM Ti-6Al-4V lattices was also assessed post-processing using the LECO metal extraction system. Oxygen, nitrogen and carbon contamination is a common issue found during titanium component production using different fabrication methods (Shbeh and Goodall, 2015). These results confirmed a lower content of interstitial elements (Table 4.4) in the SLM Ti-6Al-4V structures compared to the higher levels reported for titanium foams produced by different manufacturing methods such as Metal Injection Molding (Shbeh and Goodall, 2015). Previously reported studies have shown that the SLM process can give low levels of these interstitial elements in comparison to other fabrication methods (Murr et al., 2010). However, other work by Vaithilingam et al, 2016 claimed that even with the presence of argon atmosphere and low oxygen concentration with the SLM process, there is a chance that titanium interacts with the available oxygen and forms its oxide. Also, the rate of carbon dioxide in the build atmosphere/chamber is still undetermined and cannot be monitored during the SLM process. Even though the maximum amount of carbon in Ti-6Al-4V is found to be 0.08%, a modest amount of carbon is also found in the starting Ti-6Al-4V powder due to air contamination (Vaithilingam et al., 2016).

The interconnected porosity was confirmed by MicroCT analysis of the variant SLM Ti-6Al-4V lattices. The porosity within the Ti-6Al-4V constructs was controlled by varying the pore size and strut thickness. Different methods of porosity determination have shown a high level of agreement. The total porosity results, when measured in the Archimedes and MicroCT methods, were generally comparable (Table 4.6) and (Figure 4.14), although there was higher variability in the porosity of structures that have been measured by Archimedes. Even though an effort was made to reduce the appearance of air bubbles, these could still have been present, resulting in a higher density and lower porosity measurement. This outcome is consistent with the study of Slotwinski et al., which revealed a general agreement in the porosity measurement of CoCr components produced by additive manufacturing technology using Archimedes, mass/volume, and X-ray CT (Slotwinski et al., 2014). In recent years, open porosity has been shown as a common approach for strong and durable bone fixation. Open porosity enables body fluids to be transported extensively through the porous components, which should support implant fixation and bone formation (Xue et al., 2007). On the other hand, the porous structures should be rigid enough to maintain the physiological loads.

The stress and strain curves of the different SLM Ti-6Al-4V lattices during compression were relatively typical (Figure 4.16) of what is usually found for these types of lattice materials (van Grunsven et al., 2014). One factor is that they are more highly reproducible sample-to-sample than random structured porous materials, such as foams and sponges. This is because the structure of each sample is more repeatable. For the actual stress-strain curves, there is an initial elastic stage (approximately linear) corresponding to the bending of the struts but with a lower gradient than a dense material would have. Then there is a yield event where a particular strut fails, which can be followed by a certain degree of work hardening, like in a solid, but which more

commonly leads to a decrease in load as part of the structure collapses into the available free space, in the manner of a porous solid. With regard to the mechanism (Figure 4.15), at a mesoscale, we identify that collapse begins in one horizontal layer, on a random basis, likely mediated by a defect. This layer then begins to crush to a high density, before the stress raises in another layer to a sufficiently high level to initiate failure, and the process is repeated. This is the origin of the cycles seen most clearly in the P400 sample (though present in some others); each peak is the point of failure initiation in a new layer, which causes a drop in load. Once the layer is crushed, the load begins to build up again. The uniform size of the layers explains the uniform engineering strain level over which the repeats occur. This progressive failure is significantly affected by a dense core, as this resists collapse and causes more distributed deformation. In samples with a core, we do not see the repeated cycles of load increase and decrease. While the lattices here were not examined at sufficient detail to draw conclusions on the mechanism of failure in individual struts, from other work on EBM lattices, it is known that the struts generally display very limited plasticity (Hernández-Nava et al., 2016), and so the failure is likely to be in a brittle mode.

Force-displacement curves obtained by the three-point bending test for the different Ti-6Al-4V lattices; P400, P400/1C, P400/2C, GP/400-300 and 'Spider Web' also displayed highly consistent behaviours for the same tested design due to the structure reproducibility as seen in figure 4.19. The curves generally showed three regions. The initial elastic region explains the elastic deformation of the struts. Then there was a plastic yield occurrence where an individual strut failed, which was then followed by a decrease in load as part of the structure failed. The plastic deformation of all sample designs initiated on the lower side of samples opposite to the loading side. Lattices with a 2 mm dense core were the stiffest samples against bending (Figure 4.20), the possible

reason is that the dense material is more significant in the structure; therefore, the sample can tolerate a higher force, and the flexural strength is greater. Flexural strength decreased from 537 to 304 MPa when a dense core was not incorporated with the uniform porous structure with 400 micron pore size. From the porosity curve versus flexural strength, it can be seen that bending stiffness increases with decreasing porosity.

As would be expected, the differences in porosity result in differences in compression and bending strength, which are higher at lower porosities. A large variety of values have been reported for Young's modulus of cancellous bone depending on species, preparation methods and types of bone, for example, the range for cancellous bone in the mandible is 1.5-4.5 GPa as reviewed in the literature (Andani et al., 2014). A lower range of Young's modulus (0.1 - 2 GPa) also been reported (Wen, 2017). The maximum bending strength for human cortical bone is approximately 110 -184 MPa (Li et al., 2014). The structures used in this study were of a similar range to these values ranging from 0.7 - 6 GPa (Table 4.7) in compression and from 2.6 - 6.1 GPa (Table 4.9) in bending. The compressive strength was in the range 16–224 MPa and flexural strength in the range 304 - 537 MPa. The root part of the natural tooth is made from dentine which is covered by cementum, the tooth is held into the bone via periodontal ligament. Forces of mastication for each tooth are transferred from enamel through dentine to the root, then from cementum through the periodontal ligament to the cancellous bone to the end at the ramus of the jaw (Currey, 2012). In the literature, there is some debate about Young's modulus of dentine. Generally, it is reported at around 20-25 GPa (Kinney et al., 2003) which is comparable to cortical bone (17–20 GPa) (Wally et al., 2015). However, in artificial implants, there is direct contact between bone and the implant structure which induces bone ingrowth. Dental implants should withstand the

physiological function during mastication. The maximum biting force is from 230 - 450 N in the molar region (Wen, 2017).

As can be seen, the mechanical properties of biomaterials such as titanium and its alloys will determine their applications. These properties should have high strength and low modulus in the range that satisfies the requirements of calcified human tissue.

The compression test was conducted in this study to compare the basic structural mechanical properties of the structures produced in different batches. All scaffolds showed highly reproductive behaviour, which is due to the regular morphology of SLM components. This corresponds to previous work on cubes of lattice structures where a very high flexible initial region of the stress - curve was demonstrated by Ti-6Al-4V scaffolds based on the diamond unit cell and produced via EBM (van Grunsven, 2014). The properties of the strength of porous biomaterials can be improved with increased density (Balla et al., 2010). Interestingly, the "spider web" lattices were the strongest scaffolds in compression in relation to their porosity but were the weakest in bending, in line with the relationship between porosity and strength. A possible explanation for this result may be the low degree of isotropy in this structure, where it is mechanically effective along the axial direction. Recent research has shown that additively manufactured structures display anisotropic behaviour (Ataee et al., 2018), but that this difference becomes insignificant for larger unit cells, and derives from the smaller samples in that work not accurately replicating the CAD model shape - the anisotropy in properties may come from differences in the porous structure, not inherent directionality in the properties of the metal from which it is made. The only structures that did not have sufficient strength compared to bone were non-core based lattices of 650  $\mu\text{m}$  pore size and 300  $\mu\text{m}$  strut thickness (P650) that had the lowest strength and

stiffness. These are too porous and do not have enough solid material to resist deformation.

Previous research has also documented that fully porous metal structures for orthopaedics or dental implants are not able to provide sufficient strength to withstand physiological loading (Ryan et al., 2006). To improve the mechanical properties, a dense core was integrated into the structures. As expected, lattices with a core were stronger than fully porous scaffolds. This finding has also been confirmed in the literature, where it was found that implants which have two different regions, a dense core and an irregular porous shell, are more suitable for load bearing devices as in a study with a dental root implant produced by combining selective laser sintering of porous coating and selective laser melting of the dense core (Tolochko et al., 2002). The main advantage of this SLM method is that the porous structure and a dense core are manufactured in one build of one material, compared to the preparation of the structure first and then integrating this with a porous coating. Structural modifications, including the increased diameter of the dense core of the regular porous structures, and the strut thickness of the graded structures lead to a significant improvement in Young's modulus and yield strength (Table 2), which is then more able to support the load.

Graded porous implants allow rapid bone growth, while the low porosity part of the component provides the strength to maintain the physiological load (Soon et al., 2011). Afshar et al studied the deformation mechanisms of regular and graduated porosity structures for stretching and bending. They concluded that the graded porous structures were less deformed than regular ones. They also reported that energy absorption and elastic-plastic deformation were high for struts oriented in the direction of loading (Afshar et al., 2016). In terms of the mechanical properties of our tests, the graded structures have characteristics that correspond almost to their total density. This is

expected as they were tested with different density zones (and dense core if present) in parallel, showing that the properties combine arithmetically, rather than having more complex interactions between the different density layers. This is in agreement with earlier work (van Grunsven et al., 2014) where the layers were tested in a series, and elastic deformation was found to expand according to Young's modulus, and the plastic deformation of the progress of the least dense layer to the highest. The samples here are tested in bending, where the outer layers experience a higher strain than the centre, the difference between the graded and non-graded lattices would be more significant. These results demonstrate the feasibility of designing overall mechanical properties by combining different lattices in a graded structure.

#### **4.6 Chapter summary**

1. Overall the SLM technique is extremely promising as a fabrication method for production of a range of well-controlled porous Ti-6Al-4V structures with uniform and graded porosity of a suitable size for dental implants which could be more cost-effective and allow better implant stability than those currently available.
2. All structures had compressive and bending mechanical properties in the range of those previously reported for cancellous bone, except for the 650-micron pore size scaffolds.
3. The presence of a dense core led to an improvement in mechanical properties of the lattice structures in compression and three-point bending tests.
4. The graded structures were found to behave in line with their average density.
5. The structure with 'spider web' design displayed a lower degree of isotropy, being more mechanically effective along the axial direction.



## **Chapter 5 : Biological Assessment of Porous Ti-6Al-4V Lattices**

Part of this chapter has been published in the Journal of the Mechanical Behavior of Biomedical Materials as: Zena J Wally, Abdul M Haque, Antonio Feteira, Frederik Claeysens, Russell Goodall and Gwendolen C Reilly, “Selective Laser Melting processed Ti-6Al-4V lattices with graded porosities for dental applications”. *J. Mech. Behav. Biomed. Mater.* 90, 20–29. A full copy of this publication is available in the appendix, 9.2.

### **5.1 Introduction**

Implant materials aim to support cell attachment by creating appropriate surfaces for cell adhesion (Rosales-Leal et al., 2010). Titanium and its alloys are commonly used in dental implant applications, due to the capability of the bone cells to firmly attach and grow on surfaces made from these materials. Ti-6Al-4V contains an anti-corrosion protective oxide layer that provides a desired biological surface for bone growth (Cheng et al., 2014). Cell behaviour has been shown to be affected by the characteristic features of the implant. Porous titanium surfaces offer enhanced osteoblast attachment, cell proliferation and extracellular matrix formation (Elias et al., 2008). Porosity provides a higher surface area which encourages more bone cells to attach compared to a dense surface, this, in turn, enables bone ingrowth into the implant material and improves bone-implant integration (Cheng et al., 2014). A high surface area eliminates early micromotion of implants (de Vasconcellos et al., 2010) which promotes fibrous tissue rather than osseointegration and causes initial instability (Ramírez Fernández et al., 2017). Interconnected porosity also helps blood vessel formation, transport of nutrients (Wysocki et al., 2016) and bone-to-implant contact; for metallic implants this would tend to generate a mechanical modulus which is closer to that of bone compared to traditional bulk implants (Yoshikawa et al., 2009). A graded porous architecture has

also been suggested to offer the potential to improve bone cell ingrowth (van Grunsven, 2014). However, there is no clear identification of the optimum pore geometry for bone ingrowth. As can be seen, pore parameters such as size, shape and the overall amount of porosity have been shown to play a vital role in bone cell ingrowth (Rosales-Leal et al., 2010). This necessitates using a processing method able to produce appropriate porosity in a metallic biomaterial, as achieving both the required biological and mechanical properties is essential for implant applications.

Excellent bone ingrowth into porous titanium implants was observed in several *in vitro* and *in vivo* experiments using different manufacturing techniques to fabricate porous titanium. Additive manufacturing, including EBM and SLM, have been increasingly considered as economically viable techniques to fabricate challenging structures (Koike et al., 2011). With SLM, dental and orthopaedic implant prototypes have been developed with irregular complex pore geometries by melting Ti powder microparticles using a focused laser beam according to a computer-generated three-dimensional design (Tolochko et al., 2002, Mullen et al., 2009 and Moin et al., 2013).

However, with SLM processed cellular structures a risk might arise related to removal of unmelted powder particles that can be toxic to cells (Wysocki et al., 2016). Different techniques have been suggested to remove the unmelted particles from the porous components using chemical or electrochemical methods.

Though a variety of methods are used for cleaning additively manufactured metal lattices such as sandblasting, chemical polishing and ultrasonic cleaning, it is not clear if all loose particles are entirely removed. Moreover, there is another concern with the biological response of released non-melted materials such as Ti-6Al-4V. Such metal particles have been a problem as they might be released into the body and possibly be

toxic to cells. The amount of unfused Ti-6Al-4V particles removal post-processing, the cytotoxic effect of Ti-6Al-4V particles on bone cells and the optimal pore structure for bone cell ingrowth remain to be elucidated. In chapter 4 we showed that Ti-6Al-4V scaffolds could be printed with a range of regular and graded porosity, however the affect on bone growth was unknown and needs to be evaluated.

## **5.2 Aim**

This chapter aims to evaluate the biological performance of the SLM Ti-6Al-4V component lattices fabricated as described in section 4.3.1.2 with different pore geometries. The following objectives were addressed:

1. Estimate the amount and diameter of the unfused Ti-6Al-4V particles removed from the built component using an ultrasonic cleaning bath over a series of cleaning periods (15 mins, 30 mins, 1, 2, 4, 8, 16, 32, 64 and 128 hours).
2. Determine whether there was a cytotoxic effect of the of micro Ti-6Al-4V powder particles used for the SLM process on two types of bone cells, MLO-A5 and hBMSCs.
3. Investigate and compare the ability of SLM Ti-6Al-4V lattices with different designs (P400, P400/1C, P650, P650/1C, GP/650-400 and 'Spider Web') to support bone cell growth and extracellular matrix deposition using MLO-A5 cells.

## **5.3 Methods**

### **5.3.1 Ultrasonic cleaning of components and measurement of unfused particles released**

To estimate the amount of loose Ti-6Al-4V particles that can be removed from the built components, ten samples (5 × 30 mm) of one design (P400) were used as a 'case study'. Samples were placed in 50 ml centrifuge tube containing 15 ml distilled water and washed several times in an ultrasonic bath cleaner. A series of cleaning periods (15

mins, 30 mins, 1, 2, 4, 8, 16, 32, 64 and 128 hours) were used with the same samples. After each cleaning period, samples were transferred to a new centrifuge tube after drying in air at room temperature. As the ultrasonic cycle creates heat energy over long hours of cleaning and to provide consistent heat environment, the maximum temperature (65 -75 °C) reached was used for all cleaning periods. After suspending the particles in water, 15 µl from each tube was added to a hemocytometer in triplicate. Microscope images were taken for each cleaning period. The images were analysed in Image J software by measuring the average number of particles on four corner squares of the hemocytometer and diameter of the loose Ti-6Al-4V particles after each cleaning time (Figure 5.1).

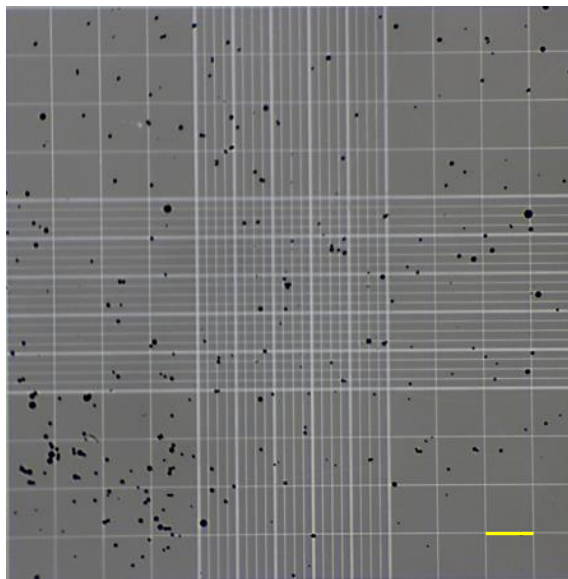


Figure 5.1 Representative image under a light microscope showing particle distribution (black dots) on squares of the haemocytometer, scale bar=250 µm.

### **5.3.2 Cytotoxicity analysis of Ti-6Al-4V particles on bone cells growth**

A cell viability test based on metabolic activity was performed to evaluate the cytotoxic effect of micro Ti-6Al-4V powder particles used for the SLM process on two types of bone cells, namely, MLO-A5 and primary hBMSCs. Different concentrations (2.5, 5, 7.5, 10, 25, 50 and 100 mg/ml) of Ti-6Al-4V particles were used and compared. To

prepare Ti-6Al-4V particles for cell culture, they were dispersed in PBS in an autoclavable container and autoclaved for 30 minutes at 121°C. Before cell exposure to particles, cells were cultured in monolayer in a 12-well plate at density 10,000 for MLO-A5 and 20,000 for hBMSCs per well with 1 ml cell culture medium (Figure 5.2). After 24 hours standard incubation the culture media was removed and replaced with new culture media containing Ti-6Al-4V particles of different concentrations per well (2.5, 5, 7.5, 10, 25, 50 and 100 mg/ml), as a final concentration. After directly subjecting cells to Ti-6Al-4V particles, the metabolic activity of cells was evaluated at day 1, 4 and 7 for MLO-A5 cells and at day 1, 4, 7 and 14 for hBMSCs cells using the RR metabolic activity assay as described in section 3.7.6. Different wells were used for each time-point to ensure the particles remained in the culture. Osteogenic and non-osteogenic media were used and compared for hBMSCs cells. To permit cell differentiation, a selective sub group of hBMSCs cells were incubated with osteogenic media for 7 days before exposing them to Ti-6Al-4V particles. The passage number used for MLO-A5 was 42-45 and hBMSCs was 1-2. Media were changed every 2-3 days during the experimental process. Percentage of cell viability was calculated using the equation 5.1:

$$\text{Cell viability (\%)} = (A - B / C - B) \times 100 \quad 5.1$$

where A is the average of the treated group, B is the average of the blank and C is the average of the control group (Luo et al., 2017).

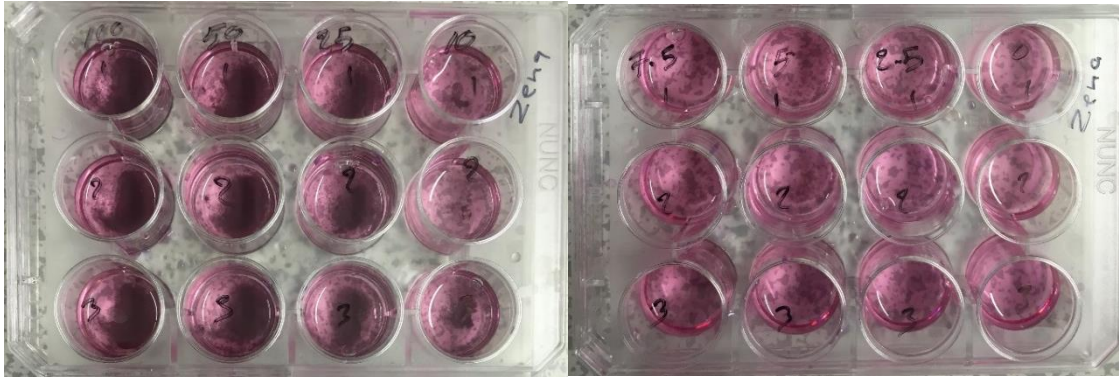


Figure 5.2 Photograph of well plates used for *in vitro* 2D cytotoxicity test of Ti-6Al-4V microparticles used for two types of bone cells (MLO-A5 and hBMSCs).

### 5.3.3 Cell culture on SLM Ti-6Al-4V lattices

Resazurin reduction assay is one of the most well-known tools for assessing cell viability *in vitro* cell culture on biomaterials. Initially, a 2D standard curve was made on a series of known cell numbers to confirm that the assay was linear and to estimate the suitable concentration and incubation time for testing Ti-6Al-4V lattices. MLO-A5 cells were seeded directly onto well plates at 2,500, 5,000, 10,000, 20,000 and 40,000 in triplicate in 2ml of BCM. Three negative controls were also used. The cells were incubated overnight to allow full cell attachment and then incubated in of resazurin-containing medium as described in section 3.7.6. The fluorescence of each density was plotted against the seeding density (Figure 5.3). This curve was used to estimate the number of cells attached to the tested titanium lattices. This based on the linear equation (5.2) below.

$$y = a x + b \quad 5.2$$

where  $y$  is the fluorescence intensity,  $a$  and  $b$  are constant obtained from the standard curve and  $x$  is cell number.

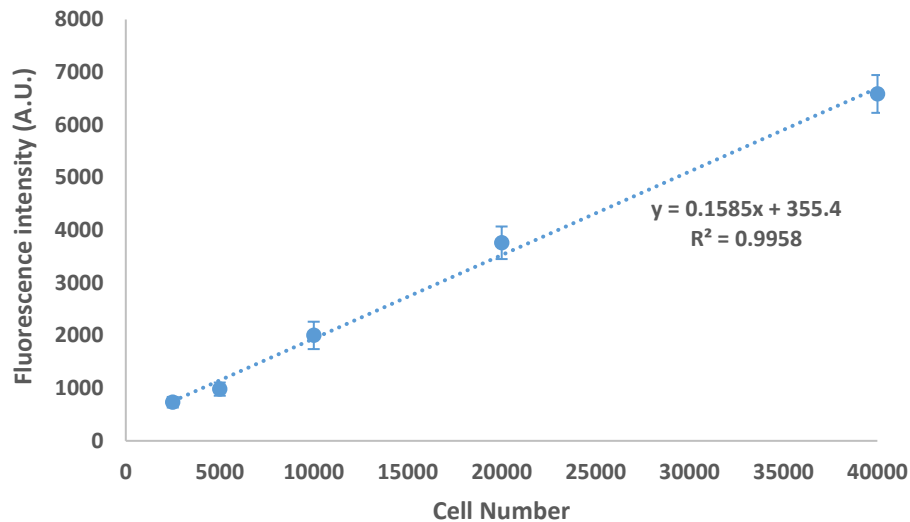


Figure 5.3 Cell viability standard curve of 2D cell culture on different cell numbers. Points represent mean  $\pm$  SD, n=6.

To prepare Ti-6Al-4V lattices for cell culture work, they were cut into  $5 \times 7$  mm (diameter  $\times$  height) cylinders as described in section 3.4.1. In an autoclavable bag, samples were autoclaved at  $121^{\circ}\text{C}$  for 30 minutes prior to cell seeding. After cooling at room temperature, they were submerged in culture medium for 30 minutes with incubation at  $37^{\circ}\text{C}$  and 5%  $\text{CO}_2$  humid environment to allow protein attachment onto the surface of the scaffolds. Expansion media was aspirated and replaced with a seeding suspension of 2,500 cells in 25  $\mu\text{l}$  expansion media on both sides of the scaffolds. MLO-A5 cells were seeded into the scaffolds by a ‘drop’ method (directly pipetting on the small volume) in an untreated 24 well plate with 45 minutes incubation for each side of the scaffold to permit cell attachment; negative controls (immersed in media but without cells) were also used. 2mls of EM were added to each scaffold and incubated overnight. The passage number of cells used for experiments was between 44 -50. Media was changed every 2-3 days during the experiment period. The next day, scaffolds were transferred to a new well plate and cultured in supplemented medium for the rest of the experiment. Cell viability after seeding was assessed over six different time points (day

1, 4, 7, 14, 21 and 28) using RR metabolic activity assay as described in section 3.7.6. At the end of the experiment, scaffolds were fixed with 10% formalin for 30 min and kept in PBS prior to calcium and collagen deposition analysis using ARS Stain Assay and SR Stain Assay, respectively as described in section 3.7.7 and 3.7.8. SEM with EDX was used to observe and analyse cell layers on the titanium scaffolds after 28 days of cell culture (Section 3.3.1); the fixed cells were dehydrated with an ethanol gradient as described in section (3.7.10).

## **5.4 Results**

### **5.4.1 Removal of Unfused Ti-6Al-4V Powder Particles from SLM Processed Components**

#### **5.4.1.1 The number of loose particles significantly reduced with time 2h post cleaning.**

The highest number of particles of Ti-6Al-4V particles released was observed between 1 and 2 hours of cleaning in an ultrasonic bath. After that, the number started to decrease gradually with increasing cleaning time as shown in figure 5.4 (A). Interestingly, even after many hours of cleaning (128 hr), there were still a few particles observed as shown in figure 5.4 (B).



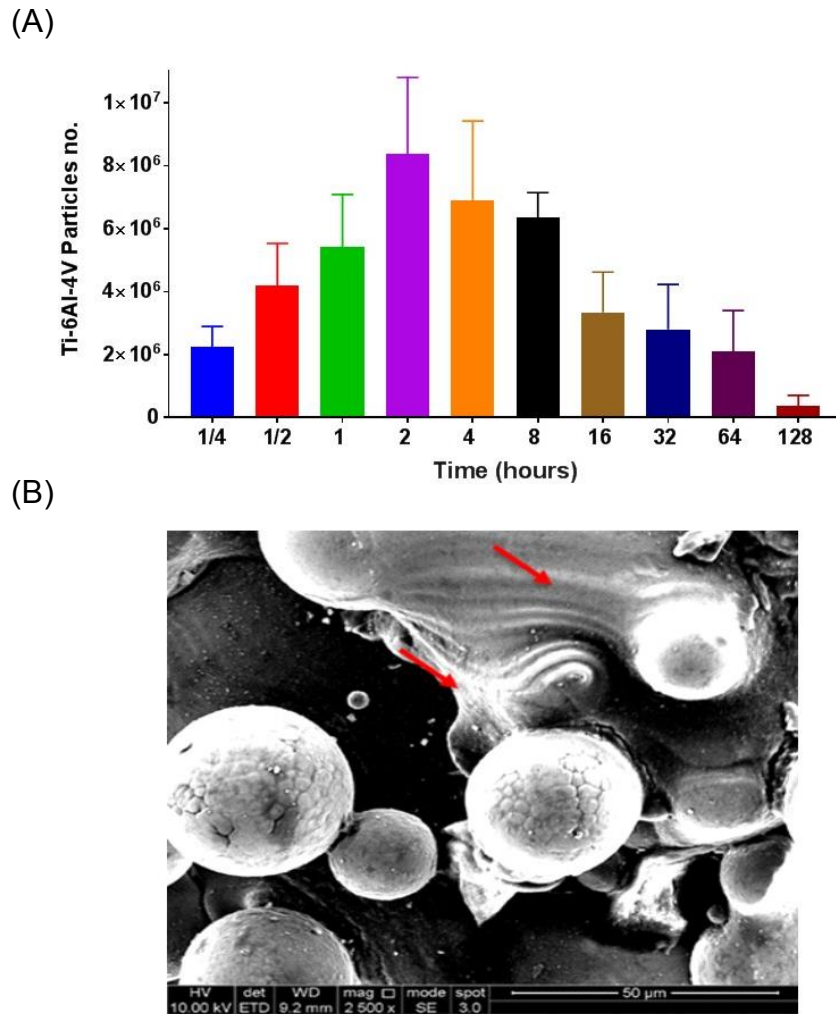


Figure 5.4 (A) Number of Ti-6Al-4V particles released from SLM Ti-6Al-4V lattices after different cleaning periods (15, 30 mins and, 1, 2, 4, 8, 16, 32, 64 and 128 hours) in an ultrasonic bath. (B) SEM image reveals partially fused particles in the SLM Ti-6Al-4V lattices after the longest cleaning time.

#### 5.4.1.2 Particles ranged 15-25 micron were the highest at all cleaning periods

There were no significant differences in the diameter of Ti-6Al-4V particles after ultrasonic cleaning at all cleaning periods. The majority of particles released after each cleaning time ranged from 15-25 microns in diameter. In contrast the particles in the size range from 45-55 microns were present in the lowest proportion in all groups (Figure 5.5).

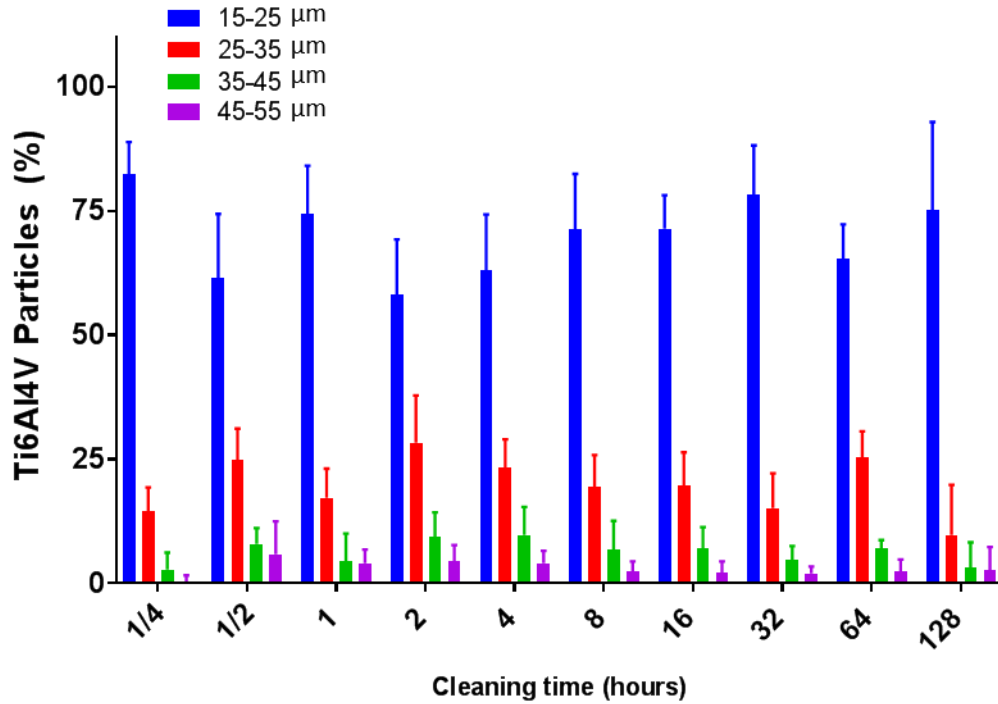


Figure 5.5 Percentage of Ti-6Al-4V particles at each diameter range ( $\mu\text{m}$ ) released from SLM Ti-6Al-4V lattices after different cleaning periods (15, 30 mins and 1, 2, 4, 8, 16, 32, 64 and 128 hours) in an ultrasonic bath.

#### 5.4.1.3 The average mass of total particles release form 30 mm Ti-6Al-4V lattices was about 30 mg.

The mass of released particles obtained after defined cleaning periods increased from 15 minutes cleaning to reach the highest point after two hours then the mass of particles decreased gradually with increasing cumulative cleaning time (Figure 5.6 (A-B)). By 32 hours about 92% of the particles were removed as shown in the cumulative graph (Figure 5.6 (B)). The total mass of Ti-6Al-4V particles released in all periods was evaluated by the summation of the mass of the particles from each period. The average total Ti-6Al-4V particle mass was about 31 mg as shown in right bar chart (Figure 5.6 (C)).

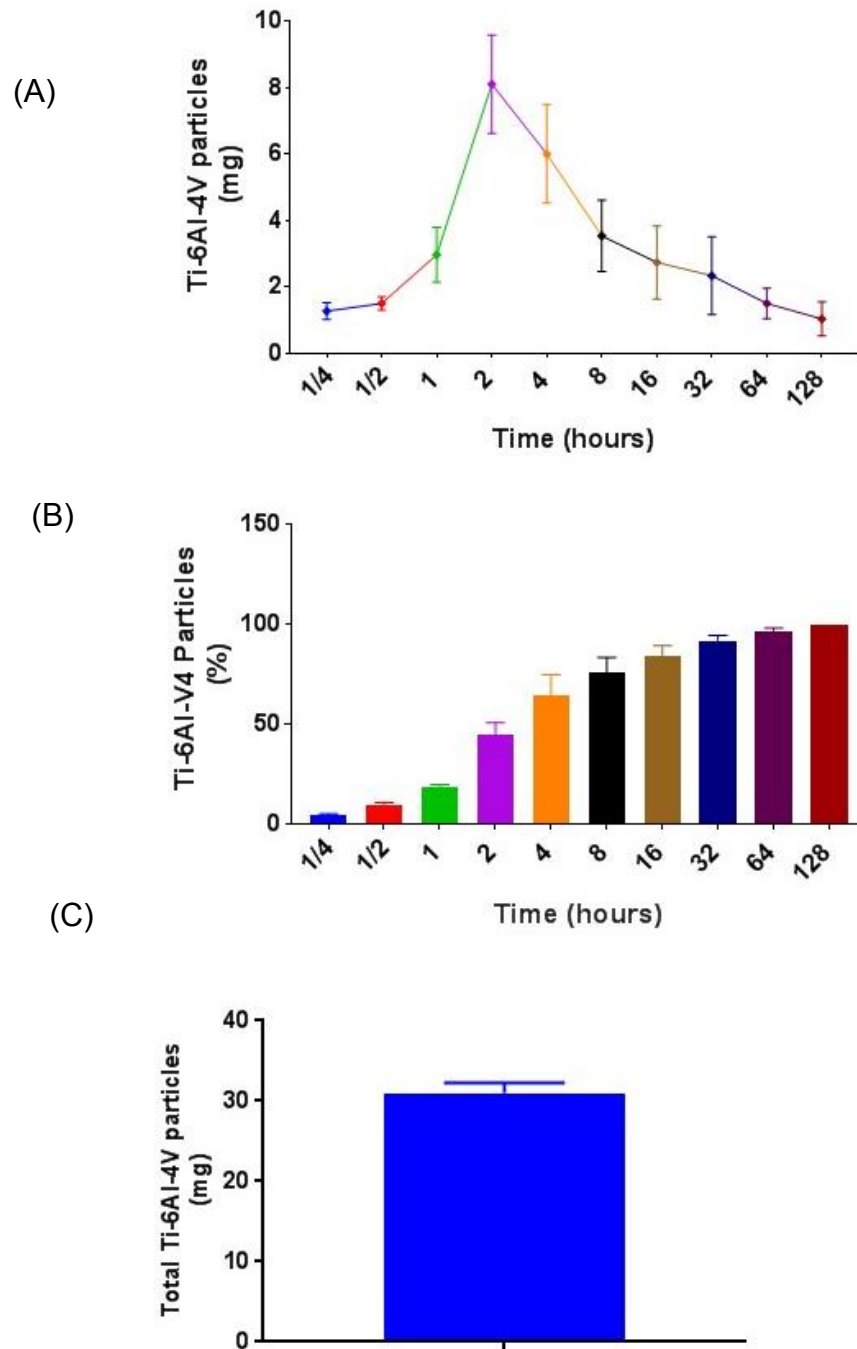


Figure 5.6 (A): Mass (mg) of Ti-6Al-4V particles released from SLM Ti-6Al-4V lattices after different cleaning periods (1/4, 1/2, 1, 2, 4, 8, 16, 32, 64 and 128 hours) in an ultrasonic bath. (B): Percent of Ti-6Al-4V particles released from SLM Ti-6Al-4V lattices at each cleaning period. (C) An average of total mass of Ti-6Al-4V particles collected from all cleaning periods (n=3).

## **5.4.2 Cytotoxicity**

### **5.4.2.1 No toxic effect of Ti-6Al-4V particles up to 10 mg/ml on MLO-A5**

The results of the cytotoxicity of MLO-A5 cells due to direct exposure to Ti-6Al-4V microparticles at different time intervals are shown in figure 5.7. Generally, the fluorescence intensity of MLO-A5 cells increased significantly over time at all particle doses (2.5, 5, 7.5, 10, 25, 50 and 100 mg/ml). Cell viability with Ti-6Al-4V particles of more than 25 mg/ml was relatively lower at day 3 of cell culture. However, the cell viability recovered from this dip by day 7 as shown in figure 5.7 (A). Cell viability of below 50% was seen by day 3 for concentrations more than 25 mg/ml; then this was increased by day 7 to be between 60-90 % (Figure 5.7 (B)). There was no significant variation in cell viability % at each time point with Ti-6Al-4V particles less than 10 mg/ml in comparison to high doses which were mostly reduced by day 3 and improved by day 7 as shown in figure 5.7 (C). Images under the light microscope were taken which also confirmed MLO-A5 cell growth at different concentrations (0, 2.5, 5, 7.5, 10, 25, 50 and 100 mg/ml) of Ti-6Al-4V powder particles over 7 days as shown in figure 5.8.

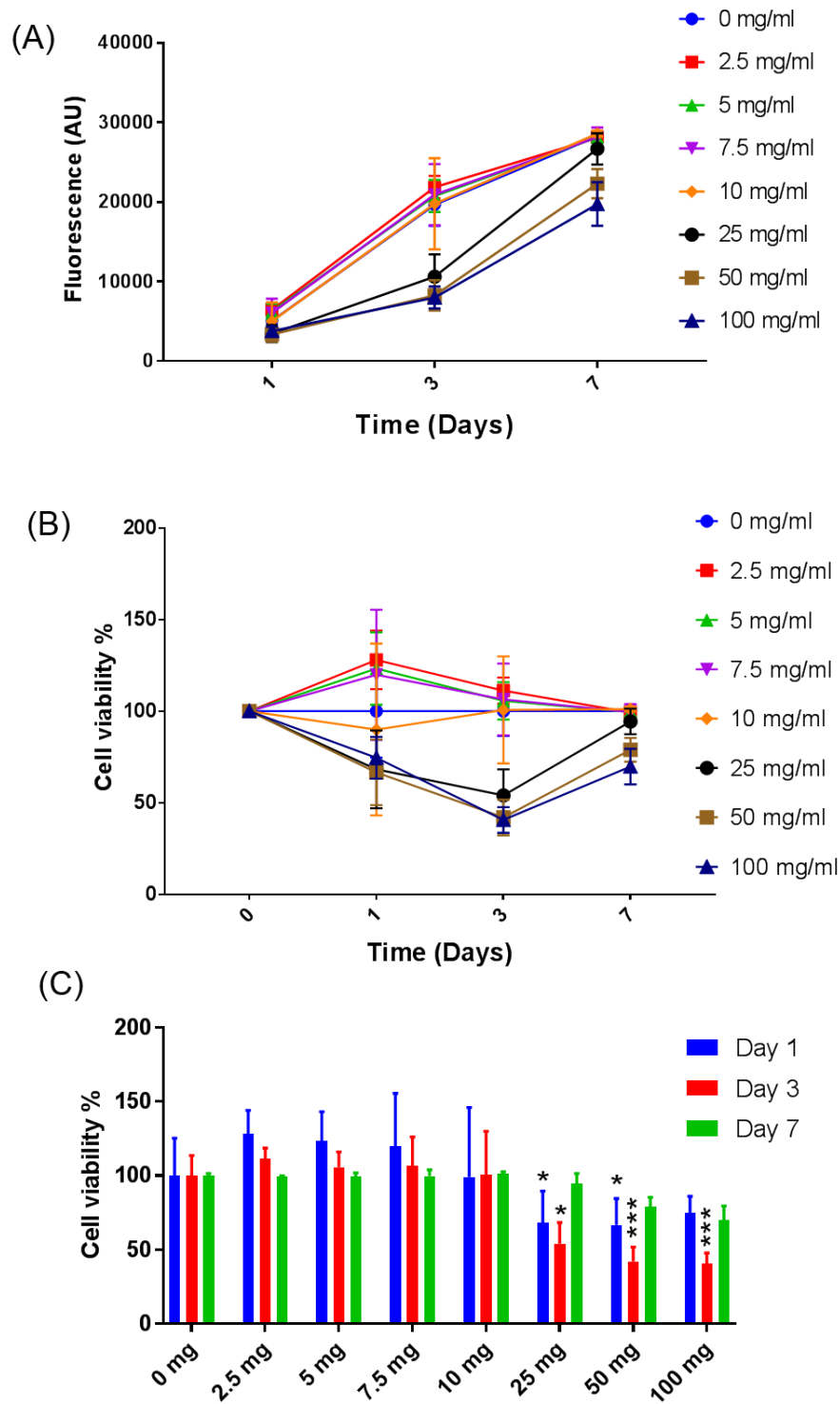


Figure 5.7 Cytotoxicity of Ti-6Al-4V micro particles with different concentrations (0, 2.5, 5, 7.5, 10, 25, 50 and 100 mg/ml) on the metabolic activities of MLO-A5 cells seeded on 2D well plate over 7 days in respect of (A) fluorescence value of RR to time, (B) relative viability to time and (C) relative viability to the mass of particles. These data are expressed as the means  $\pm$  SD of three independent experiments performed in triplicate (n=9).

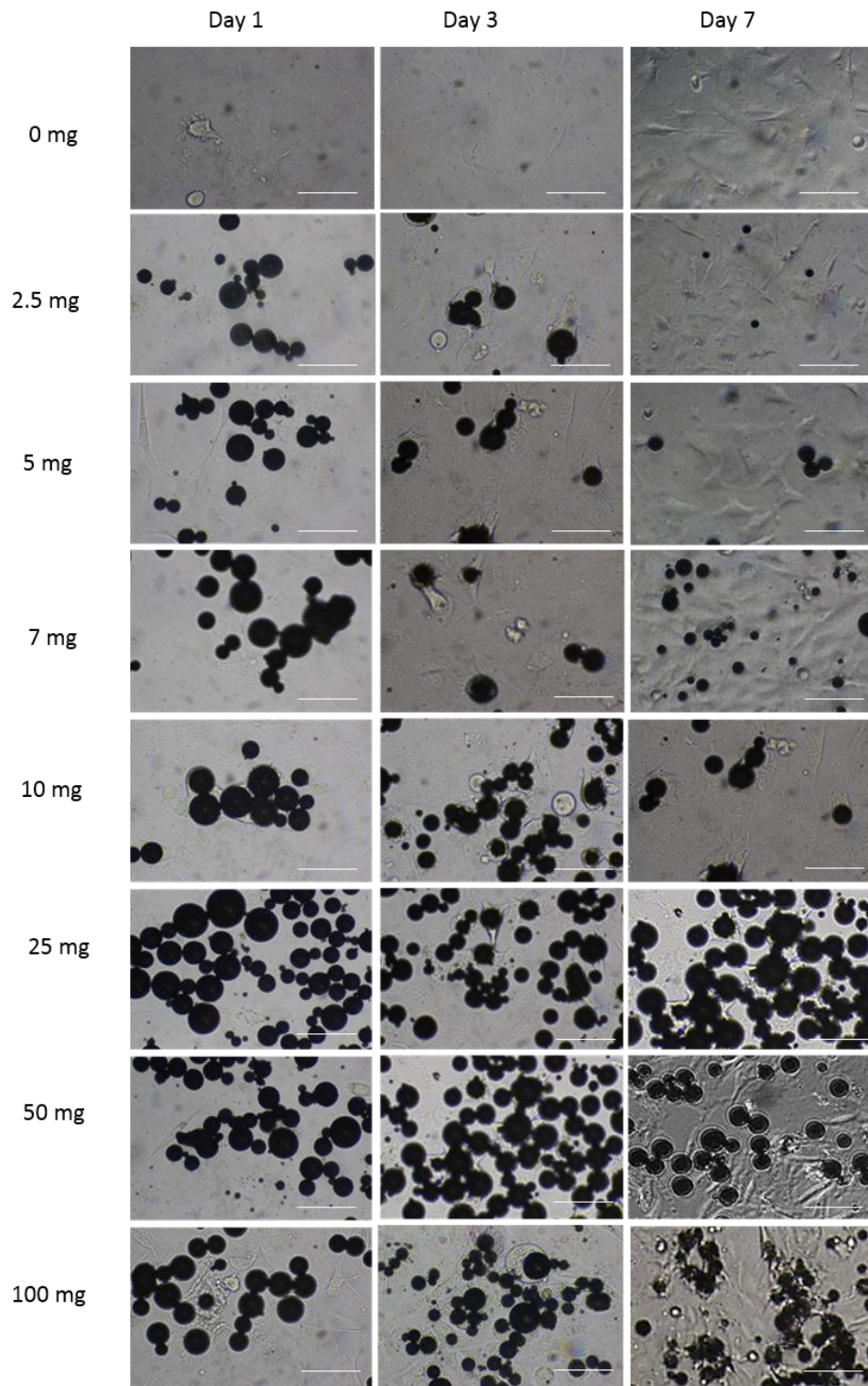


Figure 5.8 Representative images under light microscope showing MLO-A5 cell growth on a 2D well plate with different concentrations (0, 2.5, 5, 7.5, 10, 25, 50 and 100 mg/ml) of Ti-6Al-4V powder particles after day 1, 3 and 7, scale bar= 100  $\mu$ m.

#### **5.4.2.2 No toxic effect of Ti-6Al-4V particles up to 10 mg/ml on hBMSCs cells**

The results of cytotoxicity of Ti-6Al-4V microparticles with all tested concentrations (2.5, 5, 7.5, 10, 25, 50 and 100 mg/ml) on hBMSCs cells at different times are shown in figure 5.9. In general, cell viability of hBMSCs cells with all particle doses increased considerably over 14 days of cell culture. The metabolic activity of cells with Ti-6Al-4V particles less than 25 mg/ml showed higher values by day 14 of cell culture as shown in figure 5.9 (A). Relative viability for concentrations of less than 25 mg/ml decreased slightly at day 7 then recovered by day 14 to be similar to control group (cells without particles) as shown in figure 5.9 (B). Cell viability with higher particle concentrations (more than 25 mg/ml) was slightly increased at day 1 of cell culture. However, this was reduced by day 3 as shown in figure 5.9 (C). There was no significant variation in cell viability as a percentage to the control with Ti-6Al-4V particles less than 10 mg/ml at each time point in comparison to those with particles more than 10 mg/ml as shown in figure 5.9 (C). Images under a light microscope also confirmed hBMSCs cell growth over 14 with different concentrations (0, 2.5, 5, 7.5, 10, 25, 50 and 100 mg/ml) of Ti-6Al-4V powder particles (Figure 5.10).

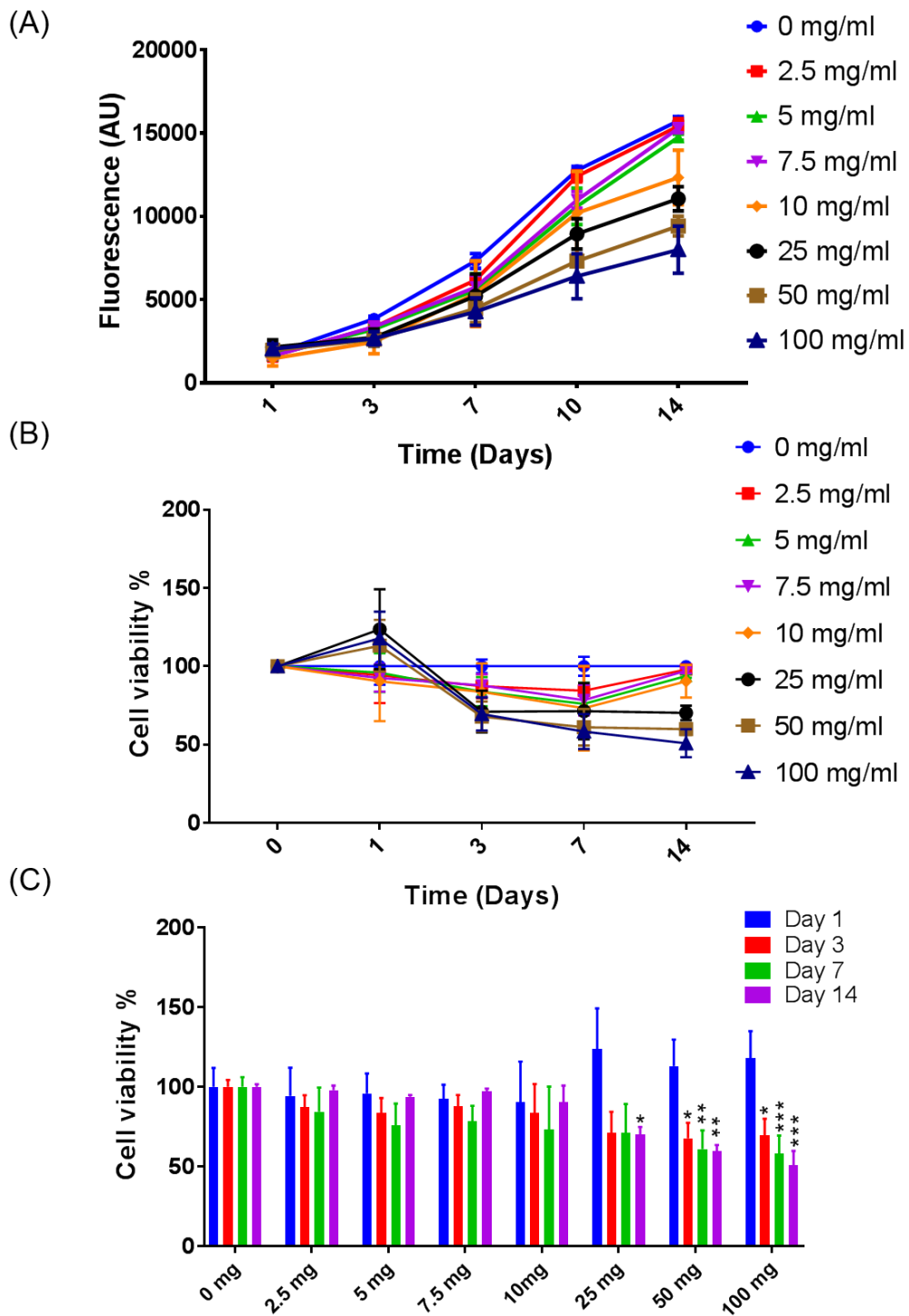


Figure 5.9 Cytotoxicity of Ti-6Al-4V micro particles with different concentrations (0, 2.5, 5, 7.5, 10, 25, 50 and 100 mg/ml) on the metabolic activities of hBMSCs cells seeded on 2D well plate over 14 days in respect of A= fluorescence value of RR, B= relative viability to time and C= relative viability to mass of particles. These data are expressed as the means  $\pm$  SD of three independent experiments performed in triplicate for (n=9).



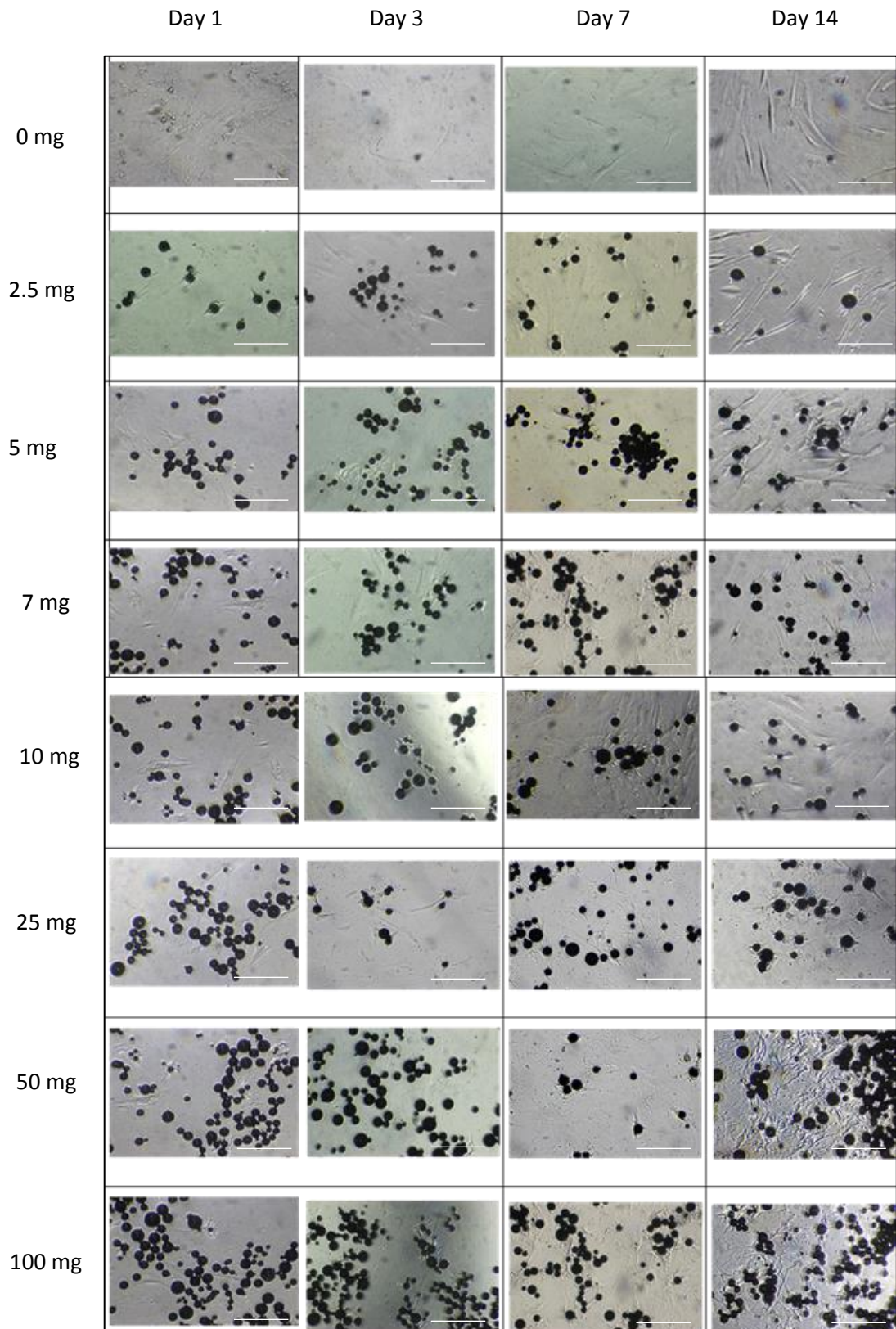


Figure 5.10 Representative images under light microscope showing hBMSCs cells growth on 2D well plate with different concentrations (0, 2.5, 5, 7.5, 10, 25, 50 and 100 mg/ml) of Ti-6Al-4V powder particles after day 1, 3, 7 and 14, scale bar = 100  $\mu$ m.

### **5.4.2.3 No toxic effect of Ti-6Al-4V particles up to 10 mg/ml on hBMSCs cells with OGM**

Generally, the results of the metabolic activities of hBMSCs cells exposed to Ti-6Al-4V microparticles with different concentrations (2.5, 5, 7.5, 10, 25, 50 and 100 mg/ml) with OGM (supplemented with  $\beta$ GP, AA-2P and Dex) were similar to the previous results obtained without OGM media. It can be seen that the fluorescence intensity significantly increased from day 3 to day 14 for cells with Ti-6Al-4V particles less than 10 mg/ml as seen in figure 5.11 (A). The viability of cells with particles more than 25 mg/ml declined significantly after day 3 to be less than 50% by day 14 (Figure 5.11 (B)). There were no significant differences in cell viability % with Ti-6Al-4V particles less than 10 mg/ml at all time points, in contrast to those exposed to particles more than 10 mg/ml)). The viability of cells with particles more than 25 mg/ml was high at day 1 of cell culture compared to low dose groups, though this was decreased by day three as shown in figure 5.11 (C). Images under the light microscope also confirmed hBMSCs cells growth with OGM over 14 days with different Ti-6Al-4V powder particles concentrations (0, 2.5, 5, 7.5, 10, 25, 50 and 100 mg/ml) as shown in figure 5.12.

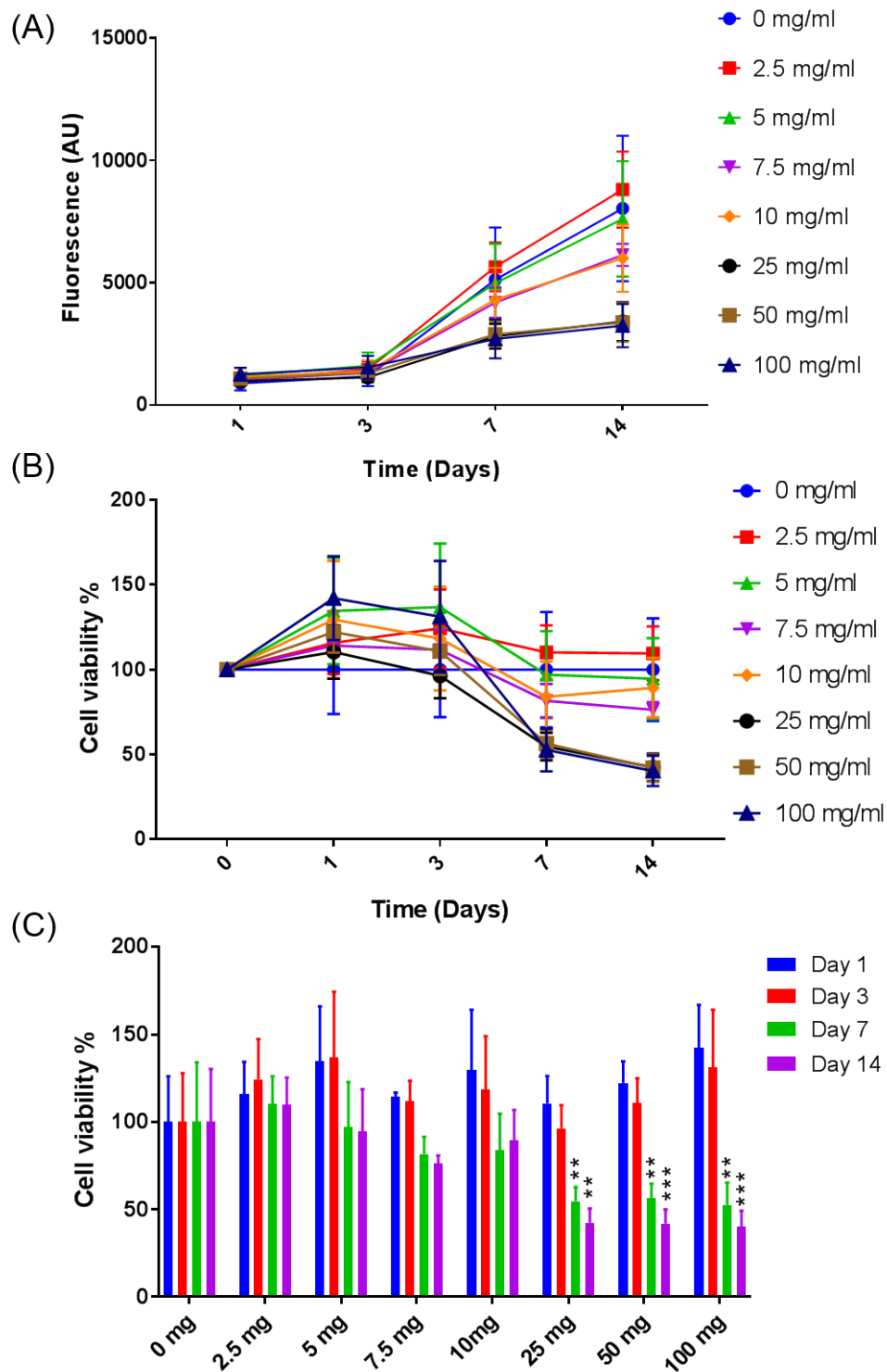


Figure 5.11 Cytotoxicity of Ti-6Al-4V micro particles on hBMSCs cells precultured with OGM at different concentrations (0, 2.5, 5, 7.5, 10, 25, 50 and 100 mg/ml). Metabolic activity of cells seeded on 2D well plate over 14 days measured by RR assay. (A) fluorescence value, (B) relative viability to time and (C) relative viability to mass of particles. These data are expressed as the means  $\pm$  SD of three independent experiments performed in triplicate for (n=9).

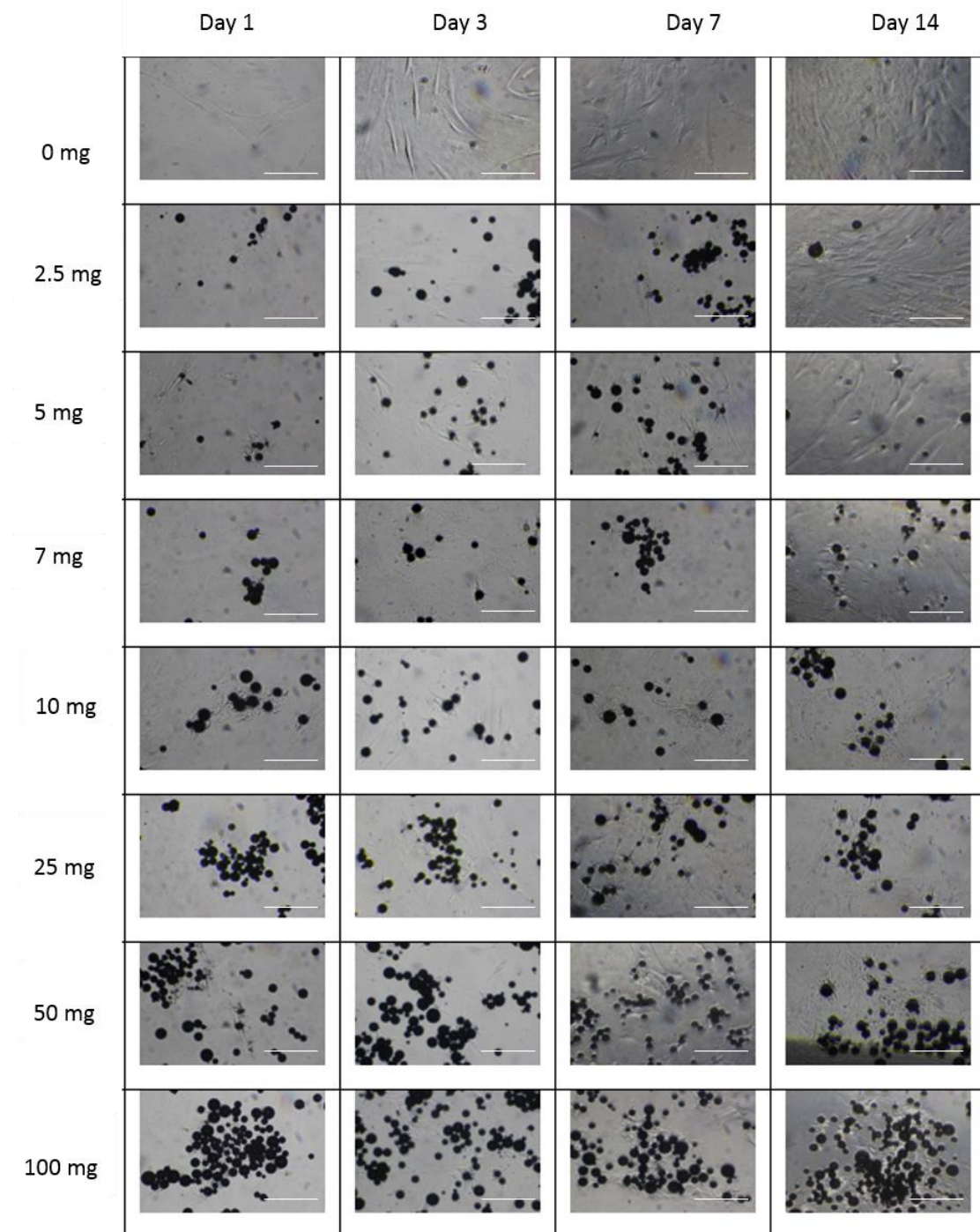


Figure 5.12 Representative images under light microscope showing hBMSCs cell growth on 2D well plate with OGM and different concentrations (0, 2.5, 5, 7.5, 10, 25, 50 and 100 mg/ml) of Ti-6Al-4V powder particles after day 1, 3, 7 and 14, scale bar = 100  $\mu$ m.

### 5.4.3 Cell culture on Ti-6Al-4V scaffolds

#### 5.4.3.1 SLM Ti-6Al-4V scaffolds supported cell viability of MLO-A5 cells over 28 days of cell culture

The preliminary results of cell culture on P400, P400/1C, P650, P650/1C, GP/650-400 and ‘Spider Web’ showed that attachment of MLO-A5 cells across scaffolds was comparable (Figure 5.13 (A)). In general, osteoblast cells were viable in all the porous scaffolds during the 28 days of cell culture. The metabolic activity of the cells increased steadily from day 4 to day 7 in all tested scaffolds without significant differences at each time point as shown in figure 5.13 (B). Interestingly, the results indicate that large pore sizes (650 microns) do not enhance cell growth and confirm that any pore size between 250 and 650 microns is a desirable surface for bone cell ingrowth.

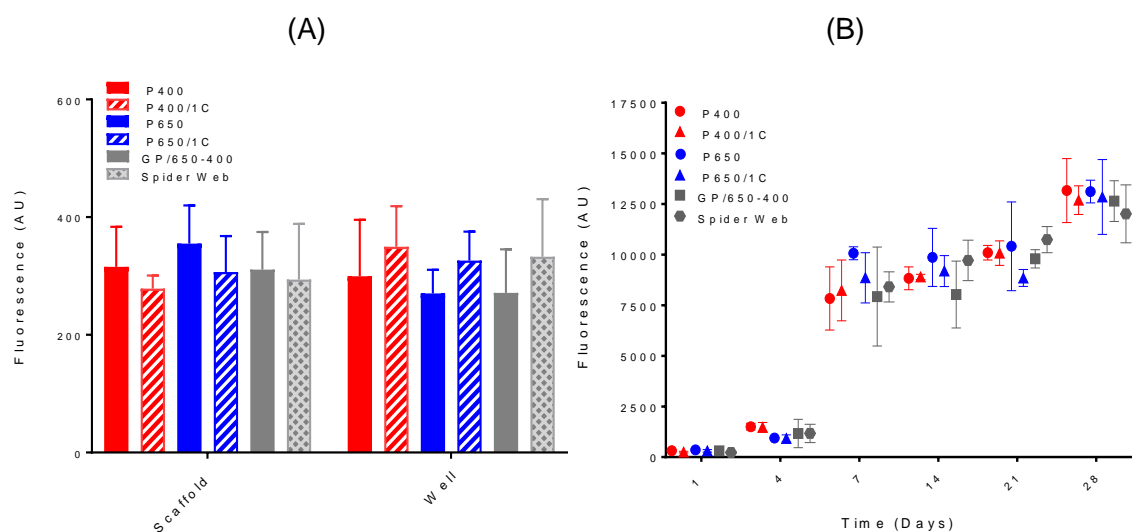


Figure 5.13 Mean  $\pm$  SD of preliminary results of resazurin fluorescence as a measure of (A) cell attachment at day 1 and (B) metabolic activity of MLO-A5 cells on P400, P400/1C, P650, P650/1C, GP/650-400 and ‘Spider Web’ scaffolds over 28 days of cell culture, (n=6).

A comparable result was found with the cell attachment and viability of osteoblast cells with the P400, P400/1C, P400/2C, GP400-300 and ‘Spider Web’ scaffolds (Figure 5.14

(B-C)). They all support MLO-A5 cells growth with no significant variability between scaffolds over the experiment period. Close inspection under a light microscope of the ‘Spider Web’ scaffolds after 28 days of cell seeding indicated that cells were covering most parts of the porosity, as shown by the yellow arrows in figure 5.14 (A).

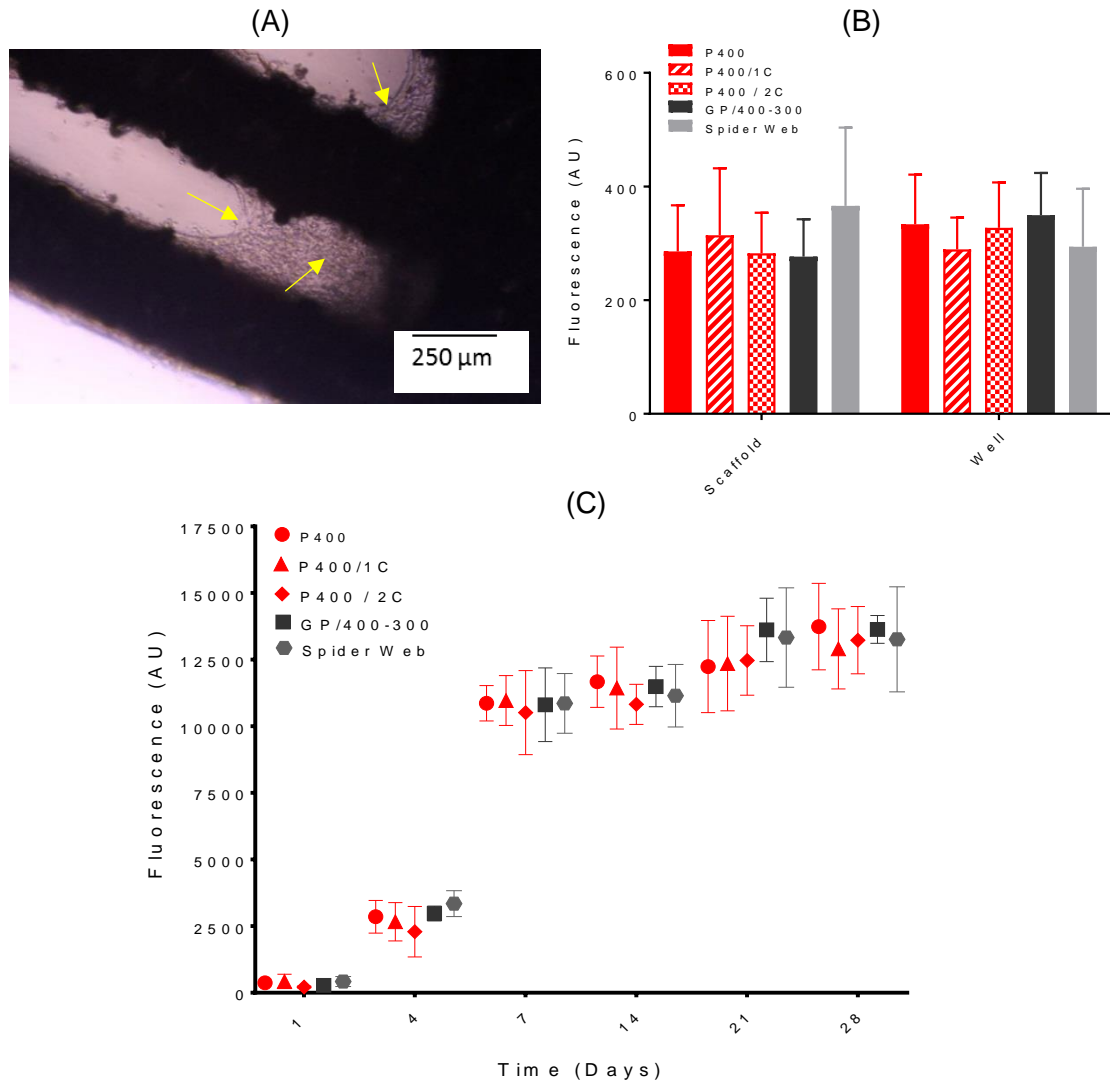


Figure 5.14 Yellow arrows on light microscopic image show MLO-A5 cells attachment on ‘Spider Web’ scaffold after 28 days (A). Mean  $\pm$  SD of resazurin fluorescence as a measure of (B) cell attachment and (C) metabolic activity of MLO-A5 cells on P400, P400/1C, P400/2C, GP/400-300 and ‘Spider Web’ scaffolds over 28 days of cell culture, (n=9).

### 5.4.3.2 Calcium and collagen staining

After 28 days of cell culture, the ability of Ti-6Al-4V scaffolds to support bone-matrix deposition was investigated. Calcium and collagen matrix staining using alizarin red and Sirius red, respectively, were used initially on P400, P400/1C, P650, P650/1C, GP/650-400 and ‘Spider Web’ then on P400, P400/1C, P400/2C, GP/400-300 and ‘Spider Web’ scaffolds. Photographic images of the titanium scaffolds after calcium and collagen staining indicated good deposition mineral and collagen extracellular matrix as shown in figure 5.15.

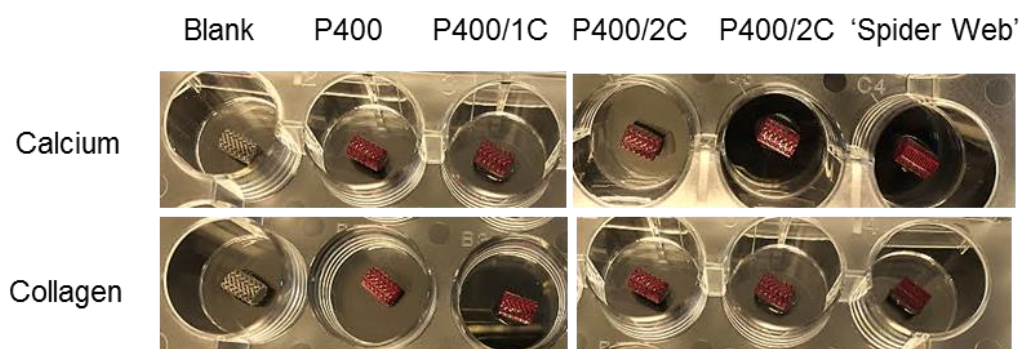


Figure 5.15 Day 28 Calcium and collagen staining before destaining on P400, P400/1C, P400/2C, GP/400-300 and ‘Spider Web’ scaffolds seeded with MLO-A5 cells.

A quantitative analysis by Alizarin red absorbance after destaining scaffolds showed that all titanium scaffolds supported mineral production. Values of mineralisation on cell seeded P400 scaffolds were significantly higher than that on spider web scaffolds as shown in (Figure 5.16 (A)) and (Figure 5.17 (A)).

A comparable result was found for collagen staining, where all scaffolds support extracellular matrix production. Though, there were no significant differences between the seeding groups (Figure 5.16 (B)) and (Figure 5.17 (B)).

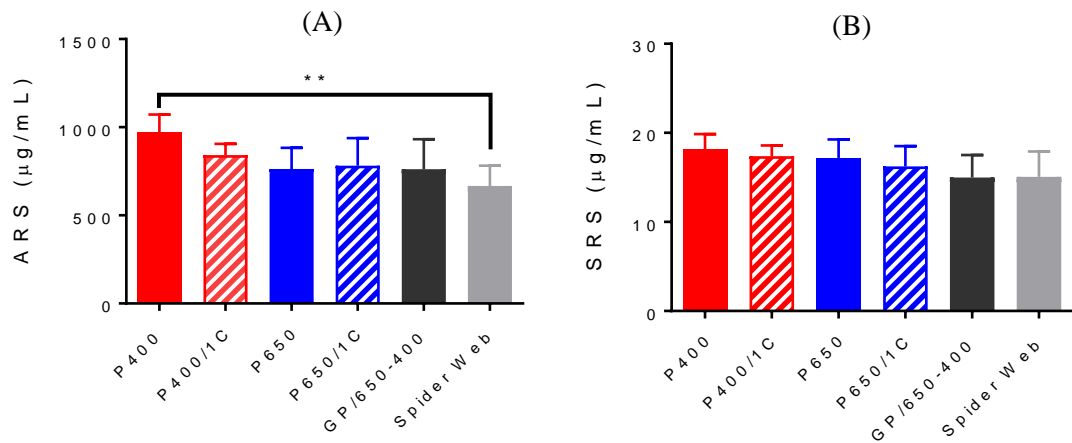


Figure 5.16 Mean  $\pm$  SD for (A) ARS staining of MLO-A5on P400, P400/1C, P650, P650/1C, GP/650-400 and ‘Spider Web’ scaffolds (B) SR staining on day 28 of cell culture, (n=6).

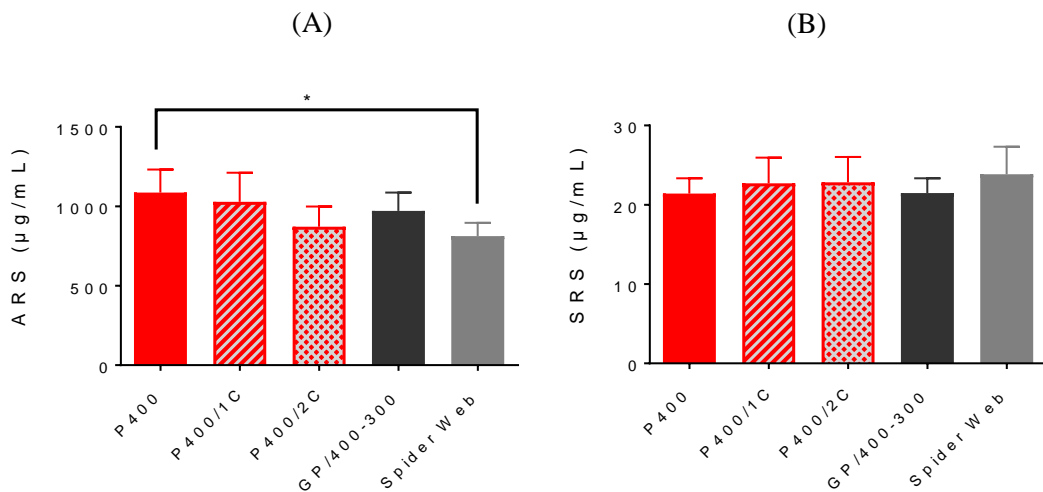


Figure 5.17 Mean  $\pm$  SD for (A) ARS staining of MLO-A5on P400, P400/1C, P400/2C, GP/400-300 and ‘Spider Web’ scaffolds (B) SR staining on day 28 of cell culture, (n=9).



### **5.4.3.3 Scanning electron microscopy**

SEM images of titanium lattices after 28 days of cell culture, showed organic deposition of mineralised matrix sheets produced by MLO-A5 cells (Figure 5.18). Comparable cell morphologies were found on all Ti-6Al-4V lattices and integrated through the surfaces of porosity. Dense sheet-like depositions of the matrix covered the partially fused Ti-6Al-4V powder particles and followed the geometry of the entire porosity. Several mineralised nodules were seen as bright areas at low magnification on porous scaffolds. Analysis by EDX of several spectra on Ti-6Al-4V lattices confirmed the presence of calcium and phosphorous elements beside Ti, Al and V as shown in figure 5.19, indicating that SLM Ti-6Al-4V lattices are desirable surfaces for osteoblast cell attachment, proliferation and extracellular matrix production.

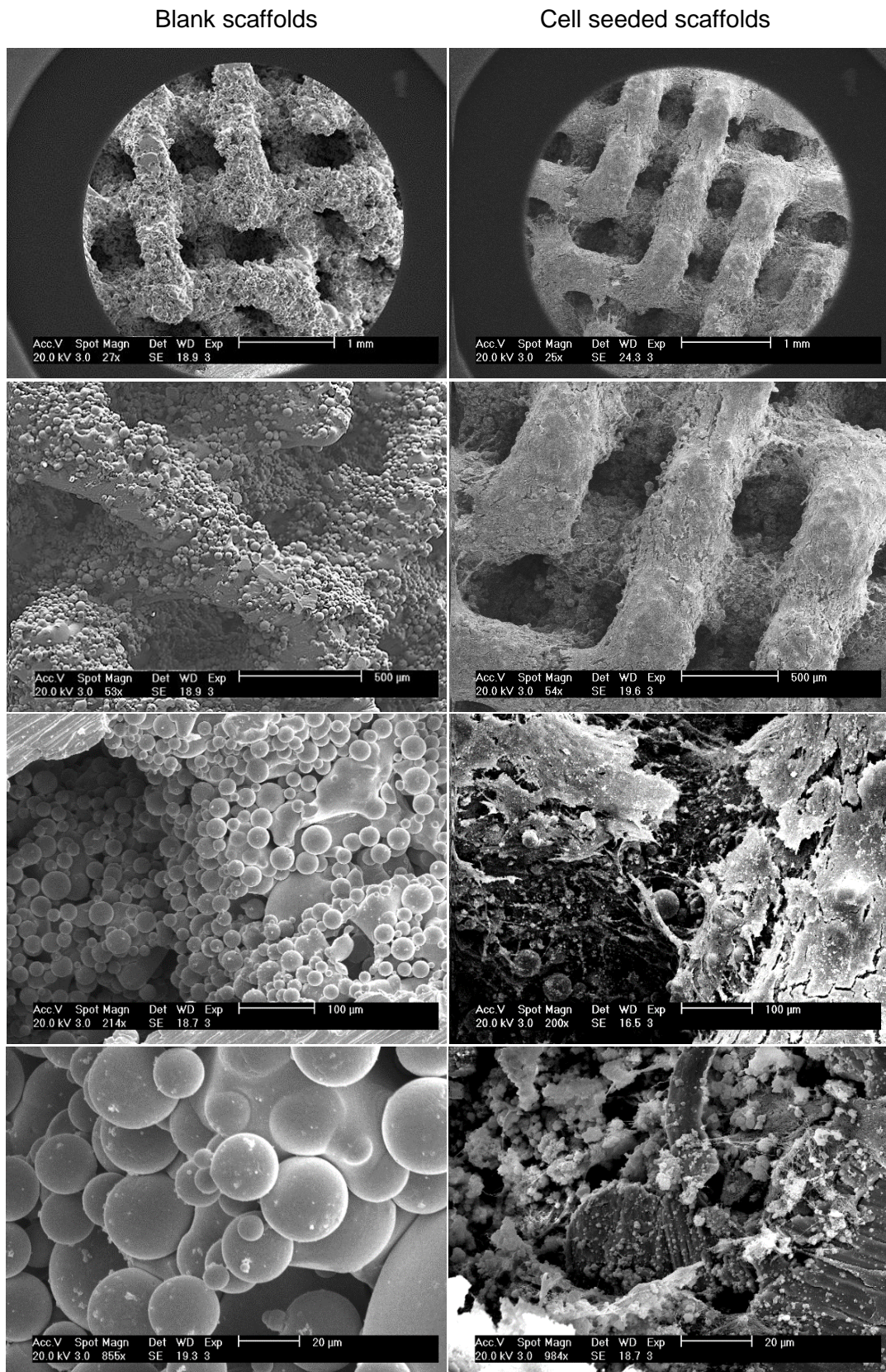
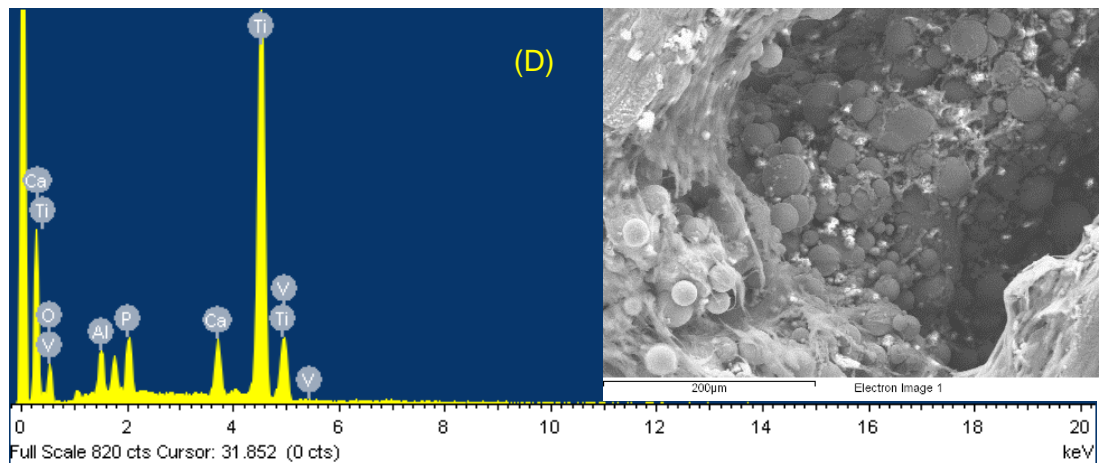
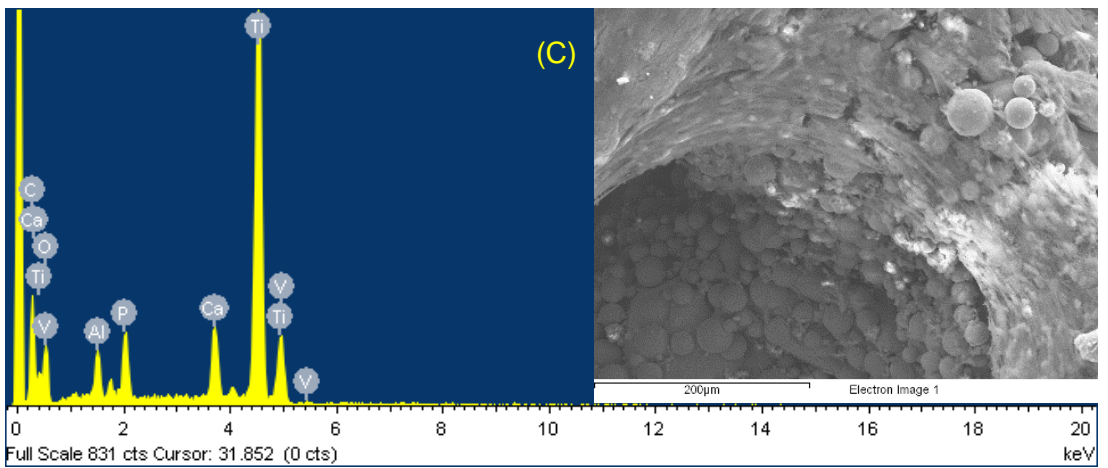
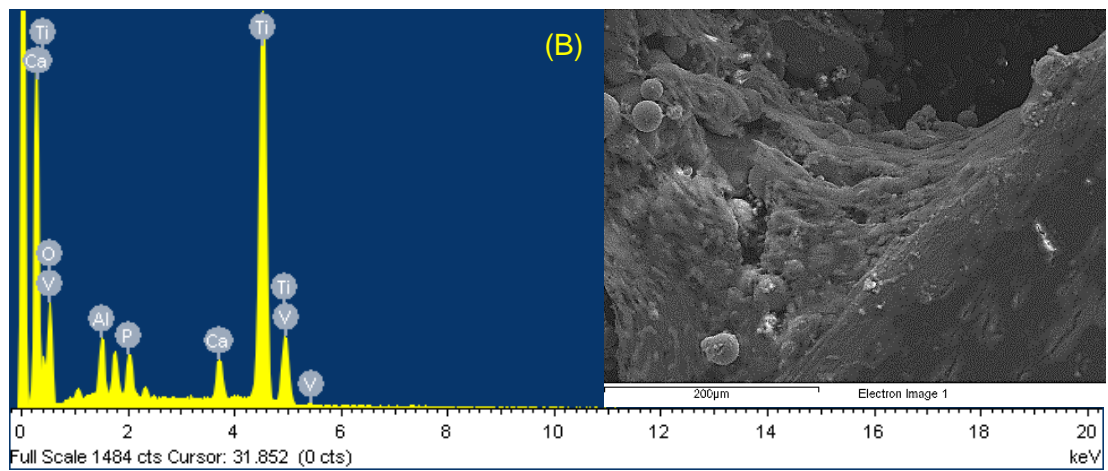
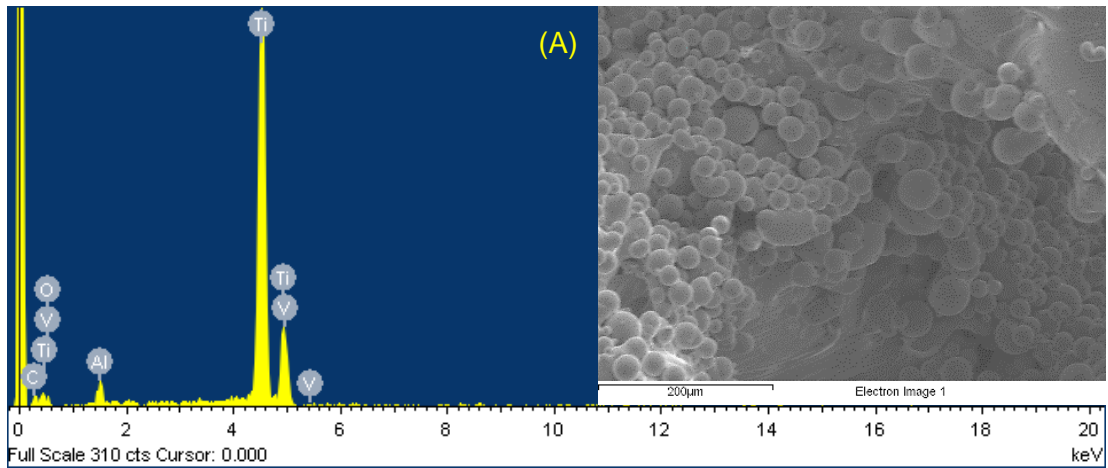


Figure 5.18 Representative SEM images of scaffolds only (left) and MLO-A5 cells on P400 after 28 days of cell culture using different scale bars (1000, 500, 100 and 20 µm). The scaffold surface is covered with cellular material.



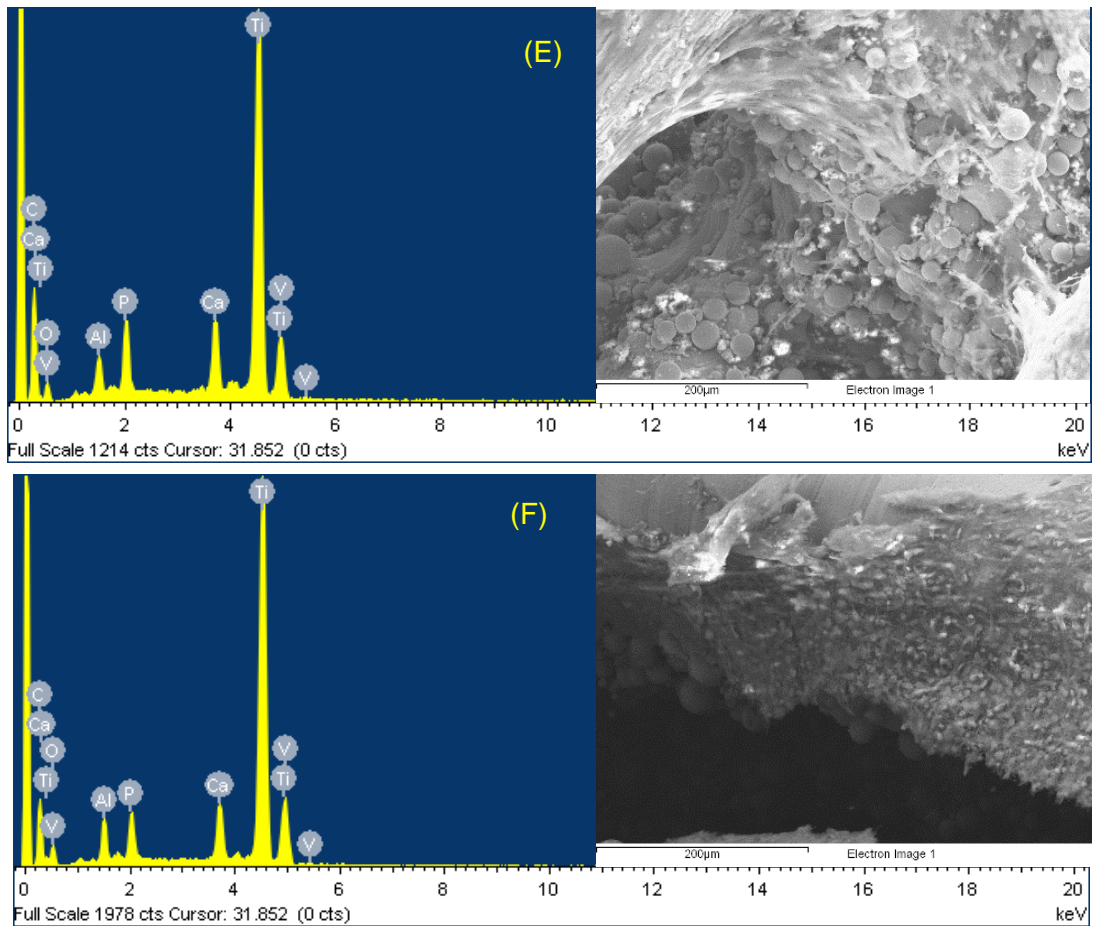


Figure 5.19 EDX spectrum analysis of carbon coated Ti-6Al-4V components (A) blank P400 and the extracellular matrix deposition produced by MLO-A5 cells on cell seeded (B) P400, (C) P400/1C, (D) P400/2C, (E) GP/400-300 and (F) spider web after 28 of cell culture. The result of EDX shows the presence of the calcium and phosphorous beside Ti-6Al-4V elements, scale bar 200  $\mu\text{m}$ .

## **5.5 Discussion**

Currently, with the increasing interest of 3D porous titanium as an effective candidate for bone ingrowth into dental and orthopaedic implants, several pore geometries have emerged which potentially enhance bone ingrowth and implant stability, created using different advanced manufacturing methods. However, these methods have the risk that loosely attached particles, inherent to the processing route, could detach in the body and potentially be toxic to cells. An initial objective of this stage of the project was to evaluate the removal of unfused Ti-6Al-4V particles from the SLM built components using ultrasonic cleaning over a series of cleaning periods (15 min, 30 min and 1, 2, 4, 8, 16, 32, 64 and 128 hours). Hence we investigated the cytotoxic effect of Ti-6Al-4V particles used for SLM process in different concentrations (2.5, 5, 7.5, 10, 25, 50 and 100 mg/ml) on growth of two types of bone cells, MLO-A5 and hBMSCs which represent the cell type likely to encounter the implant early in the osseointegration process. Then the biocompatibility of an approximately cylindrical shape of SLM Ti-6Al-4V components with different pore designs (P400, P400/1C, P400/2C, P650, P650/1C, GP/650-400, GP/400-300 and 'Spider Web') was evaluated using MLO-A5 cells.

Selective laser melting is considered to be an exceptional processing method for metallic biomaterials such as titanium and its alloys, due to its feasibility for producing complex porous geometries in a one step process. However, the presence of the unmelted powder particles within the post built porous structures could be harmful (Wysocki et al., 2016). Structural characterisation of SLM porous titanium used in our study also exposed unfused Ti-6Al-4V microparticles within the structures as described in section 5.4.1. Powder removal analysis in this study provided an estimation of the number and mass of particles released from the Ti-6Al-4V lattices after different

cleaning periods in an ultrasonic bath. Ultrasonic cleaning was able to induce particle removal over time, continuing up to long time periods. The average mass of total particles released from 30 mm Ti-6Al-4V lattices was found to be about 30 mg. However, the weight of particles versus the weight of the lattice (as the amount of material in a certain volume could vary enormously for different lattices). The smallest particles ranged from 15-25 micron and were present in the highest number after all cleaning periods. To the best of knowledge, this is the only study that has provided a simple way to evaluate the mass and diameter of the unmelted Ti-6Al-4V microparticles from the SLM porous components using long durations (128 hours) of ultrasonic cleaning. Different cleaning methods have been reported to remove unfused powder particles from the post-build porous structures. Some of these trials focused on chemical and electrochemical approaches rather than the conventional post-processing (machining or vibro-abrasive machining). Polishing with chemicals such as hydrofluoric acid or hydrofluoric/nitric acid solutions was used for cleaning 3D printed porous titanium (Wysocki et al., 2016). The cleaning efficacy was found to be influenced by the concentration and composition of these acids. However, these acids are very dangerous and toxic chemicals and might negatively affect surface quality (Łyczkowska et al., 2014). Other important practical implications are pore size and unit cell morphology which were shown to influence the cleaning process. For example, powder particles were effectively removed from samples with cubes and 400–420  $\mu\text{m}$  porosity using ultrasonic cleaning (Łyczkowska et al., 2014). Whereas particle trapping was reported within the components of a 600  $\mu\text{m}$  pore size and hexagon unit cell after polishing (Hasib et al., 2015). This indicates that the removal of unmelted powder particles from the SLM built component is still restricted and dependant on the cleaning method and pore geometry. These results showed that about 92% of particles were

removed by 32 hours cleaning in the ultrasonic bath, however even after 128 hours a few particles continued to be released indicating it is difficult to fully remove all particles with this cleaning method. This leads to the importance of the toxicity examination of particles.

The cell cytotoxicity of MLO-A5 and hBMSCs cells due to the direct exposure to different concentrations (2.5, 5, 7.5, 10, 25, 50 and 100 mg/ml) of Ti-6Al-4V particles was performed to observe any possible impact on the cell behaviour. These concentrations were chosen because they are higher than what one would expect the concentration would be in the body especially if the structure was cleaned well as recommended above, however it is important to find the “worst case scenario” of how a high concentration would affect cells and also identify whether there was a threshold above which the particles become toxic. Our results indicated that the cell viability of both bone cells used was not influenced with Ti-6Al-4V particles up to 10 mg/ml at each time point of cell culture. In contrast to the viability of cells with particles more than 25 mg/ml exposed inhibited cell growth by day 3 of cell culture, however this was recovered by day 7 to be not significant in comparison to the control (cells without particles). The difference is likely due to inhibition of proliferation rather than direct toxicity as the overall metabolic activity of the cells was still increased between day 1 and 3. However, the Resazurin assay does not directly measure cell death so the lower relative number of cells at day 3 could be related to a combined effect of the cell death and inhibition of proliferation. This could be related to the presence of a high amount of aluminium and vanadium with higher Ti-6Al-4V particle concentrations which may inhibit cell proliferation. There is an apprehension concerning the biological response of vanadium and aluminium containing materials which directs many researchers to test the effect of the ionic release on bone cell behaviour. The high amount of vanadium and

aluminium has been suggested to be a risk for cell toxicity (Velasco-Ortega et al., 2010), but it is not known if these ions would be released into the media in this time scale. For future work, it is important to measure ion concentration in the media at the different particle doses. Although titanium-based alloys including Ti-6Al-4V have been considered as biomaterials for medical applications, in recent research aluminium and vanadium have been shown to cause toxic effects on cell viability and tissue in some *in vitro* and *in vivo* studies (Velasco-Ortega et al., 2010).

The higher cell attachment at day 1 compared to control (no particles) could be related to the higher surface area provided by the particles. The recovery of cell viability at day 7 could be due to the formation of a protective TiO<sub>2</sub> layer over a period of time. This would be in agreement with the study by Chandar *et al.*, 2017, their results showed a significant decline in cytotoxicity of commercially pure titanium and its alloy Ti-6Al-4V to the human gingival fibroblast cells. They attributed this reduction to the TiO<sub>2</sub> production over time (Chandar et al., 2017). While bone cells used in our study were not affected by low doses of Ti-6Al-4V particles, white blood cells might be, so in the body there still could be an inflammatory reaction which we were not able to test here.

Various studies have assessed the effect of pore morphology of porous components on the biological response to osteoblast cells. Pore size of less than 200 µm were recommended by most of these to improve attachment and bone deposition. In contrast to the other studies, they suggested a larger pore size with regular morphology for enhanced bone ingrowth. The current study aimed to examine the biological response to highly regular Ti-6Al-4V lattice structures with designated pore sizes (250, 300, 400 and 650 µm). SLM was chosen to produce Ti-6Al-4V lattices due to its ability to produce controllable and regular pore sizes. Although titanium and its alloys have been reported to be bioinert and biocompatible materials for orthopaedic and dental implant



applications (Stevenson et al., 2016), it is essential that constructs from these materials produced via advanced manufacturing technology are assessed for biofunctional properties. These structures may have characteristics different to bulk implants such as higher surface area and particle release.

In *in vitro* cell culture on P400, P400/1C, P400/2C, GP400-300 and ‘Spider Web’ designs showed that osteoblastic cells readily attached to porous Ti-6Al-4V. Implants with rough surfaces have been shown to stimulate osteoblast cells attachment (Mour et al., 2010), and proliferation as stated by Karageorgiou and Kaplan (Karageorgiou and Kaplan, 2005). The metabolic activity of cells significantly increases over 28 days of cell culture (figure 4.13), likely due to a large surface area which promotes cell proliferation, and subsequent extracellular matrix production. Stevenson et al. examined the potential of osteosarcoma cells (MG63) and primary human osteoblast cells to proliferate and mineralise on titanium surfaces with different porosities (Slotwinski et al., 2014). In that study, fine surface coatings supported less mineralisation than coarse surfaces. Interconnected porosity has also been shown to induce the attachment and proliferation of bone cells (Soon et al., 2011) such as a graded porous structure of different materials HA-CaCO<sub>3</sub>-Ti with macro- (100-350  $\mu\text{m}$ ), micro- (0.2–90  $\mu\text{m}$ ) and nano-(100 nm) porosity which stimulated bone formation (Fu et al., 2011). Current study shows no significant variation in cell viability when comparing scaffolds with different pore size, shape and percentage. However, the pore sizes are all within the broad range recommended in the literature where it is not easy to define ‘optimum’ pore size, within the structures we produced. This result is in agreement with Cheng et al., where even with the high metabolic activity of osteoblasts (MG63 cells) that has been observed on porous titanium constructs with average pore diameter 177, 383 and 653  $\mu\text{m}$ , there were no differences shown among variant scaffolds (Cheng et al., 2014).

Nevertheless, Markhoff et al. evaluated the metabolic activity of human osteoblast cells on porous titanium scaffolds with cubic, pyramidal and diagonal basic structures under static and dynamic culture. They reported a significantly higher metabolic cell activity on pyramidal basic structure scaffolds with 400-620  $\mu\text{m}$  pore size and 75% porosity with no significant differences between static and dynamic culture conditions (Markhoff et al., 2015). In another *in vitro* observation, human osteoblasts cells were cultured on direct laser formed Ti-6Al-4V porous scaffolds with 500, 700 and 1000  $\mu\text{m}$  pore size, after 14 days of cell culture cells covered most of the pores with 500  $\mu\text{m}$  pore size. While the pore size of 700 and 1000  $\mu\text{m}$  formed a circular-shaped growth pattern around the pore walls (Hollander et al., 2006). Our results were different from what was found in the above-mentioned studies; this could be related to their pore structures, which had greater differences than what we used or that their cells were more sensitive to pore size. Additionally, the assay used in this study to measure metabolic activity of cells did not directly measure the number of cells, although there is nothing to suggest metabolic activity would be affected by the structural differences since the chemistry is the same.

Overall, all scaffolds supported calcium and collagen formation indicating their suitability to support bone ingrowth; scaffolds with P400 exhibiting the highest calcium deposition. This could be related to the high surface area which provides more spaces to deposit mineralized matrix. Pore sizes between 100 and 400  $\mu\text{m}$  are suggested for bone mineralisation (Ryan et al., 2006). Our study showed no effect of pore size and shape on matrix production by MLO-A5. As can be observed the effect of pore size on matrix growth is not straightforward and is probably governed by contributing factors such as roughness or pore wall size or structure and nutrient accessibility. Frosch et al. have also demonstrated that collagen production is not influenced by the pore size (over

the range 300-1000  $\mu\text{m}$ ) of titanium scaffolds (Frosch et al., 2004). In contrast to our study indicating no effect of pore shape; within the structures used by Markhoff et al. collagen formation was significantly less supported on diagonal compared to cubic and pyramidal structures (Markhoff et al., 2015). Based on present results, all Ti-6Al-4V scaffolds were shown to sustain MLO-A5 cell viability and mineralisation. MLO-A5 cells have been described as a typical post-osteoblast phenotype and are able to produce a honey-comb like a mineralized matrix in sheets. However, MLO-A5 are prone to proliferate rapidly and produce much matrix (Rosser and Bonewald, 2012), so may be less able to discriminate and less representative of adult human osteoblasts. Further *in vitro* experiments can be performed to investigate the behaviour of these scaffolds with primary cells.

## **5.6 Chapter summary**

1. The continued removal unfused Ti-6Al-4V particles from the built component was found even after long cleaning hours in an ultrasonic bath. Approximately 92% of particles had been released by 32 hours of cleaning.
2. The majority of particles released for each cleaning period ranged from 15-25 microns in diameter.
3. There were no toxic effects of micro Ti-6Al-4V powder particles up to 10 mg/ml on the growth of two types of bone cells, MLO-A5 and hBMSCs.
4. All SLM Ti-6Al-4V structures strongly supported cell growth and mineralised matrix deposition which was not affected by pore size except that the maximum calcium deposition was seen on scaffolds with 400-micron pores.

## Chapter 6 : *In vitro* 3D Culture Model for Testing 3D Printed Porous Dental Implant

### 6.1 Introduction

In recent years, several surface treatments and new implant designs have been introduced to improve dental implant osseointegration. All surface modifications have been aimed at stimulating bone cell differentiation and matrix deposition in the bone healing process following implant insertion. Preceding clinical applications, all new surface properties have to be biologically validated for their effects on bone-implant integration. For this purpose, testing protocols are used to assess several new biomaterials, which should initially be tested in *in vitro*, then in *in vivo* animal testing to determine their effectiveness.

Two-dimensional (2D) *in vitro* cell culture is one of the most well-known tools for testing implant materials. Even though monolayer culture is currently used in biological research to study the molecular mechanisms of cell differentiation and proliferation, there is a limitation that it is unable to correlate with the *in vivo* bone environment (Tortelli and Cancedda, 2009). Additionally, this method is not capable of replicating the complex geometry and dynamic environment of native tissue and unable to examine the interactions at the bone-implant interface. Moreover, the signals that direct cellular processes are lost when cells are growing in two dimensions (Zanoni et al., 2016). Furthermore, *in vivo* animal testing is an essential step to validate the obtained *in vitro* analysis before clinical applications in human.

Animal models are the currently available 3-dimensional tests for evaluating bone-implant interactions for orthopaedic and dental implants. Goats, sheep, dogs (Sivolella et al., 2015) and rats (Figure 6.1) are widely used animal models in implant research due to their biological responses to external substances being comparable to that of

human beings (Semenoff-Segundo et al., 2015). These implants are inserted surgically into the holes or cuts made in an animal's bone and implanted over a period of time. Subsequently, animals are sacrificed, and implants are extracted and tested histologically and biomechanically, for example bone density measurements, removal torque tests, push-out and pull-out tests to determine the value of force or torque required to separate the implant from the bone. However, this kind of approaches carries various well-known limitations, such as animals are lost at the end of the test, and the laws that restricts using animals for scientific experiments (Parliament and Union, 2010). Although animal models are capable of replicating many aspects of the complex human environment, the biological behaviour and structure of human and animal cells can be different, especially in terms of age, genetic variability, diet and previous exposure to environmental damage. Moreover, such tests are not cheap, it is costly and time-consuming to offer care, diet and housing for the animals during the experiment. The limitations associated with the use of animal testing have motivated the development of an *in vitro* 3D bone model for human-specific and eventually patient-specific testing in recent years.



Figure 6.1 Image shows dental implant placing into the mandible of Wistar male rat, Adapted from (Semenoff-Segundo et al., 2015).

The use of three-dimensional (3D) structures loaded with bone cells in bone tissue engineering for regenerative purposes holds substantial benefits such as the 3D bone system may provide more physiologically relevant information, and data prediction for *in vivo* experiments (Edmondson et al., 2014). *In vitro*, 3D bone models could be used in cancer research since bone is recognised as the preferred site of breast cancer metastasis (Chen et al., 2010 and Holen et al. 2015). This system could also be a way of understanding the mechanisms between bone and implant materials. It is therefore likely that such a model possibly be an alternative to the costly conventional animal studies for testing new implant designs. However, such a model requires scaffold materials that are easy to fabricate and capable of supporting bone matrix deposition. To our knowledge, an ideal *in vitro* 3D bone model has not yet been developed for implant testing. A trial has been reported by Sivoletta et al., (2015), blocks of natural carbonated hydroxyapatite of bovine origin seeded with adipose-derived stem cells (ADSCs) were used to implant dental implants for 30 days using osteo-endothelial cultured media. These blocks were found able to replicate the osseointegration process *in vitro*. After implant removal, there was an osteoblast morphology on the surface of implants. Pull-out tests were also performed on these implants, the implants placed in bone blocks with ADSCs showed higher strength value than those without stem cells (Sivoletta et al., 2015). Our laboratory developed an *in vitro* 3D bone model for testing small implants, where osteoconductive composite of polyurethane-hydroxyapatite (PU-HA) scaffolds were used to implant dense titanium screws for 28 days. These scaffolds were capable of supporting cell attachment, proliferation and calcified matrix deposition. Also, there was an observation of extracellular matrix deposition onto the inserted screws after D28 (Tetteh et al., 2016). However, these studies did not go further to quantify mineralised extracellular matrix formation on the implanted screws. The

present work aimed to investigate the possibility of using PU foam seeded with bone cells as an *in vitro* 3D bone model for testing 3 D printed porous dental implants.

## **6.2 Aim**

The main aim of this chapter is to reproduce the osseointegration process *in vitro* by developing a novel 3D bone model for testing 3D printed porous implants.

The following objectives were addressed:

1. To determine whether an industrial PU foam would be suitable for a long-term *in vitro* 3 D culture model.
2. To compare different insertion conditions, and identify the best time point, for inserting titanium constructs to support cell migration and extracellular matrix deposition into the implanted constructs.
3. To compare the effect of different implantation periods on the extracellular matrix deposition into the implanted constructs.
3. To use the model to compare bone matrix deposition on two different designs of 3D printed porous Ti-6Al-4V lattices; GP/300-400 and spider web.
4. To demonstrate the ability of the method to determine human bone ingrowth using bone marrow derived mesenchymal stem cells from a single human adult donor.

## **6.3 Methods**

### **6.3.1 Cell migration using Eclipse fluorescent microscope**

Cell migration is an essential dynamic process in the growth and maintenance of multicellular organisms. In order to decide whether to create the model used in this work from MLO-A5 or MG63 cells, the migration potential of MLO-A5 cells were evaluated and compared with a standard cell line MG63, using time-lapse video microscopy.

This test was carried out by monitoring cell movement in a monolayer culture plate. A low cell density (2,000) of MLO-A5 and MG63 cells was cultured in basal culture

media in triplicates in 6-well plates. To permit cell attachment, cells were incubated for 4 hours at 37°C. Then well plates were transferred to the microscope stage of the live cell environmental control chamber as shown in figure 6.2, which is connected with CO<sub>2</sub>, to provide an appropriate physiological environment for cells. The microscope was set with 5% CO<sub>2</sub> and temperature of 37°C. Cell movement was investigated by taking pictures at regular intervals (20 minutes) over 24 hours using a camera fitted to the microscope. Using ImageJ version 1.49, cell movement was calculated by measuring distance moved in pixels of selected cells across the range of the field view. Ten cells from each well were tracked manually, and the average of total cell displacement was calculated.

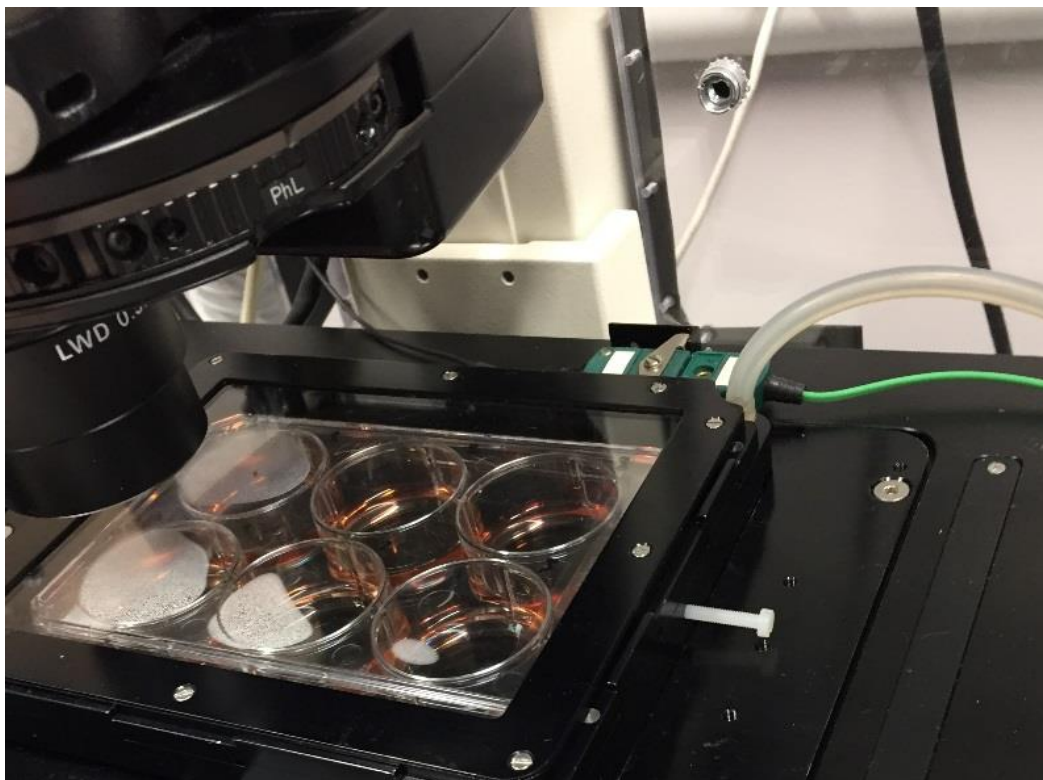


Figure 6.2 Cell migration measurement of MLO-A5 and MG63 cells in two dimensions culture under Eclipse fluorescent microscope chamber, the microscope was controlled by 5% CO<sub>2</sub> at 37°C. Cells were monitored by taking pictures at 20 minutes regular intervals over 24 hours.



### **6.3.2 Cell culture**

To investigate the suitability of an industrial PU foam to act as an *in vitro* bone model for small porous implants, cylindrical rings of PU scaffolds with 4.5 and 3.5 mm inner diameter were prepared by laser cutting as described in section 3.4.2. Selective laser melted Ti-6Al-4V lattices were cut into 5 x 7 mm see section 3.4.1.

Prior to cell culture, PU scaffolds and Ti-6Al-4V lattices were sterilised at 121°C for 30 minutes in an autoclavable glass bottle containing 0.1% gelatine solution for the PU scaffolds and an autoclavable bag for the Ti-6Al-4V lattices. All samples were immersed in a culture medium with 30 minutes incubation at 37°C and 5% CO<sub>2</sub> humid environment to allow protein attachment onto the surface of the scaffolds. After removing expansion media MLO-A5, cells were seeded onto the PU scaffolds in an untreated 12 well plate, using different cell densities 15,000, 30,000 and 60,000 in 150 µl expansion media per scaffold. The passage number of cells used was between 42 - 49. To allow cell attachment, scaffolds were incubated for 45 minutes for each side. Scaffolds immersed in media but without cells (negative controls) were also used. 2 ml of EM was added to each scaffold and incubated overnight. The next day scaffolds were transferred to new well plates to evaluate cell attachment into the scaffolds; this was by testing the metabolic activity of cells on the original and new the well plates using resazurin reduction assay as described in section 3.7.6. The same test was used to monitor cell growth over different time points of the cell culture period. Media was changed every 2-3 days during the experiment period. At the end of the experiment, all samples were fixed with formalin see section 3.7.10. Then the deposition of mineral and extracellular matrix on both PU scaffolds and titanium lattices was quantified using ARS and SRS staining as described in sections 3.7.7 and 3.7.8 respectively. SEM was used to investigate cell migration to implanted titanium. Xylenol orange was also used

to observe mineralised nodule deposition using confocal microscopy as described in section 3.7.9. 3D printed titanium lattices were inserted into the inner diameter of PU scaffolds as shown in figure 6.3. Different insertion times and implantation periods were used as described in the following section 6.3.3.

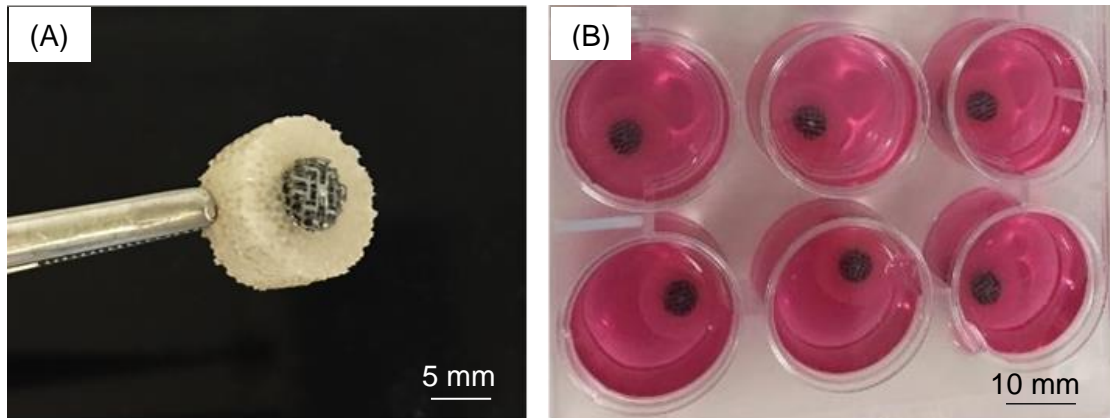


Figure 6.3 3D *in vitro* bone model for implant testing, PU scaffolds implanted with 3D printed titanium lattices (scale bar = 5 mm) (A) and maintained over long-term (28 and 42 days) in a cultured media (scale bar = 10 mm) (B), images taken at day 0 insertion.

### **6.3.3 Culture conditions**

Different culture conditions were tested, including varying insertion and implantation times, to determine which resulted in the best cell migration and extracellular matrix deposition. The first step in this study was to investigate the effect of different insertion methods on the extracellular matrix deposition into the implanted titanium samples. Initially, three insertion conditions were used, in 1) titanium lattices were inserted prior to cell seeding (day 0). 2) cells were cultured in PU for 4 days and then the titanium samples inserted (day 4). 3) 28 days after cell seeding titanium lattices were implanted (day 28). In all methods, titanium samples were maintained in the PU construct for a further 28 days of culture under static conditions. As shown in figure 6.4 (A). The next step was to extend the implantation time to 42 days and compare it with 28 days. The insertion conditions were reduced to day 0 and 7 as shown in figure 6.4 (B).

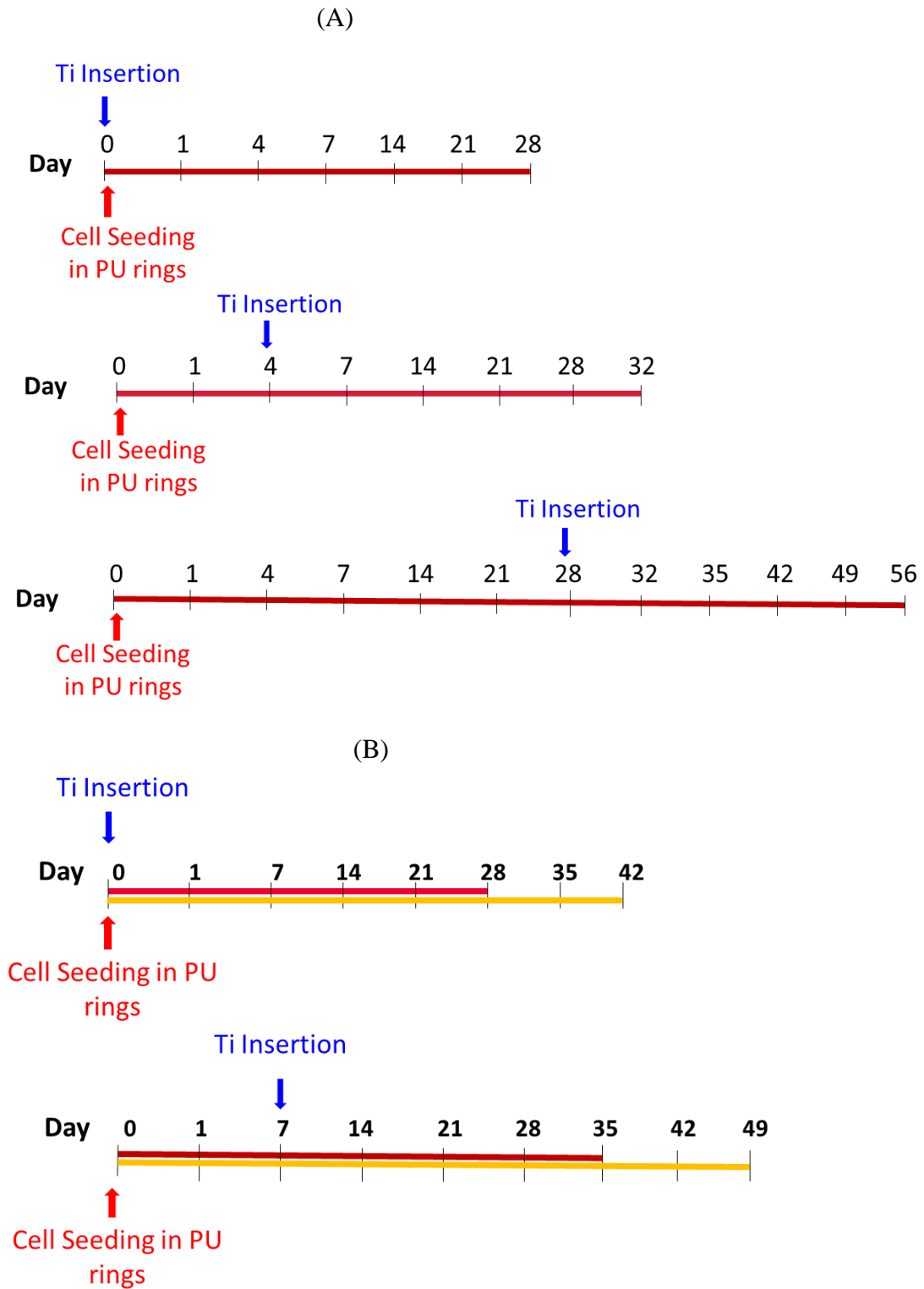


Figure 6.4 Culture conditions used for the *in vitro* 3D bone model including time of insertion titanium implants into PU scaffolds and duration of implantation period, A-titanium inserted at day 0, 4 and 28 and implanted for 28 days. B-titanium inserted at day 0 and 7 and implanted either for 28 or 42 days.

### 6.3.4 Experimental groups

In this study, many trials were performed to develop the *in vitro* bone model to represent the *in vivo* environment and enable bone formation into the implanted titanium lattices. It had to determine whether to make the model from MLO-A5 or MG63 cells. Therefore, initially, the migration potential of MLO-A5 cells was evaluated and compared with MG63 cells as described in section 6.3.1. The results showed a higher migration ability in MLO-A5 than MG63 cells. Thus, MLO-A5 cells were used to perform the following experimental attempts:

**1. Preliminary trial (1):** aimed to validate the capability of PU scaffolds to support bone cells growth over long-term (49 days). PU scaffolds with 4.5 inner diameters were seeded with 15,000 MLO-A5 cells, Ti-6Al-4V lattices of GP300-400 were inserted into PU scaffolds at day 0, 4 and 28. They were implanted for 28 days as described in section 6.3.2 and shown in figure 6.3.

**2. Experiment (2):** used a modified insertion method with day 0 and 7 as described in section 6.3.3. Higher cell densities 30,000 and 60,000 were used and implants assessed for calcified extracellular matrix deposition on implanted Ti-6Al-4V lattices

**3. Experiment (3):** aimed to evaluate the effect of a narrower connection between PU scaffolds and implanted titanium on cell migration into the implanted lattices; and compare PU scaffolds with two different inner diameters 3.5 and 4.5 mm using same cell density 60,000 cells.

**4. Experiment (4):** the influence of the implantation period on extracellular matrix deposition into two different designs of Ti-6Al-4V lattices (GP/400-300 and SW) was also investigated. Titanium samples were implanting either for 28 or 42 days. The

metabolic activity of cells was evaluated after explanting titanium lattices from PU scaffolds.

**5. Experiment (5):** the last part of this study was to use the optimised condition with different cell types, one donor of hBMSCs cells (passage number 2 and 3) with 500,000 cells per scaffold. Titanium samples were implanting for 42 days. For more clarification, a summary of the different conditions used in this study is shown in table 6.1.

Each trial was repeated three times in triplicate. Cell viability was evaluated at several time points (1, 7, 14, 21 and 28) using resazurin reduction assay as described in section 3.7.6. After removal of titanium lattices from the surrounding PU scaffolds, bone matrix deposition was quantified using Calcium ARS and SRS Collagen staining describes in sections 3.7.7 and 3.7.8 respectively. Xylenol orange was also used in experiment 4 and 5 to observe mineralised nodule deposition using confocal microscopy describes in sections 3.7.9.

Table 6.1 A summary of the experimental trials of different culture conditions used to optimise the *in vitro* 3D bone model. Trials are grouped according to the inner diameter of PU scaffolds, cell type, cell density, the design of Ti-6Al-4V lattices, and insertion time of titanium into PU scaffolds and duration of implantation.

Experimental trial	PU diameter (mm)	Cell type	Cell density	Ti-6Al-4V design	Insertion time (days)	Implantation time (days)
1	4.5	MLOA5	15,000	GP/400-300	0, 4 and 28	28
2	4.5	MLOA5	30,000 and 60,000	GP/400-300	0 and 7	28
3	3.5 and 4.5	MLOA5	60,000	GP/400-300	0 and 7	28
4	3.5	MLOA5	60,000	GP/400-300 and SW	0 and 7	28 and 42
5	3.5	bMHMSC	500,000	GP/400-300	0 and 7	42

## 6.4 Results

### 6.4.1 The migration potential of MLO-A5 cells is higher than that of MG63 cells

From cell migration analysis as shown in the line graph of figure 6.5, MLO-A5 cells (A) moved greater distances within a 24 hour period compared to MG63 cells (C). The individual cell movements during 20 minutes are presented by the yellow arrows on the image (B) of MLO-A5 cell and (D) of MG63 cells. There was a significant difference in the average total distance moved between MLO-A5 and MG63 as displayed by the bar chart (E).

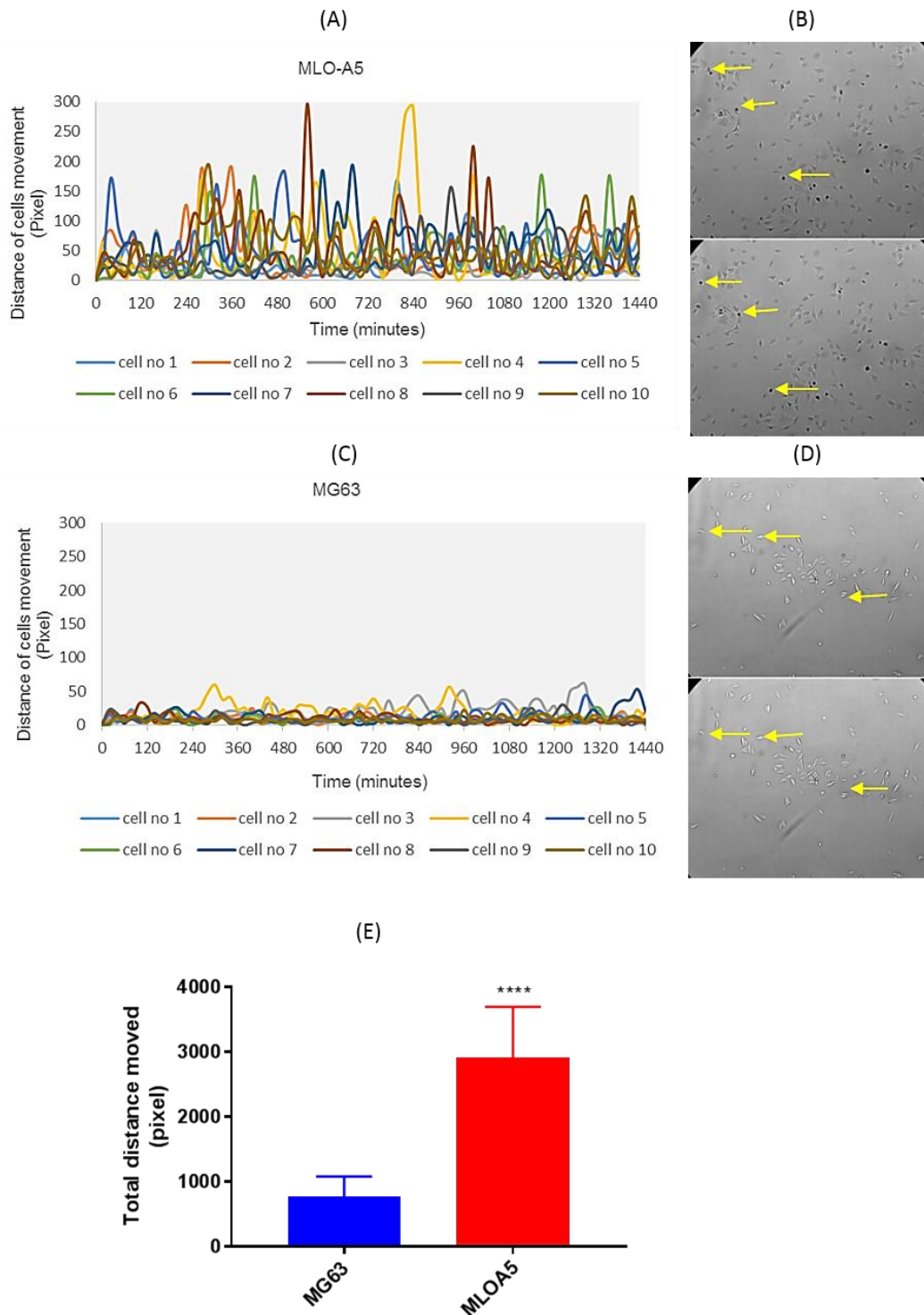


Figure 6.5 An overview of cell migration analysis of MLO-A5 and MG63 cells. The migration potential of 10 cells of (A) MLO-A5 and (C) MG63 from each well was determined every 20 minutes over 24 hours (1440 minutes). The yellow arrows on two images show individual (B) MLO-A5 and (C) MG63 cell movement during 20 minutes. (E) The bar chart represents mean  $\pm$  SD for significant differences in average total distance movement in pixel per 24 hours.

## 6.4.2 Experiment 1: PU scaffolds can support MLO-A5 cells attachment and proliferation over long-term (56 days)

### 6.4.2.1 Cell Viability

To evaluate cell attachment and viability of cells over a long-term culture period, RR cell viability assay was carried on MLO-A5 cell seeded PU with titanium lattices inserted on day 0, 4 and 28. On day 1, the cell attachment of MLO-A5 on PU scaffolds of all insertion condition groups was higher compared to their well plates, while there were no significant differences observed among all insertion groups (Figure 6.6).

As shown in figure 6.6 (B), the metabolic activity of MLO-A5 cells of all insertion conditions increased significantly between day 1 and 7. However, there was no significant change in cell viability (as measured by metabolic activity) regarding the time of insertion (day 0, 4, 28). Therefore, it appears that regardless of the insertion time of implanted titanium, PU scaffolds can support MLO-A5 cells attachment and proliferation over long-term (56 days).

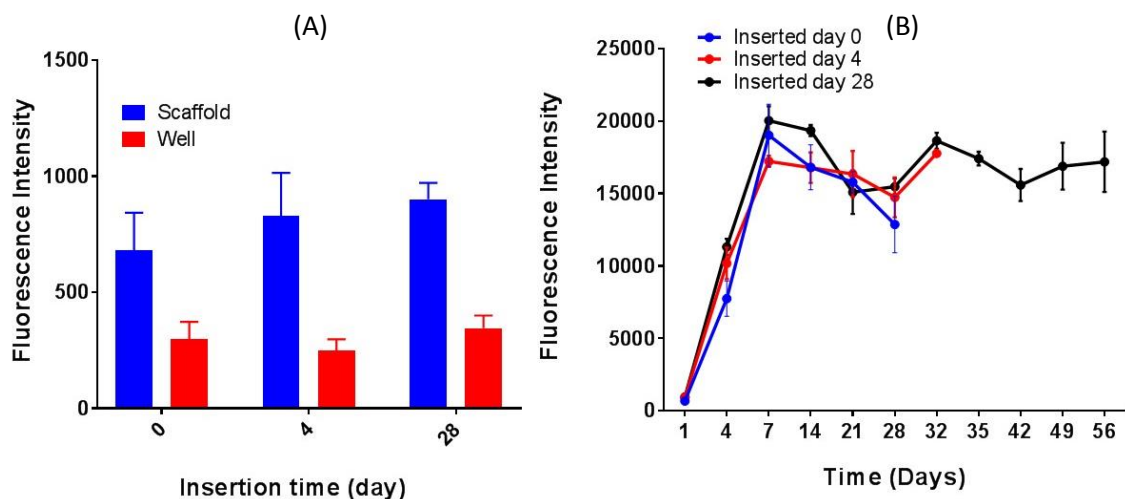


Figure 6.6 Metabolic activity of MLO-A5 cells on PU scaffold and titanium with different insertion times (day 0, 4 and 28) at (A) day 1 after cell seeding which represent cell attachment on PU scaffolds and well plates (B) several time points (1, 4, 7, 14, 21, 28, 32, 35, 42, 49 and 56) (n=9).



### 6.4.2.2 Calcium and collagen production

Alizarin red and Sirius red staining discussed in the previous chapters were used on both PU scaffolds and explanted titanium to examine their ability to support calcified matrix deposition and extracellular matrix production. PU scaffolds seeded with MLO-A5 cells and implanted with titanium lattices for the three insertion groups (day 0, 4 and 28) were stained after 28 days of insertion. As shown in the quantitative analysis, Figure 6.7, all PU scaffolds supported calcified deposition and extracellular matrix formation. The highest calcium deposition was supported by PU scaffolds which were used for 28 day insertion. However, no calcium or collagen deposition was found on the implanted titanium lattices.

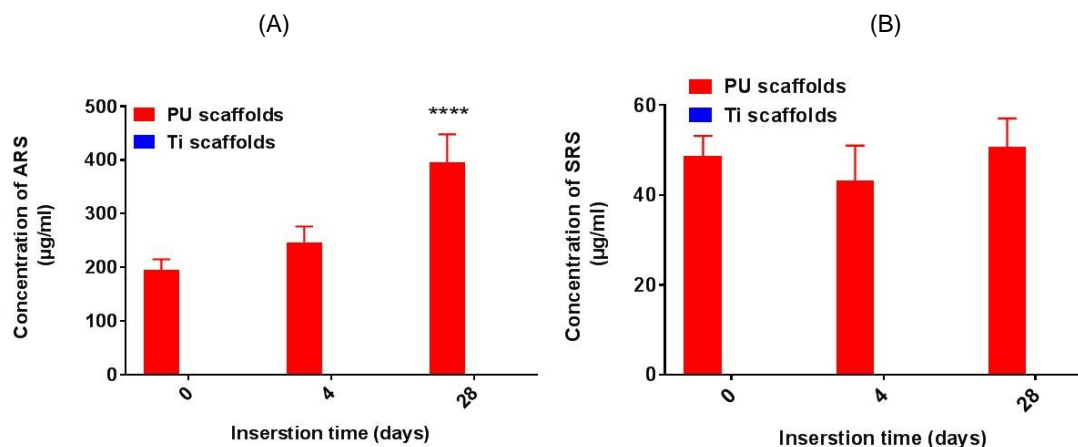


Figure 6.7 Mean  $\pm$  SD for (A) ARS staining and (B) SRS staining of MLO-A5 cells on PU scaffold on day 28 of cell culture, (n=9).

### **6.4.3 Experiment 2: Increasing cell density (30,000 and 60,000) of MLO-A5 does not affect calcified minerals and extracellular deposition on implanted Ti-6Al-4V lattices**

To examine the effect of seeding density on the ability of MLO-A5 cells to migrate from PU scaffolds into the implanted titanium lattices, PU scaffolds were seeded at either 30,000 or 60,000 cells per scaffold and cultured for 28 days after titanium insertion, two insertion times (day 0 and 7) were used and compared. Metabolic activity of cells was analysed at different time points then calcified matrix deposition and extracellular deposition were evaluated after 28 days of titanium insertion.

#### **6.4.3.1 Cell Viability**

The attachment of MLO-A5 cells on PU scaffolds with two different cell densities and insertion times is depicted in figure 6.8. From the fluorescence values for day 1, the metabolic activity of cells which attached on PU scaffolds and wells at higher cell density (60,000) was significantly higher than that of lower density (30,000). Additionally, in for both cell densities, there were no significant differences in cell attachment on PU scaffolds with implanted titanium (day 0 insertion) and PU scaffolds only which were used for day 7 insertion.

MLO-A5 cell viability of all tested groups increased sharply from D1 to D7. Within the higher cell density group (60,000), MLO-A5 cells had higher viabilities from D1 to D14 compared to low cell density PU seeded scaffolds. After 28 days of implanting titanium, all conditions achieved at a similar overall cell viability with PU scaffolds of day 0 insertion and 60,000 cells being slightly higher, but this difference was not statistically significant.

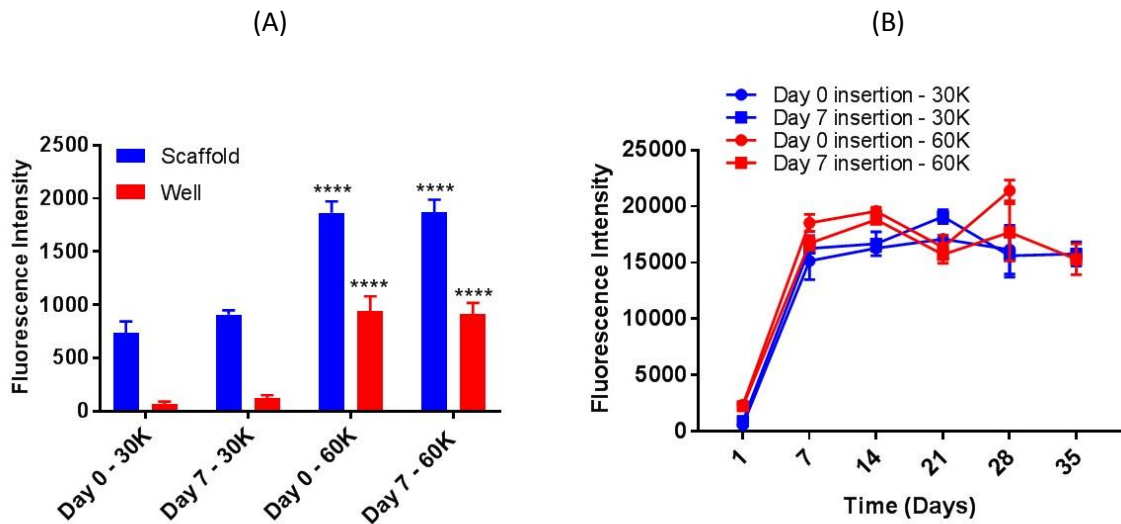


Figure 6.8 Mean  $\pm$  SD for the metabolic activity of MLO-A5 cells with different cell densities (30,000 and 60,000) on PU scaffold and titanium inserted either at day 0 and 7, at (A) day 1 after cell seeding which represents cell attachment on PU scaffolds and well plates (B) at several time points (1, 7, 14, 21, 28, and 35),  $n=9$ . \*\*\*\* indicates  $p<0.0001$ .

#### 6.4.3.2 Calcium and collagen production

The values of alizarin red and Sirius red staining on PU scaffolds and titanium lattices are shown in figure 6.9. In general, the deposition of calcium and collagen on PU scaffolds increased significantly with a higher cell density of 60,000 cells. The highest values of calcium and collagen formation were noted on the PU scaffold of day 7 titanium insertion for both cell densities used (30,000 and 60,000). However, this increase did not support cell migration and extracellular matrix deposition into the implanted lattices. A closer examination of the explanted titanium lattices showed only a small amount of alizarin red stain on the bottom side of the lattices as shown in figure 6.9.

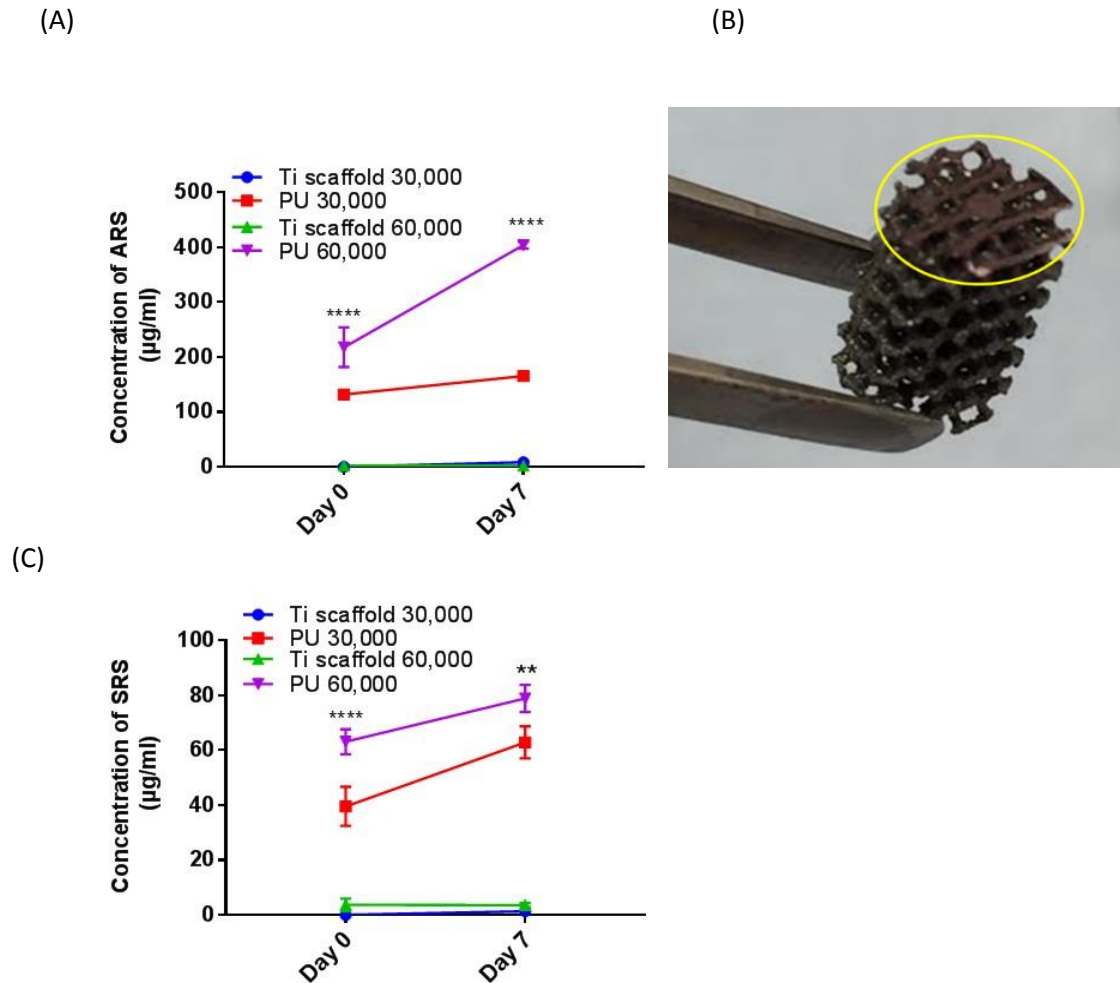


Figure 6.9 Mean  $\pm$  SD for the quantitative analysis of (A- B) Alizarin Red Destaining and (C) Sirius Red Destaining of MLO-A5 cells on PU Scaffold and extracted titanium after 28 days, (n=9). \*\*\*\* indicates  $p < 0.0001$ .

#### 6.4.4 Experiment 3: A narrow connection between PU and Ti scaffolds enables cell migration and bone matrix deposition

To examine the effects of a narrower connection between PU scaffolds and implanted titanium lattices on the ability of the 3 D model to enable cell migration from the PU to the implanted material, MLO-A5 cells were seeded at 60,000 cells per scaffold into PU scaffolds with either 4.5 mm or 3.5 mm of inner diameter at the same time. Titanium lattices were inserted at day 0 and 7 and maintained for 28 days. Metabolic activity of cells was evaluated at various time points and after extraction from PU scaffolds, to

examine cell migration into the implanted titanium. Alizarin red and Sirius red staining were used to quantify calcium and collagen deposition.

#### **6.4.4.1 Cell Viability**

It can be seen from the data in figure 6.10, that MLO-A5 cells were viable on all PU scaffolds, with metabolic activity increased significantly from D1 to D7 and sustained for 28 days. Cell attachment and viability of MLO-A5 were generally similar on PU scaffolds with variable size of inner diameter and insertion time of the implanted titanium.

After 28 days of implantation, cell migration was confirmed by the metabolic activity of MLO-A5 on extracted implants from PU scaffolds with 3.5 mm internal diameter which were significantly higher than those inserted in PU scaffolds 4.5 mm. However, there was no significant difference between the values of fluorescence of day 0 insertion and day 7 insertion. A closer inspection under a light microscope also showed osteoblast cells had moved from PU scaffolds into porous implants as in figure 6.10.

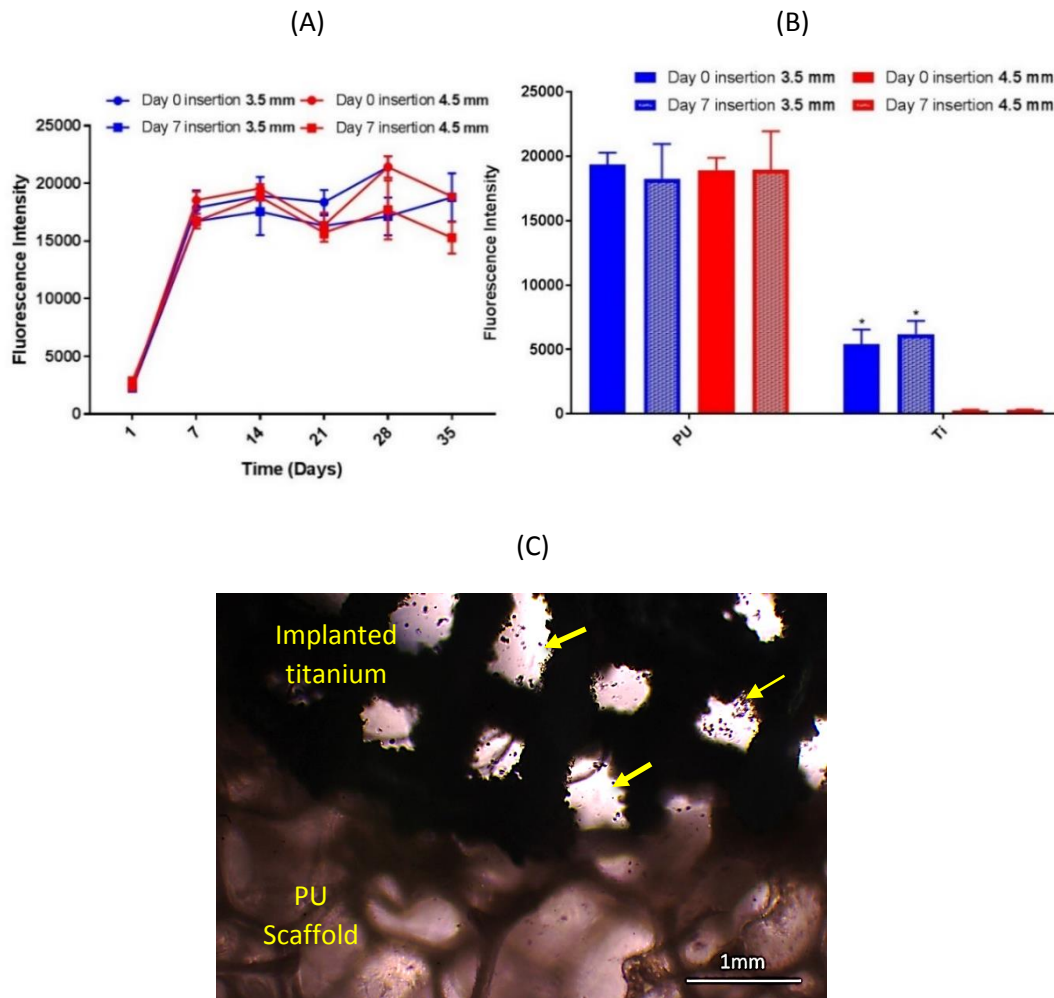


Figure 6.10 Mean  $\pm$  SD for the metabolic activity of MLO-A5 cells on (A) PU scaffolds with a different inner diameter (4.5 and 3.5 mm) and titanium inserted at day 0 and 7 at different time points over 28 days of implantation. (B) PU and titanium after extraction with 28 days implantation. (C) Microscopic photographs show MLO-A5 cells migration from PU scaffolds into implanted titanium after 28 days implantation,  $n=9$ . \* indicates  $p < 0.05$ .

#### 6.4.4.2 Calcium and collagen production

Quantitative analysis by Alizarin Red and Sirius Red staining confirmed extracellular matrix deposition on the implanted titanium. In general, the results of both calcium and collagen staining after 28 days were comparable. The differences in values of Alizarin red and Sirius Red staining on extracted titanium from PU with 3.5 and 4.5 mm internal diameter are highlighted in figure 6.11. Titanium lattices implanted in PU with 3.5 mm

reported significantly more calcium and collagen deposition than those inserted in PU with 4.5 mm. No significant differences were found between day 0 and 7 insertions.

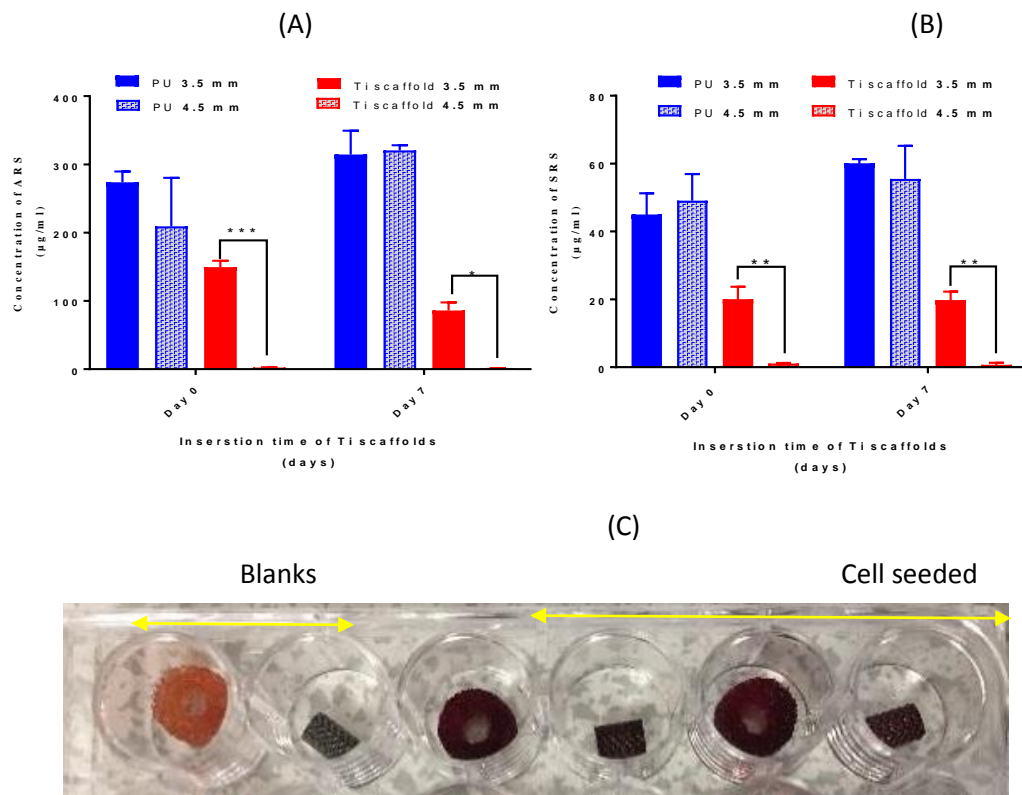


Figure 6.11 Mean  $\pm$  SD for calcium (A) and collagen (B) staining of MLO-A5 cells on the PU scaffolds with 3.5 and 4.5 mm inner diameter and titanium with day 0 and 7 insertions after 28 days. (C) Photograph of mineral deposition on extracted titanium and PU scaffolds with 3.5 mm inner diameter after 28 days implantation, (n=9).

#### 6.4.5 Experiment 4: The migration of osteoblasts and deposition of extracellular matrix into the implanted Ti-6Al-4V lattices (GP/400-300 and SW) increased with longer implantation time.

##### 6.4.5.1 Cell Viability

PU scaffolds with GP/400-300 and SW implants supported cell attachment with no significant differences between two insertion conditions (day 0 and day 7, figure 6.11). Metabolic activity of MLO-A5 cells on all scaffolds increased significantly from D1 to D7 maintained over long duration time (28 and 42 days), there were no significant differences between tested groups (Figure 6.12). The removal GP/400-300 and SW

lattices after 42 days of implantation showed higher cell viability than those with shorter implantation time (28 days). Though, there was no significant difference between the two insertion conditions (day 0 and day 7).

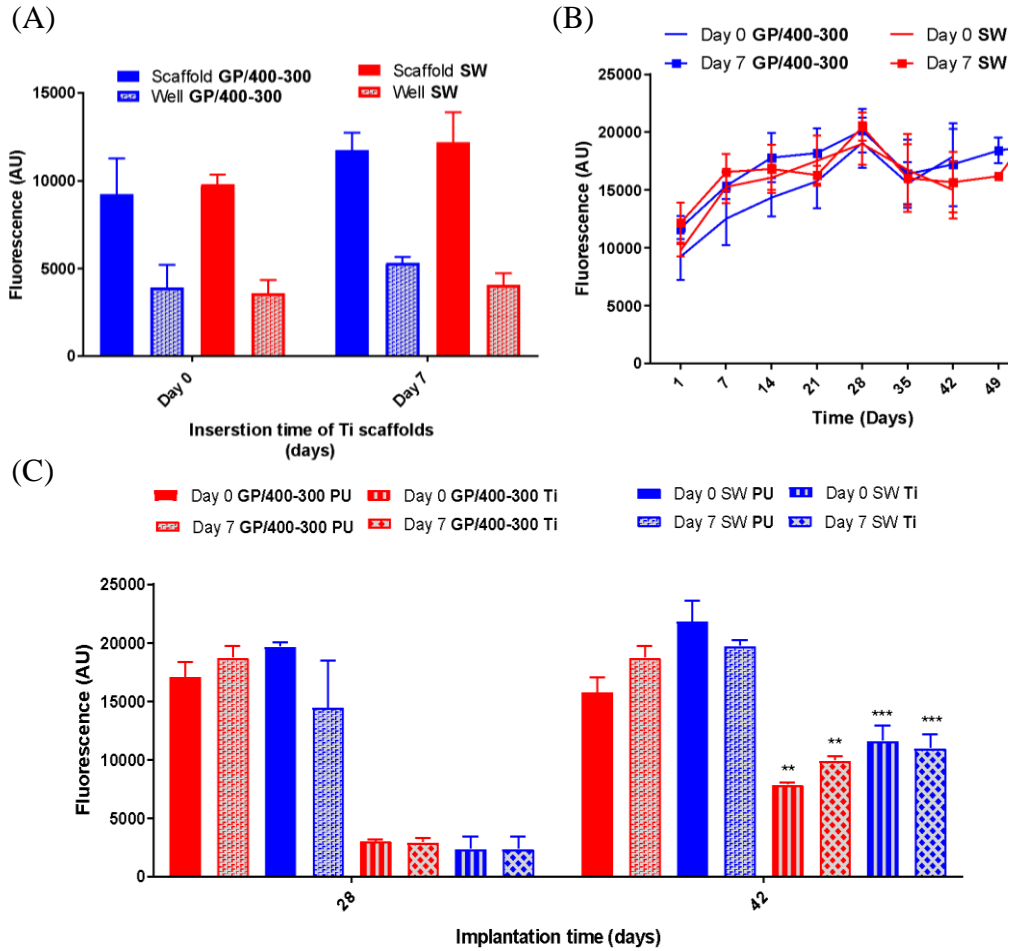


Figure 6.12 Mean  $\pm$  SD for the cell viability of MLO-A5 cells on PU scaffold, and titanium lattices (GP/400-300 and SW) inserted at day 0 and 7 at (A) Indicates cell attachment on PU scaffolds and wells at day 1 after cell seeding and (B) at several time points (1, 7, 14, 21, 28, 35, 42, 49, and 56) (C) After 28 and 42 days of explanting titanium from PU scaffolds, (n=9).

#### 6.4.5.2 Calcium and collagen production

Bone-matrix deposition after long culture periods (28 and 42 days) on two types of implanted titanium (GP/400-300 and SW) with different insertion times (day 0 and 7) are shown in figure 6.13. Concentrations of Alizarin red and Sirius red staining on PU



scaffolds and titanium lattices were generally comparable. All prolonged implantation time groups (42 days) had higher mineralisation and collagen production than the 28 days. There were no significant differences between day 0 and 7 insertions. These results verified the migration of osteoblast cells into implanted titanium and continued deposition of extracellular matrix over time.

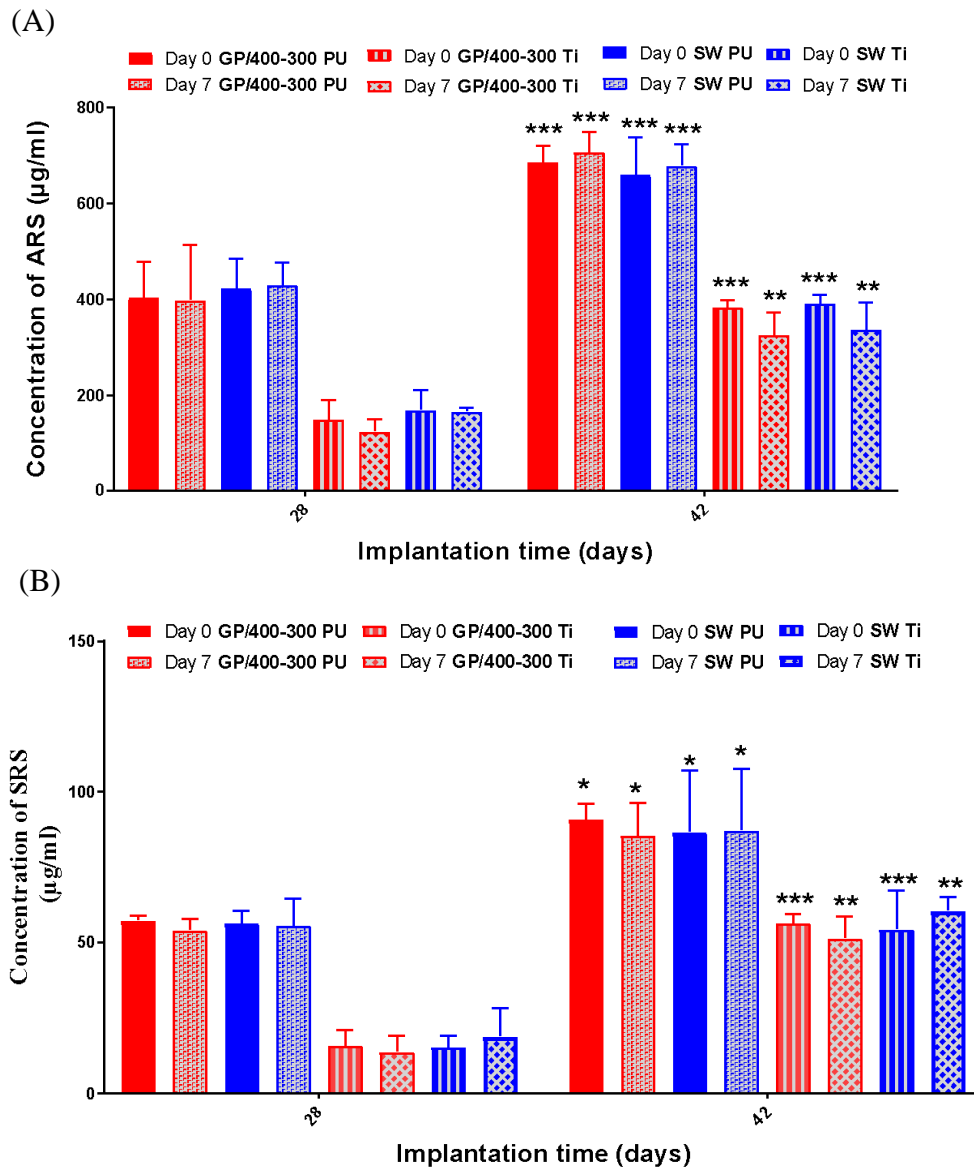


Figure 6.13 Mean  $\pm$  SD for calcium (A) and collagen (B) staining of MLO-A5 cells after 28 days implantation on the PU scaffolds 3.5 mm inner diameter and titanium (GP/400-300 and SW) inserted at day 0 and 7 and implanted for 28 and 42 days, (n=9).

### 6.4.5.3 Scanning electron microscopy

After extracting implanted titanium lattices from their PU scaffolds, MLO-A5 cell migration and distribution on the implanted titanium lattices after 42 days was confirmed by SEM examination (figure 6.14). MLO-A5 cells were found to cover Ti-6Al-4V surfaces and were distributed through the porosity. Dense sheets of cell layers were found coating PU scaffolds surfaces. Cells followed the curvature of the porosity for both implanted titanium and PU scaffolds.

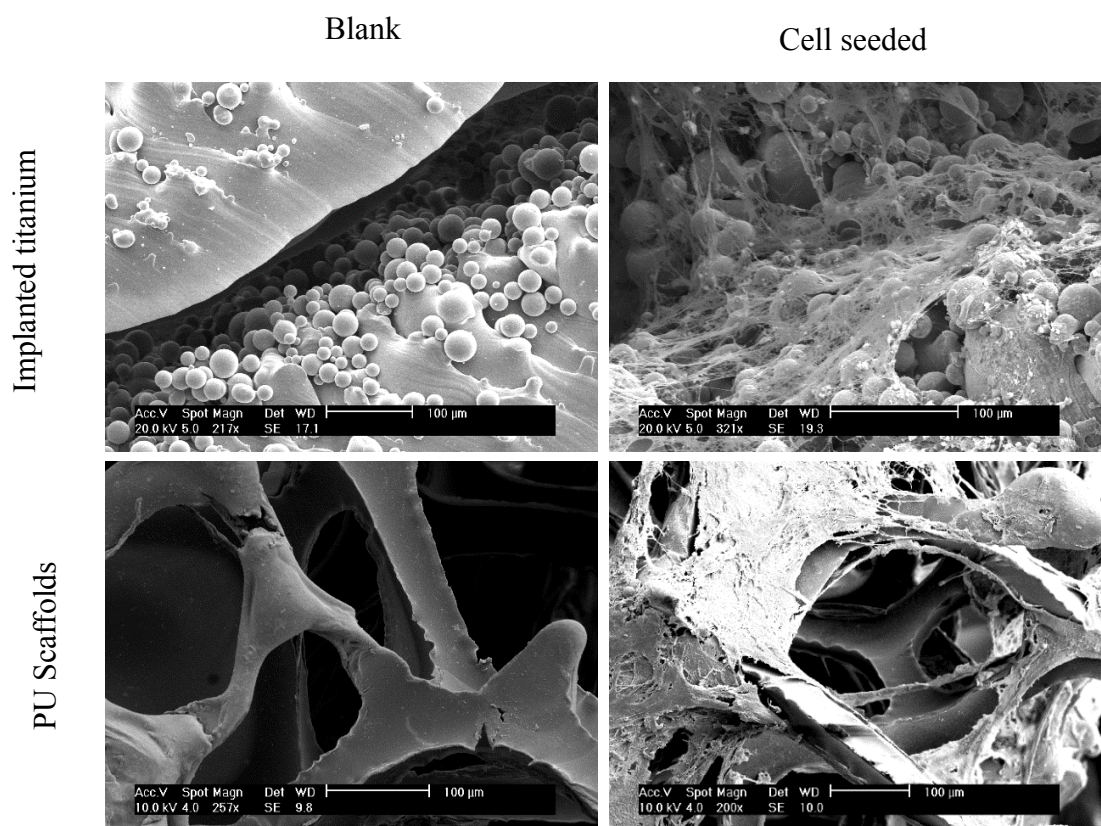


Figure 6.14 Organic material, and extracellular matrix cover cell seeded Ti-6Al-4V surfaces and are distributed across the porosity after 42 days of insertion into PU scaffolds. A dense cell layer was found covering the entire surfaces of PU scaffolds.

#### **6.4.5.4 Xylenol orange staining**

Xylenol orange staining and confocal microscopy were used to detect mineralisation by osteoblast MLO-A5 cells either after 28 days or 24 days as shown in figure 6.15. Negative controls (no cells) were used to distinguish between background fluorescence and cell deposition. Stained nodules were detected on all surfaces of PU scaffolds and implanted titanium with all culture conditions used, revealing that MLO-A5 mineralisation had occurred. A higher amount of stained nodules were observed on the implanted titanium versus blank samples. More positively stained nodules were observed on the titanium that had been implanted for 42 days compared to that of 28 days implantation.

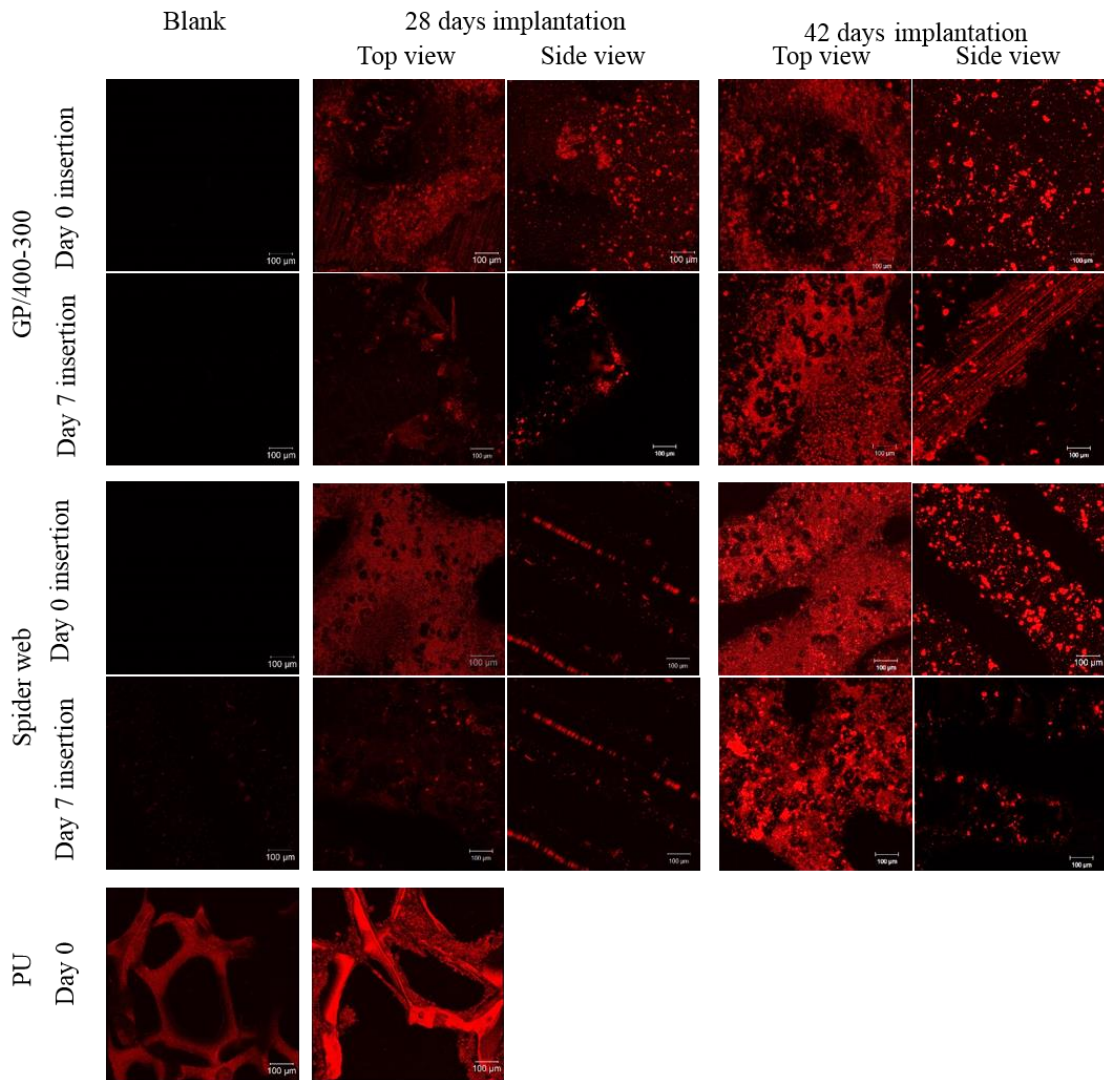


Figure 6.15 Confocal microscopy images of xylenol orange stained mineralised deposits of MLO-A5 cells cultured on auto-fluorescent PU scaffolds and implanted titanium lattices (GP/400-300 and spider web) implanted for 28 and 42 days using two insertion conditions (day 0 and day7), scale bar=100  $\mu\text{m}$ .

**6.4.6 Experiment 5: Bone marrow human mesenchymal stem cells (hBMSCs) are able to migrate into the implanted constructs after 42 days of implantation and produce a mineralised extracellular matrix**

**6.4.6.1 Cell Viability**

As can be seen from figure 6.16, PU scaffolds with GP/400-300 supported cell attachment with no significant differences between two insertion conditions (day 0 and day 7). Metabolic activity of hBMSCs cells on all scaffolds increased significantly from D1 to D7 and was maintained over 35 days; then this declined and plateaued by day 49. There were no differences between the tested groups. Cell viability of hBMSCs on implanted titanium after extraction from surrounding PU scaffolds confirmed that some cells migrated, this was higher with longer implantation period (42 days). However, there was no significant difference between the two insertion conditions (day 0 and day 7).

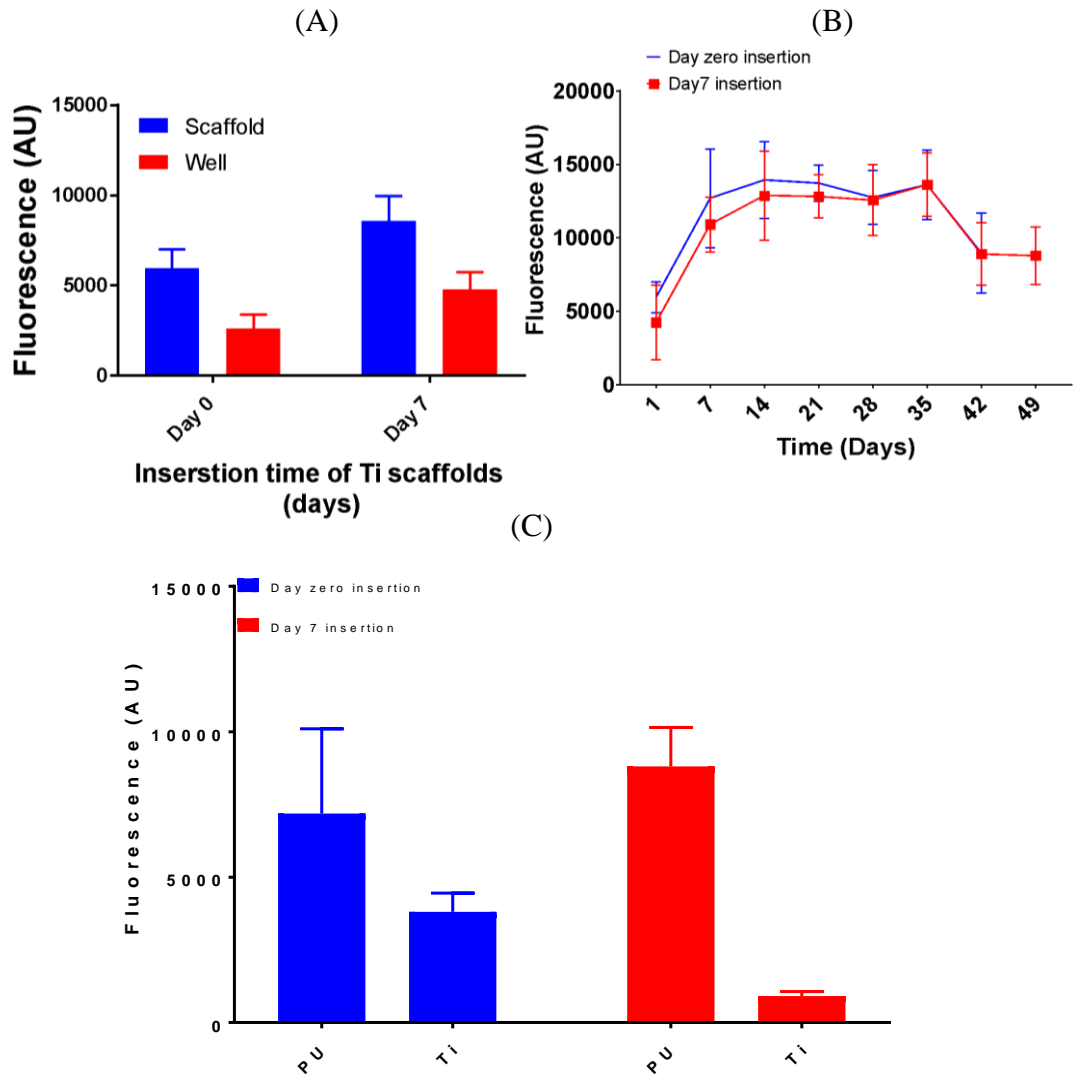


Figure 6.16 Mean  $\pm$  SD for the cell viability of hBMSCs cells on PU scaffold, and titanium lattices (GP/400-300) inserted at day 0 and 7, (A) Indicates cell attachment on PU scaffolds and well at day 1 after cell seeding (B) At several time points (1, 7, 14, 21, 28, 35, 42, 49, and 56) (C) After explanting implanted titanium from PU scaffolds with 42 days implantation, (n=6).

#### 6.4.6.2 Calcium and collagen production

Bone-matrix deposition after 42 days on implanted titanium (GP/400-300) with different insertion times (day 0 and 7) are depicted in figure 6.17. Concentrations of Alizarin red, and Sirius red staining on PU scaffolds and titanium lattices were generally comparable. All prolonged implantation time groups (42 days) had higher

mineralisation and collagen production than the 28 days groups. There were no significant differences between day 0 and 7 insertions. These results verified the migration of osteoblast cells into implanted titanium and deposition of extracellular matrix.

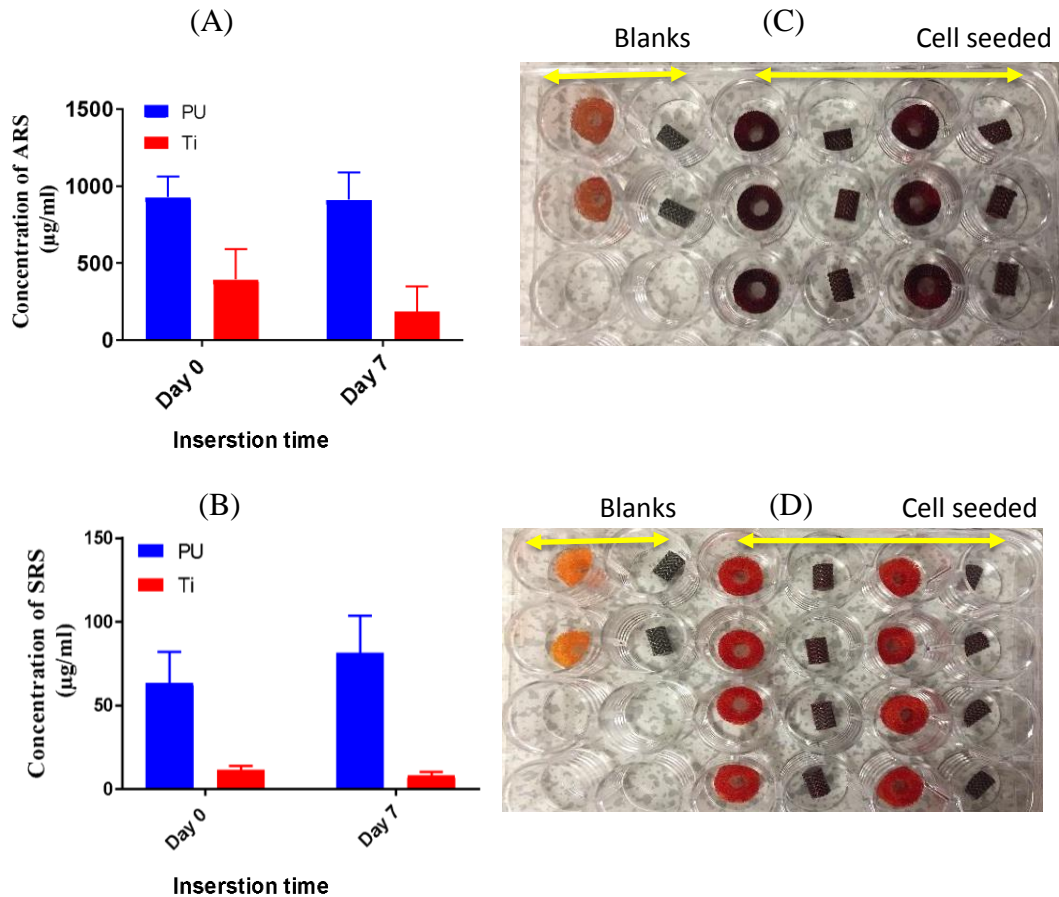


Figure 6.17 Mean  $\pm$  SD for the of calcium (A) and collagen (B) staining of hBMSCs cells on PU scaffolds with 3.5 mm inner diameter and titanium (GP/400-300) inserted at day 0 and 7 and implanted for 42 days. Photograph of (C) mineral deposition and (C) collagen production on extracted titanium and PU scaffolds, (n=6).

#### 6.4.6.3 Scanning electron microscopy

SEM images of PU scaffolds and titanium lattices after 42 days of implantation, exhibited organic material and mineralised matrix sheets deposited by hBMSCs cells as shown in figure 6.18. hBMSCs cells coated Ti-6Al-4V surfaces and were distributed across the porosity after 42 days of insertion into PU scaffolds. Thick sheets of cell

layers were found covering the entire surfaces of PU scaffolds. Cells were spread and followed the curvature of the porosity for both implanted titanium and PU scaffolds.

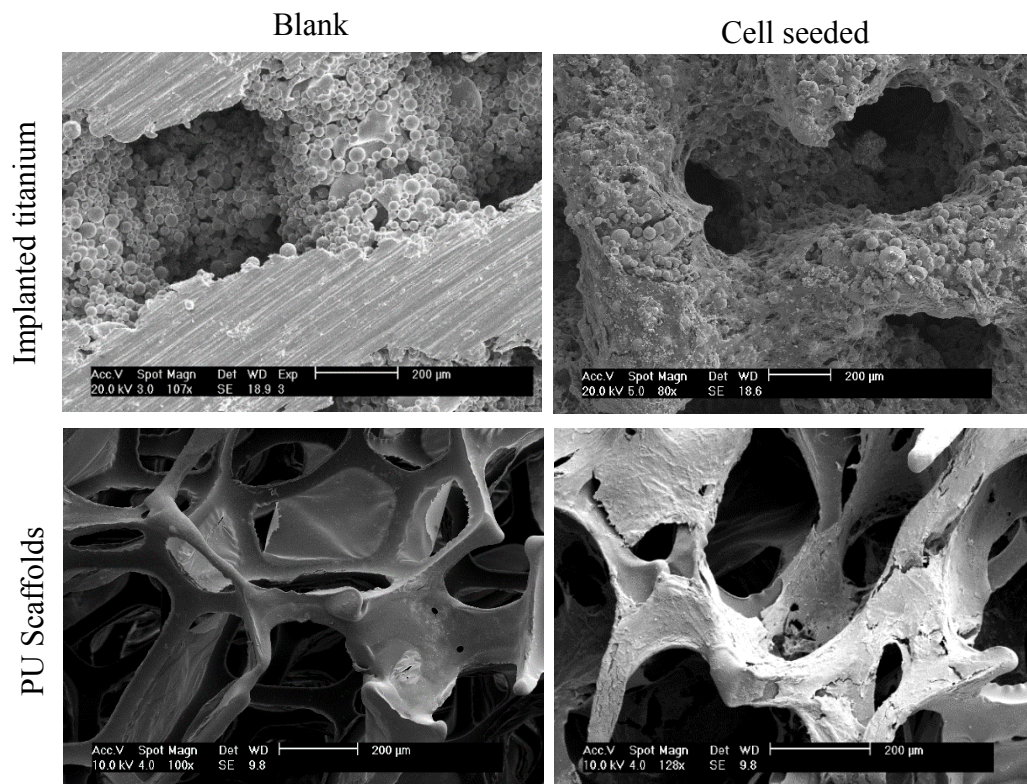


Figure 6.18 SEM images showing hBMSCs cells layers distributed on (top) implanted titanium lattices and (bottom) PU scaffolds over 24 days implantation period, scale bar= 200 µm).

#### 6.4.6.4 Xylenol orange staining

As shown in figure 6.19, mineralised nodules bound to xylenol orange showed red fluorescence on all surfaces of PU scaffolds and on implanted titanium, indicating that hBMSCs cells migrated and produced mineral on the implanted samples. Stained nodules were distinguishable on all surfaces of PU scaffolds and implanted titanium with all culture conditions using day 0 and 7 insertions after 42 days.



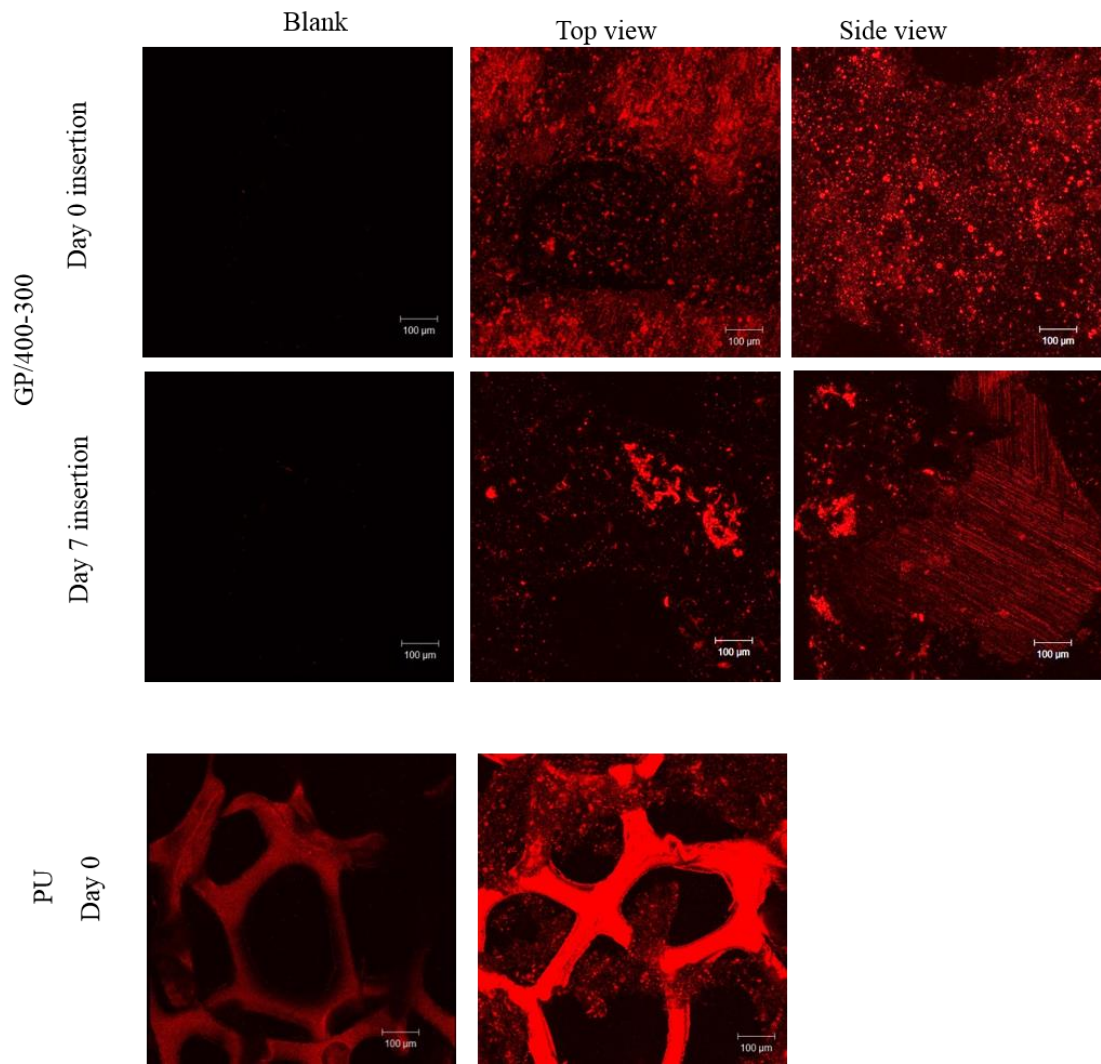


Figure 6.19 Confocal microscopy images of xylene orange stained mineralised deposits of hBMSCs cells cultured on auto-fluorescence PU scaffolds and implanted titanium lattices (GP/400-300) with 42 days implantation using two insertion conditions (day 0 and day7), scale bar=100 μm.

## **6.5 Discussion**

The current study aimed to develop an *in vitro* 3D bone model for testing small porous dental implants, which could represent the *in vivo* condition at the bone-implant interface. Using such a bone-like matrix system can be used to test new implants for orthopaedic and dental applications and offer human specific data that can be currently provided by expensive animal testing. Besides, information obtained from such low-priced models could help academic researchers and industrial bioengineers to test new biomaterials and implant designs to select the more promising designs for *in vivo* testing.

The system offered here consists of the implanting of a 3D printed porous dental implant into the inner cylindrical ring of a PU scaffold loaded with bone cells. Different insertion times, cell density, size of inner diameter and implantation time were compared with the purpose to develop a model in which bone growth into an implanted material could be measured. Two different inner diameters (3.5 and 4.5 mm) of PU scaffolds were used and compared. Two designs of titanium lattices (GP/400-300 and SW) were compared and implanted either for 28 or 42 days. To test whether this system can be used with primary human cells of clinical relevance, bone marrow derived mesenchymal stem cells from a human adult donor were also used. Metabolic activity of cells was assessed at several time points and after extracting titanium lattices from PU scaffolds. After removal from the surrounding PU, effective assays of Alizarin Red Calcium (ARS) and Sirius Red (SRS) Collagen staining were used to quantify bone matrix deposition on the titanium. Xylenol orange was also used to observe mineralised nodule deposition using confocal microscopy.

The success rate of such a bone system is influenced by different critical parameters which should be considered while designing a bone model, such as model material,

seeding density and seeding method. This study aimed to investigate the possibility of using an industrial PU foam loaded with bone cells as an *in vitro* 3D bone model. PU foam was chosen because of the several potential benefits, such as biocompatibility, mechanical flexibility, cost-effectiveness and ease of fabrication (Tetteh et al., 2016). Additionally, the macro and microstructure of PU helps to support cell attachment, proliferation and calcified matrix deposition (Tortelli and Cancedda (2009)). This encouraged researchers' interest in PU as biomaterials for medical devices and bone tissue engineering.

Osteoblast MLO-A5 cells were specified as the initial cell type for the current mode because our preliminary results showed that their migration potential is higher than that of MG63 cells. Cell proliferation, distribution, differentiation, and extracellular matrix deposition has been reported to be influenced by the initial cell seeding number (Kruyt et al., 2008). The seeding density used in our study was determined according to the preliminary results. Our study confirmed the suitability of PU to support osteoblast cell (MLO-A5) attachment, proliferation and deposition of calcified matrix as shown in (Figure 6.7). This result is in agreement with Sittichockechaiwut et al., (2009) who stated that calcium and collagen production MLO-A5 cells on open cell PU foam scaffolds increased with culture time (Sittichockechaiwut et al., 2009). As expected, after 56 days, the PU scaffolds that were used for day 28 of titanium insertion expressed the highest calcium deposition, this is because these scaffolds were effectively cultured for 28 days before titanium insertion then followed another 28 days implantation. In this work, the bone model of PU foam seeded with MLO-A5 cells was able to support extracellular matrix deposition and hold porous Ti-6Al-4V implant over long-term culture (49 days). However, the initial tests were unsuccessful in term of bone cell transition into the implanted titanium lattices. This appeared to be because there was

not close enough contact between the implanted titanium and PU scaffold, but when the diameter was reduced to 3.5 mm successful cell migration and calcium and collagen deposition was clearly detectable on the inserted titanium. The ingrowth was not different between the two different designs (GP/400-300 and SW) investigated, but we would expect differences when we are looking at very different materials or porosities. Findings by Tetteh et al., (2016) showed a higher metabolic activity and matrix deposition by hESMP and MLO-A5 osteoblastic cells on PU-HA components in comparison to pure PU scaffolds over 56 days (Tetteh et al., 2016).

Another important factor was the implantation period, over time the quantity of calcium and collagen deposited on PU scaffolds and inserted titanium increased as shown in Figure 6.13. This result seems to be logical as bone formation and mineralisation increases during culture. These observations are very interesting as mineralised extracellular matrix production is essential for improving the bone-implant integration process. Finding from other research also confirmed that longer culture time (more than 14 days) are necessary for bone-like matrix deposition (Tortelli and Cancedda, 2009).

Using hBMSCs in the current model also confirmed human cell migration into the implanted constructs after 42 days and produced mineral and extracellular matrix. Xylenol orange and confocal microscopy of MLO-A5 and hBMSCs confirmed a high level of mineralisation on all PU scaffolds and implanted porous titanium. Stevenson et al., 2015 also used Xylenol orange staining to detect mineral deposition produced by primary human osteoblast cells on 3D porous titanium surfaces. However, in their work, bone cells were directly seeded on the porous surfaces so that was unable to mimic cell ingrowth.

To the best of knowledge, only two trials have been reported to develop an *in vitro* 3D bone model for testing small implants; in study by Tetteh et al., 2016, osteoconductive

composite (PU-HA) scaffolds seeded with MLO-A5 were used to implant titanium screws for 28 days. (Tetteh et al., 2016). Another study used blocks of carbonated hydroxyapatite from bovine bone seeded with adipose-derived stem cells also been used to implant dental implants over 30 days and then undertook a pull-out test to measure the force required to detach implant from the blocks (Sivolella et al., 2015). In both studies mentioned above, cells with an osteoblast morphology were observed to grow on the implants. This research introduced an *in vitro* bone model with the ability to identify the metabolic activity of cells and the amount of bone formation over the surface of the extracted implant.

However, the limitation of the current *in vitro* model is that it is not capable of accurately replicating the complex native environment, because it does not include angiogenesis and remodelling processes. Native bone is regulated by the remodelling process which is a dynamic balance process between bone resorption and formation (Kohli et al. 2018). Bone formation is stimulated by haematoma which occurs after implantation as a biological response to implant material. There are also different blood cells, proteins and inflammatory mediators at the implant site which participate in the healing process. The bone regeneration process starts with delicate woven bone which is then remodel to tougher lamellar bone; this process occurs within about six months. Several attempts have been reported to mimic the complex bone remodelling process by incorporating two or more cell types in a co-culture system. Different biomaterials have been used to design a co-culture model such as hydrogels (Jeon et al. 2014, Rao et al. 2012, Jeon et al. 2014 and Bersini et al. 2016), ceramics (Papadimitropoulos et al. 2011 and Kay Sinclair et al. 2011) and composites (Rao et al. 2014, Heinemann et al. 2013 and Bongio et al. 2016). In a trial by Papadimitropoulos et al. (2011) to imitate the process of bone turnover (bone mass balance resulting from bone resorption and

formation), they considered a 3D co-culture system of osteoblastic-osteoclastic-endothelial cells in 3D porous ceramic scaffolds. They aimed to capture aspects of the functional coupling of bone-like matrix deposition and resorption (Papadimitropoulos et al. 2011). Within other materials and to mimicking physiological vasculogenesis, 3D fibrin gels were used with human endothelial cells and human bone marrow-derived mesenchymal stem cells to develop a functional 3D microvascular network within a microfluidic system (Jeon et al. 2014). Resorbable 3D bone graft substitutes were also used to explain the correlation between human MSCs and osteoclasts (Kay Sinclair et al. 2011).

As can be seen, the material properties, implantation period, the involvement of osteoblasts, osteoclasts and immune cells are essential requirements for future *in vitro* model for bone regeneration purposes to demonstrate effectiveness in replicating the stages of bone healing following implantation.

In this work, a more advanced technique was developed which particularly mimics the native environment and may be used for testing small porous dental implants. So far an *in vitro* 3D bone model which holds porous dental implants for a long duration with the capability of measuring bone ingrowth and extracellular matrix deposition has been achieved. Overall this technique is extremely promising as a fabrication method for dental implants which could be more cost-effective and allow better osseointegration than those currently available.

## **6.6 Chapter summary**

- From the preliminary conditions tested, industrial PU foam was found to support osteoblast cell (MLO-A5) attachment and growth and stimulated them to produce mineral over a long-term (56 days).

- Reducing the inner diameter of PU scaffolds to 3.5 mm created a higher level of connection between PU scaffolds and implanted titanium, this was found to induce bone cells migration and extracellular matrix deposition into the implanted components.
- The developed *in vitro* 3D model supported bone cell ingrowth into the porous implants regardless of their designed porosity and insertion time.
- Prolonged implantation times of up to 42 days significantly increased cell migration, calcium and collagen production on both PU scaffolds and implanted titanium.
- The developed *in vitro* 3D model was able to support hBMSCs cell ingrowth and extracellular matrix deposition on the implants.
- Here, we have shown a cost-effective approach for testing 3D printed porous dental implants, maintained over long-term which showed that extracellular matrix deposition can occur into the implants that would mimic the native bone environment.

## **Chapter 7 : Conclusions and future perspectives**

### **7.1: Conclusions**

The introduction of porosity into dental implant surfaces has been shown to increase surface area and reduce stiffness, thus improving bone-implant integration (Nouri et al., 2010). This thesis aimed to produce 3D printed Ti-6Al-4V components with regular and graded porosity to be used as an alternative to bulk titanium dental implants for patients with compromised bone healing. An SLM system was selected for the production of Ti-6Al-4V lattices because it can produce structures of complex pore geometries rapidly, with minimum waste production. Ti-6Al-4V was used as a raw material due to its excellent combination of biocompatibility, high corrosion resistance and high strength to low weight ratio.

To accomplish the aim of this project, a simple cylindrical design with volume representing dental implants was invented and used to produce a novel 'spider web' design and variety of porous Ti-6Al-4V structures. The dimensions of the cylindrical lattices were  $5 \times 7 \pm 0.2$  mm mimicking the size of the current dental implant. These lattices were built on a diamond unit cell with variable pore sizes (300, 400 and 650  $\mu\text{m}$ ) and strut thicknesses (300 and 400  $\mu\text{m}$ ) with and without a dense core. A diamond lattice was chosen because of its simple structure and relatively low stiffness compared to its density. A novel 'Spider Web' design was also invented with radial spokes and circumferential connecting struts, 250  $\mu\text{m}$  size was used for strut thickness and spacing between struts. The 'Spider Web' was an effective way to create a structure with graded porosity, to the best of our knowledge, this was the first time a radial pore structure was produced and evaluated for its suitability for medical implants. The removal of unprocessed Ti-6Al-4V powder particles from the 3D printed cellular component has been a matter of concern, as these particles might release into the body and perhaps



## ***Chapter 7: Conclusions and Future Prospective***

cause toxicity to cells. The observation of unfused Ti-6Al-4V particles within the lattices was also confirmed by the SEM images of this project. This directed the current study to estimate the amount and size of particle removal from the lattices using a conventional ultrasonic bath. The possible cytotoxic effect of the Ti-6Al-4V microparticles on two types of bone forming cell, MLO-A5 and hBMSCs was assessed here. Different physical, mechanical and biological tests were carried out to assess the optimum strength, stiffness and bioactivity. The last part of this thesis aimed to develop a novel *in vitro* 3D bone model for testing small porous dental implants, which could mimic the *in vivo* environment at the bone-implant interface. Such an inexpensive model may offer reliable information to help academic researchers and industrial bioengineers to test new biomaterials and implant designs, to select the more promising designs for *in vivo* testing.

The first objective was to design and manufacture a novel ‘Spider Web’ design and a range of titanium alloy micro-lattice structures based on a diamond unit cell using an SLM system. Different pore sizes (250, 300, 400 and 650  $\mu\text{m}$ ) and strut thicknesses (250, 300 and 400  $\mu\text{m}$ ) and graded porous structures with and without a dense core were used and compared. All structures were assessed for surface chemistry, structural and mechanical properties in compression and three-point bending. The conclusions from this work were:

- Analysis by SEM,  $\mu\text{CT}$  confirmed that SLM process is a promising method to construct a range of well-controlled interconnected porous Ti-6Al-4V components with a regular and graded porosity of an appropriate size for dental implants. These structures can be more cost-effective and provide better implant integration than those currently available.

### *Chapter 7: Conclusions and Future Prospective*

- Surface chemistry analysis by an EDX spectrum, ICP system and LECO metal extraction system of Ti-6Al-4V components confirmed Ti, Al and V as the main elements of the built Ti-6Al-4V lattices with a lower content of interstitial elements (O, N and C).
- Mechanical properties in compression and three-point bending of most lattices were within the range of those previously stated for cancellous bone. The presence of a dense core improved the mechanical properties of these lattices. The graded porosity was found to perform in line with the average density. ‘Spider web’ design demonstrated a lower degree of isotropy, being more mechanically effective along the axial direction.

The second objectives of this study were focused on the biological performance of the Ti-6Al-4V microparticles and SLM Ti-6Al-4V components with different pore geometries (P400, P400/1C, P400/2C, P650, P650/1C, GP/650-400, GP/400-300 and ‘Spider Web’) using osteoblast MLO-A5 cells. The removal of unprocessed Ti-6Al-4V powder particles from the 3D printed cellular component has been a matter of concern, as these particles might release into the body and perhaps cause toxicity to cells. The observation of unfused Ti-6Al-4V particles within the lattices was also confirmed by the SEM images of this project. This directed the current study to estimate the amount and size of particle removal from the lattices using a series of cleaning periods (15 mins, 30 mins, 1, 2, 4, 8, 16, 32, 64 and 128 hours). Then we studied whether there was a cytotoxic influence of the Ti-6Al-4V microparticles of different concentrations (2.5, 5, 7.5, 10, 25, 50 and 100 mg/ml) on two types of bone cell growth, MLO-A5 and hBMSCs which represent the cell type contacting the implant surface in the osseointegration process. The main observations of these objectives were:

### ***Chapter 7: Conclusions and Future Prospective***

- The release of unprocessed Ti-6Al-4V microparticles from the built lattices was seen even after long cleaning hours in an ultrasonic bath. The majority of particles released for each cleaning period ranged from 15-25 microns in diameter.
- There was no toxic effect of micro Ti-6Al-4V powder particles up to 10 mg/ml on the growth of two types of bone cells, MLO-A5 and bone marrow hBMSCs.
- All SLM Ti-6Al-4V structures provided desirable surface cell growth and mineralised matrix deposition which was not affected by pore size except that the maximum calcium deposition was seen on scaffolds with 400-micron pores.

The final objective of this work was to mimic some aspects of the *in vivo* condition at the bone-implant interface by developing a novel *in vitro* 3D bone model for testing 3D printed porous implants. A bone-like matrix system could be utilised to test new implants for orthopaedic and dental applications and to provide reliable data, which is currently provided through the expensive animal model. This model may also ideally be suitable for reducing the use of *in vivo* models. In this model, the cylinders of SLM Ti-6Al-V structures were inserted into cylindrical rings of an industrial PU foam previously seeded with bone cells. PU foam was selected due to the attractive macro and microstructural features which support cell attachment, proliferation and calcified matrix deposition. In addition, PU is biocompatible, mechanically flexible, cost-effective and easy to fabricate. Different insertion conditions, cell density, inner diameter of PU scaffold and implantation periods were compared with the aim of developing a model in which bone growth could be measured in an implanted material. Initially, the aim was to determine whether an industrial PU foam would be suitable for a long-term *in vitro* 3D culture model. Different insertion conditions were compared, to

## *Chapter 7: Conclusions and Future Prospective*

identify the best time point, for inserting titanium constructs to support cell migration and extracellular matrix deposition into the implanted titanium. The effect of different implantation periods for 28 or 42 days on the extracellular matrix deposition into the implanted constructs was also compared. This model was also used to compare bone matrix deposition on two different designs of 3D printed porous Ti-6Al-4V lattices; GP/300-400 and 'spider web'. It was also to investigate the ability of the model to determine human bone ingrowth using bone marrow-derived mesenchymal stem cells from a human adult donor. The conclusions from this objective were:

- An industrial PU foam was found to support osteoblast cells (MLO-A5) attachment and growth and stimulate them to produce mineral over a long-term (49 days).
- Reducing the inner diameter of PU scaffolds to 3.5 mm provided a higher level of connection between PU scaffolds and implanted titanium, this was found to induce bone cell migration and extracellular matrix deposition into the implanted components.
- The developed *in vitro* 3D model supported bone cell ingrowth into the porous implants regardless of their designed porosity and insertion time.
- Prolonged implantation time of up to 42 days was supported significantly increased cell migration and the production of calcium and collagen on both PU scaffolds and implanted titanium.
- The developed *in vitro* 3D model was able to support hBMSCs cells ingrowth and extracellular matrix deposition on the implants.
- Here, we have demonstrated a more advanced way to test 3D printed porous dental implants, which is maintained over the long-term with the ability to measure bone ingrowth and extracellular matrix deposition.

## **7.2: Future perspectives**

For future work, it would be interesting to perform fatigue testing to understand long-term resistance, as it is one of the main required tests for implant materials. Surface roughness of the lattices also could be investigated since it has a critical role on *in vivo* and *in vitro* response of artificial implants in addition to porosity and pore size (Hernández-Nava et al., 2016).

It has been shown that a high amount of vanadium and aluminium is a risk for cell toxicity, but it is not known whether these ions would be released in the media over the time of the experiment. For future work, it might be interesting to measure the concentration of ions in the media at the different doses of particles. The effect of these particles on the ability of osteoblast to mineralise could also be investigated. Furthermore *in vitro* studies can also be performed to examine the behaviour of these lattices with human osteoblasts and primary cells. In other studies, other metal particles have been shown to activate immune cells (Luo et al., 2015), therefore it would be important to test these on white blood cells (macrophages).

Despite the promising observations obtained from the current *in vitro* 3D bone model, it is still not capable of faithfully mimicking the complex bone environments, due to the lack of angiogenesis and remodelling process. To improve this model, it could be interesting to include osteoclast cells and examine their effects on the cell ingrowth. Further improvement would be to adjust the mechanical properties of the external scaffold system by incorporating hydroxyapatite into PU, to create a stiffer bone-like construct. This might provide the potential to enable pull-out tests to be performed to measure the required force to detach the implant from the model. In the future,

## ***Chapter 7: Conclusions and Future Prospective***

histological examinations could also be performed on the current model and compared to *in vivo* testing.

In summary, a range of promising designs (P400, P400/1C, P400/2C, GP/400-300 and ‘Spider Web’) that could use in structuring dental implants for patients with compromised bone healing. Typical dental implants would either include a thread, press fit or tapered (Alghamdi, 2018), therefore consultation with dental companies would be required to understand how best to modify these designs to be applicable in dental implant applications.

**Chapter 8 : References**

- Afshar, M., Anaraki, A.P., Montazerian, H., Kadkhodapour, J., 2016. Additive manufacturing and mechanical characterization of graded porosity scaffolds designed based on triply periodic minimal surface architectures. *J. Mech. Behav. Biomed. Mater.* 62, 481–494. <https://doi.org/10.1016/J.JMBBM.2016.05.027>
- Ahmadi, S.M., Campoli, G., Amin Yavari, S., Sajadi, B., Wauthle, R., Schrooten, J., Weinans, H., Zadpoor, A.A., 2014. Mechanical behavior of regular open-cell porous biomaterials made of diamond lattice unit cells. *J. Mech. Behav. Biomed. Mater.* 34, 106–115. <https://doi.org/10.1016/J.JMBBM.2014.02.003>
- Al-Maawi, S., Orłowska, A., Sader, R., James Kirkpatrick, C., Ghanaati, S., 2017. In vivo cellular reactions to different biomaterials-Physiological and pathological aspects and their consequences. *Semin. Immunol.* 29, 49–61. <https://doi.org/10.1016/j.smim.2017.06.001>
- Alghamdi, H.S., 2018. Methods to Improve Osseointegration of Dental Implants in Low Quality (Type-IV) Bone: An Overview. *J. Funct. Biomater.* 9. <https://doi.org/10.3390/jfb9010007>
- Alghamdi, H.S., Bosco, R., van den Beucken, J.J.J.P., Walboomers, X.F., Jansen, J.A., 2013. Osteogenicity of titanium implants coated with calcium phosphate or collagen type-I in osteoporotic rats. *Biomaterials* 34, 3747–3757. <https://doi.org/10.1016/j.biomaterials.2013.02.033>
- Aly, M.S., Bleck, W., Scholz, P.-F., 2005. How metal foams behave if the temperature rises. *Met. Powder Rep.* 60, 38–45. [https://doi.org/10.1016/S0026-0657\(05\)70502-6](https://doi.org/10.1016/S0026-0657(05)70502-6)
- Andani, M.T., Shayesteh Moghaddam, N., Haberland, C., Dean, D., Miller, M.J., Elahinia, M., 2014. Metals for bone implants. Part 1. Powder metallurgy and implant rendering. *Acta Biomater.* 10, 4058–4070. <https://doi.org/10.1016/j.actbio.2014.06.025>
- Arifvianto, B., Zhou, J., 2014. Fabrication of Metallic Biomedical Scaffolds with the Space Holder Method: A Review. *Materials (Basel).* 7, 3588–3622. <https://doi.org/10.3390/ma7053588>

## References

- Ataee, A., Li, Y., Fraser, D., Song, G., Wen, C., 2018. Anisotropic Ti-6Al-4V gyroid scaffolds manufactured by electron beam melting (EBM) for bone implant applications. *Mater. Des.* 137, 345–354.  
<https://doi.org/10.1016/J.MATDES.2017.10.040>
- Bahraminasab, M., Sahari, B. B., 2013. NiTi shape memory alloys, Promising materials in orthopedic applications. *Shape Mem. Alloy. Process. Charact. Appl.* 261–278.  
<https://doi.org/10.5772/2576>
- Baltic Osseointegration Academy. URL <http://www.boaoffice.lt/EN/9/> (Date accessed 19/10/2018).
- Balla, V.K., Bodhak, S., Bose, S., Bandyopadhyay, A., 2010. Porous tantalum structures for bone implants: Fabrication, mechanical and *in vitro* biological properties. *Acta Biomater.* 6, 3349–3359. <https://doi.org/10.1016/J.ACTBIO.2010.01.046>
- Bandyopadhyay, A., Espana, F., Balla, V.K., Bose, S., Ohgami, Y., Davies, N.M., 2010. Influence of porosity on mechanical properties and *in vivo* response of Ti6Al4V implants. *Acta Biomater.* 6, 1640–1648. <https://doi.org/10.1016/J.ACTBIO.2009.11.011>
- Banfi, A., Muraglia, A., Dozin, B., Mastrogiacomo, M., Cancedda, R., Quarto, R., 2000. Proliferation kinetics and differentiation potential of *ex vivo* expanded human bone marrow stromal cells: Implications for their use in cell therapy. *Exp. Hematol.* 28, 707–15.
- Bansiddhi, A., Dunand, D.C., 2008. Shape-memory NiTi foams produced by replication of NaCl space-holders. *Acta Biomater.* 4, 1996–2007. <https://doi.org/10.1016/j.actbio.2008.06.005>
- Bansiddhi, A., Dunand, D.C., 2007. Shape-memory NiTi foams produced by solid-state replication with NaF. *Intermetallics* 15, 1612–1622. <https://doi.org/10.1016/j.intermet.2007.06.013>
- Bártolo, P., 2005. Virtual modeling and rapid manufacturing : advanced research in virtual and rapid prototyping. Taylor & Francis.
- Benayahu, D., Shur, I., Marom, R., Meller, I., Issakov, J., 2002. Cellular and molecular



## References

- properties associated with osteosarcoma cells. *J. Cell. Biochem.* 84, 108–114. <https://doi.org/10.1002/jcb.1270>
- Bencharit, S., Byrd, W.C., Altarawneh, S., Hosseini, B., Leong, A., Reside, G., Morelli, T., Offenbacher, S., 2014. Development and Applications of Porous Tantalum Trabecular Metal-Enhanced Titanium Dental Implants. *Clin. Implant Dent. Relat. Res.* 16, 817–826. <https://doi.org/10.1111/cid.12059>
- Bersini, S., Yazdi, I.K., Talò, G., Shin, S.R., Moretti, M., Khademhosseini, A., 2016. Cell-microenvironment interactions and architectures in microvascular systems. *Biotechnol. Adv.* 34, 1113–1130. <https://doi.org/10.1016/J.BIOTECHADV.2016.07.002>
- Bidan, C.M., Kommareddy, K.P., Rumpler, M., Kollmannsberger, P., Fratzl, P., Dunlop, J.W.C., 2013. Geometry as a factor for tissue growth: towards shape optimization of tissue engineering scaffolds. *Adv. Healthc. Mater.* 2, 186–94. <https://doi.org/10.1002/adhm.201200159>
- Boehler, R.M., Graham, J.G., Shea, L.D., 2011. Tissue engineering tools for modulation of the immune response. *Biotechniques* 51, 239–40, 242, 244 passim. <https://doi.org/10.2144/000113754>
- Boerrigter, E.M., Geertman, M.E., Van Oort, R.P., Bouma, J., Raghoobar, G.M., van Waas, M.A., van't Hof, M.A., Boering, G., Kalk, W., 1995. Patient satisfaction with implant-retained mandibular overdentures. A comparison with new complete dentures not retained by implants--a multicentre randomized clinical trial. *Br. J. Oral Maxillofac. Surg.* 33, 282–8.
- Bone Density Pocket Dentistry. URL <https://pocketdentistry.com/11-bone-density/> (Da accessed 19/10/2018).
- Bonfield, W., 1971. Mechanisms of deformation and fracture in bone. *Composites* 2, 173–175. [https://doi.org/10.1016/0010-4361\(71\)90956-6](https://doi.org/10.1016/0010-4361(71)90956-6)
- Bongio, M., Lopa, S., Gilardi, M., Bersini, S., Moretti, M., 2016. A 3D vascularized bone remodeling model combining osteoblasts and osteoclasts in a CaP nanoparticle-enriched matrix. *Nanomedicine* 11, 1073–1091. <https://doi.org/10.2217/nmm-2015-0021>

## References

- Burr, D.B., Martin, R.B., 1989. Errors in bone remodeling: Toward a unified theory of metabolic bone disease. *Am. J. Anat.* 186, 186–216. <https://doi.org/10.1002/aja.1001860208>
- Campoli, G., Borleffs, M.S., Amin Yavari, S., Wauthle, R., Weinans, H., Zadpoor, A.A., 2013. Mechanical properties of open-cell metallic biomaterials manufactured using additive manufacturing. *Mater. Des.* 49, 957–965. <https://doi.org/10.1016/j.matdes.2013.01.071>
- Caplan, A.I., 2005. *Review: Mesenchymal Stem Cells: Cell-Based Reconstructive Therapy in Orthopedics.* *Tissue Eng.* 11, 1198–1211. <https://doi.org/10.1089/ten.2005.11.1198>
- Çelen, S., Özden, H., 2012. Laser-induced novel patterns: As smart strain actuators for new-age dental implant surfaces. *Appl. Surf. Sci.* 263, 579–585. <https://doi.org/10.1016/J.APSUSC.2012.09.112>
- Chandar, S., Kotian, R., Madhyastha, P., Kabekkodu, S., Rao, P., 2017. *In vitro* evaluation of cytotoxicity and corrosion behavior of commercially pure titanium and Ti-6Al-4V alloy for dental implants. *J. Indian Prosthodont. Soc.* 17, 4–8. <https://doi.org/10.4103/0972-4052.197936>
- Chaudhry, S., Jaiswal, R., Sachdeva, S., 2016. Dental considerations in cardiovascular patients: A practical perspective. *Indian Heart J.* 68, 572–575. <https://doi.org/10.1016/j.ihj.2015.11.034>
- Chen, H., Wang, C., Zhu, X., Zhang, K., Fan, Y., Zhang, X., 2014. Fabrication of porous titanium scaffolds by stack sintering of microporous titanium spheres produced with centrifugal granulation technology. *Mater. Sci. Eng. C* 43, 182–188. <https://doi.org/10.1016/J.MSEC.2014.07.026>
- Chen, Y.-C., Sosnoski, D.M., Mastro, A.M., 2010. Breast cancer metastasis to the bone: mechanisms of bone loss. *Breast Cancer Res.* 12, 215. <https://doi.org/10.1186/bcr2781>
- Cheng, A., Humayun, A., Cohen, D.J., Boyan, B.D., Schwartz, Z., 2014. Additively manufactured 3D porous Ti-6Al-4V constructs mimic trabecular bone structure and regulate osteoblast proliferation, differentiation and local factor production in a porosity and surface roughness dependent manner. *Biofabrication* 6, 045007.

- <https://doi.org/10.1088/1758-5082/6/4/045007>
- Chia, H.N., Wu, B.M., 2015. Recent advances in 3D printing of biomaterials. *J. Biol. Eng.* 9, 4. <https://doi.org/10.1186/s13036-015-0001-4>
- Choi, J., Wicker, R.B., Cho, S., Ha, C., Lee, S., 2009. Cure depth control for complex 3D microstructure fabrication in dynamic mask projection microstereolithography. *Rapid Prototyp. J.* 15, 59–70. <https://doi.org/10.1108/13552540910925072>
- Clarke, B., 2008. Normal bone anatomy and physiology. *Clin. J. Am. Soc. Nephrol.* 3 Suppl 3, S131-9. <https://doi.org/10.2215/CJN.04151206>
- Clover, J., Gowen, M., 1994. Are MG-63 and HOS TE85 human osteosarcoma cell lines representative models of the osteoblastic phenotype? *Bone* 15, 585–91.
- Compston, J. E. and of London, R. C. o. P., 1996. *Osteoporosis: New Perspectives on Causes, Prevention and Treatment.* Royal College of Physicians.
- Cook, S.D., Thongpreda, N., Anderson, R.C., Haddad, R.J., 1988. The effect of post-sintering heat treatments on the fatigue properties of porous coated Ti-6Al-4V alloy. *J. Biomed. Mater. Res.* 22, 287–302.
- Currey, J.D., 2012. The structure and mechanics of bone. *J. Mater. Sci.* 47, 41–54. <https://doi.org/10.1007/s10853-011-5914-9>
- Dabrowski, B., Swieszkowski, W., Godlinski, D., Kurzydowski, K.J., 2010. Highly porous titanium scaffolds for orthopaedic applications. *J. Biomed. Mater. Res. B. Appl. Biomater.* 95, 53–61. <https://doi.org/10.1002/jbm.b.31682>
- Data sheets - Additive manufacturing. URL <https://www.renishaw.com/en/data-sheets-additive-manufacturing-17862> (Dat accessed 19/10/2018).
- Davies, J.E., 2003. Understanding peri-implant endosseous healing. *J. Dent. Educ.* 67, 932–49.
- De Fries, R., Mitsuhashi, M., 1995. Quantification of mitogen induced human lymphocyte proliferation: Comparison of alamarbluetm assay to 3h-thymidine incorporation assay. *J. Clin. Lab. Anal.* 9, 89–95. <https://doi.org/10.1002/jcla.1860090203>
- de Vasconcellos, L.-M.-R., Leite, D.O., Nascimento, F.-O., de Vasconcellos, L.-G.-O.,

## References

- Graça, M.-L.A., Carvalho, Y.-R., Cairo, C.-A.-A., 2010. Porous titanium for biomedical applications: an experimental study on rabbits. *Med. Oral Patol. Oral Cir. Bucal* 15, e407-12.
- de Wild, M., Schumacher, R., Mayer, K., Schkommodau, E., Thoma, D., Bredell, M., Kruse Gujer, A., Grätz, K.W., Weber, F.E., 2013. Bone regeneration by the osteoconductivity of porous titanium implants manufactured by selective laser melting: a histological and micro computed tomography study in the rabbit. *Tissue Eng. Part A* 19, 2645–54. <https://doi.org/10.1089/ten.TEA.2012.0753>
- Deligianni, D.D., Katsala, N.D., Koutsoukos, P.G., Missirlis, Y.F., 2000. Effect of surface roughness of hydroxyapatite on human bone marrow cell adhesion, proliferation, differentiation and detachment strength. *Biomaterials* 22, 87–96. [https://doi.org/10.1016/S0142-9612\(00\)00174-5](https://doi.org/10.1016/S0142-9612(00)00174-5)
- Duraccio, D., Mussano, F., Faga, M.G., 2015. Biomaterials for dental implants: current and future trends. *J. Mater. Sci.* 50, 4779–4812. <https://doi.org/10.1007/s10853-015-9056-3>
- Edmondson, R., Broglie, J.J., Adcock, A.F., Yang, L., 2014. Three-dimensional cell culture systems and their applications in drug discovery and cell-based biosensors. *Assay Drug Dev. Technol.* 12, 207–218. <https://doi.org/10.1089/adt.2014.573>
- Elias, C.N., 2011. *Factors Affecting the Success of Dental Implants*. New York: InTech.
- Elias, C.N., Oshida, Y., Lima, J.H.C., Muller, C.A., 2008. Relationship between surface properties (roughness, wettability and morphology) of titanium and dental implant removal torque. *J. Mech. Behav. Biomed. Mater.* 1, 234–42. <https://doi.org/10.1016/j.jmbbm.2007.12.002>
- Feldman, D., Marcus, R., Nelson, D., and Rosen, C. J., 2007. *Osteoporosis*. Elsevier
- Fields, R.D., Lancaster, M. V, 1993. Dual-attribute continuous monitoring of cell proliferation/cytotoxicity. *Am. Biotechnol. Lab.* 11, 48–50.
- Frosch, K.-H., Barvencik, F., Viereck, V., Lohmann, C.H., Dresing, K., Breme, J., Brunner, E., Stürmer, K.M., 2004. Growth behavior, matrix production, and gene expression of human osteoblasts in defined cylindrical titanium channels. *J. Biomed. Mater. Res. Part A* 68A, 325–334. <https://doi.org/10.1002/jbm.a.20010>

## References

- Frost, H.M., 1966. Bone dynamics in metabolic bone disease. *J. Bone Joint Surg. Am.* 48, 1192–203. <http://www.ncbi.nlm.nih.gov/pubmed/5331235>
- Fu, Q., Hong, Y., Liu, X., Fan, H., Zhang, X., 2011. A hierarchically graded bioactive scaffold bonded to titanium substrates for attachment to bone. *Biomaterials* 32, 7333–7346. <https://doi.org/10.1016/J.BIOMATERIALS.2011.06.051>
- Fusion Implants. URL <https://www.fusionimplants.com/r-d/> (Date accessed 19/10/2018).
- Gaviria, L., Salcido, J.P., Guda, T., Ong, J.L., 2014. Current trends in dental implants. *J. Korean Assoc. Oral Maxillofac. Surg.* 40, 50–60. <https://doi.org/10.5125/jkaoms.2014.40.2.50>
- Gebhardt, A., Schmidt, F.-M., Hötter, J.-S., Sokalla, W., Sokalla, P., 2010. Additive Manufacturing by selective laser melting the realizer desktop machine and its application for the dental industry. *Phys. Procedia* 5, 543–549. <https://doi.org/10.1016/J.PHPRO.2010.08.082>
- George, J., Kuboki, Y., Miyata, T., 2006. Differentiation of Mesenchymal Stem Cells Into Osteoblasts on Honeycomb Collagen Scaffolds. <https://doi.org/10.1002/bit>
- Gibson, I., Rosen, D.W., Stucker, B., 2010. *Additive Manufacturing Technologies*. Springer US, Boston, MA. <https://doi.org/10.1007/978-1-4419-1120-9>
- Gong, C.W., Wang, Y.N., Yang, D.Z., 2006. Phase transformation and second phases in ternary Ni–Ti–Ta shape memory alloys. *Mater. Chem. Phys.* 96, 183–187. <https://doi.org/10.1016/j.matchemphys.2005.06.057>
- Goodall, R., Mortensen, A., 2014. Porous Metals. *Phys. Metall.* 2399–2595. <https://doi.org/10.1016/B978-0-444-53770-6.00024-1>
- Gregory, C.A., Grady Gunn, W., Peister, A., Prockop, D.J., 2004. An Alizarin red-based assay of mineralization by adherent cells in culture: comparison with cetylpyridinium chloride extraction. *Anal. Biochem.* 329, 77–84. <https://doi.org/10.1016/j.ab.2004.02.002>
- Halgrin, J., Chaari, F., Markiewicz, É., 2012. On the effect of marrow in the mechanical behavior and crush response of trabecular bone. *J. Mech. Behav. Biomed. Mater.* 5, 231–237. <https://doi.org/10.1016/J.JMBBM.2011.09.003>

## References

- Hansson, S., Halldin, A., 2012. Alveolar ridge resorption after tooth extraction: A consequence of a fundamental principle of bone physiology. *J. Dent. Biomech.* 3, 1758736012456543. <https://doi.org/10.1177/1758736012456543>
- Harrysson, O.L.A., Cansizoglu, O., Marcellin-Little, D.J., Cormier, D.R., West, H.A., 2008. Direct metal fabrication of titanium implants with tailored materials and mechanical properties using electron beam melting technology. *Mater. Sci. Eng. C* 28, 366–373. <https://doi.org/10.1016/j.msec.2007.04.022>
- Hasib, H., Harrysson, O.L.A., West, H.A., 2015. Powder Removal from Ti-6Al-4V Cellular Structures Fabricated via Electron Beam Melting. *JOM* 67, 639–646. <https://doi.org/10.1007/s11837-015-1307-x>
- Heinemann, S., Heinemann, C., Wenisch, S., Alt, V., Worch, H., Hanke, T., 2013. Calcium phosphate phases integrated in silica/collagen nanocomposite xerogels enhance the bioactivity and ultimately manipulate the osteoblast/osteoclast ratio in a human co-culture model. *Acta Biomater.* 9, 4878–4888. <https://doi.org/10.1016/J.ACTBIO.2012.10.010>
- Heinl, P., Körner, C., Singer, R.F., 2008. Selective Electron Beam Melting of Cellular Titanium: Mechanical Properties. *Adv. Eng. Mater.* 10, 882–888. <https://doi.org/10.1002/adem.200800137>
- Heinl, P., Müller, L., Körner, C., Singer, R.F., Müller, F.A., 2008. Cellular Ti-6Al-4V structures with interconnected macro porosity for bone implants fabricated by selective electron beam melting. *Acta Biomater.* 4, 1536–44. <https://doi.org/10.1016/j.actbio.2008.03.013>
- Hernández-Nava, E., Smith, C.J., Derguti, F., Tammam-Williams, S., Leonard, F., Withers, P.J., Todd, I., Goodall, R., 2016. The effect of defects on the mechanical response of Ti-6Al-4V cubic lattice structures fabricated by electron beam melting. *Acta Mater.* 108, 279–292. <https://doi.org/10.1016/J.ACTAMAT.2016.02.029>
- Hoffmann, W., Bormann, T., Rossi, A., Müller, B., Schumacher, R., Martin, I., de Wild, M., Wendt, D., 2014. Rapid prototyped porous nickel–titanium scaffolds as bone substitutes. *J. Tissue Eng.* 5, 204173141454067. <https://doi.org/10.1177/2041731414540674>
- Holen, I., Nutter, F., Wilkinson, J.M., Evans, C.A., Avgoustou, P., Ottewill, P.D., 2015.

## References

- Human breast cancer bone metastasis *in vitro* and *in vivo*: a novel 3D model system for studies of tumour cell-bone cell interactions. *Clin. Exp. Metastasis* 32(7), 689–702. <https://doi.org/10.1007/s10585-015-9737-y>
- Hollander, D.A., von Walter, M., Wirtz, T., Sellei, R., Schmidt-Rohlfing, B., Paar, O., Erli, H.-J., 2006. Structural, mechanical and *in vitro* characterization of individually structured Ti–6Al–4V produced by direct laser forming. *Biomaterials* 27, 955–963. <https://doi.org/10.1016/J.BIOMATERIALS.2005.07.041>
- Holtrop, M. E., 1967. The potencies of the epiphyseal cartilage in endochondral ossification. *Proceedings of the Koninklijke Nederlandse Akademie van Wetenschappen. Series C. Biological and medical sciences*, 70 (1):21-28.
- Hrabe, N.W., Heinl, P., Flinn, B., Körner, C., Bordia, R.K., 2011. Compression-compression fatigue of selective electron beam melted cellular titanium (Ti-6Al-4V). *J. Biomed. Mater. Res. Part B Appl. Biomater.* 99B, 313–320. <https://doi.org/10.1002/jbm.b.31901>
- Isidor, F., 2006. Influence of forces on peri-implant bone. *Clin. Oral Implants Res.* 17, 8–18. <https://doi.org/10.1111/j.1600-0501.2006.01360>.
- ISO 12986-2:2014 - Carbonaceous materials used in the production of aluminium -- Prebaked anodes and cathode blocks -- Part 2: Determination of flexural strength by the four-point method <https://www.iso.org/standard/63048.html> (accessed 1.27.19).
- ISO 17340:2014 - Metallic materials -- Ductility testing -- High speed compression test for porous and cellular metals. <https://www.iso.org/standard/59594.html> (accessed 1.27.19).
- Jakubowicz, J., Adamek, G., Dewidar, M., 2013. Titanium foam made with saccharose as a space holder. *J. Porous Mater.* 20, 1137–1141. <https://doi.org/10.1007/s10934-013-9696-0>
- Jaquiéry, C., Schaeren, S., Farhadi, J., Mainil-Varlet, P., Kunz, C., Zeilhofer, H.-F., Heberer, M., Martin, I., 2005. *In vitro* osteogenic differentiation and *in vivo* bone-forming capacity of human isogenic jaw periosteal cells and bone marrow stromal cells. *Ann. Surg.* 242, 859–67, discussion 867-8.

## References

- Jee, C.S.Y., Guo, Z.X., Evans, J.R.G., Özgüven, N., 2000. Preparation of high porosity metal foams. *Metall. Mater. Trans. B* 31, 1345–1352. <https://doi.org/10.1007/s11663-000-0021-3>
- Jeon, J.S., Bersini, S., Whisler, J.A., Chen, M.B., Dubini, G., Charest, J.L., Moretti, M., Kamm, R.D., 2014. Generation of 3D functional microvascular networks with human mesenchymal stem cells in microfluidic systems. *Integr. Biol. (Camb)*. 6, 555–63. <https://doi.org/10.1039/c3ib40267c>
- Jeon, O.H., Jeong, S.H., Yoo, Y.-M., Kim, K.H., Yoon, D.S., Kim, C.H., 2012. Quantification of temporal changes in 3D osteoclastic resorption pit using confocal laser scanning microscopy. *Tissue Eng. Regen. Med.* 9, 29–35. <https://doi.org/10.1007/s13770-012-0029-1>
- Johnson, D.W., Sherborne, C., Didsbury, M.P., Pateman, C., Cameron, N.R., Claeysens, F., 2013. Macrostructuring of Emulsion-templated Porous Polymers by 3D Laser Patterning. *Adv. Mater.* 25, 3178–3181. <https://doi.org/10.1002/adma.201300552>
- Jones, A., Arns, C., Sheppard, A., Hutmacher, D., Milthorpe, B., Knackstedt, M., 2007. Assessment of bone ingrowth into porous biomaterials using MICRO-CT. *Biomaterials* 28, 2491–2504. <https://doi.org/10.1016/j.biomaterials.2007.01.046>
- Joshi, G. V., Duan, Y., Neidigh, J., Koike, M., Chahine, G., Kovacevic, R., Okabe, T., Griggs, J.A., 2013. Fatigue testing of electron beam-melted Ti-6Al-4V ELI alloy for dental implants. *J. Biomed. Mater. Res. Part B Appl. Biomater.* 101, 124–130. <https://doi.org/10.1002/jbm.b.32825>
- Junker, R., Dimakis, A., Thoneick, M., Jansen, J.A., 2009. Effects of implant surface coatings and composition on bone integration: a systematic review. *Clin. Oral Implants Res.* 20, 185–206. <https://doi.org/10.1111/j.1600-0501.2009.01777.x>
- Junqueira, L.C.U., Bignolas, G., Brentani, R.R., 1979. A simple and sensitive method for the quantitative estimation of collagen. *Anal. Biochem.* 94, 96–99. [https://doi.org/10.1016/0003-2697\(79\)90795-4](https://doi.org/10.1016/0003-2697(79)90795-4)
- Jurczyk, M.U., Jurczyk, K., Niespodziana, K., Miklaszewski, A., Jurczyk, M., 2013. Titanium–SiO<sub>2</sub> nanocomposites and their scaffolds for dental applications. *Mater. Charact.* 77, 99–108. <https://doi.org/10.1016/J.MATCHAR.2013.01.007>



## References

- Kalita, S.J., Bose, S., Hosick, H.L., Bandyopadhyay, A., 2003. Development of controlled porosity polymer-ceramic composite scaffolds via fused deposition modeling. *Mater. Sci. Eng. C* 23, 611–620. [https://doi.org/10.1016/S0928-4931\(03\)00052-3](https://doi.org/10.1016/S0928-4931(03)00052-3)
- Kane, R., Ma, P.X., 2013. Mimicking the nanostructure of bone matrix to regenerate bone. *Mater. Today* 16, 418–423. <https://doi.org/10.1016/J.MATTOD.2013.11.001>
- Karageorgiou, V., Kaplan, D., 2005. Porosity of 3D biomaterial scaffolds and osteogenesis. *Biomaterials* 26, 5474–91. <https://doi.org/10.1016/j.biomaterials.2005.02.002>
- Kato, Y., Boskey, A., Spevak, L., Dallas, M., Hori, M., Bonewald, L.F., 2001. Establishment of an Osteoid Preosteocyte-like Cell MLO-A5 That Spontaneously Mineralizes in Culture. *J. Bone Miner. Res.* 16, 1622–1633. <https://doi.org/10.1359/jbmr.2001.16.9.1622>
- Kay Sinclair, S.S., Burg, K.J.L., 2011. Effect of Osteoclast Co-culture on the Differentiation of Human Mesenchymal Stem Cells Grown on Bone Graft Granules. *J. Biomater. Sci. Polym. Ed.* 22, 789–808. <https://doi.org/10.1163/092050610X496260>
- Kim, H.-J., Yu, S.-K., Lee, M.-H., Lee, H.-J., Kim, H.-J., Chung, C.-H., 2012. Cortical and cancellous bone thickness on the anterior region of alveolar bone in Korean: a study of dentate human cadavers. *J. Adv. Prosthodont.* 4, 146–52. <https://doi.org/10.4047/jap.2012.4.3.146>
- Kim, S.W., Jung, H.-D., Kang, M.-H., Kim, H.-E., Koh, Y.-H., Estrin, Y., 2013. Fabrication of porous titanium scaffold with controlled porous structure and net-shape using magnesium as spacer. *Mater. Sci. Eng. C* 33, 2808–2815. <https://doi.org/10.1016/J.MSEC.2013.03.011>
- Kinney, J.H., Marshall, S.J., Marshall, G.W., 2003. The mechanical properties of human dentin: a critical review and re-evaluation of the dental literature. *Crit. Rev. Oral Biol. Med.* 14, 13–29.
- Kohli, N., Ho, S., Brown, S.J., Sawadkar, P., Sharma, V., Snow, M., García-Gareta, E., 2018. Bone remodelling in vitro: Where are we headed? *Bone* 110, 38–46.

<https://doi.org/10.1016/j.bone.2018.01.015>

- Koike, M., Greer, P., Owen, K., Lilly, G., Murr, L.E., Gaytan, S.M., Martinez, E., Okabe, T., 2011. Evaluation of Titanium Alloys Fabricated Using Rapid Prototyping Technologies—Electron Beam Melting and Laser Beam Melting. *Materials (Basel)*. 4, 1776–1792. <https://doi.org/10.3390/ma4101776>
- Kruyt, M., de Bruijn, J., Rouwkema, J., van Blitterswijk, C., Oner, C., Verbout, A., Dhert, W., 2008. Analysis of the Dynamics of Bone Formation, Effect of Cell Seeding Density, and Potential of Allogeneic Cells in Cell-Based Bone Tissue Engineering in Goats. *Tissue Eng. Part A* 14, 1081–1088. <https://doi.org/10.1089/ten.tea.2007.0111>
- Kumar, G., Tison, C.K., Chatterjee, K., Pine, P.S., McDaniel, J.H., Salit, M.L., Young, M.F., Simon, C.G., 2011. The determination of stem cell fate by 3D scaffold structures through the control of cell shape. *Biomaterials* 32, 9188–9196. <https://doi.org/10.1016/j.biomaterials.2011.08.054>
- Kuroda, D., Niinomi, M., Morinaga, M., Kato, Y., Yashiro, T., 1998. Design and mechanical properties of new  $\beta$  type titanium alloys for implant materials. *Mater. Sci. Eng. A* 243, 244–249. [https://doi.org/10.1016/S0921-5093\(97\)00808-3](https://doi.org/10.1016/S0921-5093(97)00808-3)
- Kutty, M.G., Bhaduri, S., Bhaduri, S.B., 2004. Gradient surface porosity in titanium dental implants: relation between processing parameters and microstructure. *J. Mater. Sci. Mater. Med.* 15, 145–150. <https://doi.org/10.1023/B:JMSM.0000011815.50383.bd>
- Kutty, M.G., Bhaduri, S., Jokisaari, J.R., Bhaduri, S.B., 2001. Development of gradient porosities in Ti dental implant, in: *Ceramic Engineering and Science Proceedings*. pp. 587–592.
- Laoui, T., Santos, E., Osakada, K., Shiomi, M., Morita, M., Shaik, S.K., Tolochko, N.K., Abe, F., Takahashi, M., 2006a. Properties of Titanium Dental Implant Models Made by Laser Processing. *Proc. Inst. Mech. Eng. Part C J. Mech. Eng. Sci.* 220, 857–863. <https://doi.org/10.1243/09544062JMES133>
- Laoui, T., Santos, E., Osakada, K., Shiomi, M., Morita, M., Shaik, S.K., Tolochko, N.K., Abe, F., Takahashi, M., 2006b. Properties of Titanium Dental Implant Models Made by Laser Processing. *Proc. Inst. Mech. Eng. Part C J. Mech. Eng.*

- Sci. 220, 857–863. <https://doi.org/10.1243/09544062JMES133>
- Laptev, A., Bram, M., Buchkremer, H.P., Stöver, D., 2004. Study of production route for titanium parts combining very high porosity and complex shape. *Powder Metall.* 47, 85–92. <https://doi.org/10.1179/003258904225015536>
- Lee, T.C., Taylor, D., 1999. Bone remodelling: Should we cry wolff? *Ir. J. Med. Sci.* 168, 102–105. <https://doi.org/10.1007/BF02946474>
- Le Guéhennec, L., Soueidan, A., Layrolle, P., Amouriq, Y., 2007. Surface treatments of titanium dental implants for rapid osseointegration. *Dent. Mater.* 23, 844–854. <https://doi.org/10.1016/j.dental.2006.06.025>
- Li, J.P., Li, S.H., Van Blitterswijk, C. a, de Groot, K., 2005. A novel porous Ti6Al4V: characterization and cell attachment. *J. Biomed. Mater. Res. A* 73, 223–33. <https://doi.org/10.1002/jbm.a.30278>
- Li, X., Wang, C., Zhang, W., Li, Y., 2010. Fabrication and compressive properties of Ti6Al4V implant with honeycomb-like structure for biomedical applications. *Rapid Prototyp. J.* 16, 44–49. <https://doi.org/10.1108/13552541011011703>
- Li, Y., Wong, C., Xiong, J., Hodgson, P., Wen, C., 2010. Cytotoxicity of Titanium and Titanium Alloying Elements. *J. Dent. Res.* 89, 493–497. <https://doi.org/10.1177/0022034510363675>
- Li, Y., Yang, C., Zhao, H., Qu, S., Li, X., Li, Y., 2014. New Developments of Ti-Based Alloys for Biomedical Applications. *Materials (Basel)*. 7, 1709–1800. <https://doi.org/10.3390/ma7031709>
- Lifland, M.I., Kim, D.K., Okazaki, K., 1993. Mechanical properties of a Ti-6Al-4V dental implant produced by electro-discharge compaction. *Clin. Mater.* 14, 13–19. [https://doi.org/10.1016/0267-6605\(93\)90042-6](https://doi.org/10.1016/0267-6605(93)90042-6)
- Liu, Y., Bao, C., Wismeijer, D., Wu, G., 2015. The physicochemical/biological properties of porous tantalum and the potential surface modification techniques to improve its clinical application in dental implantology. *Mater. Sci. Eng. C* 49, 323–329. <https://doi.org/10.1016/J.MSEC.2015.01.007>
- Luo, C., Wang, X., An, C., Hwang, C.F., Miao, W., Yang, L., Xu, M., Bai, A., Deng, S., 2017. Molecular inhibition mechanisms of cell migration and invasion by coix

## References

- polysaccharides in A549 NSCLC cells via targeting S100A4. *Mol. Med. Rep.* 15, 309–316. <https://doi.org/10.3892/mmr.2016.5985>
- Luo, Y.-H., Chang, L.W., Lin, P., 2015. Metal-Based Nanoparticles and the Immune System: Activation, Inflammation, and Potential Applications. *Biomed Res. Int.* 2015, 143720. <https://doi.org/10.1155/2015/143720>
- Łyczkowska, E., Szymczyk, P., Dybała, B., Chlebus, E., 2014. Chemical polishing of scaffolds made of Ti–6Al–7Nb alloy by additive manufacturing. *Arch. Civ. Mech. Eng.* 14, 586–594. <https://doi.org/10.1016/J.ACME.2014.03.001>
- Mangano, C., Mangano, F.G., Shibli, J.A., Ricci, M., Perrotti, V., d’Avila, S., Piattelli, A., 2012. Immediate Loading of Mandibular Overdentures Supported by Unsplinted Direct Laser Metal-Forming Implants: Results From a 1-Year Prospective Study. *J. Periodontol.* 83, 70–78. <https://doi.org/10.1902/jop.2011.110079>
- Mangano, C., Piattelli, A., d’Avila, S., Iezzi, G., Mangano, F., Onuma, T., Shibli, J.A., 2010. Early Human Bone Response to Laser Metal Sintering Surface Topography: A Histologic Report. *J. Oral Implantol.* 36, 91–96. <https://doi.org/10.1563/AAID-JOI-D-09-00003>
- Mangano, C., Raspanti, M., Traini, T., Piattelli, A., Sammons, R., 2009. Stereo imaging and cytocompatibility of a model dental implant surface formed by direct laser fabrication. *J. Biomed. Mater. Res. Part A* 88A, 823–831. <https://doi.org/10.1002/jbm.a.32033>
- Mangano, F.G., Caprioglio, A., Levrini, L., Farronato, D., Zecca, P. a, Mangano, C., 2014. IF. G. Mangano, A. Caprioglio, L. Levrini, D. Farronato, P. A. Zecca, and C. Mangano, “Immediate loading of mandibularoverdentures supported by one-piece, direct metal laser sin-tering mini-implants: a short-term prospective clinical study,”*Journal of Peri. J. Periodontol.* 1–13. <https://doi.org/10.1902/jop.2014.140343>
- Markhoff, J., Wieding, J., Weissmann, V., Pasold, J., Jonitz-Heincke, A., Bader, R., 2015. Influence of Different Three-Dimensional Open Porous Titanium Scaffold Designs on Human Osteoblasts Behavior in Static and Dynamic Cell Investigations. *Materials (Basel).* 8, 5490–5507.

<https://doi.org/10.3390/ma8085259>

- Matsumoto, H., Watanabe, S., Hanada, S., 2005. Beta TiNbSn Alloys with Low Young's Modulus and High Strength. *Mater. Trans.* 46, 1070–1078. <https://doi.org/10.2320/matertrans.46.1070>
- Mehrali, M., Shirazi, F.S., Mehrali, M., Metselaar, H.S.C., Kadri, N.A. Bin, Osman, N.A.A., 2013. Dental implants from functionally graded materials. *J. Biomed. Mater. Res. Part A* 101, 3046–3057. <https://doi.org/10.1002/jbm.a.34588>
- Meinel, L., Karageorgiou, V., Hofmann, S., Fajardo, R., Snyder, B., Li, C., Zichner, L., Langer, R., Vunjak-Novakovic, G., Kaplan, D.L., 2004. Engineering bone-like tissue in vitro using human bone marrow stem cells and silk scaffolds. *J. Biomed. Mater. Res.* 71A, 25–34. <https://doi.org/10.1002/jbm.a.30117>
- Mello, A.S. da S., dos Santos, P.L., Marquesi, A., Queiroz, T.P., Margonar, R., de Souza Faloni, A.P., 2016. Some aspects of bone remodeling around dental implants. *Rev. Clínica Periodoncia, Implantol. Rehabil. Oral.* <https://doi.org/10.1016/J.PIRO.2015.12.001>
- Mendonça, G., Mendonça, D.B.S., Aragão, F.J.L., Cooper, L.F., 2008. Advancing dental implant surface technology--from micron- to nanotopography. *Biomaterials* 29, 3822–35. <https://doi.org/10.1016/j.biomaterials.2008.05.012>
- Mezzetta, J., 2016. Process-Property Relationships of Ti6Al4V Fabricated through Selective Laser Melting Department of Mining and Materials Engineering.
- Mohandas, G., Oskolkov, N., McMahon, M.T., Walczak, P., Janowski, M., 2014. Porous tantalum and tantalum oxide nanoparticles for regenerative medicine. *Acta Neurobiol. Exp. (Wars)*. 74, 188–196.
- Moin, D.A., Hassan, B., Mercelis, P., Wismeijer, D., 2013a. Designing a novel dental root analogue implant using cone beam computed tomography and CAD/CAM technology. *Clin. Oral Implants Res.* 24 Suppl A, 25–7. <https://doi.org/10.1111/j.1600-0501.2011.02359.x>
- Moin, D.A., Hassan, B., Mercelis, P., Wismeijer, D., 2013b. Designing a novel dental root analogue implant using cone beam computed tomography and CAD/CAM technology. *Clin. Oral Implants Res.* 24, 25–27. <https://doi.org/10.1111/j.1600->

0501.2011.02359.x

- Mour, M., Das, D., Winkler, T., Hoenig, E., Mielke, G., Morlock, M.M., Schilling, A.F., Mour, M., Das, D., Winkler, T., Hoenig, E., Mielke, G., Morlock, M.M., Schilling, A.F., 2010. Advances in Porous Biomaterials for Dental and Orthopaedic Applications. *Materials (Basel)*. 3, 2947–2974.  
<https://doi.org/10.3390/ma3052947>
- Mullen, L., Stamp, R.C., Brooks, W.K., Jones, E., Sutcliffe, C.J., 2009a. Selective Laser Melting: a regular unit cell approach for the manufacture of porous, titanium, bone in-growth constructs, suitable for orthopedic applications. *J. Biomed. Mater. Res. B. Appl. Biomater.* 89, 325–34. <https://doi.org/10.1002/jbm.b.31219>
- Mullen, L., Stamp, R.C., Brooks, W.K., Jones, E., Sutcliffe, C.J., 2009b. Selective Laser Melting: A regular unit cell approach for the manufacture of porous, titanium, bone in-growth constructs, suitable for orthopedic applications. *J. Biomed. Mater. Res. Part B Appl. Biomater.* 89B, 325–334. <https://doi.org/10.1002/jbm.b.31219>
- Murphy, C.M., Haugh, M.G., O'Brien, F.J., 2010. The effect of mean pore size on cell attachment, proliferation and migration in collagen-glycosaminoglycan scaffolds for bone tissue engineering. *Biomaterials* 31, 461–6.  
<https://doi.org/10.1016/j.biomaterials.2009.09.063>
- Murr, L.E., Gaytan, S.M., Medina, F., Lopez, H., Martinez, E., Machado, B.I., Hernandez, D.H., Martinez, L., Lopez, M.I., Wicker, R.B., Bracke, J., 2010. Next-generation biomedical implants using additive manufacturing of complex, cellular and functional mesh arrays. *Philos. Trans. A. Math. Phys. Eng. Sci.* 368, 1999–2032. <https://doi.org/10.1098/rsta.2010.0010>
- Murray, G.A., Semple, J.C., 1981. Transfer of tensile loads from a prosthesis to bone using porous titanium. *J. Bone Joint Surg. Br.* 63–B, 138–41.
- Narayan, R.J., Doraiswamy, A., Chrisey, D.B., Chichkov, B.N., 2010. Medical prototyping using two photon polymerization. *Mater. Today* 13, 42–48.  
[https://doi.org/10.1016/S1369-7021\(10\)70223-6](https://doi.org/10.1016/S1369-7021(10)70223-6)
- Nelson, C., 2011. Factors Affecting the Success of Dental Implants, in: *Implant Dentistry - A Rapidly Evolving Practice*. InTech. <https://doi.org/10.5772/18746>

## References

- Niinomi, M.; Hattori, T. and Niwa, S., 2004. Material characteristics and biocompatibility of low rigidity titanium alloys for biomedical applications, In: Biomaterials in Orthopedics, Yaszemski, M.J., Trantolo, D.J., Lewandrowski, K.U. et al, (Ed.), , Marcel Dekker.Inc, New York 41–62.
- Nomura, N., Kohama, T., Oh, I.H., Hanada, S., Chiba, A., Kanehira, M., Sasaki, K., 2005. Mechanical properties of porous Ti–15Mo–5Zr–3Al compacts prepared by powder sintering. *Mater. Sci. Eng. C* 25, 330–335. <https://doi.org/10.1016/J.MSEC.2005.04.001>
- Nomura, N., Sakamoto, K., Takahashi, K., Kato, S., Abe, Y., Doi, H., Tsutsumi, Y., Kobayashi, M., Kobayashi, E., Kim, W.-J., Kim, K.-H., Hanawa, T., 2010. Fabrication and Mechanical Properties of Porous Ti/HA Composites for Bone Fixation Devices. *Mater. Trans.* 51, 1449–1454. <https://doi.org/10.2320/matertrans.M2010092>
- Nouri, A., D., P., We, C., 2010. Biomimetic Porous Titanium Scaffolds for Orthopedic and Dental Applications, in: Biomimetics Learning from Nature. InTech. <https://doi.org/10.5772/8787>
- Novaes Jr, A.B., Souza, S.L.S. de, Barros, R.R.M. de, Pereira, K.K.Y., Iezzi, G., Piattelli, A., 2010. Influence of implant surfaces on osseointegration. *Braz. Dent. J.* 21, 471–481. <https://doi.org/10.1590/S0103-64402010000600001>
- O'Brien, J., Wilson, I., Orton, T., Pognan, F., 2000. Investigation of the Alamar Blue (resazurin) fluorescent dye for the assessment of mammalian cell cytotoxicity. *Eur. J. Biochem.* 267, 5421–6.
- Otsuki, B., Takemoto, M., Fujibayashi, S., Neo, M., Kokubo, T., Nakamura, T., 2006. Pore throat size and connectivity determine bone and tissue ingrowth into porous implants: three-dimensional MicroCT based structural analyses of porous bioactive titanium implants. *Biomaterials* 27, 5892–900. <https://doi.org/10.1016/j.biomaterials.2006.08.013>
- Owen, R., Reilly, G.C., 2018. *In vitro* models for studying bone remodelling. *Front. Bioeng. Biotechnol.* 6, 134. <https://doi.org/10.3389/FBIOE.2018.00134>
- Özcan, M., Hämmerle, C., 2012. Titanium as a Reconstruction and Implant Material in Dentistry: Advantages and Pitfalls. *Materials (Basel)*. 5, 1528–1545.

<https://doi.org/10.3390/ma5091528>

- Parliament, T. E. and Union, T. C. O. T. E. (2010). Directive 2010/63/eu of the european parliament and of the council of 22 september 2010 on the protection of animals used for scientific purposes. <http://data.europa.eu/eli/dir/2010/63/oj> Date Accessed: 14/10/2018.
- Parthasarathy, J., Starly, B., Raman, S., Christensen, A., 2010. Mechanical evaluation of porous titanium (Ti6Al4V) structures with electron beam melting (EBM). *J. Mech. Behav. Biomed. Mater.* 3, 249–259.  
<https://doi.org/10.1016/J.JMBBM.2009.10.006>
- Papadimitropoulos, A., Scherberich, A., Güven, S., Theilgaard, N., Crooijmans, H.J.A., Santini, F., Scheffler, K., Zallone, A., Martin, I., 2011. A 3D in vitro bone organ model using human progenitor cells. *Eur. Cell. Mater.* 21, 445–58; discussion 458.
- Pautke, C., Schieker, M., Tischer, T., Kolk, A., Neth, P., Mutschler, W., Milz, S., 2004. Characterization of osteosarcoma cell lines MG-63, Saos-2 and U-2 OS in comparison to human osteoblasts. *Anticancer Res.* 24, 3743–8.
- Pelaez-Vargas, a, Gallego-Perez, D., Magallanes-Perdomo, M., Fernandes, M.H., Hansford, D.J., De Aza, a H., Pena, P., Monteiro, F.J., 2011. Isotropic micropatterned silica coatings on zirconia induce guided cell growth for dental implants. *Dent. Mater.* 27, 581–9. <https://doi.org/10.1016/j.dental.2011.02.014>
- Petite, H., Viateau, V., Bensaïd, W., Meunier, A., de Pollak, C., Bourguignon, M., Oudina, K., Sedel, L., Guillemain, G., 2000. Tissue-engineered bone regeneration. *Nat. Biotechnol.* 18, 959–963. <https://doi.org/10.1038/79449>
- President, V., Affairs, C., 2012. Trabecular Metal™ Dental Implants : Overview of design and developmental research 24–27.
- Rack, H.J., Qazi, J.I., 2006. Titanium alloys for biomedical applications. *Mater. Sci. Eng. C* 26, 1269–1277. <https://doi.org/10.1016/J.MSEC.2005.08.032>
- Ralston, S.H., 2009. Bone structure and metabolism. *Medicine (Baltimore)*. 37, 469–474. <https://doi.org/10.1016/j.mpmed.2009.06.014>
- Ramírez Fernández, M.P., Gehrke, S.A., Mazón, P., Calvo-Guirado, J.L., De Aza, P.N., 2017. Implant Stability of Biological Hydroxyapatites Used in Dentistry. *Mater.*



- (Basel, Switzerland) 10. <https://doi.org/10.3390/ma10060644>
- Rao, R.R., Ceccarelli, J., Vigen, M.L., Gudur, M., Singh, R., Deng, C.X., Putnam, A.J., Stegemann, J.P., 2014. Effects of hydroxyapatite on endothelial network formation in collagen/fibrin composite hydrogels in vitro and in vivo. *Acta Biomater.* 10, 3091–3097. <https://doi.org/10.1016/J.ACTBIO.2014.03.010>
- Rehman, I., Bonfield, W., 1997. Characterization of hydroxyapatite and carbonated apatite by photo acoustic FTIR spectroscopy. *J. Mater. Sci. Mater. Med.* 8, 1–4. [www.ncbi.nlm.nih.gov/pubmed/15348834](http://www.ncbi.nlm.nih.gov/pubmed/15348834)
- Rho, J.-Y., Kuhn-Spearing, L., Zioupos, P., 1998. Mechanical properties and the hierarchical structure of bone. *Med. Eng. Phys.* 20, 92–102. [https://doi.org/10.1016/S1350-4533\(98\)00007-1](https://doi.org/10.1016/S1350-4533(98)00007-1)
- Rosales-Leal, J.I., Rodríguez-Valverde, M.A., Mazzaglia, G., Ramón-Torregrosa, P.J., Díaz-Rodríguez, L., García-Martínez, O., Vallecillo-Capilla, M., Ruiz, C., Cabrerizo-Vílchez, M.A., 2010. Effect of roughness, wettability and morphology of engineered titanium surfaces on osteoblast-like cell adhesion. *Colloids Surfaces A Physicochem. Eng. Asp.* 365, 222–229. <https://doi.org/10.1016/j.colsurfa.2009.12.017>
- Rosser, J., Bonewald, L.F., 2012. Studying Osteocyte Function Using the Cell Lines MLO-Y4 and MLO-A5, in: *Methods in Molecular Biology (Clifton, N.J.)*. pp. 67–81. [https://doi.org/10.1007/978-1-61779-415-5\\_6](https://doi.org/10.1007/978-1-61779-415-5_6)
- Rumpler, M., Woesz, A., Dunlop, J.W.C., van Dongen, J.T., Fratzl, P., 2008. The effect of geometry on three-dimensional tissue growth. *J. R. Soc. Interface* 5, 1173–80. <https://doi.org/10.1098/rsif.2008.0064>
- Ryan, G., Pandit, A., Apatsidis, D.P., 2006b. Fabrication methods of porous metals for use in orthopaedic applications. *Biomaterials* 27, 2651–2670. <https://doi.org/10.1016/J.BIOMATERIALS.2005.12.002>
- Schiefer, H., Bram, M., Buchkremer, H.P., Stöver, D., 2009. Mechanical examinations on dental implants with porous titanium coating. *J. Mater. Sci. Mater. Med.* 20, 1763–1770. <https://doi.org/10.1007/s10856-009-3733-1>
- Schindeler, A., McDonald, M.M., Bokko, P., Little, D.G., 2008. Bone remodeling

## References

- during fracture repair: The cellular picture. *Semin. Cell Dev. Biol.* 19, 459–466. <https://doi.org/10.1016/j.semcdb.2008.07.004>
- Seah, K.H.W., Thampuran, R., 1998. The influence of pore morphology 40, 547–556. [https://doi.org/10.1016/S0010-938X\(97\)00152-2](https://doi.org/10.1016/S0010-938X(97)00152-2)
- Seth S., Kalra.P., 2013. Effect of dental implant parameters on stress distribution at bone-implant interface. *Inter J Sci Res* 2, 121–124. <http://docshare04.docshare.tips/files/17339/173394526.pdf>
- Semenoff-Segundo, A., da Silva, N.F., Palma, V.C., Marcal Vieira, E.M., Borges, A.H., Vedove Semenoff, T.A.D., 2015. Proposal for a new site to insertion of dental implants for osseointegration test: Research methodology. *Sci. J. Dent.* 2, 17–21. <https://doi.org/10.15713/ins.sjod.17>
- Shbeh, M.M., Goodall, R., 2015. Design of water debinding and dissolution stages of metal injection moulded porous Ti foam production. *Mater. Des.* 87, 295–302. <https://doi.org/10.1016/J.MATDES.2015.08.018>
- Shea, L.D., Wang, D., Franceschi, R.T., Mooney, D.J., 2000. Engineered Bone Development from a Pre-Osteoblast Cell Line on Three-Dimensional Scaffolds. *Tissue Eng.* 6, 605–617. <https://doi.org/10.1089/10763270050199550>
- Shibli, J.A., Mangano, C., D’avila, S., Piattelli, A., Pecora, G.E., Mangano, F., Onuma, T., Cardoso, L.A., Ferrari, D.S., Aguiar, K.C., Iezzi, G., 2009. Influence of direct laser fabrication implant topography on type IV bone: A histomorphometric study in humans. *J. Biomed. Mater. Res. Part A* 9999A, NA-NA. <https://doi.org/10.1002/jbm.a.32566>
- Shishkovsky, I. V., 2005. Shape Memory Effect in Porous Volume NiTi Articles Fabricated by Selective Laser Sintering. *Tech. Phys. Lett.* 31, 186. <https://doi.org/10.1134/1.1894427>
- Sidambe, A., 2014. Biocompatibility of Advanced Manufactured Titanium Implants—A Review. *Materials (Basel)*. 7, 8168–8188. <https://doi.org/10.3390/ma7128168>
- Simonelli, M., 2014. Microstructure evolution and mechanical properties of selective laser melted Ti-6Al-4V. © Marco Simonelli.
- Sittichokechaiwut, A., Scutt, A.M., Ryan, A.J., Bonewald, L.F., Reilly, G.C., 2009.

## References

- Use of rapidly mineralising osteoblasts and short periods of mechanical loading to accelerate matrix maturation in 3D scaffolds. *Bone* 44, 822–829. <https://doi.org/10.1016/j.bone.2008.12.027>
- Sivolella, S., Brunello, G., Ferroni, L., Berengo, M., Meneghello, R., Savio, G., Piattelli, A., Gardin, C., Zavan, B., 2015. A Novel *In vitro* Technique for Assessing Dental Implant Osseointegration. *Tissue Eng. Part C. Methods*. <https://doi.org/10.1089/ten.TEC.2015.0158>
- Slotwinski, J.A., Garboczi, E.J., Hebenstreit, K.M., 2014. Porosity Measurements and Analysis for Metal Additive Manufacturing Process Control. *J. Res. Natl. Inst. Stand. Technol.* 119, 494. <https://doi.org/10.6028/jres.119.019>
- Sommerfeldt D. and Rubin C., 2001. Biology of bone and how it orchestrates the form and function of the skeleton. *Eur. Spine J.* 10, 86–95. <https://doi.org/10.1007/s005860100283>
- Soon, Y.-M., Shin, K.-H., Koh, Y.-H., Lee, J.-H., Choi, W.-Y., Kim, H.-E., 2011. Fabrication and compressive strength of porous hydroxyapatite scaffolds with a functionally graded core/shell structure. *J. Eur. Ceram. Soc.* 31, 13–18. <https://doi.org/10.1016/J.JEURCERAMSOC.2010.09.008>
- Slotwinski J.A., Garboczi E.J., Hebenstreit K.M., 2014. Porosity Measurements and Analysis for Metal Additive Manufacturing Process Control. *Res. Natl. Inst. Stand. Technol.*, 119, 494-528.
- Steigenga, J.T., al-Shammari, K.F., Nociti, F.H., Misch, C.E., Wang, H.-L., 2003. Dental implant design and its relationship to long-term implant success. *Implant Dent.* 12, 306–17.
- Stevenson, G., Rehman, S., Draper, E., Hernández-Nava, E., Hunt, J., Haycock, J.W., 2016. Combining 3D human *in vitro* methods for a 3Rs evaluation of novel titanium surfaces in orthopaedic applications. *Biotechnol. Bioeng.* 113, 1586–1599. <https://doi.org/10.1002/bit.25919>
- Sykaras, N., Iacopino, A.M., Marker, V.A., Triplett, R.G., Woody, R.D., 2000. Implant materials, designs, and surface topographies: their effect on osseointegration. A literature review. *Int. J. Oral Maxillofac. Implants* 15, 675–90.

## References

- Teixeira, L.N., Crippa, G.E., Lefebvre, L.-P., De Oliveira, P.T., Rosa, A.L., Beloti, M.M., 2012. The influence of pore size on osteoblast phenotype expression in cultures grown on porous titanium. *Int. J. Oral Maxillofac. Surg.* 41, 1097–1101. <https://doi.org/10.1016/J.IJOM.2012.02.020>
- Tetteh, G., 2016. Polyurethane-based Scaffolds for Bone Tissue Engineering. The Role of Hydroxyapatite Particles, Solvent Combinations, Electrospun Fibre Orientations, In Vivo & In vitro Characterisation, and Particulate Leached Foams for creating 3-D Bone Models. PhD thesis, University of Sheffield., Sheffield, UK. <http://etheses.whiterose.ac.uk/id/eprint/16015>
- Tetteh, G., Pogorielov, M., Rehman, I., Reilly, G., 2016. A 3-dimensional biomimetic in-vitro bone model for testing small orthopaedic implants. *Front. Bioeng. Biotechnol.* 4. <https://doi.org/10.3389/conf.FBIOE.2016.01.01432>
- Thiyagasundaram, P., Sankar, B. V., Arakere, N.K., 2010. Elastic Properties of Open-Cell Foams with Tetrakaidecahedral Cells Using Finite Element Analysis. *AIAA J.* 48, 818–828. <https://doi.org/10.2514/1.J050022>
- Tolochko, N.K., Savich, V. V., Laoui, T., Froyen, L., Onofrio, G., Signorelli, E., Titov, V.I., 2002. Dental root implants produced by the combined selective laser sintering/melting of titanium powders. *Proc. Inst. Mech. Eng. Part L J. Mater. Des. Appl.* 216, 267–270. <https://doi.org/10.1177/146442070221600406>
- Tomisa, A.P., Launey, M.E., Lee, J.S., Mankani, M.H., Wegst, U.G.K., Saiz, E., 2011. Nanotechnology approaches to improve dental implants. *Int. J. Oral Maxillofac. Implants* 26 Suppl, 25-44; discussion 25–49.
- Tortelli, F., Cancedda, R., 2009. Three-dimensional cultures of osteogenic and chondrogenic cells: a tissue engineering approach to mimic bone and cartilage in vitro. *Eur. Cell. Mater.* 17, 1–14.
- Traini, T., Mangano, C., Sammons, R.L., Mangano, F., Macchi, A., Piattelli, A., 2008. Direct laser metal sintering as a new approach to fabrication of an isoelastic functionally graded material for manufacture of porous titanium dental implants. *Dent. Mater.* 24, 1525–1533. <https://doi.org/10.1016/j.dental.2008.03.029>
- Turner, C.H., 2006. Bone Strength: Current Concepts. *Ann. N. Y. Acad. Sci.* 1068, 429–446. <https://doi.org/10.1196/annals.1346.039>

## References

- Vaithilingam, J., Prina, E., Goodridge, R.D., Hague, R.J.M., Edmondson, S., Rose, F.R.A.J., Christie, S.D.R., 2016. Surface chemistry of Ti6Al4V components fabricated using selective laser melting for biomedical applications. *Mater. Sci. Eng. C* 67, 294–303. <https://doi.org/10.1016/J.MSEC.2016.05.054>
- van Grunsven, W., 2014. Porous metal implants for enhanced bone ingrowth and stability Ph.D. Thesis, University of Sheffield, Sheffield, UK. <https://etheses.whiterose.ac.uk/id/eprint/8612>
- van Grunsven, W., Goodall, R., Reilly, G.C., 2012. Highly Porous Titanium Alloy: Fabrication and Mechanical Properties. *J. Biomech.* 45, S339. [https://doi.org/10.1016/S0021-9290\(12\)70340-8](https://doi.org/10.1016/S0021-9290(12)70340-8)
- van Grunsven, W., Hernandez-Nava, E., Reilly, G., Goodall, R., 2014a. Fabrication and Mechanical Characterisation of Titanium Lattices with Graded Porosity. *Metals (Basel)*. 4, 401–409. <https://doi.org/10.3390/met4030401>
- Van Noort, R., 1987. Titanium: The implant material of today. *J. Mater. Sci.* 22, 3801–3811. <https://doi.org/10.1007/BF01133326>
- Vasconcellos, L.M.R. de, Oliveira, M.V. de, Graça, M.L. de A., Vasconcellos, L.G.O. de, Carvalho, Y.R., Cairo, C.A.A., 2008. Porous titanium scaffolds produced by powder metallurgy for biomedical applications. *Mater. Res.* 11, 275–280. <https://doi.org/10.1590/S1516-14392008000300008>
- Velasco-Ortega, E., Jos, A., Cameán, A.M., Pato-Mourelo, J., Segura-Egea, J.J., 2010. *In vitro* evaluation of cytotoxicity and genotoxicity of a commercial titanium alloy for dental implantology. *Mutat. Res. Toxicol. Environ. Mutagen.* 702, 17–23. <https://doi.org/10.1016/j.mrgentox.2010.06.013>
- Velmurugan, D., Santha, A.M., Sarate, S.G., 2017. Dental implant materials, implant design, and role of FEA. *J. Evol. Med. Dent. Sci.* 6, 3487–3492.
- Verborgt, O., Gibson, G.J., Schaffler, M.B., 2000. Loss of Osteocyte Integrity in Association with Microdamage and Bone Remodeling After Fatigue In Vivo. *J. Bone Miner. Res.* 15, 60–67. <https://doi.org/10.1359/jbmr.2000.15.1.60>
- Wally, Z.J., van Grunsven, W., Claeysens, F., Goodall, R., Reilly, G.C., 2015. Porous Titanium for Dental Implant Applications. *Metals (Basel)*. 5, 1902–1920.

- <https://doi.org/10.3390/met5041902>
- Wehmöller, M., Warnke, P.H., Zilian, C., Eufinger, H., 2005. Implant design and production a new approach by selective laser melting. *Int. Congr. Ser.* 1281, 690–695. <https://doi.org/10.1016/J.ICS.2005.03.155>
- Wen, C., Mabuchi, M., Yamada, Y., Shimojima, K., Chino, Y., Asahina, T., 2001. Processing of biocompatible porous Ti and Mg. *Scr. Mater.* 45, 1147–1153. [https://doi.org/10.1016/S1359-6462\(01\)01132-0](https://doi.org/10.1016/S1359-6462(01)01132-0)
- Wen, C., 2017. *Metallic foam bone, 5-Titanium foam scaffolds for dental applications* Woodhead Pub./Elsevier, Oxford, 131-160.
- Wennerberg, A., Albrektsson, T., 2009. Effects of titanium surface topography on bone integration: a systematic review. *Clin. Oral Implants Res.* 20, 172–184. <https://doi.org/10.1111/j.1600-0501.2009.01775>.
- Witek, L., Marin, C., Granato, R., Bonfante, E.A., Campos, F., Bisinotto, J., Suzuki, M., Coelho, P.G., 2012. Characterization and in vivo evaluation of laser sintered dental endosseous implants in dogs. *J. Biomed. Mater. Res. Part B Appl. Biomater.* 100B, 1566–1573. <https://doi.org/10.1002/jbm.b.32725>
- Wu, S., Liu, X., Yeung, K.W.K., Liu, C., Yang, X., 2014. Biomimetic porous scaffolds for bone tissue engineering. *Mater. Sci. Eng. R Reports* 80, 1–36. <https://doi.org/10.1016/J.MSER.2014.04.001>
- Wysocki, B., Idaszek, J., Szlązak, K., Strzelczyk, K., Brynk, T., Kurzydłowski, K., Świączkowski, W., 2016. Post Processing and Biological Evaluation of the Titanium Scaffolds for Bone Tissue Engineering. *Materials (Basel)*. 9, 197. <https://doi.org/10.3390/ma9030197>
- Xue, W., Krishna, B.V., Bandyopadhyay, A., Bose, S., 2007. Processing and biocompatibility evaluation of laser processed porous titanium. *Acta Biomater.* 3, 1007–18. <https://doi.org/10.1016/j.actbio.2007.05.009>
- Yi, Y.-A., Park, Y.-B., Choi, H., Lee, K.-W., Kim, S.-J., Kim, K.-M., Oh, S., Shim, J.-S., 2015. The Evaluation of Osseointegration of Dental Implant Surface with Different Size of TiO<sub>2</sub> Nanotube in Rats. *J. Nanomater.* 2015, 1–11. <https://doi.org/10.1155/2015/581713>

## References

- Yoshikawa, H., Tamai, N., Murase, T., Myoui, A., 2009. Interconnected porous hydroxyapatite ceramics for bone tissue engineering. *J. R. Soc. Interface* 6 Suppl 3, S341-8. <https://doi.org/10.1098/rsif.2008.0425.focus>
- Zanoni, M., Piccinini, F., Arienti, C., Zamagni, A., Santi, S., Polico, R., Bevilacqua, A., and Tesei, A., 2016. 3d tumor spheroid models for *in vitro* therapeutic screening: a systematic approach to enhance the biological relevance of data obtained. *Sci. Rep.* 6, 19103; <https://doi.10.1038/srep19103>
- Zheng, X., Lee, H., Weisgraber, T.H., Shusteff, M., DeOtte, J., Duoss, E.B., Kuntz, J.D., Biener, M.M., Ge, Q., Jackson, J. a, Kucheyev, S.O., Fang, N.X., Spadaccini, C.M., 2014. Ultralight, ultrastiff mechanical metamaterials. *Science* 344, 1373–7. <https://doi.org/10.1126/science.1252291>

## Chapter 9 : Appendix

## 9.1 Porous Titanium for Dental Implant Applications

*Metals* **2015**, *5*, 1902-1920; doi:10.3390/met5041902

OPEN ACCESS

*metals*

ISSN 2075-4701

www.mdpi.com/journal/metals/

Review

## Porous Titanium for Dental Implant Applications

Zena J. Wally <sup>1,2,3</sup>, William van Grunsven <sup>1,2</sup>, Frederik Claeysens <sup>1,2,3</sup>, Russell Goodall <sup>1</sup>  
and Gwendolen C. Reilly <sup>1,3,\*</sup>

<sup>1</sup> Department of Materials Science and Engineering, University of Sheffield, Sir Robert Hadfield Building, Mappin St, Sheffield S1 3JD, UK; E-Mails: zjwally1@sheffield.ac.uk (Z.J.W.); w.vangrunsven@gmail.com (W.G.); f.claeysens@sheffield.ac.uk (F.C.); r.goodall@sheffield.ac.uk (R.G.)

<sup>2</sup> Kroto Research Institute, University of Sheffield, Broad Lane, Sheffield S3 7HQ, UK

<sup>3</sup> Insigneo Institute for in silico Medicine, University of Sheffield, Pam Liversidge Building, Mappin St, Sheffield S1 3JD, UK

\* Author to whom correspondence should be addressed; E-Mail: g.reilly@sheffield.ac.uk; Tel.: +44-0-114-222-5986; Fax: +44-0-114-222-5943.

Academic Editors: Mark T. Whittaker and Hugo F. Lopez

Received: 17 July 2015 / Accepted: 10 October 2015 / Published: 21 October 2015

---

**Abstract:** Recently, an increasing amount of research has focused on the biological and mechanical behavior of highly porous structures of metallic biomaterials, as implant materials for dental implants. Particularly, pure titanium and its alloys are typically used due to their outstanding mechanical and biological properties. However, these materials have high stiffness (Young's modulus) in comparison to that of the host bone, which necessitates careful implant design to ensure appropriate distribution of stresses to the adjoining bone, to avoid stress-shielding or overloading, both of which lead to bone resorption. Additionally, many coating and roughening techniques are used to improve cell and bone-bonding to the implant surface. To date, several studies have revealed that porous geometry may be a promising alternative to bulk structures for dental implant applications. This review aims to summarize the evidence in the literature for the importance of porosity in the integration of dental implants with bone tissue and the different fabrication methods currently being investigated. In particular, additive manufacturing shows promise as a technique to control pore size and shape for optimum biological properties.



**Keywords:** dental implant; titanium; porosity; osseointegration; fabrication methods

---

## 1. Introduction

Dental implants are an effective treatment to replace the root part of the naturally missing tooth [1], in order to restore patients' appearance, speech and health [2]. They are completely placed into the jaw bone and give support to a dental prosthesis [1]. They are categorized according to their shape, surface roughness, surface treatment and the connection type with the prosthetic part. The length and diameter of commercially available dental implants vary according to the clinical treatment requirements. For example, the dimensions of cylindrical thread dental implants range from 3.25–6.0 mm in diameter and 5–18 mm in length [1]. Over the last decade, there has been a universal growing interest in dental implants, which are used to treat about one million people per year around the world [3]. The increasing demand for dental implants can be mostly attributed to their ability to completely restore dentition, the significant increase in the mean age of the world population, the higher number of elderly people in the population and higher public awareness [1]. Additionally, there are complications associated with conventional removable dentures, fixed crowns and bridges; for example, the reduced bearing area that supports the removable prosthesis due to the gradual bone resorption of the residual ridge following tooth extraction. Thus, using endosseous titanium implants is more convenient with better functionality than conventional dentures [4].

Nevertheless, dental implants, along with orthopedic implants face certain limitations, especially when used in smokers, diabetics, elderly osteoporotic patients and people with low bone density, such as a lack of biological interaction and interfacial stability with bone tissue [5]. Fundamentally, implants need to be constructed from biomaterials compatible with the human body environment. Titanium and its alloys have been reported as the materials of choice for most orthopedic and dental implants due to their outstanding mechanical properties and biocompatibility [6]. However, the Young's modulus of these materials is higher than that of mineralized tissue. Furthermore, the traditional structure of titanium for medical and dental implants is non-porous; this dense structure of implants can cause a mismatch between the Young's modulus of the titanium implant (110 GPa) and natural cortical (17–20 GPa) and cancellous bone (around 4 GPa) [7–9].

The high Young's modulus of titanium implants leads to stress shielding and inadequate loading of the underlying bone tissue [10]. Since bone is a living tissue which is continuously modified by the bone cells in response to external signals, reduced mechanical loading leads to resorption of bone, implant loosening and ultimately failure, which has particularly been a problem for orthopaedic implants in the past [9]. Alternatively, overloading also creates high stresses in local regions of bone which can also initiate resorption [11]. Accordingly, many attempts have been undertaken to develop biomaterials with mechanical properties well-suited to the bone tissue. Most of these studies have aimed at optimising the important features of interactions between the implant surface and bone tissue. Advances in orthopaedic and dental implant design, as well as scaffolds for bone tissue engineering, have all contributed to the fabrication of novel porous titanium structures, and these fields draw on each other's technologies.

Implant morphology has a crucial role in bone-implant contact and can enhance the osseointegration process. To improve dental implant stability different surface modifications have been proposed to adapt the properties of titanium dental implants [12]. Modifying the implant surface can improve the implant to bone interaction, however, there is not always a clear explanation for the mechanism of improvement. For example, a morphological or a chemical mechanism, such as roughening the implant surface can also create modifications in the chemistry of the dental implant surface [13]. Plasma spraying with different powder particles such as titanium oxide, calcium phosphate and hydroxyapatite has been used to coat dental implants [14]. Sand blasting with stiff particles such as alumina, TiO<sub>2</sub> and ceramic has also been suggested to roughen the dental implant surface [3]. Çelen & Özden in 2012 advocated another more controllable technique of laser micro-machining of commercially pure titanium dental implant [15]. Materials with nanometer-scale porosity such as TiO<sub>2</sub> nanotubes have also been used recently as implant surface-treatments. These materials can be generated on the titanium dental implant by controlling the anodizing process (Figure 1) [16].

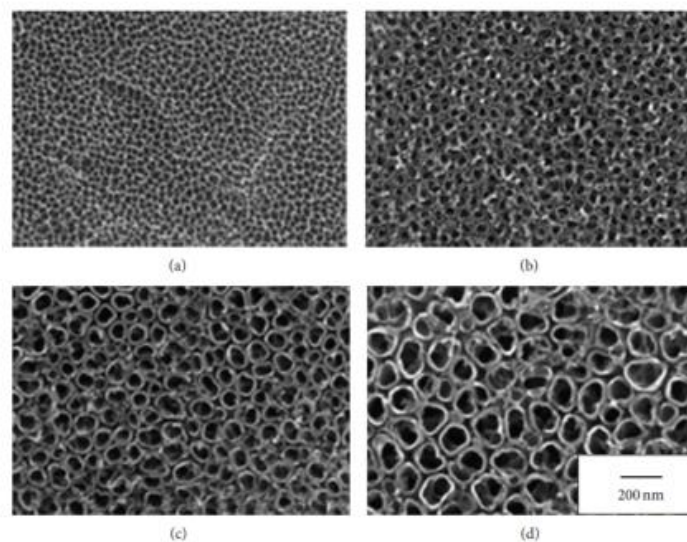


**Figure 1.** SEM images of different diameter sizes of TiO<sub>2</sub> nanotubes, (a) 30; (b) 50; (c) 70 and (d) 100 nm using 200 nm scale bar. Adapted from Ref. [16].

Despite being very successful, there are some shortcomings associated with these procedures; the bulk structure is still high-density titanium, the coating materials can dissolve over a long period of time. Moreover, coating particles that break away from the surface could have a negative biological effect on the adjacent tissue such as peri-implantitis [14]. Therefore, several alternative approaches have been proposed to overcome these drawbacks of coating materials by creating porous biomaterials as a substitute for the classical solid structure. Cellular structures can provide a suitable biological environment for the host tissue to grow into the pores [6], providing improved early implant stability, as demonstrated by commercially available dental implants from Zimmer with a porous tantalum central

region. To our knowledge, the Zimmer implant is the only porous dental implant on the market and animal and short-term clinical studies indicate excellent bone integration and implant stability [17]. However, tantalum is an expensive material which may not be affordable to many seeking dental implant treatments, and, therefore, methods of providing a porous structure in titanium or a titanium alloy is of strong interest to the dental implant community [18].

To date, numerous studies have been undertaken to manipulate the mechanical and topographical properties of titanium implants. In many studies, micro- and nanoporous titanium has been proposed as a promising alternative to solid structures for biomedical and dental implant applications. Many fabrication methods have been used to fabricate porous titanium for medical purposes. However, the size, shape, percentage and distribution of pores were variable and need further optimization [19]. This review article aims to summarize the evidence in the literature of the benefits of using porous structures to improve integration of titanium dental implants with bone tissue. Furthermore, the most widely used fabrication methods for porous titanium are discussed as well as their potential to be used for dental implants.

## 2. Titanium and Its Alloys as Implant Materials

Ever since the 1960s, commercially pure titanium and its alloys have been shown to be versatile biomaterials that can be used to produce a variety of medical devices including those used in dentistry [7]. This is mostly related to their unique properties such as excellent mechanical behavior, superior corrosion [20], as well as high ratio of strength to weight [21]. Titanium is biocompatible because it is biologically nearly inert and well tolerated by the environment of the human body. According to the British Standards for surgical implants, the oxygen percentage should not exceed 0.5% [22]. Furthermore, the properties of titanium are influenced by its structure which is made up of two allotropic structures: a close packed hexagonal ( $\alpha$  phase) and body-centered cubic crystal ( $\beta$  phase). These phases enable titanium to undergo a reversible transformation; at room temperature it tends to be categorized as  $\alpha$  phase and transfer to  $\beta$  phase as the temperature exceeds 883 °C [8].

The strength properties of commercially pure titanium are weaker than that required for medical implants [23]. Thus, to improve these properties, titanium alloys have been proposed via incorporation of variable types and quantities of elements such as Al, Mo, V, Nb, Ta, Mn, Fe, Cr, Co, Ni and Cu. Each of these elements has a different impact on the transition temperature of titanium alloys. Those that increase the transition temperature, such as aluminium, are identified as  $\alpha$  stabilizing element, whereas those that decrease it, such as vanadium, are referred to as  $\beta$  stabilizing elements. Accordingly, alloys are classified into three main types ( $\alpha$ ,  $\beta$ , and  $\alpha + \beta$  alloys) depending on their transition temperature [23].

Through the years, several types of titanium alloys have been developed as implant biomaterials such as Ti-6Al-4V, Ti-Nb-Ta-Zr [23], Ti-Ni-Ta [24], Ti-15Mo-5Zr-3Al [25], Ni-Ti [26] and Ti-Sn-Nb [27]. Among the aforementioned alloys, Ti-6Al-4V [28] and Ni-Ti [29] have been reported as the most widely used biomedical materials for bone replacement devices, also in comparison to other medical grade alloys such as stainless steel and Co-29Cr-6Mo. This is due to the better mechanical performance of these titanium alloys [28], and their significant corrosion resistance, especially for the interconnected porous titanium structures due to the free flow fluid inside the pores [30]. This allows

them to be used as load-bearing implants for tissue engineering scaffolds [31]. Nevertheless, Andani *et al.* stated that despite the flexible modulus of elasticity of NiTi, it was not straightforward to design interconnected porous structured scaffolds with this alloy because of its high melting point [32]. Even with the popularity of Ti-6Al-4V and NiTi the potentially adverse biological reaction to their elements by the living tissue still remains a matter of concern. This has directed researchers to keep developing alloys aimed at improving biocompatibility such as Ti-6Al-7Nb, Ti-13Nb-13Zr. These are more likely to mimic the biological and mechanical properties of Ti-6Al-4V [33].

The elastic modulus of pure titanium and its alloy (Ti-6Al-4V) is half that of Co-Cr, thus stress shielding is lower [34]. In order to produce titanium alloy with reduced Young's modulus and adequate strength for orthopaedic implants, various attempts have been reported in the literature. For instance, in 1998, Kuroda *et al.* introduced Ti-Nb-Ta-Zr, Ti-Nb-Ta-Mo and Ti-Nb-Ta-Sn [35]. Matsumoto *et al.* (2005) introduced B-type titanium alloys (Ti-29Nb-13Ta-4.6Zr) and (Ti-Nb-Sn) which showed a remarkably lower Young's modulus [36]. Attempts have also been made to produce porous Ti alloy compacts (Ti-15Mo-5Zr-3Al) using a hot-pressing technique, which could reduce the Young's modulus to within the range of cortical bone [25]. Another possibility is to incorporate hydroxyapatite particles with titanium powder using an infiltration method and sintering [37]. The addition of hydroxyapatite has the additional aim of improving bone fixation because bone cells attach well to hydroxyapatite surfaces [38]. The Young's modulus of porous titanium-hydroxyapatite composites can be controlled by changing the percentage of hydroxyapatite particles [37].

### 3. Characteristic Features of Porous Metal

Due to their morphology, physical and mechanical properties, porous metal structures have many possible applications in several different industries [39], including medicine [40]. Several classification systems have been used in the literature for porous metals of different types; these can, for example, be based on the structure, applications, properties or fabrication processes used. For bone applications, porous metal is typically classified into three main forms, which describe the nature of the whole component: completely porous across the whole metal parts, an entirely or partially porous layer coating a dense core or structure composed of a fully solid and a porous metal part joined together [34]. Considering the porous part on its own, Goodall *et al.* classified porous metals according to their structure, producing five groups: materials containing isolated porosity, true metal foams, particle packing to form a porous body, precursor based metal foams and lattices [41]. Additionally, for any of these types, porosity can be designed in a graduated manner, for example, by increasing in quantity from the core to the superficial layer [42,43]. Nevertheless, due to the reduction in mechanical properties that the incorporation of porosity brings, an entirely porous metal structure is unlikely to be suitable for an implant with a load bearing requirement. Therefore, a porous cover on a solid substrate is often preferentially chosen for dental implants to ensure sufficient strength to tolerate the physiological loads [34].

Porous metals exist in both closed (fully isolated pores) and open cell forms (connected with each other and the external environment). Although both types are widely used, the open type is evidently better for medical implant applications, because a degree of ingrowth into the structure is desired [44]. As well as providing a suitable environment for the bone cells such that they infiltrate into the porosity,

an interconnected foam with sufficiently large pores allows the formation of the vascular system required for bone maintenance [28,45].

Within the porous metals and the classification system used by Goodall *et al.* [41], lattices are those structures made up of a regular repeating array of simple structural elements. These have certain attractive features, such as the fact that the properties can in principle be predicted to greater accuracy than when the pores are randomly located, though they have formerly been difficult to produce in anything other than elementary forms and small sizes, barring certain structures such as honeycombs. However, this is changing with the growth in, and further development of, additive manufacturing technologies, which deposit or fuse material, building up a 3D structure (as detailed in Section 4). Within the lattices, the regular repeating unit cell structure has a dominant role in determining the mechanical properties of the structure overall [40]. An almost infinite array of designs is possible, and many have been produced, two dimensional honeycombs [46], simple cubic lattices [47], rhombic dodecahedron [48] and diamond lattice (a cubic unit cell where the struts are positioned in the same way as the atomic structure of diamond) [49,50]. Graded lattices are also possible; recently, van Grunsven *et al.* used different strut thicknesses to produce a diamond lattice structure with graded porosity (Figure 2). In this study, it was found that the mechanical properties that could be achieved could be relevant for orthopedic implants [51]. Analytical and numerical solutions for the mechanical properties of a diamond lattice structure of Ti-6Al-4V were reported by Ahmadi *et al.* The results were compared with experimental observations. According to their findings, there was a good agreement between the analytical solutions and experimental observations, whereas the prediction of the finite element models was less likely to be accurate when compared with the experimental observations [40]. This is somewhat unexpected as finite element methods should allow more complex behavior to be captured, but may indicate imperfect input parameters for the base alloy. It has been pointed out that the mechanical properties of the porous Ti-6Al-4V alloy with the diamond unit cell are similar to those of trabecular bone [52]. A similar approach, but for random porous structures, has been used by Cheng *et al.*, in which they used human trabecular bone as a template to define a structure allowing an interconnected porous Ti-6Al-4V structure to be created using different levels of porosity (15%–70%). By increasing the porosity, a structure was created which closely mimics that of trabecular bone [5].

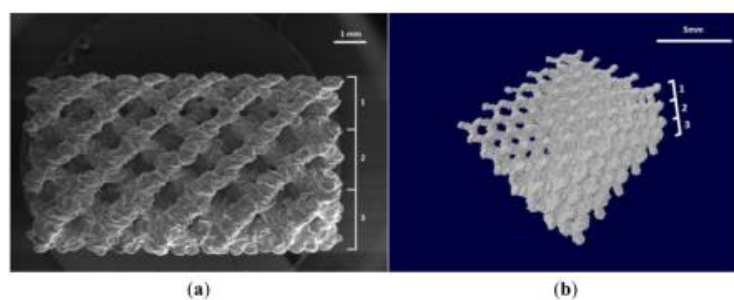


**Figure 2.** (a) SEM image of graded diamond lattice structure; (b) Micro CT scan of 3D image shows different strut thicknesses. Adapted from Ref. [51].

Typically, a porosity of 75%–85% and a pore size of more than 100  $\mu\text{m}$  are considered to be preferable for rapid bone ingrowth [19]. Wen *et al.* revealed that porous titanium with pore size ranging from 200–500  $\mu\text{m}$  was sufficient for adequate bone formation and fluid transport [53]. Otsuki *et al.* have examined sintered porous titanium implants with different levels of porosity (50% and 70%) and pore sizes (250–500  $\mu\text{m}$ ) and (500–1500  $\mu\text{m}$ ). The results indicated 500–1500  $\mu\text{m}$  was the optimal pore size for bone tissue ingrowth for both levels of porosity [54], whereas Murphy *et al.* stated that the ideal pore size for bone ingrowth was around 325  $\mu\text{m}$  [55]. A graded structure as a coating with macro and nanoporosity (at a level of more than 70%) on titanium substrates was another approach developed by Fu *et al.* Three different materials (hydroxyapatite, calcium carbonate and titanium) and a combination of a modified plasma spray method and anodic oxidation process were used to produce porous scaffolds with macro-, micro- and nanopores (100–350  $\mu\text{m}$ , 0.2–90  $\mu\text{m}$  and 100 nm, respectively). The result showed that the mechanical properties were close to those of bone [56]. Chen *et al.* created titanium scaffolds with a uniform and highly porous structure. The porous specimens were produced by stack sintering of micro porous Ti spheres using centrifuge granulation technique. Based on the properties of the original titanium powders specimens should have micro- and macroporosity of 6.1–11.8  $\mu\text{m}$  and 180.0–341.8  $\mu\text{m}$ , respectively, and the mechanical properties were reported as being suitable for implant applications in load-bearing areas [57].

As can be seen, there is no clear identification of the optimum pore size for bone ingrowth. In general, the mechanical and biological performance of the porous metal structure is governed by the combined effects of characteristic features of the porosity such as pore shape, size, distribution and their interconnectivity, as well as the base metal from which the porous structure is made [58]. Thus, with the current level of understanding the pore geometry needs to be optimized for each specific case to achieve a suitable environment for the surrounding bone tissue. Furthermore, it should be noted that not only the properties of the coating, but also those of the underlying base material will have an effect on the mechanical properties of the final product.

#### 4. Fabrication Methods and Mechanical Evaluation of Porous Titanium Dental Implants

Titanium is well known as a relatively high cost engineering material due to the difficulties in the extraction, forming and machining processes [59]. Traditionally, a titanium alloy dental root implant is manufactured via a casting or powder metallurgy route [60]. With the casting method, in particular, machining and other finishing steps are required with a large amount of waste material [8]. Furthermore, the high melting temperature of the titanium base alloy and the high reactivity of titanium with atmospheric gasses at elevated temperatures make it difficult to adapt many existing techniques which were developed for lower melting point metals, such as aluminium [34]. Powder metallurgy has more recently been promoted for titanium implant production. It is less expensive and has reduced amounts of waste compared to the other production methods available [8]. Relatively simple techniques for the production of porous materials include sintering hollow spheres or the use of thermal decomposition of, for example,  $\text{TiH}_2$ . Fairly homogenous foam structures have been made from high melting temperature metals such as titanium and its alloys [19] and this method is also suitable for the production of titanium foams with pore sizes meeting the standard requirements considered to be suitable for bone ingrowth [6].

Improving the compaction process of alloy powder also has an influence on the accuracy and degree of porosity of the final part [61].

For porous materials as a whole, there are certain potential disadvantages for use as implants. For example, the fatigue strength is unlikely to satisfy the requirements of implant devices. Nevertheless, this can be improved. It has, for example, been shown that, for cases where a foaming agent is combined with metal powder, the fatigue life can be increased by having a more uniform foam structure through reduced stress concentrations. This is achieved by adjustments to the mixing strategy for the powder of foaming agent, metal and binder as reviewed by Ryan *et al.* [34]. Other methods have shown their suitability for the production of medical grade titanium alloy for medical applications, including sintering of powders, compressing and sintering of titanium beads or fibers to create interconnected porous structures [62].

For more regular titanium pore geometry, a controlled mix of removable space holder and titanium metal powder particles has been suggested and explored by a considerable number of studies. The range of materials used as a space holder include saccharose crystals [63], NaF [64], NaCl [65,66] and polymer granules [67]. Magnesium has also been used as a space holder to produce porous dental and orthopedic implants [68]. Jurczyk *et al.* recommended ammonium hydrogen carbonate to produce a porous nanocomposite scaffold using titanium containing 10 wt. % SiO<sub>2</sub> appropriate for dental applications [69]. Caution is recommended though as a strong reaction has been reported between titanium and some space holders with both high and low melting temperatures, leading to the formation of impurities within the foam [70].

With all the aforementioned approaches, titanium implants can be made with an entirely porous or solid structure though it is not straightforward to produce a porous shell on a solid core. A variety of methods have been developed over the last few decades to create dental root implants which mimic the morphology and mechanical properties of natural dental roots [60]. One method involving an electron-discharge compaction has also been reported to produce porous surface on the commercially dental implant, porosity on a compact core was created using input energy 1–2.5 kJ/g to atomized the Ti–6Al–4V powder [71]. A one-step microwave processing method has also been suggested to sinter titanium powders in order to produce dental implants, with gradient porosity, microwave power energy of 1–1.5 kW and a 30 min soaking period used. The pore size was about 30–100 μm and thickness was ranging from 100–200 μm, as determined by the level of microwave power [62].

Among these methods, additive manufacturing technology has been developed considerably [72] including selective laser sintering (SLS) [73], selective laser melting (SLM) and electron beam melting (EBM) [74]. The additive manufacturing approach is based on building up a three-dimensional structure from a computer aided design (CAD) model [34]. Each fabrication method will have many variables; for example, for SLS, parameters would include laser power, scanning speed, laser beam diameter and layer thickness [72]. Additive processes are in general less time consuming overall [72] and allow the creation of porous structures with different unit cells [40] and high resolution (*i.e.*, small cell sizes) [75].

Additive manufacturing technology has more specifically been applied to produce non-porous parts with complex geometry for use in implants, such as dental, craniofacial, maxillofacial and orthopedic implants [59]. In 2002, Tolochko *et al.* demonstrated the possibility of producing dental root implants from Ti powders with two different zones, comprising a compact core and irregular porous shell by incorporating (SLS) for the porous surface and (SLM) for the solid core. The thickness of both layers

was determined by the laser power. Microscopical examination showed that the average pore size was 100–200  $\mu\text{m}$  and the porosity 40%–45% [60]. Dental implant models with a dense core and porous layer consisting of a series of channels which are 1 mm in depth and 1 mm in diameter have been considered. Laser-forming techniques with continuous wave and pulsed lasers were used. The channel diameters of the products were lower than those of the CAD model. The fatigue and tensile strength of the titanium samples produced were influenced by the different processing parameters utilized in this study. These variables include the scanning speed of the laser, the laser peak power and the hatching pitch, all of which combine to alter the amount of energy input into the material, and thus influence the solidification and cooling. The effect is to alter the microstructure of the material, and as the flow of thermal energy is also affected by part shape and location in the part. This can occur in complex ways. The processing parameters were found to be optimal at a scan speed of 6 mm/s, a laser peak power of 1 kW, and a hatching pitch of 0.4 mm [76]. Traini *et al.* have also produced titanium dental implants incorporating graduated porosity from the inner core of the structure to the outer surface using titanium alloy (Ti–6Al–4V) powders with a laser sintering procedure. The average porosity was 28.7% and the modulus value of the dense core was similar to that of a machined titanium implant whereas the porous part was comparable to that of bone tissue [73]. The study of Mangano *et al.* did not go quite as far as producing a fully porous structure, rather stating that direct laser fabrication is an economical technique that has potential to produce dental implants with irregular and narrow intercommunicating crevices and shallow depressions using titanium alloy powder. The surfaces were analyzed under stereo scanning electron microscopy. However, there was a residue of metal particles on the implant surface. Thus, they suggested acid etching as treatment to eliminate the adherent particles [77].

Schiefer *et al.* examined the long term stability and mechanical properties of two types of porous dental implants under static and dynamic conditions. Implants were surrounded by porous layers that were made using ammonium hydrogen-carbonate ( $\text{NH}_4\text{HCO}_3$ ) as space holder particles. Samples were tested in fatigue according to modified ISO 14801 and finite element analysis (FEA) was used to predict the fatigue behavior of these implants. This suggested that implants will struggle to perform well against forces in a range similar to that produced by human jaw. Moreover, pore alignment can affect the mechanical properties of porous titanium [10]. Murr *et al.* in 2010 used electron beam melting (EBM) to produce Ti–6Al–4V open cellular foams with different cell wall structures (solid and hollow). The elastic moduli were found to decrease with increasing porosity as widely known for porous metals of all types. However, the micro indentation hardness of the solid cell wall structure was lower than that of the hollow cell wall [75]. Li *et al.* established that the electron beam melting process has the potential to process Ti–6Al–4V implants with versatile pore geometry. The compressive properties of porous implants are variable with pore architecture and can be similar to those of natural bone [46]. To improve the surface wear resistance of the titanium structures, Laoui *et al.* applied laser gas nitriding using a CW Nd:YAG laser, and the coating layer was able to withstand more cycles without fracturing [76].

One of the essential requirements of dental implants is to have a rough surface with macroscopic grooves and threads or a porous surface to provide primarily mechanical stabilization between implants and bone tissues [60]. Furthermore, sufficient mechanical support should be provided between the root of the dental implant and its superstructure crown. This can be achieved by creating a solid core and porous shell as a substitute to an entirely porous structure [60]. One concern is that stress concentrations could arise at the junction area of the shell and core of the implant where the mechanical properties



change rapidly [34]. This weakens the bond between the covering layer of the implant and the core. To reduce the component of this problem that is related to residual stresses, a post-sintering heat treatment has been suggested by Cook and co-workers, which showed an improvement in the fatigue strength of titanium alloy by about 15% [78]. Nevertheless, the idea of creating functionally graded structures can be helpful to avoid the stress concentration between the interface layers where the elastic modulus changes suddenly [79]. The concept of creation of functionally graded structures in porous materials by changing the structure of the lattice has also been investigated [80].

**Table 1.** Comparison table of the main fabrication methods used for creating rough and porous implants with potential dental and/or orthopedic applications.

Fabrication Methods	References
Plasma spraying with different powder particles such as: -titanium oxide -calcium phosphate -hydroxyapatite	[14]
Sand blasted with stiff particles such as: -alumina -TiO <sub>2</sub> -ceramic	[3]
Laser micro-machining technique	[15]
Anodization TiO <sub>2</sub> nanotube	[16]
Electron-discharge compaction	[71]
One-step microwave processing method	[62]
Powder metallurgy -sintering hollow spheres -thermal decomposition -sintering of powders, compressing and sintering of titanium beads or fibers	[19,62]
Removable space holder and titanium metal powder particles: -saccharose crystals -NaF -NaCl -polymer granules -Magnesium -ammonium hydrogen carbonate	[63–69]
Additive manufacturing technology: -selective laser sintering -selective laser melting -electron beam melting	[60,66,74]

Bandyopadhyay and colleagues suggested laser engineered net shaping (LENS<sup>TM</sup>) to construct porous structures from Ti–6Al–4V alloy across the range 23%–32% porosity with low modulus (7–60 GPa) which can be tailored to match human cortical bone [81]. Nomura *et al.* in 2010 recommended the infiltration technique in a vacuum with sintering to create porous titanium/hydroxyapatite composites. The Young's modulus was estimated using the percentage of porosity and it was tailored to be in the range of bone tissue (given by 24%–34% porosity). Porosity can be controlled by modifying the

temperature and pressure applied in a hot-pressing stage. Furthermore, Hanks' buffered salt solution was used to reduce the Young's modulus of the sintered porous titanium/hydroxyapatite composites [37]. Witek *et al.* measured the bone implant contact and removal torque of dental implants with a porous layer produced by laser sintering and compared them with sandblasted-acid etched implant (*i.e.*, those with a rough, but not porous, surface). They concluded that porous dental implants produced by the sintering process showed better biomechanical properties and biocompatibility [82]. The fabrication methods discussed in this review are listed in Table 1.

### 5. Biological Interaction and Porous Surface Geometry

Most dental implant materials aim to support cell attachment by conferring suitable area for cell adhesion [83]. It has been demonstrated that bone cell interactions are mainly modulated by the chemistry and mechanical properties of the substrate, the structure of the implanted material and the fabrication method. Cell behavior has been stated to be more influenced by the topography of the surface, it encounters than by the chemistry of implant material or processing method [84], although these effects are difficult to separate as they are all interrelated [83]. *In vivo* and *in vitro* observations of the micro- and macro-roughness of the surfaces of dental and orthopedic implants have been shown to play an important role in improving the response of bone-forming cells (osteoblasts) [3]. Rough surfaces provide better osteoblast attachment [19], improved cell proliferation and extracellular matrix formation which in turn enhance the osseointegration process and durability of dental implants [85].

A porous implant surface has a high surface area which should enable more cells to attach compared to a planar surface. *In vitro* observations have demonstrated a good range of bone ingrowth in porous titanium implant using different manufacturing techniques [6]. Teixeira *et al.* examined the osteoblastic response on porous titanium with different pore sizes (312, 130, 62  $\mu\text{m}$ ) using a powder metallurgy technique. The result showed the highest gene expression of bone markers was with 62  $\mu\text{m}$  porosity [6]. Mangano *et al.* seeded human dental pulp stem cells on direct laser metal sintered titanium scaffolds and acid etched surfaces. They observed that gene expression and protein secretion were faster on laser sintered scaffolds [86]. Another comparative study has been proposed between porous and non-porous titanium alloy Ti-6Al-4V samples. The pore diameters were 500, 700 and 1000  $\mu\text{m}$ . The result showed that the osteoblast cell viability was maintained over 14 days and the cells entirely covered the porous structure [87]. Cheng *et al.* proposed using a template from human trabecular bone to fabricate porous Ti-6Al-4V materials using additive manufacturing technology, laser sintering in particular. Different porosities (low, medium and high) ranging from 15%–70% with interconnected structure were fabricated to produce structures that mimicked the trabecular bone of the human body. After specific surface treatment with calcium phosphate particles and acid etching, the trabecular bone structure exhibited micro and nanoscale porosity which was able to enhance osteoblast cell differentiation. Thus, the trabecular structure has the potential to produce devices well-suited for dental and orthopedic implants [5]. Another attempt to improve the mechanical and biological properties of porous titanium structures also incorporated a modified sponge replication method and anodization process. Titanium scaffolds with elongated pores were produced by coating a stretched polymeric sponge template with  $\text{TiH}_2$ . The anodization of the titanium can produce a nanoporous surface that can increase osteoblast cell (MC3T3-E1) proliferation and attachment on implant surfaces [88]. Pore geometry is likely to have a

strong effect on cell attachment and matrix formation [89] but researchers rarely investigate different pore geometries within a single material and manufacturing process. Recently, such a study was undertaken by Markhoff *et al.* who evaluated the viability and proliferation of human osteoblast cells in porous Ti-6Al-4V using different scaffold designs and cultivation methods. Additive manufacturing technology was used to produce different pore geometries (cubic, diagonal, pyramidal), and static and dynamic culture methods were used. Interestingly, there were no significant differences between the static and dynamic cultivation methods, but cell activity and migration were best in the pyramidal design with a 400–620  $\mu\text{m}$  pore size and 75% porosity [90].

Although *in vitro* studies are often an essential step in the discovery of novel implant materials and structures, there are many inherent limitations to the use of cell culture to predict the long-term survival of an implant. These include the absence of a 3D environment that adequately mimics the chemical and mechanical properties of bone, the lack of mechanical forces acting at the bone-implant interface after implantation, the absence of the complex matrix of proteins and different types of bone cells that are present at the bone-implant interface *in vivo* and the difficulty of maintaining the culture for long time periods. While researchers are attempting to improve *in vitro* studies using 3D environments and bioreactors, the current information regarding long-term implant stability comes from *in vivo* studies.

*In vivo* studies by Mangano and co-workers used a laser sintering process to design titanium dental implants with interconnected pores and irregular crevices. The clinical observation showed 95% success after one year post operation [72]. In histological evaluations, Shibli *et al.* measured human bone tissue response to three types of dental implants: direct laser fabrication, sand-blasted acid-etched and machined commercially pure titanium under unloaded conditions. The result indicated that after eight weeks of implant insertion, the bone-implant contact produced by the direct laser and the sandblasted acid-etched processes was not significantly different but was higher than that of machined implant, and there were no significant differences between them. The authors attributed their finding to the surface roughness that was produced by the laser and sandblasting techniques, which enhanced the osseointegration process [91]. Another study using male Sprague-Dawley rats indicated that the biological fixation was influenced by the percentage of porosity in titanium implants (25%, 11%, 3%). After 16 weeks' examination, the concentration of calcium ions increased proportionally with the increasing porosity percentage [81]. Laoui *et al.* inserted a Ti implant into a dog's lower jaw and revealed clear bone growth into the porous structure within the porous surface layer, and no signs of inflammation at the interface were observed [76]. Tolochko *et al.* inserted a prototype porous dental implant into the lower jaw of a cadaver and demonstrated that the implant was firmly integrated into the alveolar ridge of the lower jaw with a maximum gap width of 200–300  $\mu\text{m}$  between the implant and the bone [60]. Another attempt was made to reduce the healing period required for the dental implant and bone by coating a titanium dental implant with TiO<sub>2</sub> nanotubes, which was tested in a rat femur. Variable diameter sizes were used (30 nm, 50 nm, 70 nm, and 100 nm nanotubes), the highest removal torque and osseointegration rate were observed in the 30 nm implants after two weeks whereas the 70 nm implants exhibited the highest value after six weeks for both tests [16].

## 6. Conclusions and Future Perspectives

Recent developments in the fabrication of porous architectures for bone ingrowth into dental implant materials have been reviewed. Novel materials developed for orthopaedic implants and bone tissue engineering could also be applied to dental implants due to their similar design requirements; the materials should be biocompatible, non-toxic, corrosion resistant and load bearing. It is not straightforward to create porous titanium with traditional methods. However, the development of additive manufacturing technology enables a designer to produce more regular porous structures with modulated pore sizes, shapes, percentages and distributions and to mimic the biological and mechanical properties of natural bone.

Porous dental implant prototypes manufactured with the additive manufacturing technique have been evaluated from a mechanical and biological point of view. As can be seen, introducing porosity appears to improve implant stability. The optimal pore size is probably somewhere between 200 and 1000  $\mu\text{m}$ , and roughness and surface chemistry also play an important role in determining the fate of stem cells and osteoblasts. Work in this area is promising and provides a basis for exciting improvements in dental implant design for patients with compromised bone healing. However, the body of research to date has still not clearly identified the optimal pore size, geometry and graduation for the most effective biomechanical and biological properties. Therefore, further studies are necessary to evaluate the potential of advanced manufacturing methods to optimize the porous titanium structure of dental implants.

## Acknowledgments

The authors acknowledge funding for ZJW from Iraqi Ministry of Higher Education and Scientific Research and or WvG from Orthopaedic Research UK (ORUK). The views expressed here do not necessarily represent those of ORUK.

## Author Contributions

Z.J.W. wrote the bulk of manuscript in consultation with the other authors. W.v.G. provided preliminary data and literature review and edited the manuscript. R.G., G.R. and F.C. wrote small sections, edited and advised on the final version of the manuscript.

## Conflicts of Interest

The authors declare no conflict of interest.

## References

1. Elias, C.N. *Factors Affecting the Success of Dental Implants*; Turkyilmaz, I., Ed.; InTech: New York, NY, USA, 2011.
2. Esposito, M.; Hirsch, J.; Lekholm, U.; Thomsen, P. Differential Diagnosis and Treatment Strategies for Biologic Complications and Failing Oral Implants: A Review of the Literature. *Int. J. Oral Maxillofac. Implant.* **1999**, *14*, 473–490.

3. Le Guéhennec, L.; Soucidan, A.; Layrolle, P.; Amouriq, Y. Surface treatments of titanium dental implants for rapid osseointegration. *Dent. Mater.* **2007**, *23*, 844–854.
4. Boerrigter, E.M.; Geertman, M.E.; van Oort, R.P.; Bouma, J.; Raghoobar, G.M.; van Waas, M.A.J.; van't Hof, M.A.; Boering, G.; Kalk, W. Patient satisfaction with implant-retained mandibular overdentures. A comparison with new complete dentures not retained by implants—A multicentre randomized clinical trial. *Br. J. Oral Maxillofac. Surg.* **1995**, *33*, 282–288.
5. Cheng, A.; Humayun, A.; Cohen, D.J.; Boyan, B.D.; Schwartz, Z. Additively manufactured 3D porous Ti–6Al–4V constructs mimic trabecular bone structure and regulate osteoblast proliferation, differentiation and local factor production in a porosity and surface roughness dependent manner. *Biofabrication* **2014**, doi:10.1088/1758-5082/6/4/045007.
6. Teixeira, L.N.; Crippa, G.E.; Lefebvre, L.-P.; de Oliveira, P.T.; Rosa, A.L.; Beloti, M.M. The influence of pore size on osteoblast phenotype expression in cultures grown on porous titanium. *Int. J. Oral Maxillofac. Surg.* **2012**, *41*, 1097–1101.
7. Özcan, M.; Hämmerle, C. Titanium as a Reconstruction and Implant Material in Dentistry: Advantages and Pitfalls. *Materials* **2012**, *5*, 1528–1545.
8. Nouri, A.; Hodgson, P.D.; Wen, C. *Biomimetic Porous Titanium Scaffolds for Orthopedic and Dental Applications*; InTech: New York, NY, USA, 2010; pp. 415–451.
9. Krishna, B.V.; Bose, S.; Bandyopadhyay, A. Low stiffness porous Ti structures for load-bearing implants. *Acta Biomater.* **2007**, *3*, 997–1006.
10. Schiefer, H.; Bram, M.; Buchkremer, H.P.; Stöver, D. Mechanical examinations on dental implants with porous titanium coating. *J. Mater. Sci. Mater. Med.* **2009**, *20*, 1763–1770.
11. Isidor, F. Influence of forces on peri-implant bone. *Clin. Oral Implants Res.* **2006**, *17*, 8–18.
12. Mangano, F.; Chambrone, L.; van Noort, R.; Miller, C.; Hatton, P.; Mangano, C. Direct Metal Laser Sintering Titanium Dental Implants. *Int. J. Biomater.* **2014**, doi:10.1155/2014/461534.
13. Junker, R.; Dimakis, A.; Thoneick, M.; Jansen, J.A. Effects of implant surface coatings and composition on bone integration: A systematic review. *Clin. Oral Implants Res.* **2009**, *20*, 185–206.
14. Gaviria, L.; Salcido, J.P.; Guda, T.; Ong, J.L. Current trends in dental implants. *J. Korean Assoc. Oral Maxillofac. Surg.* **2014**, *40*, 50–60.
15. Çelen, S.; Özden, H. Laser-induced novel patterns: As smart strain actuators for new-age dental implant surfaces. *Appl. Surf. Sci.* **2012**, *263*, 579–585.
16. Yi, Y.; Park, Y.; Choi, H.; Lee, K.; Kim, S.; Kim, K.; Oh, S.; Shim, J. The Evaluation of Osseointegration of Dental Implant Surface with Different Size of TiO<sub>2</sub> Nanotube in Rats. *J. Nanomater.* **2015**, doi:10.1155/2015/581713.
17. Bencharit, S.; Byrd, W.C.; Altarawneh, S.; Hosseini, B.; Leong, A.; Reside, G.; Morelli, T.; Offenbacher, S. Development and Applications of Porous Tantalum Trabecular Metal-Enhanced Titanium Dental Implants. *Clin. Implant Dent. Relat. Res.* **2013**, *16*, 817–826.
18. Mohandas, G.; Oskolkov, N.; McMahon, M.T.; Walczak, P.; Janowski, M. Porous tantalum and tantalum oxide nanoparticles for regenerative medicine. *Acta Neurobiol. Exp.* **2014**, *74*, 188–196.
19. Mour, M.; Das, D.; Winkler, T.; Hoenig, E.; Mielke, G.; Morlock, M.M.; Schilling, A.F. Advances in Porous Biomaterials for Dental and Orthopaedic Applications. *Materials* **2010**, *3*, 2947–2974.
20. Dabrowski, B.; Swieszkowski, W.; Godlinski, D.; Kurzydowski, K.J. Highly porous titanium scaffolds for orthopaedic applications. *J. Biomed. Mater. Res. B Appl. Biomater.* **2010**, *95*, 53–61.

21. Li, J.P.; de Wijn, J.R.; van Blitterswijk, C.A.; de Groot, K. Porous Ti6Al4V scaffolds directly fabricated by 3D fibre deposition technique: Effect of nozzle diameter. *J. Mater. Sci. Mater. Med.* **2005**, *16*, 1159–1163.
22. Van Noort, R. Titanium the implant material of today. *Mater. Sci.* **1987**, *22*, 3801–3811.
23. Niinomi, M.; Hattori, T.; Niwa, S. Material characteristics and biocompatibility of low rigidity titanium alloys for biomedical applications. In *Biomaterials in Orthopedics*; Yaszemski, M.J., Trantolo, D.J., Lewandrowski, K.-U., Hasirci, V., Altobelli, D.E., Wise, D.L., Eds.; Marcel Dekker Inc.: New York, NY, USA, 2004; pp. 41–62.
24. Gong, C.W.; Wang, Y.N.; Yang, D.Z. Phase transformation and second phases in ternary Ni–Ti–Ta shape memory alloys. *Mater. Chem. Phys.* **2006**, *96*, 183–187.
25. Nomura, N.; Kohama, T.; Oh, I.H.; Hanada, S.; Chiba, A.; Kanehira, M.; Sasaki, K. Mechanical properties of porous Ti–15Mo–5Zr–3Al compacts prepared by powder sintering. *Mater. Sci. Eng. C* **2005**, *25*, 330–335.
26. Shishkovsky, I.V. Shape Memory Effect in Porous Volume NiTi Articles Fabricated by Selective Laser Sintering. *Tech. Phys. Lett.* **2005**, *31*, 186–188.
27. Nouri, A.; Hodgson, P.D.; Wen, C.E. Effect of process control agent on the porous structure and mechanical properties of a biomedical Ti–Sn–Nb alloy produced by powder metallurgy. *Acta Biomater.* **2010**, *6*, 1630–1639.
28. Li, J.P.; Li, S.H.; van Blitterswijk, C.A.; de Groot, K. A novel porous Ti6Al4V: Characterization and cell attachment. *J. Biomed. Mater. Res. A* **2005**, *73*, 223–233.
29. Bahraminasab, M.; Sahari, B.B. NiTi Shape Memory Alloys, Promising Materials in Orthopedic Applications. In *Shape Memory Alloys—Processing, Characterization and Applications*; InTech: New York, NY, USA, **2013**; pp. 261–278.
30. Seah, K.H.W.; Thampuran, R.; Teoh, S.H. The influence of pore morphology on corrosion. *Corros. Sci.* **1998**, *40*, 547–556.
31. Arifvianto, B.; Zhou, J. Fabrication of Metallic Biomedical Scaffolds with the Space Holder Method: A Review. *Materials* **2014**, *7*, 3588–3622.
32. Andani, M.T.; Moghaddam, N.S.; Haberland, C.; Dean, D.; Miller, M.J.; Elahinia, M. Metals for bone implants. Part 1. Powder metallurgy and implant rendering. *Acta Biomater.* **2014**, *10*, 4058–4070.
33. Rack, H.J.; Qazi, J.I. Titanium alloys for biomedical applications. *Mater. Sci. Eng. C* **2006**, *26*, 1269–1277.
34. Ryan, G.; Pandit, A.; Apatsidis, D.P. Fabrication methods of porous metals for use in orthopaedic applications. *Biomaterials* **2006**, *27*, 2651–2670.
35. Kuroda, D.; Niinomi, M.; Morinaga, M.; Kato, Y.; Yashiro, T. Design and mechanical properties of new  $\beta$  type titanium alloys for implant materials. *Mater. Sci. Eng. A* **1998**, *243*, 244–249.
36. Matsumoto, H.; Watanabe, S.; Hanada, S.  $\beta$  TiNbSn Alloys with Low Young's Modulus and High Strength. *Mater. Trans.* **2005**, *46*, 1070–1078.
37. Nomura, N.; Sakamoto, K.; Takahashi, K.; Kato, S.; Abe, Y.; Doi, H.; Tsutsumi, Y.; Kobayashi, M.; Kobayashi, E.; Kim, W.-J.; *et al.* Fabrication and Mechanical Properties of Porous Ti/HA Composites for Bone Fixation Devices. *Mater. Trans.* **2010**, *51*, 1449–1454.

38. Deligianni, D.D.; Katsala, N.D.; Koutsoukos, P.G.; Missirlis, Y.F. Effect of surface roughness of hydroxyapatite on human bone marrow cell adhesion, proliferation, differentiation and detachment strength. *Biomaterials* **2000**, *22*, 87–96.
39. Thiyagasundaram, P.; Sankar, B.V.; Arakere, N.K. Elastic Properties of Open-Cell Foams with Tetraikadecahedral Cells Using Finite Element Analysis. *AIAA J.* **2010**, *48*, 818–828.
40. Ahmadi, S.M.; Campoli, G.; Yavari, S.A.; Sajadi, B.; Wauthle, R.; Schrooten, J.; Weinans, H.; Zadpoor, A.A. Mechanical behavior of regular open-cell porous biomaterials made of diamond lattice unit cells. *J. Mech. Behav. Biomed. Mater.* **2014**, *34*, 106–115.
41. Goodall, R.; Mortensen, A. Porous Metals. In *Physical Metallurgy*, 5th ed.; Laughlin, D., Hono, K.E., Eds.; Elsevier: Amsterdam, The Netherlands, 2014.
42. Li, D.S.; Zhang, Y.P.; Eggeler, G.; Zhang, X.P. High porosity and high-strength porous NiTi shape memory alloys with controllable pore characteristics. *J. Alloy. Compd.* **2009**, *470*, L1–L5.
43. Kuttly, M.G.; Bhaduri, S.; Jokisaari, J.R.; Bhaduri, S.B. Development of gradient porosities in Ti dental implant. In *25th Annual Conference on Composites, Advanced Ceramics, Materials, and Structures: B: Ceramic Engineering and Science Proceedings*; John Wiley & Sons, Inc.: Hoboken, NJ, USA, 2001; Volume 22, pp. 587–592.
44. Aly, M.S.; Bleck, W.; Scholz, P.-F. How metal foams behave if the temperature rises. *Met. Powder Rep.* **2005**, *60*, 38–45.
45. Murray, G.; Semple, J. Transfer of tensile loads from a prosthesis to bone using porous titanium. *J. Bone Joint Surg.* **1981**, *63*, 138–141.
46. Li, X.; Wang, C.; Zhang, W.; Li, Y. Fabrication and compressive properties of Ti6Al4V implant with honeycomb-like structure for biomedical applications. *Rapid Prototyp. J.* **2010**, *16*, 44–49.
47. Parthasarathy, J.; Starly, B.; Raman, S.; Christensen, A. Mechanical evaluation of porous titanium (Ti6Al4V) structures with electron beam melting (EBM). *J. Mech. Behav. Biomed. Mater.* **2010**, *3*, 249–259.
48. Harrysson, O.L.; Cansizoglu, O.; Marcellin-Little, D.J.; Cormier, D.R.; West, H. Direct metal fabrication of titanium implants with tailored materials and mechanical properties using electron beam melting technology. *Mater. Sci. Eng. C* **2008**, *28*, 366–373.
49. Campoli, G.; Borleffs, M.S.; Yavari, S.A.; Wauthle, R.; Weinans, H.; Zadpoor, A.A. Mechanical properties of open-cell metallic biomaterials manufactured using additive manufacturing. *Mater. Des.* **2013**, *49*, 957–965.
50. Heinel, P.; Körner, C.; Singer, R.F. Selective Electron Beam Melting of Cellular Titanium: Mechanical Properties. *Adv. Eng. Mater.* **2008**, *10*, 882–888.
51. Van Grunsven, W. Porous Metal Implants for Enhanced Bone Ingrowth and Stability. Ph.D. Thesis, University of Sheffield, Sheffield, UK, September 2014.
52. Heinel, P.; Müller, L.; Körner, C.; Singer, R.F.; Müller, F.A. Cellular Ti–6Al–4V structures with interconnected macro porosity for bone implants fabricated by selective electron beam melting. *Acta Biomater.* **2008**, *4*, 1536–1544.
53. Wen, C.; Mabuchi, M.; Yamada, Y.; Shimojima, K.; Chino, Y.; Asahina, T. Processing of biocompatible porous Ti and Mg. *Scr. Mater.* **2001**, *45*, 1147–1153.

54. Otsuki, B.; Takemoto, M.; Fujibayashi, S.; Neo, M.; Kokubo, T.; Nakamura, T. Pore throat size and connectivity determine bone and tissue ingrowth into porous implants: Three-dimensional micro-CT based structural analyses of porous bioactive titanium implants. *Biomaterials* **2006**, *27*, 5892–5900.
55. Murphy, C.M.; Haugh, M.G.; O'Brien, F.J. The effect of mean pore size on cell attachment, proliferation and migration in collagen-glycosaminoglycan scaffolds for bone tissue engineering. *Biomaterials* **2010**, *31*, 461–466.
56. Fu, Q.; Hong, Y.; Liu, X.; Fan, H.; Zhang, X. A hierarchically graded bioactive scaffold bonded to titanium substrates for attachment to bone. *Biomaterials* **2011**, *32*, 7333–7346.
57. Chen, H.; Wang, C.; Zhu, X.; Zhang, K.; Fan, Y.; Zhang, X. Fabrication of porous titanium scaffolds by stack sintering of microporous titanium spheres produced with centrifugal granulation technology. *Mater. Sci. Eng. C Mater. Biol. Appl.* **2014**, *43*, 182–188.
58. Hoffmann, W.; Bormann, T.; Rossi, A.; Müller, B.; Schumacher, R.; Martin, I.; de Wild, M.; Wendt, D. Rapid prototyped porous nickel-titanium scaffolds as bone substitutes. *J. Tissue Eng.* **2014**, doi:10.1177/2041731414540674.
59. Sidambe, A. Biocompatibility of Advanced Manufactured Titanium Implants—A Review. *Materials* **2014**, *7*, 8168–8188.
60. Tolochko, N.K.; Savich, V.V.; Laoui, T.; Froyen, L.; Onofrio, G.; Signorelli, E.; Titov, V.I. Dental root implants produced by the combined selective laser sintering/melting of titanium powders. *J. Mater. Des. Appl.* **2002**, *216*, 267–270.
61. Laptev, A.; Bram, M.; Buchkremer, H.P.; Stöver, D. Study of production route for titanium parts combining very high porosity and complex shape. *Powder Metall.* **2004**, *47*, 85–92.
62. Kutty, M.G.; Bhaduri, S.; Bhaduri, S.B. Gradient surface porosity in titanium dental implants: Relation between processing parameters and microstructure. *J. Mater. Sci. Mater. Med.* **2004**, *15*, 145–150.
63. Jakubowicz, J.; Adamek, G.; Dewidar, M. Titanium foam made with saccharose as a space holder. *J. Porous Mater.* **2013**, *20*, 1137–1141.
64. Bansiddhi, A.; Dunand, D.C. Shape-memory NiTi foams produced by solid-state replication with NaF. *Intermetallics* **2007**, *15*, 1612–1622.
65. Bansiddhi, A.; Dunand, D.C. Shape-memory NiTi foams produced by replication of NaCl space-holders. *Acta Biomater.* **2008**, *4*, 1996–2007.
66. Van Grunsven, W.; Goodall, R.; Reilly, G.C. Highly Porous Titanium Alloy: Fabrication and Mechanical Properties. *J. Biomech.* **2012**, *45*, S339.
67. Jee, C.S.Y.; Guo, Z.X.; Evans, J.R.G.; Özgüven, N. Preparation of High Porosity Metal Foams. *Metall. Mater. Trans. B* **2000**, *31*, 1345–1352.
68. Kim, S.W.; Jung, H.-D.; Kang, M.-H.; Kim, H.-E.; Koh, Y.-H.; Estrin, Y. Fabrication of porous titanium scaffold with controlled porous structure and net-shape using magnesium as spacer. *Mater. Sci. Eng. C Mater. Biol. Appl.* **2013**, *33*, 2808–2815.
69. Jurczyk, M.U.; Jurczyk, K.; Niespodziana, K.; Miklaszewski, A.; Jurczyk, M. Titanium-SiO<sub>2</sub> nanocomposites and their scaffolds for dental applications. *Mater. Charact.* **2013**, *77*, 99–108.
70. Li, Y.; Yang, C.; Zhao, H.; Qu, S.; Li, X.; Li, Y. New Developments of Ti-Based Alloys for Biomedical Applications. *Materials* **2014**, *7*, 1709–1800.



71. Lifland, M.I.; Kim, D.K.; Okazaki, K. Mechanical properties of a Ti-6Al-4V dental implant produced by electro-discharge compaction. *Clin. Mater.* **1993**, *14*, 13–19.
72. Mangano, C.; Mangano, F.G.; Shibli, J.A.; Ricci, M.; Perrotti, V.; d'Avila, S.; Piattelli, A. Immediate loading of mandibular overdentures supported by unsplinted direct laser metal-forming implants: Results from a 1-year prospective study. *J. Periodontol.* **2012**, *83*, 70–78.
73. Traini, T.; Mangano, C.; Sammons, R.L.; Mangano, F.; Macchi, A.; Piattelli, A. Direct laser metal sintering as a new approach to fabrication of an isoelastic functionally graded material for manufacture of porous titanium dental implants. Direct laser metal sintering as a new approach to fabrication of an isoelastic functionally grad. *Dent. Mater.* **2008**, *24*, 1525–1533.
74. Hrabe, N.W.; Heinel, P.; Flinn, B.; Körner, C.; Bordia, R.K. Compression-compression fatigue of selective electron beam melted cellular titanium (Ti-6Al-4V). *J. Biomed. Mater. Res. B Appl. Biomater.* **2011**, *99*, 313–320.
75. Murr, L.E.; Gaytan, S.M.; Medina, F.; Martinez, E.; Martinez, J.L.; Hernandez, D.H.; Machado, B.I.; Ramirez, D.A.; Wicker, R.B. Characterization of Ti-6Al-4V open cellular foams fabricated by additive manufacturing using electron beam melting. *Mater. Sci. Eng. A* **2010**, *527*, 1861–1868.
76. Laoui, T.; Santos, E.; Osakada, K.; Shiomi, M.; Morita, M.; Shaik, S.K.; Tolochko, N.K.; Abe, F.; Takahashi, M. Properties of Titanium Dental Implant Models Made by Laser Processing. *J. Mech. Eng. Sci.* **2006**, *220*, 857–863.
77. Mangano, C.; Raspanti, M.; Traini, T.; Piattelli, A.; Sammons, R. Stereo imaging and cytocompatibility of a model dental implant surface formed by direct laser fabrication. *J. Biomed. Mater. Res. A* **2009**, *88*, 823–831.
78. Cook, S.D.; Thongpreda, N.; Anderson, R.C.; Haddad, R.J. The effect of post-sintering heat treatments on the fatigue properties of porous coated Ti-6Al-4V alloy. *J. Biomed. Mater. Res.* **1988**, *22*, 287–302.
79. Joshi, G.V.; Duan, Y.; Neidigh, J.; Koike, M.; Chahine, G.; Kovacevic, R.; Okabe, T.; Griggs, J.A. Fatigue testing of electron beam-melted Ti-6Al-4V ELI alloy for dental implants. *J. Biomed. Mater. Res. B Appl. Biomater.* **2013**, *101*, 124–130.
80. Van Grunsven, W.; Hernandez-Nava, E.; Reilly, G.; Goodall, R. Fabrication and Mechanical Characterisation of Titanium Lattices with Graded Porosity. *Metals* **2014**, *4*, 401–409.
81. Bandyopadhyay, A.; Espana, F.; Balla, V.K.; Bose, S.; Ohgami, Y.; Davies, N.M. Influence of porosity on mechanical properties and *in vivo* response of Ti6Al4V implants. *Acta Biomater.* **2010**, *6*, 1640–1648.
82. Witek, L.; Marin, C.; Granato, R.; Bonfante, E.A.; Campos, F.; Bisinotto, J.; Suzuki, M.; Coelho, P.G. Characterization and *in vivo* evaluation of laser sintered dental endosseous implants in dogs. *J. Biomed. Mater. Res. B Appl. Biomater.* **2012**, *100*, 1566–1573.
83. Bidan, C.M.; Kommareddy, K.P.; Rumpler, M.; Kollmannsberger, P.; Fratzl, P.; Dunlop, J.W.C. Geometry as a factor for tissue growth: Towards shape optimization of tissue engineering scaffolds. *Adv. Healthc. Mater.* **2013**, *2*, 186–194.
84. Kumar, G.; Tison, C.K.; Chatterjee, K.; Pine, P.S.; McDaniel, J.H.; Salit, M.L.; Young, M.F.; Simon, C.G. The determination of stem cell fate by 3D scaffold structures through the control of cell shape. *Biomaterials* **2011**, *32*, 9188–9196.

85. De Wild, M.; Schumacher, R.; Mayer, K.; Schkommodau, E.; Thoma, D.; Bredell, M.; Gujer, A.K.; Grätz, K.W.; Weber, F.E. Bone regeneration by the osteoconductivity of porous titanium implants manufactured by selective laser melting: A histological and micro computed tomography study in the rabbit. *Tissue Eng. Part A* **2013**, *19*, 2645–2654.
86. Mangano, C.; de Rosa, A.; Desiderio, V.; d'Aquino, R.; Piattelli, A.; de Francesco, F.; Tirino, V.; Mangano, F.; Papaccio, G. The osteoblastic differentiation of dental pulp stem cells and bone formation on different titanium surface textures. *Biomaterials* **2010**, *31*, 3543–3551.
87. Hollander, D.A.; von Walter, M.; Wirtz, T.; Sellei, R.; Schmidt-Rohlfing, B.; Paar, O.; Erli, H.-J. Structural, mechanical and *in vitro* characterization of individually structured Ti–6Al–4V produced by direct laser forming. *Biomaterials* **2006**, *27*, 955–963.
88. Lee, J.-H.; Kim, H.-E.; Shin, K.-H.; Koh, Y.-H. Improving the strength and biocompatibility of porous titanium scaffolds by creating elongated pores coated with a bioactive, nanoporous TiO<sub>2</sub> layer. *Mater. Lett.* **2010**, *64*, 2526–2529.
89. Rumpler, M.; Woesz, A.; Dunlop, J.W.C.; van Dongen, J.T.; Fratzl, P. The effect of geometry on three-dimensional tissue growth. *J. R. Soc. Interface* **2008**, *5*, 1173–1180.
90. Markhoff, J.; Wieding, J.; Weissmann, V.; Pasold, J.; Jonitz-Heincke, A.; Bader, R. Influence of Different Three-Dimensional Open Porous Titanium Scaffold Designs on Human Osteoblasts Behavior in Static and Dynamic Cell Investigations. *Materials* **2015**, *8*, 5490–5507.
91. Shibli, J.A.; Mangano, C.; D'Avila, S.; Piattelli, A.; Pecora, G.E.; Mangano, F.; Onuma, T.; Cardoso, L.A.; Ferrari, D.S.; Aguiar, K.C.; *et al.* Influence of direct laser fabrication implant topography on type IV bone: A histomorphometric study in humans. *J. Biomed. Mater. Res. A* **2010**, *93*, 607–614.

© 2015 by the authors; licensee MDPI, Basel, Switzerland. This article is an open access article distributed under the terms and conditions of the Creative Commons Attribution license (<http://creativecommons.org/licenses/by/4.0/>).

## 9.2 Selective Laser Melting processed Ti6Al4V lattices with graded porosities for dental applications

Journal of the Mechanical Behavior of Biomedical Materials 90 (2019) 20–29



Contents lists available at ScienceDirect

Journal of the Mechanical Behavior of  
Biomedical Materials

journal homepage: [www.elsevier.com/locate/jmbbm](http://www.elsevier.com/locate/jmbbm)



### Selective laser melting processed Ti6Al4V lattices with graded porosities for dental applications



Zena J. Wally<sup>a,b,c,d</sup>, Abdul M. Haque<sup>e</sup>, Antonio Feteira<sup>f</sup>, Frederik Claeysens<sup>a,b,c</sup>, Russell Goodall<sup>a</sup>, Gwendolen C. Reilly<sup>a,c,\*</sup>

<sup>a</sup> Department of Materials Science and Engineering, University of Sheffield, Sir Robert Hadfield Building, Mappin St, Sheffield S1 3JD, UK

<sup>b</sup> Kroto Research Institute, University of Sheffield, Broad Lane, Sheffield S3 7HQ, UK

<sup>c</sup> INSIGNEO Institute for in silico Medicine, University of Sheffield, Pam Liversidge Building, Mappin St, Sheffield S1 3JD, UK

<sup>d</sup> Department of Prosthodontic, College of Dentistry, University of Kufa, Najaf, Iraq

<sup>e</sup> Medical Advanced Manufacturing Research Centre (AMRC), Wallis Way, Catecliffe, Rotherham S60 5TZ, UK

<sup>f</sup> Materials and Engineering Research Institute, Sheffield Hallam University, Sheffield S1 1WB, UK

#### ARTICLE INFO

##### Keywords:

Porous titanium  
Dental implant  
Graded porosity  
Selective laser melting  
Bone growth  
Osteoblasts

#### ABSTRACT

Dental implants need to support good osseointegration into the surrounding bone for full functionality. Interconnected porous structures have a lower stiffness and larger surface area compared with bulk structures, and therefore are likely to enable better bone-implant fixation. In addition, grading of the porosity may enable large pores for ingrowth on the periphery of an implant and a denser core to maintain mechanical properties. However, given the small diameter of dental implants it is very challenging to achieve gradations in porosity. This paper investigates the use of Selective Laser Melting (SLM) to produce a range of titanium structures with regular and graded porosity using various CAD models. This includes a novel 'Spider Web' design and lattices built on a diamond unit cell. Well-formed interconnecting porous structures were successfully developed in a one-step process. Mechanical testing indicated that the compression stiffness of the samples was within the range for cancellous bone tissue. Characterization by scanning electron microscopy (SEM) and X-ray micro-computed tomography ( $\mu$ CT) indicated the designed porosities were well-replicated. The structures supported bone cell growth and deposition of bone extracellular matrix.

#### 1. Introduction

Oral implants have frequently been used to replace the root portions of natural teeth that have been lost due to fracture, periodontitis (Mehrali et al., 2013) or aging (Wally et al., 2015), to support the fixation of artificial teeth (Elias, 2011) and improve the function of mastication (Deporter et al., 2014). Following implant insertion into the jaw bone, three to six months of healing are required for the placement of fixed dental prostheses (crowns or bridges) and to obtain mineralized bone (Mangano et al., 2015). Although effective, up to 10% of dental implants fail to integrate with the bone as a result of poor bone quality and quantity (Gaviria et al., 2014). Implant loosening is also reported in patients with poor bone healing, including smokers, diabetics (Mendonça et al., 2008), elderly people and those with osteoporosis (Junker et al., 2009). There is therefore still the need for implants with improved ability to support osseointegration.

Titanium and Ti-6Al-4V have been employed for dental and orthopaedic applications due to their excellent properties such as good biocompatibility, high corrosion resistance and high strength to weight ratio (Nouri et al., 2010). Bulk 'titanium-based' devices have been the traditional form used for dental implants, but the Young's modulus of solid titanium is much higher than that of bone (Wally et al., 2015). This may cause the load distribution between hard tissue and the implant to be non-uniform, and researchers have suggested that this leads to 'stress shielding' and bone resorption, resulting in the loosening and failure of the implant (Mehrali et al., 2013). Porous titanium structures have the advantage that their effective stiffness can be manipulated to match bone tissue (Wu et al., 2014) and that the porosity provides a larger surface area, which in turn encourages the attachment and proliferation of bone cells, enables bone ingrowth into the material and improves osseointegration (Oh et al., 2007). A high surface area eliminates early micromotion of implants (Vasconcellos et al., 2010) which

\* Correspondence to: INSIGNEO Institute of in silico Medicine, Department of Materials Science and Engineering, University of Sheffield, Pam Liversidge Building, Mappin St, Sheffield S1 3JD, UK

E-mail address: [g.reilly@sheffield.ac.uk](mailto:g.reilly@sheffield.ac.uk) (G.C. Reilly).

<https://doi.org/10.1016/j.jmbbm.2018.08.047>

Received 25 January 2018; Received in revised form 9 August 2018; Accepted 28 August 2018

Available online 29 August 2018

1751-6161/© 2018 Published by Elsevier Ltd.

promotes fibrous tissue rather than osseointegration and causes initial instability (Fernández et al., 2017). Since pore parameters such as size, shape and the overall amount of porosity have been shown to play a vital role in bone cell ingrowth (Vasconcellos et al., 2008), this necessitates using a processing method able to produce optimal porosity in a metallic biomaterial, as achieving both the required biological and mechanical properties is essential for implant applications.

Several studies have successfully created titanium foams or lattices either for coating or within the bulk of a structure for varied applications using processing methods such as metal injection moulding of Ti foam (Shbeh and Goodall, 2015). In recent years, additive manufacturing, including Electron Beam Melting (EBM) and Selective Laser Melting (SLM) have been increasingly considered as economically viable techniques to fabricate challenging structures (Koike et al., 2011). With SLM, dental and orthopaedic implant prototypes have been developed with complex pore geometries by melting Ti powder micro-particles using a focused laser beam according to a computer-generated three-dimensional design (Tolochko et al., 2002; Mullen et al., 2009; Moin et al., 2013). An inert gas or a vacuum is used during the fabrication process to manufacture titanium parts which are easily oxidised in air (Koike et al., 2011). However porosity within the bulk metal structure (not intended as part of the overall design) reduces mechanical properties, and as a result, unless this can be controlled, such materials are unlikely to be used for bone replacement devices in load-bearing areas (Ryan et al., 2006). In an attempt to withstand physiological loads, a structure with a dense core and porous shell has been suggested, which might be more acceptable for oral implantology (Laoui et al., 2006). Another suggestion includes graded porous architecture with a stiff core, where the core will provide mechanical stability and the graded porosity allows ingrowth (van Grunsven et al., 2014). Such a structure could also reduce the stress concentrations occurring on loading between adjacent layers with very different Young's moduli (Joshi et al., 2013), as can happen when porous materials are bonded to dense materials.

With the breadth and versatility of processing methods, the optimal pore structure for bone cell ingrowth remains to be elucidated. Here we aim to compare a range of porous titanium lattices of approximately cylindrical form, which could form the basis of a porous dental implant. In this study, the Selective Laser Melting (SLM) process was used with Ti-6Al-4V to build a range of titanium micro-lattice structures. Variable pore sizes and strut thicknesses were used to create regular and graded porous structures using a 'Spider Web' design and lattices based on a diamond unit cell. These lattices were tested under compression to determine their stiffness and strength, and in cell culture to test their ability to support bone cell growth.

## 2. Materials and methods

### 2.1. Selective laser melting for the production of porous Ti6Al4V structures

SLM was used to process different porous titanium structures, employing a Renishaw AM250 system and spherical Ti6Al4V powder micro-particles (grade 23) with particle sizes ranging from 15 to 55  $\mu\text{m}$ . The machine was equipped with 200 W laser and used with a 70  $\mu\text{m}$  diameter laser beam and 30  $\mu\text{m}$  layer thickness, 5000 mm/s laser scan speed and 0.075 mm hatch distance. The data from the CAD model (STL format) of the structure are passed into the processing system and virtually sliced in 30-micron layers with a defined laser path. Slices are fused layer-by-layer over a number of hours to form components of porous and dense metal parts. To reduce the risk of oxidation and contamination, the building procedure was carried out under inert Ar gas. Materialise 3-Matics version 9.1 software was used to create different CAD concepts (Table 1): lattice-based constructs were built on a diamond unit cell, applied to form approximately cylindrical structures with 5 mm diameter (Fig. 1a and b). Variants included different pore sizes and strut thicknesses, and the inclusion of a dense core of different

**Table 1**

A summary of the different lattice designs used here and the nomenclature employed to refer to them in this work. Samples are grouped according to the nominal pore size, strut thickness, and presence or absence of a dense core.

Model type	Pore size ( $\mu\text{m}$ )	Strut thickness ( $\mu\text{m}$ )	Dense core (mm)
P400	400	400	None
P400/1C	400	400	1
P400/2C	400	400	2
P650	650	300	None
P650/1C	650	300	1
Graded (GP/650–400)	400 (inner layer)	400 (inner layer)	1
	650 (outer layer)	300 (outer layer)	
Graded (GP/400–300)	300 (inner layer)	300 (inner layer)	1
	400 (outer layer)	400 (outer layer)	
'Spider Web'	250	250	1.73

diameters. In the diamond-based lattices, graded porosity was created by combining two layers of different strut thickness surrounding a dense core, which resulted in changes to the open 'pore size', with sizes of 400 and 650  $\mu\text{m}$  and 300 and 400  $\mu\text{m}$  being used for the inner and outer layer respectively. A 'spider web' design with 250  $\mu\text{m}$  radial spokes and circumferential connecting struts was used to form titanium hexagonal prisms (diameter: 4.33 mm and height: 6.76 mm) (Fig. 1c). Each sample was positioned onto the software platform 30° from the wiper blade position, which was performed to ensure minimal forces were induced by contact with parts during powder re-coating. All sample components were loaded onto the build platform (Ti6Al4V powder) and positioned randomly. Lattice-based samples were built vertically on the build substrate while the 'Spider Web' samples were oriented horizontally (Fig. 2).

### 2.2. Structural chemistry and characterization

To evaluate the inner architecture of the pores, titanium components were cut across the axis into cylinders of approximately 7 mm height using a Secotom-50 cutting machine with the cut surfaces ground flat on an Ecomet-250 grinder-polisher machine, using SiC papers with grits of 500 and then 1000. To remove the loose powders from the built components, they were cleaned for 30 min with an ultrasonic bath. These samples were also used to perform both mechanical and biological testing.

Surface chemistry of the built titanium lattices was analysed using Inductively Coupled Plasma Optical Emission Spectroscopy (ICP-OES) to quantify the main elements and LECO (Laboratory Equipment Corporation) to measure the interstitial elements (carbon, oxygen and nitrogen) by AMG Analytical, UK. Pore geometry and interconnectivity were evaluated by SEM (FEI Nova 200, equipped with a field emission gun) and  $\mu\text{CT}$  (Skyscan 1172) Bruker system with a medium camera binning mode (2000  $\times$  1024), 1 mm Al filter and 9.92  $\mu\text{m}$  pixel size. CTAn analysis software was used to analyse the components in three dimensions, 500 cross-sectional images were converted to binary images with a threshold value of 80, the percentage of the open and total porosity and surface area were calculated. The average pore size and strut thickness were evaluated in Image J software from recorded SEM images. Archimedes method was also used for determining % porosity for fabricated scaffolds according to the Eq. (1) below and compared with  $\mu\text{CT}$  results. This method has been used previously in the literature for measuring the density and porosity of porous cylinders (Slotwinski et al., 2014).

$$\text{Porosity} = (1 - \rho_{sc}/\rho_0) \times 100\% \quad (1)$$

where  $\rho_0$  is the known density of dense Ti6Al4V (4.43 g/cm<sup>3</sup>) and  $\rho_{sc}$  is

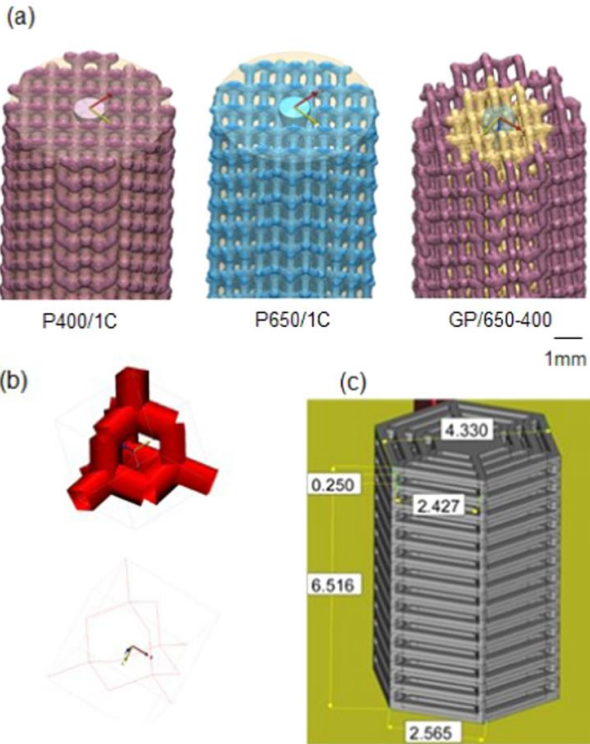


Fig. 1. The CAD models of the (a) variant lattices built on the diamond unit cell: P400/1C, P650/1C and GP/650-400, (b) diamond unit cell and (c) 'Spider Web' prototype shown in 3-matics software.

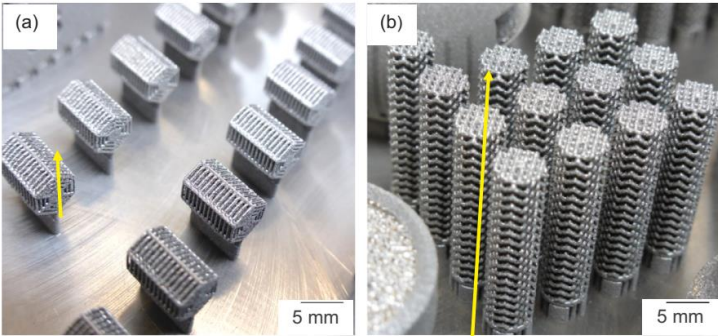


Fig. 2. Post-build Ti6Al4V samples of (a) 'Spider Web' (diameter = 4.33 mm and height = 6.76 mm) built horizontally and (b) variant of diamond unit cell lattices built vertically (diameter = 5 mm and height = 20 mm) on the building substrate, yellow arrows indicate building direction.

the density of the samples, which is measured by the weight of the sample in air ( $M_a$ ) and water ( $M_w$ ) using Eq. (2) below and a Mettler Toledo density balance with 0.1 mg resolution. The density of water  $\rho_w$  was assumed to be  $1.0 \text{ g/cm}^3$  at room temperature ( $15\text{--}25^\circ\text{C}$ ). To minimise air bubbles distilled water was used at room temperature. Slotwinski et al. (2014).

$$\rho_{sc} = ((M_a)/(M_a - M_w)) \rho_w \quad (2)$$

### 2.3. Compression testing

The mechanical properties of built Ti6Al4V scaffolds around 5 mm diameter and 7 mm height were evaluated in compression according to the international standard ISO 17340:2014 (Metallic materials - Ductility testing - High speed compression test for porous and cellular metals), using a universal testing machine (Zwick Roell) with 1 mm/min speed, 20 kN load cell and 10 kN maximum force. The long axis of the tested samples was oriented perpendicular to the loading direction and the gradient of the core base lattices was radial to the direction of loading. The resulting load-displacement curves were translated to stress-strain curves, the cross sectional area was calculated by measuring the diameter of the samples and used for the calculations of stress and strain. The initial linear elastic region was used to calculate Young's modulus and yield strength using the 0.2% offset strain. Video extensometer provided with the test machine was used during the compression process. Using the recorded videos, silhouette images of the sample changes during compression were obtained.

### 2.4. Cell culture

#### 2.4.1. Cell seeding

All chemicals used for cell culture were supplied by Sigma-Aldrich (UK) unless otherwise stated. Samples were autoclaved at  $121^\circ\text{C}$  for 30 min prior to cell seeding. After cooling to room temperature, they were submerged in a culture medium with 30 min incubation at  $37^\circ\text{C}$  and 5%  $\text{CO}_2$  humid environment to allow protein attachment onto the surface of the scaffolds. The culture medium used was Minimal Essential Medium- $\alpha$  ( $\alpha$ -MEM, Lonza, Castleford, UK). It was supplemented with 10% Foetal Bovine Serum (FBS), 1% L-Glutamine solution (0.2 M), 1% Antibiotic solution containing penicillin (10,000 U/ml) and streptomycin (10 mg/ml), Ascorbic Acid-2-Phosphate (AA, 0.2 mM), and  $\beta$ -glycerophosphate ( $\beta$ -GP, 5 mM). Expansion media was removed and MLO-A5 cells were seeded onto the scaffolds by a drop method in an untreated 24 well plate, using 2500 cells in 25  $\mu\text{l}$  expansion media with 45 min incubation for each side of the scaffold to permit cell attachment; negative controls (immersed in media but without cells) were also used. 2mls of EM were added to each scaffold and incubated overnight. Media was changed every 2–3 days during the experiment period and cell viability after seeding was assessed over six different time points. The passage number of cells used for experiments was between 44 and 50.

#### 2.4.2. Cell viability assay

Resazurin reduction (RR) metabolic activity assay was used to estimate cell viability on days 1, 4, 7, 14, 21 and 28 of culture. RR solution was prepared by adding 1 mM Resazurin Sodium Salt to deionized water and diluting this to 10 vol% in culture media. For each assay, media was removed from seeded scaffolds, and 2 ml of RR solution was added to each scaffold. Well plates containing scaffolds were wrapped in aluminium foil due to its light sensitivity and incubated for four hours at  $37^\circ\text{C}$ . The non-fluorescent blue color of the media was reduced by the metabolic activity of live cells to a fluorescent pink color. In a 96-well plate, 200  $\mu\text{l}$  of the reduced solution was transferred in triplicate, which was subsequently read with a spectrofluorometer (FLX800, BIO-TEK Instruments, Inc.) at 540 nm excitation wavelength and 590 nm emission wavelength. Fresh culture media was added after

twice washing of samples with PBS, with 20 min incubation between washes. After the day 28 assay, scaffolds were fixed with 10% formalin for 30 min and kept in PBS prior to calcium and collagen staining.

#### 2.4.3. Alizarin Red S stain assay

To determine extracellular calcium deposition, Alizarin Red S (ARS) staining analysis was performed on day 28 of cell culture. Alizarin Red S (ARS) powder was dissolved in deionized water ( $\text{dH}_2\text{O}$ ) at 1 w/v % and filtered through a 0.2  $\mu\text{m}$  filter to ensure no undissolved particles remain. The fixed scaffolds were cleaned three times with  $\text{dH}_2\text{O}$  to remove any remaining formalin solution. Each sample was submerged in 2 ml of ARS with orbital shaking for 30 min at 100 rpm. Then the ARS was removed and any excess was washed off every 5 min with  $\text{dH}_2\text{O}$  and gentle orbital shaking until the water remained clear. The scaffolds were destained with 5% of perchloric acid on an orbital shaker for 20 min. Triplicate samples of 150  $\mu\text{l}$  of destaining solution from each well were added to a clear 96 well plate and absorption was measured at 405 nm in a plate reader.

#### 2.4.4. Sirius red stain assay

To identify collagen deposition within the scaffolds Sirius Red Stain Assay (SRS) was used. Direct red 80 was dissolved in saturated picric acid (1% w/v) with 0.2  $\mu\text{m}$  filter. After the ARS assay was performed the scaffolds were washed three times with  $\text{dH}_2\text{O}$  to remove any of the ARS destain, 2 ml of SRS was then added to each sample. The well plate was placed on an orbital shaker for 18 h at 100 rpm. The SRS was removed and any excess was washed off with  $\text{dH}_2\text{O}$ . The scaffolds were de-stained with 2 ml of 0.2 M NaOH:methanol (1:1) on an orbital shaker for 20 min at 100 rpm. Triplicate samples of 150  $\mu\text{l}$  of solution from each well plate was added to a clear 96 well plate and absorption was measured at 405 nm. For both ARS and SRS a standard curve was prepared from the same working solution and used to obtain concentrations of stain from the absorbance of the eluate.

#### 2.4.5. Statistical analysis

The obtained data are displayed as means  $\pm$  standard deviation (SD). Preliminary experiments were performed with ( $n = 6$  / group) for P400, P400/1C, P400/2C, P650, P650/1C, (GP/650–400), (GP/400–300) and 'Spider Web' scaffolds used to perform compression tests and ( $n = 9$  / group) for biological tests. Data were analysed by a GraphPad Prism 7 software using one or two-way ANOVA with a Tukey's multiple comparisons post-hoc test.  $P < 0.05$  was determined to be a statistically significant difference.

## 3. Results

### 3.1. Surface chemistry and structural characterization

The results of the ICP and LECO elemental analysis (Supplementary Table 1) after production of the SLM Ti6Al4V lattices confirmed Ti, Al and V as the main surface chemistry. The levels of O, N and C were about 0.227, 0.044 and 0.023 respectively. These values are close to the content of O (0.13), N (0.08) and C (0.03) as determined in the ASTM B265-08b standard for Grade 23 titanium alloy. The SEM (Fig. 3) and micro-CT cross-sectional images (Fig. 4) revealed that selective laser melted constructs of P400, P400/1C, P400/2C, P650, P/C650, GP/650–400, GP/400–300 and spider web had mostly interconnected pores with differing amounts of porosity ranging from 50% to 80%. A very small number of closed micropores (yellow arrows) within the structures were also observed within the lattices (Fig. 3c and d). The average open and total porosity are shown in Table 2. No statistically significant differences were seen between the open and total porosity, indicating that the porosity present is mostly interconnected. The results for total porosity of titanium lattices, when measured by both the Archimedes method and  $\mu\text{CT}$ , were similar as shown in (Table 2). The struts are well-defined and continuous. The ratio between the object surface area

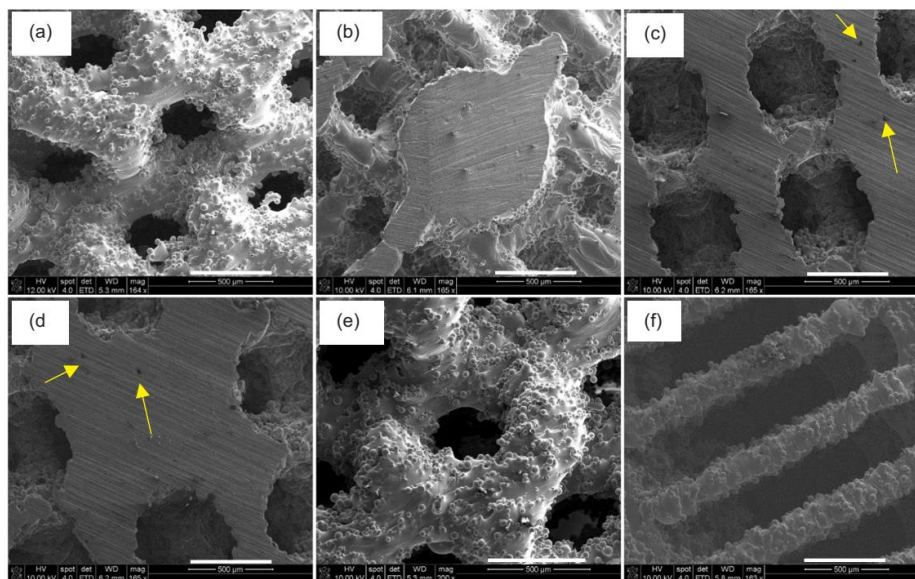


Fig. 3. SEM images of diamond unit cell lattices a- P400, b- P400/1C, c- P650, d- P650/1C, e- GP/650–400 and f-‘Spider Web’, yellow arrows indicate closed porosity, (scale bar: 500  $\mu\text{m}$ ).

to volume ratio increased with increasing porosity. The average pore size, average strut thickness and the percentages of open, closed and total porosity and object surface to volume ratio of variable titanium lattices P400, P400/1C, P400/2C, P650, P650/1C, GP/650–400, GP/400–300 and spider web are shown in Table 2.

### 3.2. Mechanical testing

Stress-strain values of titanium lattices under compression (Supplementary Fig. 1) showed an overall linear relationship in the elastic region and then plastic yield plateau. Six linear elastic regions of each design showed a highly reproducible pattern. The failure mode for the titanium lattices of P400, P400/1C, P650, P650/1C, GP/650–400, and ‘Spider Web’ (Supplementary Fig. 2) showed that the deformation of the spider-base lattices structure begin with initial core buckling and then the lattice struts break before the structure collapses. While structures without a dense core demonstrated a plastic lattice breakdown starting from the top and bottom sides of the samples leading to structure rupture. The Young’s modulus and yield strength of the regular and graded scaffolds were similar between samples of the same design, with a low standard deviation, indicating the scaffold manufacture had high reproducibility with respect to bulk mechanical properties (Table 3). There were higher mechanical properties in samples with a dense core and thicker struts. The highest Young’s moduli and yield strengths were exhibited by scaffolds with a ‘spider web’ structure and 2 mm dense core, while the weakest scaffolds were with P650. When comparing the same lattice pore sizes where both structures have a core, e.g. 400/1C compared with GP/400–300 (Supplementary Table 2) there were no significant differences between graded structures and non graded structures in compression modulus or strength. With increasing porosity, Young’s modulus and yield strength were lower, as would be expected (Fig. 5). Most samples lie on the same

general curve on a plot of mechanical properties against density, but the spider web design is notably higher for a given density. This probably reflects the lower degree of isotropy in this structure, being particularly mechanically efficient along the axial direction tested.

### 3.3. Cell culture

#### 3.3.1. Cell viability on titanium scaffolds

Cell culture assays on P400, P400/1C, P650, P650/1C, GP/650–400 and ‘Spider Web’ indicated that cells were evidently viable in all the porous structures over 28 days. Generally, the attachment of bone cells across scaffolds was comparable; the viability increased steadily from day 4 to day 7 in all scaffolds without significant differences at each time point. Interestingly, the results indicate that large pore sizes (650  $\mu\text{m}$ ) do not enhance cell ingrowth and confirm that any pore size between 250 and 650  $\mu\text{m}$  is a supportive structure for bone cells. Similar metabolic activity of bone cells was obtained from the P400, P400/1C, P400/2C, GP400–300 and ‘Spider Web’ scaffolds (Fig. 6(a)).

#### 3.3.2. Calcium and collagen staining

Calcified matrix staining on day 28 of cell culture indicated that all structures supported mineral production. Alizarin red absorbance for cells seeded on P400 scaffolds was significantly higher than that on ‘Spider Web’ scaffolds, (Fig. 6(b)). A similar result was observed for collagen analysis, where all scaffolds support extracellular matrix production. However, there were no significant differences across the seeding groups (Fig. 6(c)).

### 4. Discussion

In an effort to evaluate the feasibility of SLM to produce complex geometries of titanium for their use in dental implants to improve bone

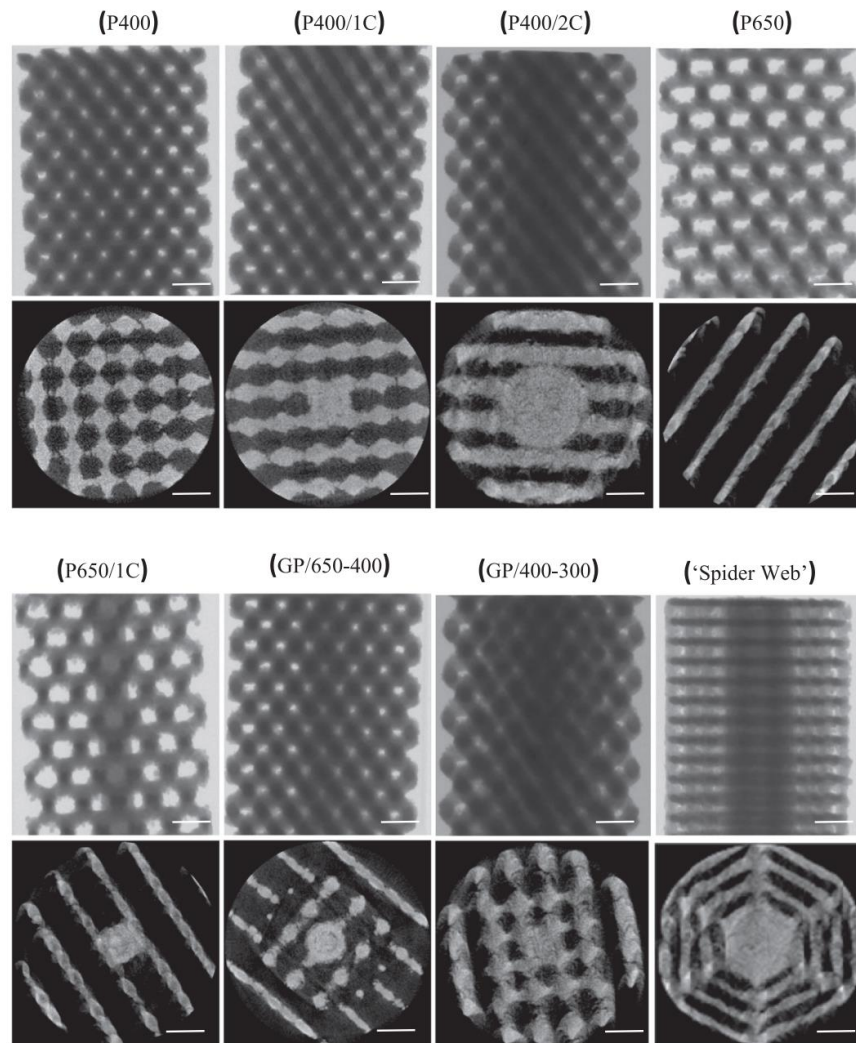


Fig. 4.  $\mu$ CT reconstruction images, top (lateral view) and bottom (cross-section) of P400, P400/1C, P400/2C, P650, P650/1C, GP/650-400, GP/400-300 and 'Spider Web' lattices, (scale bar: 1 mm).

ingrowth and implant stability, a range of porous titanium scaffolds with variable porosity were developed based on an approximate cylindrical shape of a size representing that of a dental implant. Structures were created with uniform and graded porosity using different pore shape, size and percentage with and without a dense core, designated as P400, P400/1C, P400/2C, P650, P650/1C, GP/650-400, GP/400-300 and 'Spider Web'. The structural and mechanical properties of the resulting structures were evaluated, and assessed biologically by seeding with bone cells for up to 28 days.

Several previous studies have evaluated the impact of porosity and pore shape of porous structures on the biological response to bone cells. Most of these studies focused on creating porous coatings on implants with pore sizes below 200  $\mu\text{m}$ . Creating a uniform and large pore size has been recommended to achieve good bone ingrowth and vascularization. In this study, we aimed to examine highly regular lattice structures with specific pore sizes (250, 300, 400 and 650  $\mu\text{m}$ ) in terms of their biofunctional performance. SLM was chosen to produce titanium lattices due to its potential to be used for the production of



**Table 2**

Mean  $\pm$  S.D of average pore size, average strut thickness and the percentages of open, closed and total porosity and object surface to volume ratio of various titanium lattices calculated by 3D analysis of the  $\mu$ CT cross-sectional images using CTAn software. Total porosity was also measured by the Archimedes method. These data were performed on 3 samples for each group, the average pore size and strut thickness were analysed using Image J (n = 300).

Groups	Average pore size $\mu$ m	Average strut thickness $\mu$ m	Object surface / volume ratio	Open porosity %	Closed porosity %	Total porosity %	Porosity% By Archimedes
P400	411 $\pm$ 13	421 $\pm$ 28	16.6 $\pm$ 0.6	56.8 $\pm$ 1.0	0.29 $\pm$ 0.10	56.9 $\pm$ 1.0	55.2 $\pm$ 3.0
P400/1C	421 $\pm$ 15	412 $\pm$ 22	12.3 $\pm$ 0.6	51.2 $\pm$ 0.4	0.04 $\pm$ 0.03	51.5 $\pm$ 0.4	51.8 $\pm$ 4.5
P400/2C	423 $\pm$ 24	422 $\pm$ 11	17.0 $\pm$ 1.6	48.4 $\pm$ 0.9	0.30 $\pm$ 0.02	48.6 $\pm$ 1.1	47.6 $\pm$ 2.4
P650	654 $\pm$ 25	314 $\pm$ 21	22.1 $\pm$ 0.8	82.8 $\pm$ 0.8	0.08 $\pm$ 0.02	82.9 $\pm$ 0.7	80.4 $\pm$ 3.6
P/C650	645 $\pm$ 13	333 $\pm$ 22	20.6 $\pm$ 1.6	80.9 $\pm$ 0.6	0.05 $\pm$ 0.01	80.9 $\pm$ 0.6	79.0 $\pm$ 2.9
GP/650-400	655 $\pm$ 25	302 $\pm$ 19 / 433 $\pm$ 20	19.2 $\pm$ 1.1	78.5 $\pm$ 0.4	0.12 $\pm$ 0.04	78.5 $\pm$ 0.4	76.1 $\pm$ 2.2
	420 $\pm$ 16						
GP/400-300	420 $\pm$ 25	414 $\pm$ 23 / 315 $\pm$ 27	17.9 $\pm$ 0.3	56.6 $\pm$ 0.8	0.18 $\pm$ 0.04	56.7 $\pm$ 0.8	55.7 $\pm$ 1.7
	305 $\pm$ 123						
Spider Web	254 $\pm$ 12	230 $\pm$ 18	20.2 $\pm$ 1.8	68.5 $\pm$ 1.6	0.320 $\pm$ 0.1	68.6 $\pm$ 1.5	67.4 $\pm$ 1.4

**Table 3**

Mechanical properties (Young's modulus and yield strength) of all Ti6Al4V lattices (Mean  $\pm$  SD).

Groups	Young's Modulus (GPa)	Yield Strength (MPa)
P400	3.3 $\pm$ 0.6	147 $\pm$ 10
P400/1C	4.1 $\pm$ 0.3	178 $\pm$ 10
P400/2C	4.8 $\pm$ 0.6	204 $\pm$ 33
P650	0.7 $\pm$ 0.2	16 $\pm$ 4
P650/1C	2.0 $\pm$ 0.3	55 $\pm$ 4
GP/650-400	1.7 $\pm$ 0.2	48 $\pm$ 1
GP/400-300	3.4 $\pm$ 0.4	147 $\pm$ 31
'Spider Web'	6.0 $\pm$ 0.4	224 $\pm$ 7

controllable and homogeneous pore sizes. Titanium alloy Ti6Al4V is widely used for SLM to produce medical devices. Although titanium and its alloys have been reported to be bioinert and biocompatible materials for dental and orthopaedic implants (Stevenson et al., 2016), it is necessary that constructs from these materials produced via advanced manufacturing technology are evaluated for biofunctional properties.

The unit cell of choice used was a diamond lattice (Fig. 1(b)), because it is a simple structure which has a relatively low stiffness relative to its density and has been previously used for similar medical applications to mimic the properties of cancellous bone (van Grunsven et al., 2014). A novel design of 'Spider Web' was also used and compared as this was an effective way to produce a graded pore structure but to our knowledge such a radial pore structure has never been assessed for its suitability for a medical implant design.

The low interstitial elements value in the built SLM Ti6Al4V structures when compared to the higher levels found with titanium foams produced by different fabrication methods such as metal injection moulded (Shbeh and Goodall, 2015) indicates the low risk of contamination with the SLM process which may exert less effect on the strength properties. The degree of porosity in the built lattices was controlled via changing the pore size and strut thickness. The different approaches for determining porosity revealed a high level of agreement. The results for the total porosity, when measured by the Archimedes and micro-CT methods, were generally comparable (Table 2), though there was higher variability for the lattices porosities measured by Archimedes. Although an attempt was made to minimise the presence of air bubbles these could still have been present, leading to a higher measured density to be measured and lower apparent porosity. This finding is in agreement with the study of Slotwinski et al., which showed general agreement in porosity measurement of additively manufactured CoCr components using Archimedes, mass/volume, and X-ray CT (Slotwinski et al., 2014).

The stress-strain curves of the different Ti6Al4V lattices used in this study are relatively typical of what we see for these kinds of lattice materials (van Grunsven et al., 2014). One factor is that they are more highly reproducible sample-to-sample than random structured porous materials, such as foams and sponges. This is due to the structure of each sample being more highly repeatable. For the actual stress-strain curves, there is an initial elastic stage (approximately linear) corresponding to bending of the struts but giving rise to a lower gradient than a dense material would. Then there is a yield event where a

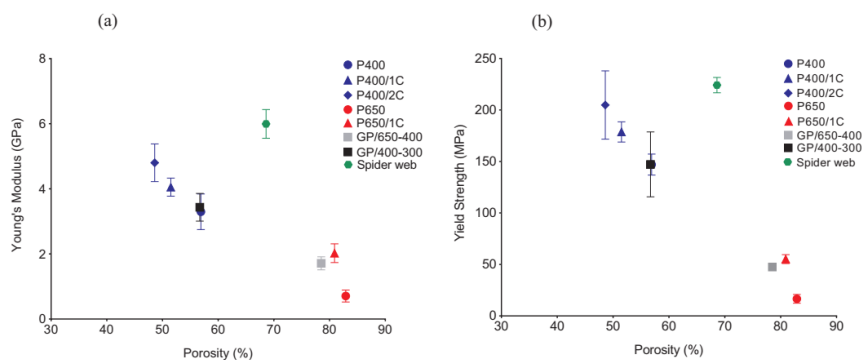


Fig. 5. A comparison of the mechanical properties (a) Mean  $\pm$  SD Young's modulus, (b) Mean  $\pm$  SD yield strength of the regular and graded Ti6Al4V lattices plotted against % mean porosity by volume as assessed by CT scan.

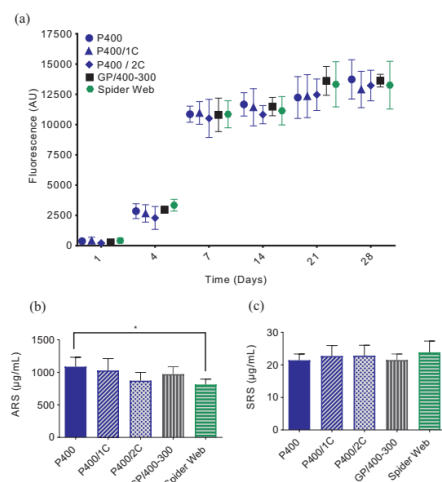


Fig. 6. Mean  $\pm$  SD for (a) resazurin fluorescence as a measure of cell viability of MLO-A5s on P400, P400/1C, P400/2C, GP/400-300 and 'Spider Web' scaffolds over 28 days (b) ARS staining and (c) SRS staining on day 28 of cell culture, ( $n = 9$ ).

particular strut fails, which may be followed by some degree of work hardening, like in a solid, but which more commonly leads to a decrease in load as part of the structure collapses into the available free space, in the manner of a porous solid. In terms of the mechanism (Supplementary Fig. 2), at a mesoscale we identify that collapse begins in one horizontal layer, on a random basis, likely mediated by a defect. This layer then proceeds to crush to a high density, before the stress raises in another layer to a sufficiently high level to initiate failure and the process repeats. This is the origin of the cycles seen most clearly in the P400 sample (though present in some others); each peak is the point of failure initiation in a new layer, which causes a drop in load. Once the layer is crushed, the load starts to build up again. The uniform size of the layers explains the uniform engineering strain level over which the repeats occur. This progressive failure is significantly affected by a solid core, as the core resists collapse and causes more distributed deformation. In core-based samples we do not see the repeated cycles of load increase and decrease. While the samples here were not examined at sufficient detail to draw conclusions on the mechanism of failure in individual struts, from other work on EBM lattices it is known that the struts generally display very limited plasticity (Hernandez-Nava *et al.*, 2016), and so the failure is likely to be in a brittle mode.

As would be expected, the differences in porosity result in differences in Young's modulus and yield strength, which are lower at higher porosities. A large variety of values have been reported for Young's modulus of cancellous bone depending on species, preparation methods and types of bone, for example, the range for cancellous bone in the mandible is 1.5–4.5 GPa as reviewed in the literature (Andani *et al.*, 2014). A lower range of Young's modulus (0.1–2 GPa) also been reported (Wen, 2017). The structures used in this study were of a similar range to these values ranging from 0.7 to 6 GPa. The root part of the natural tooth is made from dentine which is covered by cementum and the tooth is held into the bone via periodontal ligament. Forces of mastication for each tooth are transferred from enamel through dentine to the root, then from cementum through the periodontal ligament to the cancellous bone to the end at the ramus of the jaw (Currey, 2012).

In the literature there is some debate about the Young's modulus of dentine, generally it is reported as around 20–25 GPa (Kinney *et al.*, 2003) which is comparable to cortical bone (17–20 GPa) (Wally *et al.*, 2015). However, in artificial implants there is a direct contact between bone and the implant structure which induces bone ingrowth. Dental implants should withstand the physiological function during mastication. The maximum biting force is from 230 to 450 N in the molar region (Wen, 2017).

Compression testing was performed in this study to compare the basic structural mechanical properties of structures which were produced from different batches, all scaffolds demonstrated a highly reproducible behaviour, which is attributed to the uniform geometry of the SLM lattices. This is in agreement with previous work in our laboratory on cubes of lattice structures in which a highly reproducible initial elastic region of the stress-strain curve was exhibited by Ti6Al4V scaffolds built on diamond unit cell and produced via EBM (Van Grunsven, 2014). Strength properties of porous biomaterials can be improved with increasing density (Balla *et al.*, 2010). Interestingly, 'Spider Web' lattices were the strongest scaffolds in compression in relation to their porosity. A possible explanation for this result may be the lower degree of isotropy in this structure, being particularly mechanically efficient along the axial direction tested. Recent research has shown that additively manufactured structures exhibit anisotropic behaviour (Ataee *et al.*, 2018), but that this difference becomes insignificant for larger unit cells, and derives from the smaller samples in that work not accurately replicating the CAD model shape - the anisotropy in property comes from differences in the porous structure, not inherent directionality in the properties of the metal from which it is made.

The only structures which did not have adequate strength compared to bone were the non-core based lattices with a 650  $\mu\text{m}$  pore size and 300  $\mu\text{m}$  strut thickness (P650) which were the least stiff and strong scaffolds. This is likely because these were the highest porosity structures and so had the least amount of solid to resist deformation. Previous research has also documented that completely porous metal structures for both orthopaedics or dental implants are not able to provide sufficient strength to withstand physiological loading (Ryan *et al.*, 2006). To improve the mechanical properties, a compact dense core was incorporated into the structures. As expected, core based lattices were stronger than the entirely porous scaffolds. This finding has also been confirmed in the literature, where implants with two different zones, a dense core and irregular porous shell have been found to be more appropriate for load bearing devices such as dental implants, such as in a study with a dental root implant produced by incorporating selective laser sintering for the porous coating and selective laser melting for the dense core (Tolochko *et al.*, 2002). A major advantage of SLM is that the porous structure and a solid core are made in one build of one material, compared to making a structure first and then combining this with a porous coating. Structural modifications including increasing the diameter of the dense core of the regular pore structures and strut thickness of the graded structures result in significant improvement of Young's modulus and yield strength (Table 2), as there is then more solid to support load.

Implants with graded porosity enable rapid bone ingrowth while the low-porosity part of the component provides strength to sustain the physiological load (Soon *et al.*, 2011). The deformation mechanisms of uniform and graded porous structures for stretching and bending were studied by Afshar *et al.* They concluded that graded structures deform less than uniform ones. They also stated that the energy absorption and elastic-plastic deformation were high for struts oriented in the loading direction (Afshar *et al.*, 2016). In terms of mechanical properties found in our tests, the graded structures have properties that roughly correspond with their overall density. This is to be expected as they have been tested with the different density regions (and dense core if present) in parallel, and shows that the properties combine arithmetically, rather than there being more complex interactions between the different density layers. This is in agreement with earlier work (van

Grunsvan et al., 2014) where the layers were tested in series, and elastic deformation was found to spread according to Young's modulus, and plastic deformation to progress from the lowest density layer to the highest. Were the samples here to be tested in bending, where the outer layers experience higher strain than the centre, the difference between the graded and non-graded lattices would be more significant. These results demonstrate the feasibility to design overall mechanical properties by combining different lattices in a graded structure.

*In vitro* cell culture on P400, P400/1C, P400/2C, GP400–300 and 'Spider Web' designs showed that osteoblastic cells readily attached to porous Ti6Al4V. Implants with rough surfaces have been shown to promote osteoblast cells attachment (Mour et al., 2010), and proliferation as referred by Karageorgiou and Kaplan (Karageorgiou and Kaplan, 2005). The metabolic activity of cells showed significant increases over 28 days of cell culture (Fig. 6), likely due to a large surface area which promotes cell proliferation, and subsequent extracellular matrix production. Previous research has indicated that porous titanium surfaces have a positive effect on bone cell growth and matrix production. Stevenson et al. examined the potential of osteosarcoma cell line (MG63) and primary human osteoblast cells to proliferate and mineralize on titanium surfaces with different porosities (Slotwinski et al., 2014). In that study fine surface coatings supported less mineralization than coarse surfaces. Interconnected porosity has also been shown to induce the attachment and proliferation of bone cells (Soon et al., 2011) such as a graded porous structure of different materials HA-CaCO<sub>3</sub>-Ti with macro- (100–350 µm), micro- (0.2–90 µm) and nano- (100 nm) porosity which stimulated bone formation (Fu et al., 2011). Our study shows no significant variation in cell viability when comparing scaffolds with different pore size, shape and percentage. This result is in agreement with Cheng et al., where even with the high metabolic activity of osteoblasts (MG63 cells) that has been observed on porous titanium constructs with average pore diameter 177, 383 and 653, there were no differences shown among variant scaffolds (Cheng et al., 2014). Nevertheless, Markhoff et al. evaluated the metabolic activity of human osteoblast cells on porous titanium scaffolds with cubic, pyramidal and diagonal basic structures under static and dynamic culture. They reported a significantly higher metabolic cell activity on pyramidal basic structure scaffolds with 400–620 µm pore size and 75% porosity with no significant differences between the culture methods (Markhoff et al., 2015). In another *in vitro* observation, human osteoblasts cells were cultured on direct laser formed Ti6Al4V porous scaffolds with 500, 700 and 1000 µm pore size, after 14 days of cell culture cells covered most of the pores with 500 µm pore size. While the pore size of 700 and 1000 µm formed a circular-shaped growth pattern around the pore walls (Hollander et al., 2006).

Overall, all scaffolds supported calcium and collagen formation indicating their suitability to support bone ingrowth; scaffolds with P400 exhibited the highest calcium deposition. Pore sizes between 100 and 400 µm are suggested for bone mineralization (Ryan et al., 2006). Our study showed no effect of pore size and shape on matrix production by MLO-A5s. As can be observed the effect of pore size on matrix growth is not straightforward and is probably governed by contributing factors such as roughness or pore wall size or structure and nutrient accessibility. Frosch et al. have also demonstrated that collagen production is not influenced by the pore size (over the range 300–1000 µm) of titanium scaffolds (Frosch et al., 2004). In contrast to our study indicating no effect of pore shape; within the structures used by Markhoff et al. collagen formation was significantly less supported on diagonal compared to cubic and pyramidal structures (Markhoff et al., 2015). Based on our results, all Ti6Al4V scaffolds were shown to sustain MLOA5s cell viability and mineralization. However, MLO-A5s are prone to proliferate rapidly and produce a lot of matrix, and more subtle differences may be seen with primary human cells. Further *in vitro* experiments can be performed to investigate the behaviour of these scaffolds with primary cells.

## 5. Conclusion

In conclusion, here we verified that the SLM technique could produce a range of well-controlled porous Ti6Al4V structures with uniform and graded porosity of a suitable size for dental implants. All structures had compressive mechanical properties in the range of those previously reported for cancellous bone, except for the 650-micron pore size scaffolds. The presence of a dense core led to an improvement in the compressive mechanical properties of the lattice structures while graded structures were found to behave in line with their average density. All structures strongly supported cell growth and mineralized matrix deposition which was not affected by pore size except that the maximum calcium deposition was seen on scaffolds with 400-micron pores. Although it did not support maximal calcium deposition, the spider web scaffold seems to strike a balance between good resistance to compression and high porosity and may be a promising structure to take forward to incorporate into a dental implant-shaped structure. Overall this technique is extremely promising as a fabrication method for dental implants which could be more cost-effective and allow better osseointegration than those currently available.

## Acknowledgements

The authors would like to thank The Medical Advanced Manufacturing Research Centre (AMRC) for access to equipment to manufacture the experimental structures, Sheffield Hallam University for access to characterization facilities and the Iraqi Ministry of Higher Education and Scientific Research for funding.

## Appendix A. Supporting information

Supplementary data associated with this article can be found in the online version at doi:10.1016/j.jmbmm.2018.08.047.

## References

- Afshar, M., Anaraki, A.P., Montazerian, H., Kadkhodapour, J., 2016. Additive manufacturing and mechanical characterization of graded porosity scaffolds designed based on triply periodic minimal surface architectures. *J. Mech. Behav. Biomed. Mater.* 62, 481–494.
- Andani, M.T., Moghaddam, N.S., Haberland, C., Dean, D., Miller, M.J., Elahinia, M., 2014. Metals for bone implants. Part 1. Powder metallurgy and implant rendering. *Acta Biomater.* 10, 4058–4070.
- Ataee, A., Li, Y., Fraser, D., Song, G., Wen, C., 2018. Anisotropic Ti-6Al-4V gyroid scaffolds manufactured by electron beam melting (EBM) for bone implant applications. *Mater. Des.* 137, 345–354.
- Balla, V.K., Bodhak, S., Bose, S., Bandyopadhyay, A., 2010. Porous tantalum structures for bone implants: fabrication, mechanical and *in vitro* biological properties. *Acta Biomater.* 6, 3349–3359.
- Cheng, A., Humayun, A., Cohen, D.J., Boyan, B.D., Schwartz, Z., 2014. Additively manufactured 3D porous Ti-6Al-4V constructs mimic trabecular bone structure and regulate osteoblast proliferation, differentiation and local factor production in a porosity and surface roughness dependent manner. *Biofabrication* 6, 045007.
- Currey, J.D., 2012. The structure and mechanics of bone. *J. Mater. Sci.* 47, 41–54.
- Deporter, D., Pharoah, M., Yeh, S., Todescan, R., Atenafu, E.G., 2014. Performance of titanium alloy sintered porous-surfaced (SPS) implants supporting mandibular overdentures during a 20-year prospective study. *Clin. Oral. Implants Res.* 25, e189–e195.
- Elias, C.N., 2011. Factors affecting the success of dental implants. In: Turkyilmaz, I. (Ed.), *Implant Dentistry – A Rapidly Evolving Practice*. InTech, New York, pp. 319–364.
- Fernández, M.P.R., Gehrke, S.A., Mazzon, P., Calvo-Guirado, J.L., De Aza, P.N., 2017. Implant stability of biological hydroxyapatites used in dentistry. *Materials* 10, 1–15.
- Frosch, K.-H., Barvenek, F., Viereck, V., Lohmann, C.H., Dresing, K., Breme, J., Brunner, E., Stürmer, K.M., 2004. Growth behavior, matrix production, and gene expression of human osteoblasts in defined cylindrical titanium channels. *J. Biomed. Mater. Res. A* 68, 325–334.
- Fu, Q., Hong, Y., Liu, X., Fan, H., Zhang, X., 2011. A hierarchically graded bioactive scaffold bonded to titanium substrates for attachment to bone. *Biomaterials* 32, 7333–7346.
- Gaviria, L., Salcido, J.P., Guda, T., Ong, J.L., 2014. Current trends in dental implants. *J. Korean Assoc. Oral. Maxillofac. Surg.* 40, 50–60.
- Hernandez-Nava, E., Smith, C.J., Derguti, F., Tammas-Williams, S., Leonard, F., Withers, P.J., Todd, I., Goodall, R., 2016. The effect of defects on the mechanical response of Ti-6Al-4V cubic lattice structures fabricated by electron beam melting. *Acta Mater.* 108, 279–292.

- Hollander, D.A., Von Walter, M., Wirtz, T., Sellei, R., Schmidt-Rehling, B., Paar, O., Erii, H.-J., 2006. Structural, mechanical and in vitro characterization of individually structured Ti-6Al-4V produced by direct laser forming. *Biomaterials* 27, 955–963.
- Joshi, G.V., Duan, Y., Neidigh, J., Koike, M., Chahine, G., Kovacevic, R., Okabe, T., Griggs, J.A., 2013. Fatigue testing of electron beam-melted Ti-6Al-4V ELI alloy for dental implants. *J. Biomed. Mater. Res. B. Appl. Biomater.* 101, 124–130.
- Junker, R., Dimakis, A., Thoneick, M., Jansen, J.A., 2009. Effects of implant surface coatings and composition on bone integration: a systematic review. *Clin. Oral. Implants Res.* 20 (Suppl 4), 185–206.
- Karageorgiou, V., Kaplan, D., 2005. Porosity of 3D biomaterial scaffolds and osteogenesis. *Biomaterials* 26, 5474–5491.
- Kinney, J.H., Marshall, S.J., Marshall, G.W., 2003. The mechanical properties of human dentin: a critical review and re-evaluation of the dental literature. *Crit. Rev. Oral. Biol. Med.* 14, 13–29.
- Koike, M., Greer, P., Owen, K., Lilly, G., Murr, L.E., Gaytan, S.M., Martinez, E., Okabe, T., 2011. Evaluation of titanium alloys fabricated using rapid prototyping technologies—electron beam melting and laser beam melting. *Materials (Basel)* 4, 1776–1792.
- Laoui, T., Santos, E., Osakada, K., Shiomi, M., Morita, M., Shaik, S.K., Tolochko, N.K., Abe, F., Takahashi, M., 2006. Properties of titanium dental implant models made by laser processing. *Proc. Inst. Mech. Eng. Part C. J. Mech. Eng. Sci.* 220, 857–863.
- Mangano, F.G., Caprioglio, A., Levirini, L., Farronato, D., Zecca, P.A., Mangano, C., 2015. Immediate loading of mandibular overdentures supported by one-piece, direct metal laser sintering mini-implants: a short-term prospective clinical study. *J. Periodontol.* 86, 192–200.
- Markhoff, J., Wieding, J., Weissmann, V., Pasold, J., Heincke, A.J., Bader, R., 2015. Influence of different three-dimensional open porous titanium scaffold designs on human osteoblasts behavior in static and dynamic cell investigations. *Materials (Basel)* 8, 5490–5507.
- Mehrali, M., Shirazi, F.S., Mehrali, M., Metselaar, H.S.C., Kadri, N.A.B., Osman, N.A.A., 2013. Dental implants from functionally graded materials. *J. Biomed. Mater. Res. A* 101, 3046–3057.
- Mendonça, G., Mendonça, D.B.S., Aragão, F.J.L., Cooper, L.F., 2008. Advancing dental implant surface technology—from micron- to nanotopography. *Biomaterials* 29, 3822–3835.
- Moin, D.A., Hassan, B., Merceles, P., Wismeyer, D., 2013. Designing a novel dental root analogue implant using cone beam computed tomography and CAD/CAM technology. *Clin. Oral. Implants Res.* 24, 25–27.
- Mour, M., Das, D., Winkler, T., Hoenig, E., Mielke, G., Morlock, M.M., Schilling, A.F., 2010. Advances in porous biomaterials for dental and orthopaedic applications. *Materials (Basel)* 3, 2947–2974.
- Mullen, L., Stamp, R.C., Brooks, W.K., Jones, E., Sutcliffe, C.J., 2009. Selective Laser Melting: a regular unit cell approach for the manufacture of porous, titanium, bone in-growth constructs, suitable for orthopaedic applications. *J. Biomed. Mater. Res. B. Appl. Biomater.* 89, 325–334.
- Nouri, A., Hodgson, P.D., Wen, C., 2010. Biomimetic porous titanium scaffolds for orthopaedic and dental applications. In: Mukherjee, A. (Ed.), *Biomimetics Learning from Nature*. InTech Pub, pp. 415–450.
- Oh, S.H., Park, L.K., Kim, J.M., Lee, J.H., 2007. In vitro and in vivo characteristics of PCL scaffolds with pore size gradient fabricated by a centrifugation method. *Biomaterials* 28, 1664–1671.
- Ryan, G., Pandit, A., Apatidis, D.P., 2006. Fabrication methods of porous metals for use in orthopaedic applications. *Biomaterials* 27, 2651–2670.
- Shbeh, M.M., Goodall, R., 2015. Design of water debinding and dissolution stages of metal injection moulded porous Ti foam production. *Mater. Des.* 87, 295–302.
- Slotwinski, J.A., Garboczi, E.J., Hebenstreit, K.M., 2014. Porosity measurements and analysis for metal additive manufacturing process control. *J. Res. Natl. Inst. Stand. Technol.* 119, 494–528.
- Soon, Y.-M., Shin, K.-H., Koh, Y.H., Lee, J.-H., Choi, W.-Y., Kim, H.-E., 2011. Fabrication and compressive strength of porous hydroxyapatite scaffolds with a functionally graded core/shell structure. *J. Eur. Ceram. Soc.* 31, 13–18.
- Stevenson, G., Rehman, S., Draper, E., Hernandez-Nava, E., Hunt, J., Haycock, J.W., 2016. Combining 3D human in vitro methods for a 3Rs evaluation of novel titanium surfaces in orthopaedic applications. *Biotechnol. Bioeng.* 113, 1586–1599.
- Tolochko, N.K., Savich, V.V., Laoui, T., Froyen, L., Onofrio, G., Signorelli, E., Titov, V.I., 2002. Dental root implants produced by the combined selective laser sintering/melting of titanium powders. *Proc. Inst. Mech. Eng. Part L. J. Mater. Des. Appl.* 216, 267–270.
- van Grunsven, W., Hernandez-Nava, E., Reilly, G., Goodall, R., 2014. Fabrication and mechanical characterisation of titanium lattices with graded porosity. *Metals (Basel)* 4, 401–409.
- Van Grunsven, W., 2014. Porous Metal Implants for Enhanced Bone Ingrowth and Stability (Ph.D. Thesis). University of Sheffield, Sheffield, UK September.
- Vasconcellos, L.M.R., Leite, D.O., Nascimento, F.O., Vasconcellos, L.G.O., Graça, M.L.A., Carvalho, Y.R., Cairo, C.A.A., 2010. Porous titanium for biomedical applications: an experimental study on rabbits. *Med. Oral. Patol. Oral. Cir. Bucal* 15, 407–412.
- Vasconcellos, L.M.R., De, Oliveira, M.V.D., Graça, M.L.D.A., Vasconcellos, L.G.O.D., Carvalho, Y.R., Cairo, C.A.A., 2008. Porous titanium scaffolds produced by powder metallurgy for biomedical applications. *Mater. Res.* 11, 275–280.
- Wally, Z., van Grunsven, W., Claeysens, F., Goodall, R., Reilly, G., 2015. Porous titanium for dental implant applications. *Metals (Basel)* 5, 1902–1920.
- Wen, C. (Ed.), 2017. *Metallic Foam Bone*. Woodhead Pub./Elsevier, Oxford.
- Wu, S., Liu, X., Yeung, K.W.K., Liu, C., Yang, X., 2014. Biomimetic porous scaffolds for bone tissue engineering. *Mater. Sci. Eng. R. Rep.* 80, 1–36.

### **9.3 Fabrication of 3- Dimensional Porous Poly (ethylene glycol) Diacrylate Template by Microstereolithography.**

#### **9.3.1 Introduction**

Stereolithography (SL) is a type of rapid prototyping technology that appeared in the 1980's (Narayan et al., 2010), and the technique was patented in 1984 by Chuck Hull, founder of 3D Systems. It shows a wide range of applications in tissue scaffolds and medical devices. This technology fundamentally needs a source of laser to produce controllable structures using liquid photocurable resin, based on a CAD model (Bártolo, 2005). When producing microstructures with millimetre and micron scales resolution this technique is called microstereolithography ( $\mu$ SL). Projection and scanning  $\mu$ SL is the widely used system. Projection  $\mu$ SL is capable of producing 3D microstructures by progressively stacking sequence layers. This system necessarily requires a focused ultraviolet (UV) laser beam to cross-link the photopolymer liquid to form a desired form and width layer (Choi et al., 2009). Light generation from a laser lamp is reflected from the Digital Micromirror Device (DMD), which will focus the previously designed image of a two-dimensional sliced section onto z-axis stage within a container containing the photocurable resin. The stage is controlled by a computerised motor which enables it to move down slowly after each layer builds to produce a 3D structure. While in scanning  $\mu$ SL the laser spot is translated over the photocurable liquid resin by direct writing of the desired image following the computational model (Johnson et al., 2013). Despite the ability of  $\mu$ SL to create complex microstructures, the main concern is the scarcity of biocompatible polymers and photoinitiators used could be toxic. In addition to that the lower mechanical properties of photopolymerized resin limit its use in hard tissue engineering (Chia and Wu, 2015). Over the last years, several researchers have focused on the possibilities of using projection  $\mu$ SL in combination with nanoscale

coating and post-processing techniques to produce ultralight microlattices with high mechanical efficiencies. Polymer lattices produced by projection  $\mu$ SL have been used as templates which were converted by coating into metallic microlattices for medical devices. Electroless nickel plating was used to produce metallic hollow-tube nickel-phosphorus (Ni-P) with nano and micro metal film. Atomic layer deposition was also used to produce hollow-tube aluminium oxide (amorphous  $\text{Al}_2\text{O}_3$ , alumina) with nanoscale alumina coating (Zheng et al., 2014).  $\mu$ SL was also used to produce polymeric dental root implants with a dense core and porous covering using photocurable resin using a laser power (Bártolo, 2005). Nevertheless, the common issue with the projection ( $\mu$ SL) is the uncontrolled penetration of the laser into the photocurable resin during the building operation. A UVA light absorber has been suggested to control the penetration depth (Choi et al., 2009). This study aimed to investigate the feasibility of projection  $\mu$ SL to produce 3D micro-lattices with graded and interconnected porosity on a dense core using different DMD parameters and UVA light absorber concentrations. The long-term objective is to use the polymeric micro-lattices as a template which could be converted to metallic microlattices for dental implants using an appropriate coating method.

### **9.3.2 Materials and methods**

In this work, projection  $\mu$ SL was utilised to produce 3D microlattice structures with graded and interconnected porosity on a dense core. In projection  $\mu$ SL photocurable liquid prepolymer, a 405 nm laser source and a digital micromirror device (DMD) were used to build up 3D structures. The DMD device consists of a numerous number of aligned aluminium coated micromirrors which can absorb or reflect the laser light. The primary issue with the projection ( $\mu$ SL) is the uncontrolled penetration of the laser into the photocurable resin during the building operation. To reduce the penetration depth, a

UVA light absorber was used with different concentrations. This would be a central element in order to create components with a small pore size which are impossible through the established methods.

### 9.3.2.1 Structure design

A ‘spider web’ design with radial spokes and circumferential connecting struts was used to form polymeric hexagonal prisms with 5 mm diameter and 7 mm height. 1 mm dense core and 4 mm diameter graded porous layer was used. This concept was kindly designed by Hossein Bahmaee using a 3D animation software (Autodesk- Maya). Two-dimensional sliced images were applied with different shapes, hexagonal and dotted using 250  $\mu\text{m}$  layer thicknesses (Figure 9.1) to produce a 3D ‘spider web’ lattice structure (Figure 9.2).

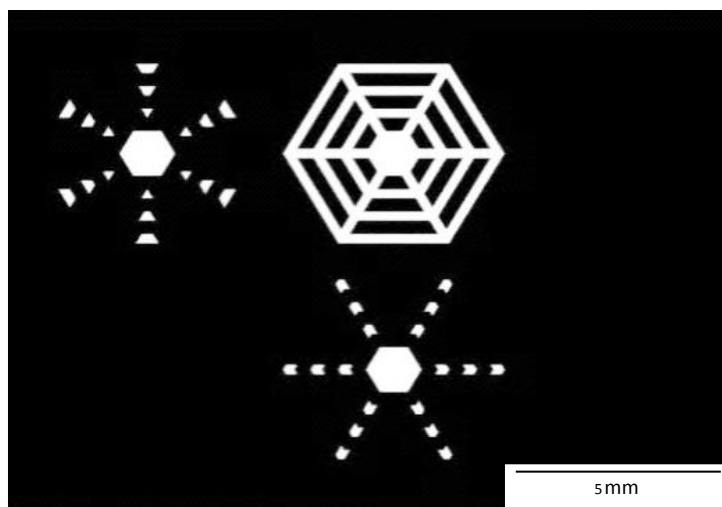


Figure 9.1: Two-dimensional images (hexagonal and dotted) used as sliced layers to make a ‘spider web’ lattice structure.

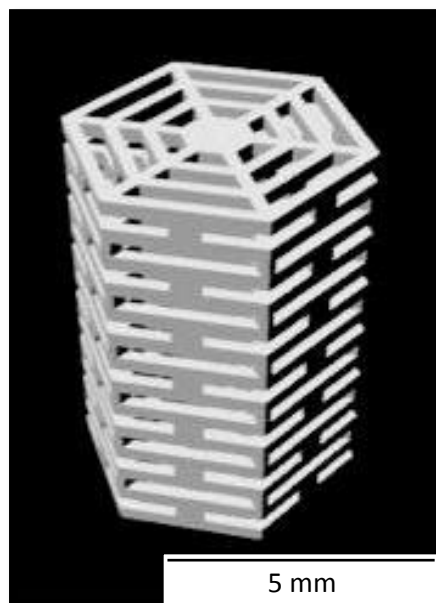


Figure 9.2: CAD model for the 'spider web' lattice structure consists of multi-sliced layers of 2 D images )hexagonal and dotted(, used for the projection microstereolithography process.

### 9.3.2.2 Preparing Prepolymer and light absorber

Poly (ethylene glycol) diacrylate (PEG-DA) is a photocurable type resin which characterised by poor biocompatibility and low cell adhesion. Nevertheless, it is widely applied to create complex scaffold structures. Initially, different molecular weights (250, 500 and 700 g/mol) of PEG-DA were used. Based on the better resulting structures, it has been determined to use PEG-DA with low molecular weight (250 g/mol). After that, PEG-DA (250 g/mol) (Sigma Aldrich, UK) was prepared using 4 % (wt/wt) photoinitiator Diphenyl-(2,4,6-trimethylbenzoyl)-phosphine oxide/2-hydroxy-2methyl-propiophenone, blend (Sigma Aldrich, UK), as indicated in the literature. To prepare 10 gr of PEG-DA, 0.4 gr of the photoinitiator was added to 9.6 g. Then the photocurable solution was mixed with a UVA light absorber, BMP (2-(2H-Benzotriazol-2-yl)-4,6-bis(1-methyl-1-phenylethyl) phenol (Sigma Aldrich, UK), using different concentration (0.05, 0.10, 0.15 and 0.20%). The mixture was vigorously stirred for 1 min and used



after 12h at room temperature to ensure homogeneous distribution of photoinitiator and light absorber.

### **9.3.2.3 Structure fabrication**

Scaffolds were fabricated using a projection microstereolithography setup with a 405 nm laser and DMD (Texas Instruments Incorporated, TX, USA), 40-100 mW laser source controlled by a software (Vortran Laser Technology Inc, Sacramento, CA, USA) and motorised z-axis translation stage apparatus and attached metal stage (L-shaped copper lip) as writing platform (Thorlabs Ltd, Cambridgeshire, UK), controlled by software for the Z-stage (APT Software, Thorlabs Ltd, Cambridgeshire, UK) (Choi et al., 2009) as shown in Figure 9.3. Two-dimensional images with variant forms were prepared using Microsoft Paint software with pixel dimensions (1024×768) and uploaded onto the DMD projector using ALP-3 Basic version 1.0.03 (ViALUX, GmbH), initially 25-s exposure time was used for each image to permit sufficient time for pre-polymer to cure. A suitable size of glass vial for the amount of prepolymer liquid and metal stage size was used. The reflected laser beam of 5 mm diameter was focused the projected image from the DMD device onto the movable z-stage within the liquid prepolymer leading it to polymerise. In the beam pathway filter, reflecting mirror and objective lens was supplied. Three-dimensional structures were formed layer by layer by lowering the stage at a constant speed (0.01- 0.02 mm/s). After the process was finished, the 3D structure was removed from the metal stage and immersed directly into iso-Propyl alcohol (IPA) to remove any unreacted prepolymer from the structures. Different trials were performed here to optimise the 3D microstructures, initially set up used was 60 mW input laser power, 0.01 mm/s z translation speed and 25 s exposure time for each 2 D image using PEG-DA with and without 15% of light absorber. The next trial was undertaken by increasing the laser power to 100 mW and z translation

speed to 0.02 mm/s and changing the exposure time to be 10 s for the hexagonal 2D image and 30 s for the dotted shapes. These modified parameters were used with different concentrations of light absorber (0.05%, 0.10%, 0.15% and 0.20%).

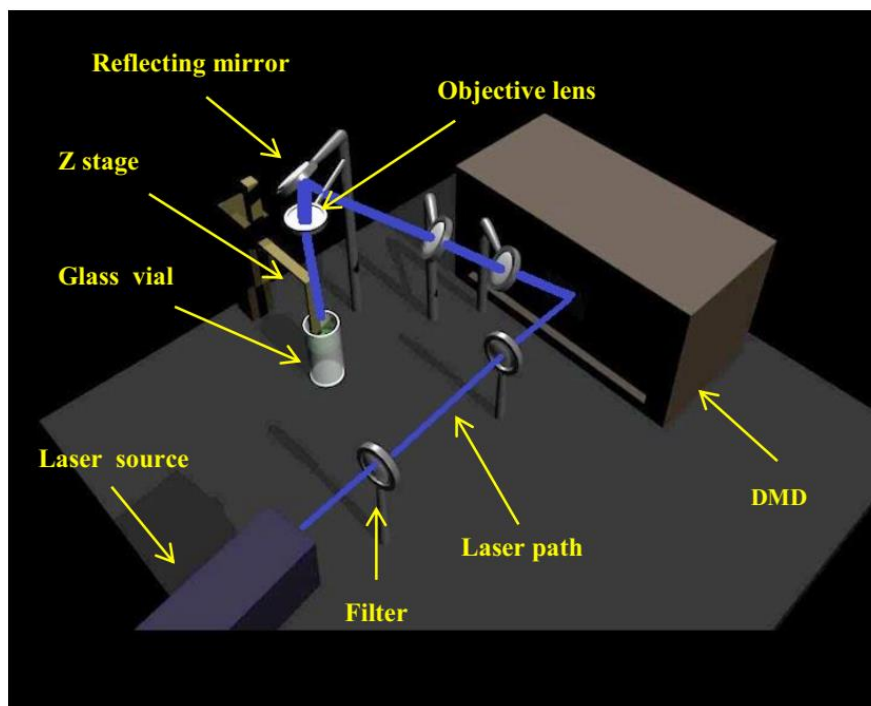


Figure 9. 3: DMD setup-based on microstereolithography system.

### 9.3.3 Results

A Motic digital phase contrast microscope was used with low magnification power to observe the microstructure of the samples produced with different DMD parameters and light absorber concentrations. Structures with the initial set up: input laser power (60 mW), z translation speed (0.01 mm/s) and 25 s exposure time for each 2 D image were entirely solid with and fused layers as shown from the top (left) and lateral (right) view (Figure 9. 4).

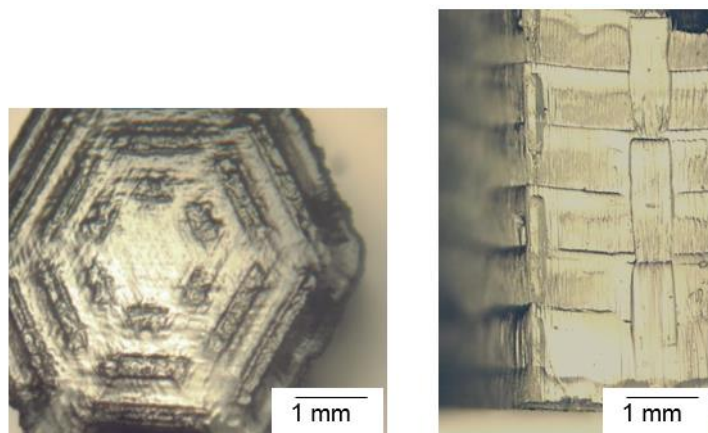


Figure 9. 4: Microscopic images of PEG-DA samples from the top (left) and lateral (right) views, using DMD parameters (z translation speed (0.01 mm/s), laser power (60 mW) and 25 s exposure time for each layer

When 15% of light absorber was mixed with pre-polymer resin using the same previous laser parameters, it was found to give a partially porous structure; however, porosity between the layers was not completed (Figure 9. 5).

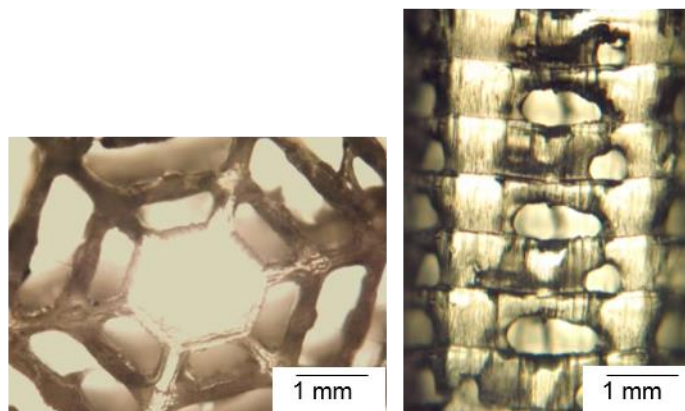


Figure 9. 5: Microscopic images of PEG-DA samples from the top (left) and lateral (right) views, using 0.15% of a light absorber and DMD parameters: z translation speed (0.01 mm/s), laser power 60 mW) and 25 s exposure time for each layer.

After increasing the DMD parameters, z translation speed into (0.02 mm/s), laser power into (100 mW) and modifying the exposure time 10 s for the hexagonal 2D image and 30 s for the dotted shapes. It was observed that the structure was not completed, and

large portions were destroyed (Figure 9.6). Light absorber did not include in this experiment.

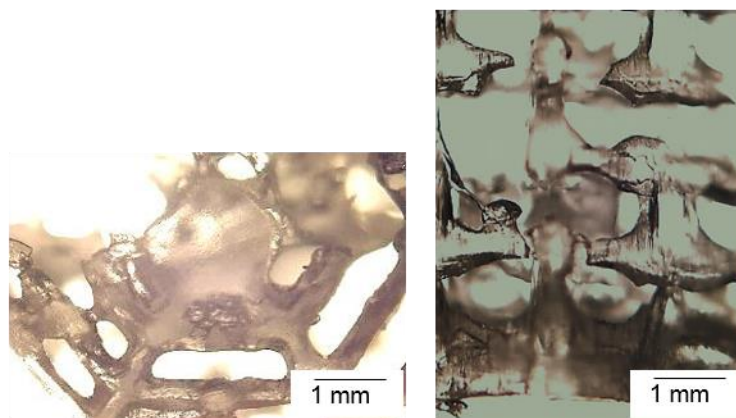


Figure 9.6: Microscopic images of PEG-DA samples from the top (left) and lateral (right) views, using DMD parameters (Z translation speed (0.02 mm/s), laser power (100 mW) and exposure time 10 and 30 s for the hexagonal and dotted images respectively.

Subsequently, different concentrations of light absorber (0.05%, 0.10%, 0.15% and 0.20%) were included with the modified DMD parameters. As shown in figure (9.7), there were clear differences in structures when the serial concentrations of light absorber were used, thereby the structure improved with 0.15% of the light absorber which was the best structure result whereas the structure destroyed with 0.20%. Although the good product in 0.15% light absorber was observed, small parts of the structure were not fully cured. To summarise and compare the results above, table 9.1 clarifies the different findings.

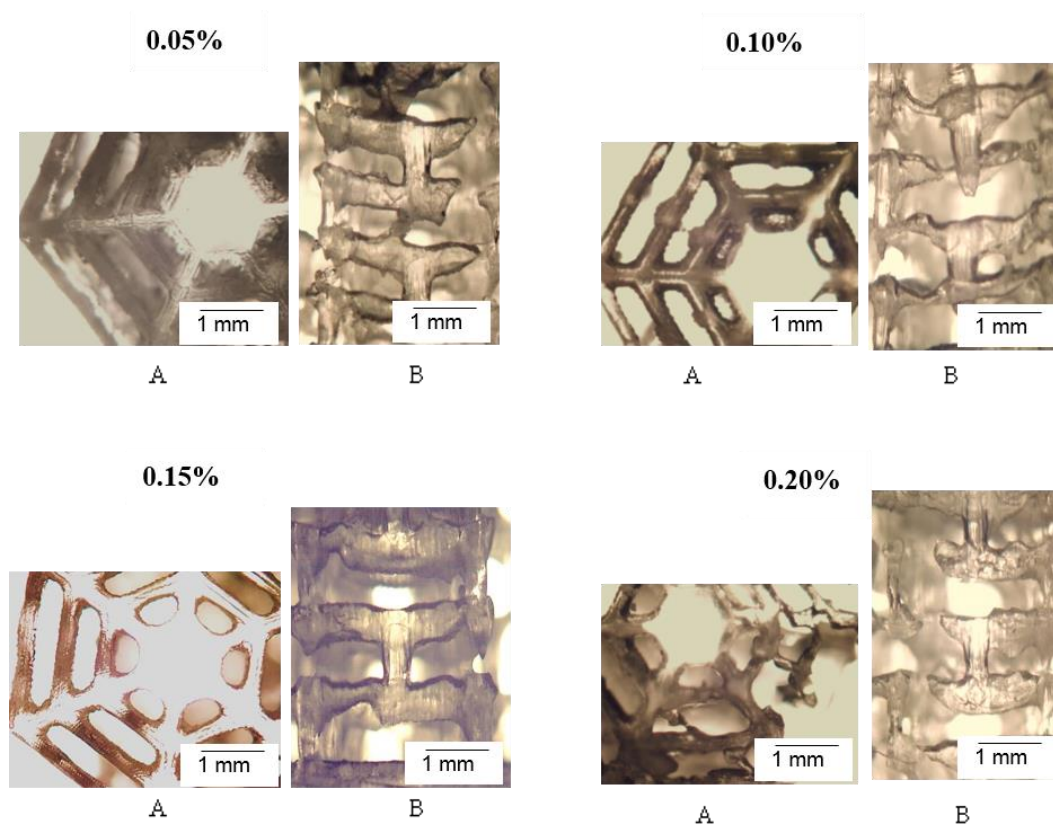
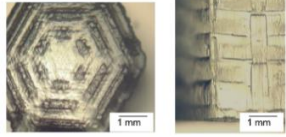
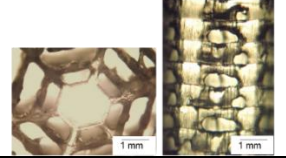
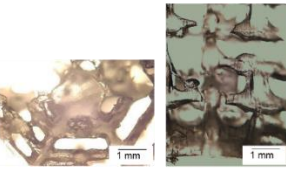
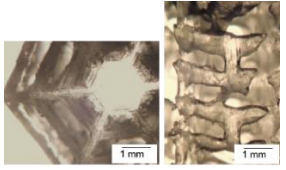
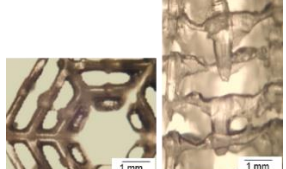
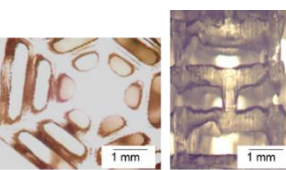
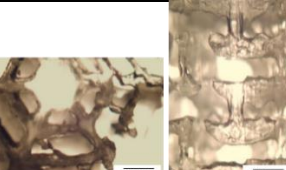


Figure 9.7: Microscopic images of PEG-DA samples from the top (A) and lateral (B) views, using DMD parameters (Z translation speed (0.02 mm/s), laser power (100 mW) and exposure time 10 and 30 s for the hexagonal and dotted images respectively. Different concentrations of light absorber used (0.05, 0.10, 0.15 and 0.20%).

Table 9.1: Comparison of the structure results of PEG-DA samples using microstereolithography with different DMD setup and light absorber concentrations.

Light absorber concentration	DMD parameters			Resulted structure
	Z translation speed	Input laser power	Exposure time	
Non (standard)	(0.01 mm/s)	(60 mW)	25 s for each 2 D image	
0.15	(0.01 mm/s)	(60 mW)	25 s for each 2 D image	
Non	(0.02 mm/s)	(100 mW)	10 s for each hexagonal image 30 s for the dotted images	
0.05	(0.02 mm/s)	(100 mW)	10 s for each hexagonal image 30 s for the dotted images	
0.10	(0.02 mm/s)	(100 mW)	10 s for each hexagonal image 30 s for the dotted images	
0.15	(0.02 mm/s)	(100 mW)	10 s for each hexagonal image 30 s for the dotted images	
0.20	(0.02 mm/s)	(100 mW)	10 s for each hexagonal image 30 s for the dotted images	

### **9.3.4 Discussion**

The work achieved here aimed to evaluate the feasibility of projection  $\mu$ SL to produce complex microporous structures which could be used as a template for metallic dental implant production. A 'spider web' design was invented because it is a suitable way to create a 3D structure with graded and interconnected porosity on a dense core. PEG-DA photocurable resin was selected due to its ability to produce complex scaffold structures (Zheng et al., 2014).

It is well known that the main concern to fabricate complex 3D structures with  $\mu$ SL systems is the uncontrolled penetration of laser into the photocurable pre-polymer. Depending on the results of Choi et.al, who introduced the concept of using light absorber with different concentration (0.00, 0.05, 0.10, and 0.15 %) to improve manufacturing of complex 3D structure using projection  $\mu$ SL setup, resulting in successful different microstructures with higher concentrations of light absorber, this significantly reduced penetration and cure depths. However, the best result obtained for each light absorber percentage were influenced by the geometry of the microstructure (Choi et al., 2009). In this work a lot of effort has been made to improve the resolution of the 3D microstructure with graded and interconnected porosity on a dense core using projection  $\mu$ SL, it was found that the resultant structures significantly influenced by the molecular weight of the PEG-DA. In addition to the DMD parameters and the percentage of the light absorber need to be standardised according to the desired geometry. In an initial experiment, PEG-DA with different molecular weight (250, 500 and 700 g/mol) were used, after many failed experiment it has been decided to use PEG-DA with a low molecular weight (250 g/mol) which produced better structures. This could be related to the low rate of viscosity; thus the pre-polymer can easily flow and settle in-between structure layers. Later, the best result was obtained with 0.15% light

absorber percentage and DMD setup (0.02 mm/s z translation speed, 100 mW laser power and, 10 and 20 s exposure time for the 2D hexagonal and dotted images respectively). Increasing light absorber, laser intensity and z-direction speed were required to provide sufficient polymerisation energy to produce porous microstructures with different layer thicknesses. Increasing the exposure time for each individual layer was necessary to improve overhanging microstructures. However, the overall manufacturing time was increased. The number of layers used can determine the total height of the sample.

Different studies have used  $\mu$ SL with additional coating process to produce metallic and ceramic microlattices with relatively stiff and low density. Electroless nickel plating was suggested to produce metallic hollow-tube nickel- phosphorus (Ni-P) with a metal films thickness ranging (100 nm-2  $\mu$ m). However, the thickness of the coating layer was determined by the plating time. Atomic layer deposition was also used to produce hollow-tube aluminium oxide (amorphous  $\text{Al}_2\text{O}_3$ , alumina) with alumina thicknesses from (40 to 210 nm) (Zheng et al., 2014).

Although the ability of 0.15% light absorber to improve the accuracy of microstructures produced in our study, small parts of hexagonal layers were still not fully cured (Figure 9.7). Therefore, further studies on prolonged exposure time and different photoinitiator percentages would be necessary to improve the accuracy of the resulted porous microstructures.

### **9.3.5 Conclusions**

Preliminary lattices with graded porous geometry on a dense core were fabricated from PEG-DA and projection  $\mu$ SL. The used process is easier, cheaper than the traditional methods as well as less time consuming and with less waste production. Adding 0.15%



of the light absorber to the photocurable prepolymer resin with specified exposure times and intensity was able to reduce penetration depths, thus improved structure result. Even though the light absorber is highly promising, further optimisation of the DMD parameters and photoinitiator is necessary to provide more accurate complex features. It would also be interesting to find out a required coating method to convert these polymeric templates to metallic implants for dental and orthopaedic applications

### **9.3.6 References**

- Bártolo, P., 2005. Virtual modeling and rapid manufacturing : advanced research in virtual and rapid prototyping. Taylor & Francis.
- Chia, H.N., Wu, B.M., 2015. Recent advances in 3D printing of biomaterials. *J. Biol. Eng.* 9, 4.
- Choi, J., Wicker, R.B., Cho, S., Ha, C., Lee, S., 2009. Cure depth control for complex 3D microstructure fabrication in dynamic mask projection microstereolithography. *Rapid Prototyp. J.* 15, 59–70.
- Johnson, D.W., Sherborne, C., Didsbury, M.P., Pateman, C., Cameron, N.R., Claeysens, F., 2013. Macrostructuring of Emulsion-templated Porous Polymers by 3D Laser Patterning. *Adv. Mater.* 25, 3178–3181.
- Narayan, R.J., Doraiswamy, A., Chrisey, D.B., Chichkov, B.N., 2010. Medical prototyping using two photon polymerization. *Mater. Today* 13, 42–48.
- Zheng, X., Lee, H., Weisgraber, T.H., Shusteff, M., DeOtte, J., Duoss, E.B., Kuntz, J.D., Biener, M.M., Ge, Q., Jackson, J. a, Kucheyev, S.O., Fang, N.X., Spadaccini, C.M., 2014. Ultralight, ultrastiff mechanical metamaterials. *Science* 344, 1373–7.

## 9.4 Renishaw system data sheet

Renishaw plc  
Whitebridge Way  
Whitebridge Park, Stone  
Staffordshire ST15 8LQ  
United Kingdom

T +44 (0) 1785 285000  
F +44 (0) 1785 885001  
E additive@renishaw.com  
www.renishaw.com/additive



**Data sheet: laser melting powder titanium alloy Ti6Al4V (grade 23)<sup>[a]</sup>**  
**Processed using AM250 with 200 W laser**

Powder composition / percent by mass								
Ti	Al	V	Fe	O	Residual	C	N	H
Balance	5.5 to 6.5	3.5 to 4.5	<0.25	<0.13	<0.1 each <0.4 total	<0.08	<0.03	<0.0125

**Material Properties**

High specific strength  
High corrosion resistance  
Excellent biocompatibility  
Good osseointegration  
Low thermal expansion  
Low thermal conductivity

**Applications**

Medical implants  
Surgical tools  
Aerospace and defence  
Motor sport  
Jewellery and art  
Maritime applications  
High-end sports equipment

Mechanical data	Stress relieved <sup>[b]</sup>		Test / ISO standard where applicable
	Min	Max	
Tensile strength (UTS) / MPa <sup>*</sup>	1 155	1 197	BS EN ISO 6892-1:2009
Yield strength (0.2%) / MPa <sup>*</sup>	1 070	1 111	BS EN ISO 6892-1:2009
Elongation at break / % <sup>*</sup>	2	8	BS EN ISO 6892-1:2009
Hardness / Vickers HV0.5 <sup>*</sup>	361	376	BS EN ISO 6507-1:1998
Surface roughness in X, Y / R <sub>a</sub> μm	4	6	JIS B 0601-2001 (ISO 97)
Surface roughness in Z / R <sub>a</sub> μm	4	7	JIS B 0601-2001 (ISO 97)
Generic data			
Density	4.42 g/cm <sup>3</sup>		Generic wrought material
Thermal conductivity at 20 °C	6 W/m·K to 8 W/m·K		Generic wrought material
Melting range	1 635 °C to 1 665 °C		Generic wrought material
Coefficient of thermal expansion <sup>[c]</sup>	8 × 10 <sup>-6</sup> K <sup>-1</sup> to 9 × 10 <sup>-6</sup> K <sup>-1</sup>		Generic wrought material

\* Tested by Nadcap and UKAS accredited independent laboratory

Minimum and maximum values quoted are  $\bar{x} \pm \sigma$ , test samples were built in both horizontal and vertical directions.

[a] Also referred to as ELI, Extra Low Interstitial.

[b] 30 μm layers on AM250 and stress-relieved under argon at 730 °C for 2 hours, machined.

[c] Mean between 0 °C and 100 °C.

©2014 Renishaw plc. All rights reserved.  
Renishaw has made considerable efforts to ensure the content of this document is correct at the date of publication but makes no warranties or representations regarding the content. Renishaw excludes liability, howsoever arising, for any inaccuracies in this document.  
RENISHAW and the probe symbol used in the RENISHAW logo are registered trade marks of Renishaw plc in the United Kingdom and other countries.  
apply innovation and names and designations of other Renishaw products and technologies are trade marks of Renishaw plc or its subsidiaries.  
All other brand names and product names used in this document are trade names, trade marks, or registered trade marks of their respective owners.

Issued 0514 Part no. H-5800-0708-02-A

**Renishaw plc**  
Whitebridge Way  
Whitebridge Park, Stone  
Staffordshire ST15 8LQ  
United Kingdom

T +44 (0) 1785 285000  
F +44 (0) 1785 885001  
E [additive@renishaw.com](mailto:additive@renishaw.com)  
[www.renishaw.com/additive](http://www.renishaw.com/additive)



Values quoted are typical values for the AM process.

All information is based on results gained from experience and tests and is believed to be accurate but is given without acceptance of liability for loss or damage attributable to reliance thereon. Users should always carry out sufficient tests to establish the suitability of any products for their intended applications.

No guarantees of machine performance are expressed or implied by these data and Renishaw reserves the right to update them at any time.

©2014 Renishaw plc. All rights reserved.  
Renishaw has made considerable efforts to ensure the content of this document is correct at the date of publication but makes no warranties or representations regarding the content. Renishaw excludes liability, howsoever arising, for any inaccuracies in this document.  
**RENISHAW** and the probe symbol used in the **RENISHAW** logo are registered trade marks of Renishaw plc in the United Kingdom and other countries.  
**apply innovation** and names and designations of other Renishaw products and technologies are trade marks of Renishaw plc or its subsidiaries.  
All other brand names and product names used in this document are trade names, trade marks, or registered trade marks of their respective owners.

Issued 0514 Part no. H-5800-0708-02-A

## 9.5 Material validation sheet of the Renishaw system

Renishaw plc  
Whitebridge Way  
Whitebridge Park, Stone  
Staffordshire ST15 8LQ  
United Kingdom

T +44 (0) 1785 285000  
F +44 (0) 1785 285001  
E [additive@renishaw.com](mailto:additive@renishaw.com)  
[www.renishaw.com/additive](http://www.renishaw.com/additive)



### Renishaw Laser Melting

#### Titanium Ti6Al4V \_30µm\_AM250-200W parameter validation

#### Summary

---

This development report details the validation of the machine parameter set for titanium alloy Ti6Al4V. This parameter set has been optimised for processing in 30 µm layers. The results are valid when processed with parameters H-5800-1016-01-A [RLM Ti64 30 AM250-200W] using Renishaw approved titanium alloy Ti6Al4V powder, part number 791351000.

#### Validated parameters and materials

---

Renishaw provides a range of suitable materials and parameter sets for the AM250 200 Watt additive manufacturing system in a range of layer thicknesses. When Renishaw materials are used with validated parameters on a calibrated Renishaw AM250 machine, along with the guidance provided in our training courses and user guide, the standards described in this document are achievable.

#### Further optimisation

---

As with any manufacturing process it is always possible to optimise to a high standard if certain specifics such as part geometry, post processes, heat treatment, and other part-specific variables need to be achieved. The validated parameters described in this document are designed to meet the highest possible standards across machines but do not fully take into account part-specific variables. On certain components such as dental restorations we have highly developed process optimisation tools and techniques to assist with the further optimisation of part-specific processing parameters, some of these tools are transferable to other geometries and applications. For further information please speak to your Renishaw representative on how our applications teams can work with you to optimise your additive manufacturing process.

#### Open system architecture

---

In addition to the validated parameters described it is also possible for users to develop their own materials using the Renishaw AM250 and software tools. Certain minimum requirements must be met for a material to process in the AM250. It is also a requirement to have access to a range of specialist metallurgical analysis technologies to examine the materials throughout the development process. Without this it is not possible to take informed iterative steps to perfect the material process parameters. Renishaw's advice is for users to ensure that they are aware of these requirements before commencing on a material development program. For further advice on process development, please contact your Renishaw representative who can guide your enquiry to our process engineering team.

©2014 Renishaw plc. All rights reserved.  
Renishaw has made considerable efforts to ensure the content of this document is correct at the date of publication but makes no warranties or representations regarding the content.  
Renishaw excludes liability, howsoever arising, for any inaccuracies in this document.  
RENISHAW and the probe symbol used in the RENISHAW logo are registered trade marks of Renishaw plc in the United Kingdom and other countries.  
apply innovation and names and designations of other Renishaw products and technologies are trade marks of Renishaw plc or its subsidiaries.  
All other brand names and product names used in this document are trade names, trade marks, or registered trade marks of their respective owners.

Issued 0514 | Part no. H-5800-1062-01-A | 1

Renishaw plc  
Whitebridge Way  
Whitebridge Park, Stone  
Staffordshire ST15 8LQ  
United Kingdom

T +44 (0) 1785 285000  
F +44 (0) 1785 285001  
E [additive@renishaw.com](mailto:additive@renishaw.com)  
[www.renishaw.com/additive](http://www.renishaw.com/additive)

**RENISHAW**  
apply innovation™

## Introduction

Titanium alloy has excellent specific strength (strength to weight ratio) which makes it an ideal choice where weight saving load structures are required. It has good corrosion resistance, making it a good substitute for aluminium when bonding to carbon fibre composites. It also has good biocompatibility and has been used for a range of surgical and dental implants.

Ti6Al4V is alloyed with 6% aluminium (Al) and 4% vanadium (V) along with small quantities of iron (Fe) and oxygen (O). Ti6Al4V is the most commonly used grade. Titanium alloys containing nickel, niobium, molybdenum, palladium, and zirconium also exist. Titanium is also used as an alloying element in, for example, high grade stainless steel and aluminium alloys.

Titanium was discovered in 1791, however, due to the difficulty of extracting pure titanium from its oxide (reducing with carbon produces titanium carbide), it was not until the 1930's that commercial extraction using the Kroll process became viable. Although abundant, the lengthy extraction process makes titanium expensive. It was used extensively from the 1950's onwards in high performance aircraft and submarines.

Titanium is used in a diverse range of applications, including medical, jewellery, high performance sports equipment, motor sport, spacecraft, chemical, marine, and extensively in aerospace.

## Material selection

There are numerous grades of titanium alloy and most contain less than one tenth alloying elements; typically aluminium, vanadium, molybdenum. By far the most common is grade 5 which is Ti6Al4V with a maximum oxygen content of up to 0.2%.

Renishaw supplies grade 23, which is often referred to as Extra Low Interstitial (ELI). ELI has maximum oxygen content of 0.13% which improves both ductility and fracture toughness.

Although Ti6Al4V grade 23 offers excellent biocompatibility, Ti6Al7Nb replaces the vanadium alloying element with niobium making it the preferred choice for medical implants.

Corrosion resistance is good, particularly against salt water, making it ideal for marine applications. This is due to rapid oxidation forming a protective passivating layer.

A good combination of strength and elongation can be achieved for Ti6Al4V either by annealing at 730 °C for 2 hours or by hot iso-static pressing at 930 °C for 2 hours at a pressure of 100 MPa.

Resistance to high temperature is reasonable and the alloy can typically be used for applications below 400 °C.

## Shipping



Titanium powder is subject to export control due to its potential military use so an export licence may be required before shipping.  
Titanium powder is also classified as dangerous goods – class 4.1 (flammable solids) which puts constraints on container volume, labelling, and potentially shipping methods.

©2014 Renishaw plc. All rights reserved.  
Renishaw has made considerable efforts to ensure the content of this document is correct at the date of publication but makes no warranties or representations regarding the content.  
Renishaw excludes liability, howsoever arising, for any inaccuracies in this document.  
RENISHAW and the probe symbol used in the RENISHAW logo are registered trade marks of Renishaw plc in the United Kingdom and other countries.  
apply innovation and names and designations of other Renishaw products and technologies are trade marks of Renishaw plc or its subsidiaries.  
All other brand names and product names used in this document are trade names, trade marks, or registered trade marks of their respective owners.

Issued 0514 | Part no. H-5800-1062-01-A | 2

Renishaw plc  
 Whitebridge Way  
 Whitebridge Park, Stone  
 Staffordshire ST15 8LQ  
 United Kingdom  
 T +44 (0) 1785 285000  
 F +44 (0) 1785 285001  
 E additive@renishaw.com  
 www.renishaw.com/additive



### Powder characterisation

To ensure health and safety requirements are met, all metallic powders are to be handled correctly, users must refer to the material safety datasheet before handling the material [H-5800-0923-01-A](#) and ensure a risk assessment is carried out and necessary safety measures implemented.

Particular care should be taken with fine titanium alloy powder. In addition to the potential for the powder itself to combust, there is also the risk of explosive hydrogen gas being liberated on contact with water, acids, or alkalis.

This material validation sheet refers only to results achieved using Renishaw's titanium alloy, Ti6Al4V (part number 791351000). Renishaw cannot guarantee that the same results will be achieved if an alternative powder is used.

Plasma atomized powder is used. The particles are spherical in shape and they are distributed in the 15 µm to 55 µm diameter range.

Powder composition / percent by mass								
Ti	Al	V	Fe	O	Residual	C	N	H
Balance	5.5 to 6.5	3.5 to 4.5	<0.25	<0.13	<0.1 each <0.4 total	<0.08	<0.03	<0.0125

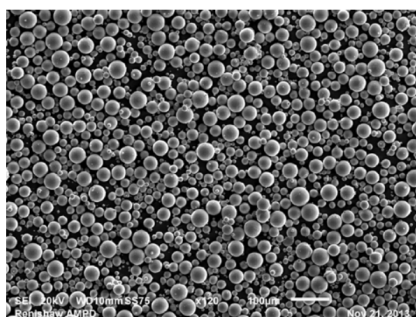


Figure 1 – Scanning electron microscope image of powder at x120 magnification

D10	20 µm to 24 µm
D50	30 µm to 34 µm
D90	46 µm to 50 µm

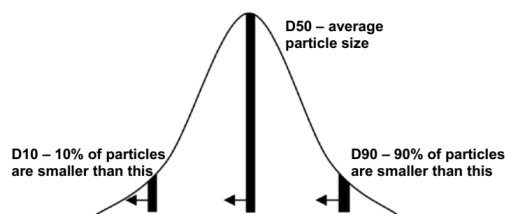


Figure 2 – Particle size distribution analysed by laser diffraction to ASTM B822

©2014 Renishaw plc. All rights reserved.  
 Renishaw has made considerable efforts to ensure the content of this document is correct at the date of publication but makes no warranties or representations regarding the content.  
 Renishaw excludes liability, howsoever arising, for any inaccuracies in this document.  
 RENISHAW and the probe symbol used in the RENISHAW logo are registered trade marks of Renishaw plc in the United Kingdom and other countries.  
 apply innovation and names and designations of other Renishaw products and technologies are trade marks of Renishaw plc or its subsidiaries.  
 All other brand names and product names used in this document are trade names, trade marks, or registered trade marks of their respective owners.

Renishaw plc  
Whitebridge Way  
Whitebridge Park, Stone  
Staffordshire ST15 8LQ  
United Kingdom

T +44 (0) 1785 285000  
F +44 (0) 1785 285001  
E additive@renishaw.com  
www.renishaw.com/additive

**RENISHAW**  
apply innovation™

## Methodology

Optimisation of machine parameters is performed by doing a series of controlled experiments. The machine inputs are characterised as fixed or variable. Multiple experiments are performed using small samples and inspecting for the desired properties (outputs).

To fully understand the interactions between variables a 6 sigma methodology is used, results are statistically analysed to determine the interactions that result in the best possible output. Finally a series of test builds and benchmarks are built for final verification. Mechanical testing is performed by an independent Nadcap and UKAS accredited laboratory to the relevant ASTM standards.

## Machine calibration

All test parts were manufactured on an AM250 machine which was calibrated to the following specification:

Focused laser spot size	Ø 70 µm ± 5 µm
Focused spot circularity	± 5 µm
Laser power at focal plane	200 W ± 10 W
Scanfield – positional correction	± 50 µm over 250 mm

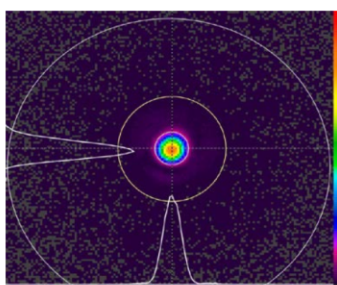


Figure 3 – Beam profile imaging

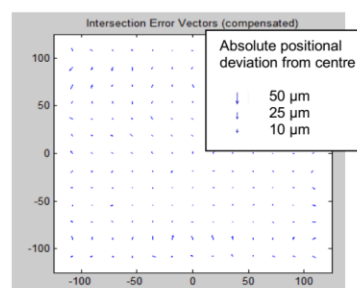


Figure 4 – Scanfield positional correction

To achieve the results described in this validation document a machine calibrated to the Renishaw standard detailed above is a key process foundation. Renishaw cannot guarantee that the same results will be achieved if the AM250 machine used is outside of these calibration values.

## Gas supply

All data published in this document have been gathered from samples processed under an argon atmosphere with purity of 99.998% and less than 1 000 parts per million oxygen content.

Titanium suffers from both oxygen and nitrogen embrittlement at elevated temperatures so the use of argon atmosphere is a key process requirement. It is essential that a low oxygen level is achieved before the build commences: with the AM250 less than 100 parts per million is possible. Renishaw cannot guarantee that the same results will be achieved if another inert gas is used.

©2014 Renishaw plc. All rights reserved.  
Renishaw has made considerable efforts to ensure the content of this document is correct at the date of publication but makes no warranties or representations regarding the content.  
Renishaw excludes liability, howsoever arising, for any inaccuracies in this document.  
RENISHAW and the probe symbol used in the RENISHAW logo are registered trade marks of Renishaw plc in the United Kingdom and other countries.  
apply innovation and names and designations of other Renishaw products and technologies are trade marks of Renishaw plc or its subsidiaries.  
All other brand names and product names used in this document are trade names, trade marks, or registered trade marks of their respective owners.

Issued 0514 | Part no. H-5800-1062-01-A | 4

Renishaw plc  
 Whitebridge Way  
 Whitebridge Park, Stone  
 Staffordshire ST15 8LQ  
 United Kingdom

T +44 (0) 1785 285000  
 F +44 (0) 1785 285001  
 E [additive@renishaw.com](mailto:additive@renishaw.com)  
[www.renishaw.com/additive](http://www.renishaw.com/additive)



## Grain structure

Crack free, dense microstructure was observed. For the as-built samples optical and scanning electron micrograph images revealed martensitic alpha ( $\alpha'$ ) phase in both the horizontal and vertical directions.



Figure 5 – macro image of XY plane at  $\times 27.5$  magnification

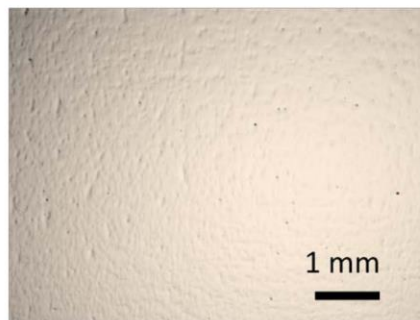


Figure 6 – macro image of XZ plane at  $\times 27.5$  magnification

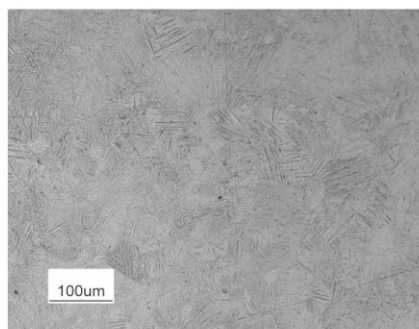


Figure 7 – Optical image of XY plane showing fine martensitic alpha ( $\alpha'$ ) in the as-built sample

©2014 Renishaw plc. All rights reserved.  
 Renishaw has made considerable efforts to ensure the content of this document is correct at the date of publication but makes no warranties or representations regarding the content.  
 Renishaw excludes liability, howsoever arising, for any inaccuracies in this document.  
 RENISHAW and the probe symbol used in the RENISHAW logo are registered trade marks of Renishaw plc in the United Kingdom and other countries.  
 apply innovation and names and designations of other Renishaw products and technologies are trade marks of Renishaw plc or its subsidiaries.  
 All other brand names and product names used in this document are trade names, trade marks, or registered trade marks of their respective owners.

Issued 0514 | Part no. H-5800-1062-01-A | 5



Renishaw plc  
 Whitebridge Way  
 Whitebridge Park, Stone  
 Staffordshire ST15 8LQ  
 United Kingdom

T +44 (0) 1785 285000  
 F +44 (0) 1785 285001  
 E additive@renishaw.com

www.renishaw.com/additive



### Benchmark build results

#### Surface finish

	R <sub>a</sub> / μm	R <sub>z</sub> / μm
As built:		
XY plane	6 to 10	28 to 50
Z plane	7 to 11	39 to 52
Bead blasted:		
XY plane	4 to 6	17 to 30
Z plane	4 to 7	20 to 33

#### Dimensional accuracy

Linear measurement in XY plane

Measurement	Tolerance
10 mm	± 40 μm
20 mm	± 40 μm
30 mm	± 40 μm

#### Fine features

Thin walls  
 Typical: 300 μm\*  
 Minimum: 150 μm\*

\*Depending on orientation, span, and part geometry.

#### Overhang

Permissible unsupported build angle is 45° to the horizontal plane. At this angle the following surface roughness can be expected:

	R <sub>a</sub> / μm	R <sub>z</sub> / μm
As built	12 to 14	60 to 72
Bead blasted	5 to 7	22 to 28

A face less than 45° to the horizontal plane will result in a rougher surface finish or may fail to build unless supports are added.

#### Density

Generic wrought material: 4.42 g/cm<sup>3</sup>

Density of cross section of sample cube: greater than 99.5% with average typically greater than 99.9% (optically determined).

Pores are typically spherical

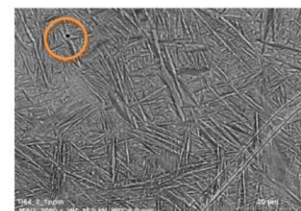


Figure 8 – Scanning electron microscope image showing spherical pore at ×2000 magnification

©2014 Renishaw plc. All rights reserved.  
 Renishaw has made considerable efforts to ensure the content of this document is correct at the date of publication but makes no warranties or representations regarding the content.  
 Renishaw excludes liability, howsoever arising, for any inaccuracies in this document.  
 RENISHAW and the probe symbol used in the RENISHAW logo are registered trade marks of Renishaw plc in the United Kingdom and other countries.  
 apply innovation and names and designations of other Renishaw products and technologies are trade marks of Renishaw plc or its subsidiaries.  
 All other brand names and product names used in this document are trade names, trade marks, or registered trade marks of their respective owners.

Renishaw plc  
 Whitebridge Way  
 Whitebridge Park, Stone  
 Staffordshire ST15 8LQ  
 United Kingdom

T +44 (0) 1785 285000  
 F +44 (0) 1785 285001  
 E [additive@renishaw.com](mailto:additive@renishaw.com)  
[www.renishaw.com/additive](http://www.renishaw.com/additive)



## Tensile test bar results

### Table of mechanical properties

	Horizontal XY <sup>[a]</sup>		Vertical Z <sup>[a]</sup>		Test / ISO standard
	Min	Max	Min	Max	
Tensile strength (UTS) / MPa <sup>*</sup>	1 194	1 197	1 147	1 166	BS EN ISO 6892-1:2009
Yield strength (0.2%) / MPa <sup>*</sup>	1 103	1 113	1 062	1 083	BS EN ISO 6892-1:2009
Elongation at break / % <sup>*</sup>	3	10	2	5	BS EN ISO 6892-1:2009
Modulus of elasticity / GPa <sup>*</sup>	110	116	112	115	BS EN ISO 6892-1:2009
Hardness / Vickers HV0.5 <sup>*</sup>	361	376	361	376	BS EN ISO 6507-1:1998
Hardness/ Rockwell C R <sub>c</sub>	38	39	38	39	BS EN ISO 6507-1:1998

\* Tested by Nadcap and UKAS accredited independent laboratory

Minimum and maximum values quoted are  $\bar{x} \pm \sigma$   
 [a] 30 µm layers on AM250. Samples are stress relieved at 730 °C for 2 hours and machined before testing.

©2014 Renishaw plc. All rights reserved.  
 Renishaw has made considerable efforts to ensure the content of this document is correct at the date of publication but makes no warranties or representations regarding the content.  
 Renishaw excludes liability, howsoever arising, for any inaccuracies in this document.  
 RENISHAW and the probe symbol used in the RENISHAW logo are registered trade marks of Renishaw plc in the United Kingdom and other countries.  
 apply innovation and names and designations of other Renishaw products and technologies are trade marks of Renishaw plc or its subsidiaries.  
 All other brand names and product names used in this document are trade names, trade marks, or registered trade marks of their respective owners.

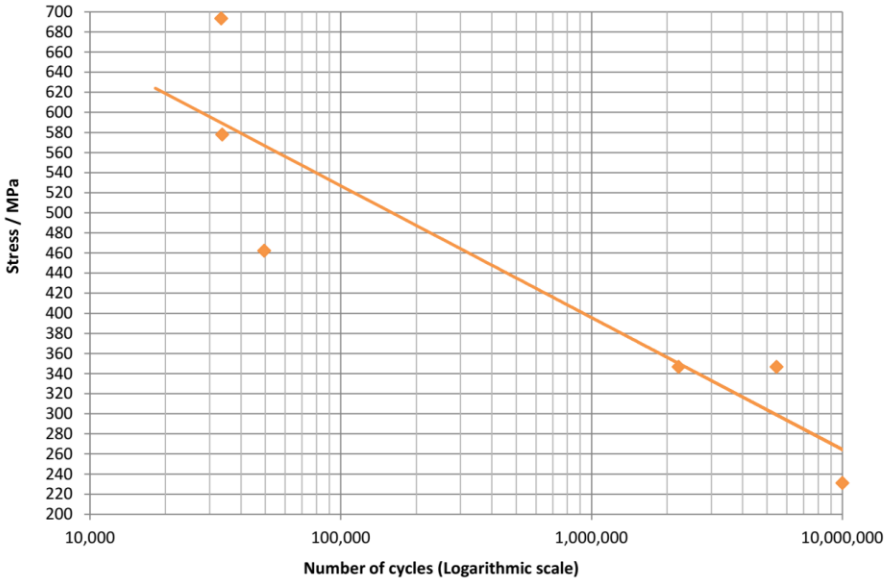
Issued 0514 | Part no. H-5800-1062-01-A | 7

Renishaw plc  
Whitebridge Way  
Whitebridge Park, Stone  
Staffordshire ST15 8LQ  
United Kingdom

T +44 (0) 1785 285000  
F +44 (0) 1785 285001  
E additive@renishaw.com  
[www.renishaw.com/additive](http://www.renishaw.com/additive)



Fatigue Data



Graph 1 – Fatigue test, stress relieved samples

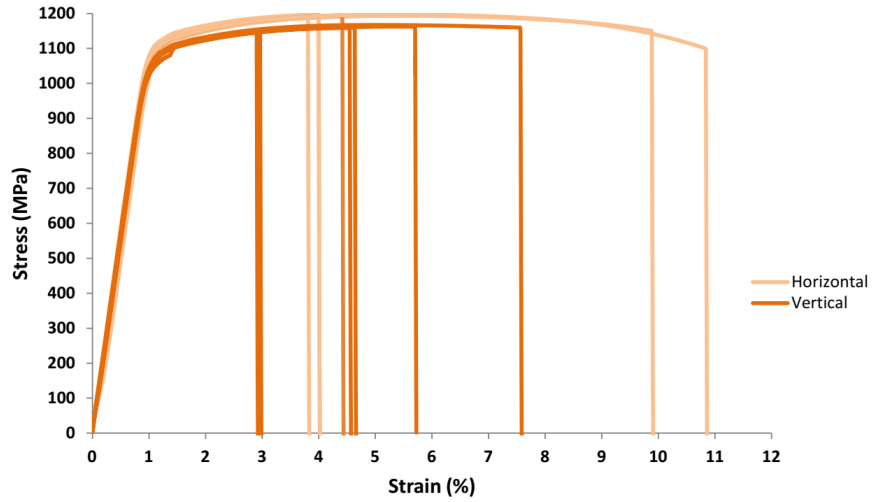
©2014 Renishaw plc. All rights reserved.  
Renishaw has made considerable efforts to ensure the content of this document is correct at the date of publication but makes no warranties or representations regarding the content.  
Renishaw excludes liability, howsoever arising, for any inaccuracies in this document.  
RENISHAW and the probe symbol used in the RENISHAW logo are registered trade marks of Renishaw plc in the United Kingdom and other countries.  
apply innovation and names and designations of other Renishaw products and technologies are trade marks of Renishaw plc or its subsidiaries.  
All other brand names and product names used in this document are trade names, trade marks, or registered trade marks of their respective owners.

Renishaw plc  
 Whitebridge Way  
 Whitebridge Park, Stone  
 Staffordshire ST15 8LQ  
 United Kingdom

T +44 (0) 1785 285000  
 F +44 (0) 1785 285001  
 E additive@renishaw.com  
 www.renishaw.com/additive



Stress – strain curves



Graph 2 – Annealed horizontal (XY) and vertical (XZ/YZ) samples yield at approximately 1 100 Mpa and 1% elongation

©2014 Renishaw plc. All rights reserved.  
 Renishaw has made considerable efforts to ensure the content of this document is correct at the date of publication but makes no warranties or representations regarding the content.  
 Renishaw excludes liability, however arising, for any inaccuracies in this document.  
 RENISHAW and the probe symbol used in the RENISHAW logo are registered trade marks of Renishaw plc in the United Kingdom and other countries.  
 apply innovation and names and designations of other Renishaw products and technologies are trade marks of Renishaw plc or its subsidiaries.  
 All other brand names and product names used in this document are trade names, trade marks, or registered trade marks of their respective owners.

Renishaw plc  
 Whitebridge Way  
 Whitebridge Park, Stone  
 Staffordshire ST15 8LQ  
 United Kingdom

T +44 (0) 1785 285000  
 F +44 (0) 1785 285001  
 E additive@renishaw.com  
 www.renishaw.com/additive



## Heat treatment procedure

All titanium alloy builds benefit from a stress relief heat treatment before removal from the substrate. A wall thickness of more than 10 mm will require a deep build plate (>25 mm). Heat treatment must be performed in an oxygen free and nitrogen free environment (otherwise embrittlement could occur). Argon protective gas shielding is recommended with a flow rate of between 15 l/minute and 20 l/minute. Note that a fresh argon bottle should last 10 hours.

During annealing the  $\alpha'$  microstructures change to lamellar  $\alpha+\beta$  microstructure ( $\beta$  phase is formed as a continuous layer between  $\alpha'$  plates).

After machining a stress relief treatment cycle should be followed.

### Annealing and stress relief

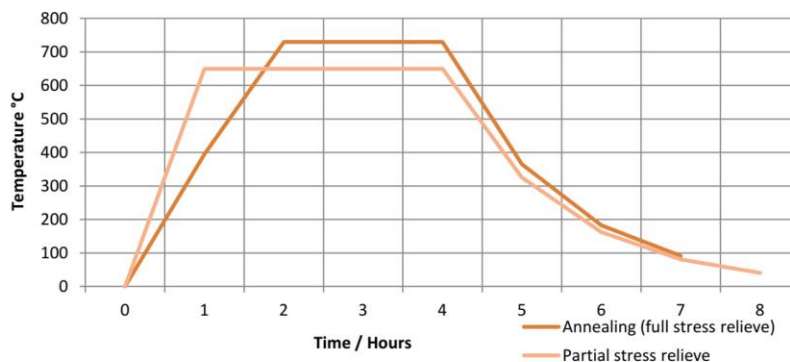
For improved ductility and fatigue strength

1. Heat to between 720 °C and 740 °C over 90 minutes at a constant rate
2. Hold at between 720 °C and 740 °C for 2 hours
3. Slow cool (furnace) to 350 °C before closing off argon gas flow

### Partial stress relief

Whilst maintaining good ultimate tensile strength and hardness

1. Heat to between 650 °C and 670 °C over 60 minutes at a constant rate
2. Hold at between 650 °C and 670 °C for 3 hours
3. Slow cool (furnace) to 350 °C before closing off argon gas flow



Graph 3 – Heat treatment temperatures and timings

## Hot Isostatic Pressing (HIP)

Contact Renishaw for details

©2014 Renishaw plc. All rights reserved.  
 Renishaw has made considerable efforts to ensure the content of this document is correct at the date of publication but makes no warranties or representations regarding the content.  
 Renishaw excludes liability, howsoever arising, for any inaccuracies in this document.  
 RENISHAW and the probe symbol used in the RENISHAW logo are registered trade marks of Renishaw plc in the United Kingdom and other countries.  
 apply innovation and names and designations of other Renishaw products and technologies are trade marks of Renishaw plc or its subsidiaries.  
 All other brand names and product names used in this document are trade names, trade marks, or registered trade marks of their respective owners.

Issued 0514 | Part no. H-5800-1062-01-A | 10